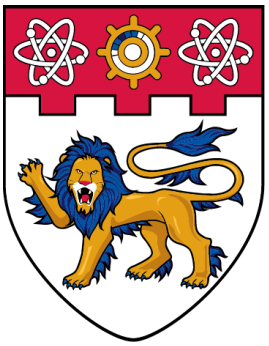

NANYANG TECHNOLOGICAL UNIVERSITY

SINGAPORE

STUDY ON PROCESS PARAMETER OPTIMIZATION FOR ELECTRON BEAM MELTING ADDITIVE MANUFACTURING

WANG CHENGCHENG

SCHOOL OF MECHANICAL AND AEROSPACE ENGINEERING

2020

Study on Process Parameter Optimization for Electron Beam Melting Additive Manufacturing

Wang Chengcheng

Supervised by

Assoc Prof Tor Shu Beng

School of Mechanical and Aerospace Engineering

A thesis submitted to

the Nanyang Technological University

in partial fulfilment of the requirements for the degree of

Doctor of Philosophy

2020

Statement of Originality

I hereby certify that the work embodied in this thesis is the result of original research, is free of plagiarised materials, and has not been submitted for a higher degree to any other University or Institution.

…...30 Jul 2020…...

Date

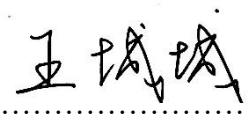

……..

Wang Chengcheng

Supervisor Declaration Statement

I have reviewed the content and presentation style of this thesis and declare it is free of plagiarism and of sufficient grammatical clarity to be examined. To the best of my knowledge, the research and writing are those of the candidate except as acknowledged in the Author Attribution Statement. I confirm that the investigations were conducted in accord with the ethics policies and integrity standards of Nanyang Technological University and that the research data are presented honestly and without prejudice.

……03 Aug 2020…… ……

Date A/P Tor Shu Beng

Authorship Attribution Statement

This thesis contains material from three papers published in the following peer-reviewed journal(s) / from one paper accepted at conferences in which I am listed as an author.

Chapter 2 contains the material from a journal article published as C. Wang, X. Tan, S.B. Tor. Machine Learning in Additive Manufacturing: State-of-the-Art and Perspectives. Additive Manufacturing 36 (2020): 101538.

The contributions of the co-authors are as follows:

- A/P Tor Shu Beng and Dr Tan Xipeng conceived the project and advised the research. Dr. Tan also helped to structure and organize the manuscript.
- I prepared the manuscript draft. The manuscript was revised together with Dr Tan Xipeng, and A/P Tor Shu Beng.
- All the co-authors contributed to the technical discussion.

Chapter 4 contains the material from a journal article published as C. Wang, X. Tan, E Liu, S.B. Tor. Process parameter optimization and mechanical properties for additively manufactured stainless steel 316L parts by selective electron beam melting. Materials & Design 147 (2018): 157-166

The contributions of the co-authors are as follows:

- A/P Tor Shu Beng and Dr Tan Xipeng conceived the project and advised the research. Dr. Tan Xipeng also helped with selective electron beam melting (SEBM) sample fabrication and data analysis.
- I prepared the manuscript draft. The manuscript was revised together with Dr Tan Xipeng, and A/P Tor Shu Beng.
- I performed SEBM sample fabrication, optical and scanning electron microscopy observation, collected X-ray diffraction and electron backscattered data, carried out tensile testing and conducted data analysis.
- All the co-authors contributed to the technical discussion.

Chapter 4 also contains the material from a conference paper published as C. Wang, X. Tan, E Liu, S.B. Tor. Process Parameter Optimization for Additively Manufactured Stainless Steel

316L Parts by Selective Electron Beam Melting. 3rd international conference on progress in additive manufacturing. (2018 May).

The contributions of the co-authors are as follows:

- A/P Tor Shu Beng and Dr Tan Xipeng conceived the project and advised the research.
- I prepared the manuscript draft. The manuscript was revised together with Dr Tan Xipeng, and A/P Tor Shu Beng.
- I performed SEBM sample fabrication, optical and scanning electron microscopy observation, and conducted data analysis.
- All the co-authors contributed to the technical discussion.

The content in Appendix A is published as C. Wang, X. Tan, Z. Du, S. Chandra, Z. Sun, C.H.J. Lim, S.B. Tor, C.S. Lim, C.H. Wong. Additive manufacturing of NiTi shape memory alloys using pre-mixed powders. Journal of Materials Processing Technology 271 (2019): 152-161.

The contributions of the co-authors are as follows:

- A/P Tor Shu Beng and Dr Tan Xipeng conceived the project and advised the research.
- I prepared the manuscript draft. The manuscript was revised together with Dr Tan Xipeng, and A/P Tor Shu Beng.
- I prepared pre-mixed Ni-Ti powder feedstock, performed SEBM printing, optical and scanning electron microscopy observation, collected X-ray diffraction pattern, carried out tensile and compression testing, and conducted data analysis.
- Dr. Sun Zhongji helped with selective laser melting (SLM) sample fabrication. Dr. Du Zehui did differential scanning calorimetry testing. Mr. Joel Lim Choon Wee helped with directed energy deposition (DED) sample fabrication.
- All the co-authors contributed to the technical discussions

…....30 Jul 2020…...
Date

……..
Wang Chengcheng

Acknowledgements

First and foremost, the author would like to express his sincere gratitude to his supervisor Associate Professor Tor Shu Beng for his guidance, constant support and patience over the past four years. Throughout this Ph.D. candidature, Prof. Tor has provided tremendous help and encouragement when the author was faced with challenges in his research works. Besides his essential advice on academic research, Prof. Tor also advised on the author's career plan. The author is genuinely thankful to conduct his Ph.D. study under such a great supervisor. Appreciation is extended to Associate Professor Liu Erjia and Associate Professor Tan Lay Poh for serving as members of the author's Thesis Advisory Committee.

The author would like to give special thanks to Senior Research Fellow Dr. Tan Xipeng for his mentorship and guidance for this work. His knowledge in materials science, insightful research directions and generous help have motivated the author to produce quality results in research. The author would like to thank all other group members, Dr. Kok Yihong, Dr. Sun Zhongji, Mr. Toh Wei Quan, Dr. Chandra Shubham, for their fruitful discussions and support.

The author would also like to express thanks to the technical staffs in Singapore Center for 3D Printing (SC3DP) for providing technical support and maintenance on the additive manufacturing machines: Mr. Daniel Yeo Yin Ping and Mr. Chester Wong Ting Jun. A heartfelt appreciation for the help received from the technical staffs in Materials Lab 1: Mr. Leong Kwok Phui, Ms. Yong Mei Yoke and Ms. Sandy Seah. The author's appreciations are also extended to Mr. Lew Sui Leung Thomas and Mr. Ho Kar Kiat in Materials Lab 2; Mr. Koh Wing Leong, Ms. Tan How Jee and Mr. Yew Ying Yeow in Manufacturing Process Lab 1.

Moreover, the author is thankful for meeting a group of good friends during his Ph.D. journey. He would like to thank Mr. Chiang Po-Ju, Dr. Weng Yiwei, Mr. Gao Shu Bo, Ms. Yang Wenjin, Mr. Huang Sheng, Dr. Tang Chao, Dr. Tan Peng Fei, Dr. Liu Zhixin for their companionship.

Finally, the author would like to give his most profound thanks to his beloved parents. Their tremendous support and unfailing love allowed the author to complete this journey. Their encouragement gave the author strength to reach for the stars and chase the dream.

Table of Contents

Abstract

Electron beam melting additive manufacturing (EBM-AM), also known as selective electron beam melting (SEBM), is a mainstream metal additive manufacturing (AM) technique that employs an electron beam to process metallic powder feedstocks in vacuum environment (~ 10^{-4} - 10^{-5} mbar) at elevated temperatures (~ 500 - 1100 °C). Moreover, due to the high absorptivity and large penetration depth (~ 3 - 4 times of layer thickness) of electrons, SEBM is capable of fabricating parts with high build rates (up to 80 cm^3/hr), minimized oxidation and residual stresses, and mechanical properties comparable to their wrought forms while superior to cast counterparts. However, the list of available materials for processing by SEBM is limited and the conventional method to obtain the optimized SEBM process parameters is by design of experiments (DoE), which is systematic but deficient in time and cost. This study aims at optimizing the process parameters for different metallic materials fabricated by SEBM with superior mechanical properties. Specifically, both the conventional DoE and the emerging machine learning (ML) methods are applied to discover the optimal process window and establish the paramount process-microstructure-property (PMP) relationships.

In the first part, DoE method is employed to optimize the process parameters for SEBM. Stainless steel 316L (SS316L), an austenitic stainless steel popular for laser-based metal AM but less investigated for SEBM, is fabricated by SEBM from the feedstocks with two different powder size distributions. The SS316L parts with flat top build surface and high relative density ($\geqslant$ 99%) are successfully built from the two kinds of powders. The samples fabricated from fine powders (nominal size ~ 20 - 63 μm) exhibit typical columnar-grain microstructure and obvious anisotropy in tensile properties, which are commonly seen in AMed metals and alloys. In contrast, the samples built from coarse powders (nominal size ~ 45 - 106 μm) show near-equiaxed-grain microstructure and isotropy in tensile testing, leading to higher tensile strength (ultimate tensile strength of 634.1 ± 8.6 MPa) and ductility (elongation of 62.8 ± 4.6%) than most of their AM-built counterparts. Secondly, fabrication of equimolar NiTi, an important shape memory alloy (SMA), is attempted by SEBM from pre-mixed elemental powders but to no avail due to the self-sustaining high-temperature synthesis (SHS) that occurs during processing.

In the second part, a ML method is leveraged for fast and precise process optimization with small datasets for SEBM. Firstly, Ti-6Al-4V is chosen to build the baseline ML models, because it is one of the most important lightweight engineering materials and also the most

extensively studied alloy in AM. Ti-6Al-4V samples are fabricated by SEBM with 56 sets of parametric combinations. Various ML models are integrated to predict the optimal process window, where samples are built with ~ 5% higher in ultimate tensile strength and ~ 87% faster in build rate than those processed by Arcam's default parameter setting. Besides, a novel ML-centered tetrahedral framework is proposed to map the paramount PMP relationships over the entire parameter space with deep learning (DL). Secondly, to verify the generalization ability of this method, SS316L is fabricated with only 24 sets of parametric combinations. Transfer learning (TL) is employed to adopt the trained weights from the Ti-6Al-4V baseline models for SS316L datasets. TL could significantly improve the performance of the models and determine the process window for SS316L with high accuracy and short time. This work has demonstrated that the ML method could speed up discovering the optimal process window up to 5 times faster and 10 times cheaper for SS316L. Moreover, the significance and potential industrial applications of the ML-centered tetrahedral framework are depicted in the general discussion chapter of the thesis.

Last but not least, the established ML-empowered methodology for process parameter optimization based on SEBM processing in this study can also be applied to other metal AM processes, such as laser-based powder bed fusion, directed energy deposition and binder jetting.

List of Publications

Peer-reviewed Journal Papers

1. **C. Wang**, X. Tan, E Liu, S.B. Tor. Process parameter optimization and mechanical properties for additively manufactured stainless steel 316L parts by selective electron beam melting. Materials & Design 147 (2018): 157-166.
2. **C. Wang**, X. Tan, Z. Du, S. Chandra, Z. Sun, C.H.J. Lim, S.B. Tor, C.S. Lim, C.H. Wong. Additive manufacturing of NiTi shape memory alloys using pre-mixed powders. Journal of Materials Processing Technology 271 (2019): 152-161.
3. **C. Wang**, X. Tan, S.B. Tor. Machine Learning in Additive Manufacturing: State-of-the-Art and Perspectives. Additive Manufacturing 36 (2020): 101538.
4. **C. Wang**, X. Tan, S.B. Tor, Rapid process parameter optimization and mapping of process-microstructure-property relationships for additively manufactured Ti-6Al-4V alloy with machine learning. Submitted (2021).
5. D.D. Xiang, P.Wang, X. Tan, S. Chandra, **C. Wang**, M.L.S. Nai, S.B. Tor, W.Q. Liu. Anisotropic microstructure and mechanical properties of additively manufactured Co-Cr-Mo alloy using selective electron beam melting for orthopaedic implants. Materials Science & Engineering A 765 (2019): 138270.
6. D.D. Xiang, X. Tan, Z. Liao, J. He, Z. Z, W. Liu, **C. Wang**, S.B. Tor, Comparison of Wear Properties of Ti6Al4V Alloy Fabricated by Wrought and Electron Beam Melting Processes in Simulated Body Fluids. Rapid Prototyping Journal 26 (2020).
7. S. Chandra, X. Tan, R.L. Narayan, **C. Wang**, M. Descoins, D. Mangelinck, G. Seet, A generalized hot cracking criterion for nickel-based superalloys additively manufactured by electron beam melting. Additive Manufacturing 37 (2020): 101633.
8. Z. Sun, X. Tan, **C. Wang**, M. Descoins, D. Mangelinck, S.B. Tor, E.A. Jägle, S. Zaefferer, D. Raabe, Reducing hot tearing by grain boundary segregation engineering in additive manufacturing: example of an AlxCoCrFeNi high-entropy alloy. Acta Materialia 204 (2020): 116505.

Conferences

1. **C. Wang**, X. Tan, E Liu, S.B. Tor. Process Parameter Optimization for Additively Manufactured Stainless Steel 316L Parts by Selective Electron Beam Melting. 3rd international conference on progress in additive manufacturing. 2018 May.
2. S. Chandra, X. Tan, **C. Wang**, Y.H. Yip, G. Seet, S.B. Tor. Additive manufacturing of a single crystal nickel-based superalloy using selective electron beam melting. 3rd international conference on progress in additive manufacturing. 2018 May.

List of Figures

List of Tables

List of Abbreviations

AM ─ Additive manufacturing

ANFIS ─ Adaptive-network-based fuzzy inference system

ANOVA ─ Analysis of variance

BCC ─ Body-centered cubic

BJ ─ Binder jetting

BSE ─ Backscattered electron

BW ─ Boundary wall

CAD ─ Computer-aided design

CAM ─ Class activation maps

CFD ─ Computational fluid dynamics

cGAN ─ Conditional generative adversarial networks

CNN ─ Convolutional neural networks

CV ─ Cross-validation

DED ─ Directed energy deposition

DEM ─ Discrete element method

DL ─ Deep learning

DoE ─ Design of experiments

DT ─ Decision Trees

EBSD ─ Electron backscatter diffraction

EDM ─ Electrical discharge machining

EDS ─ Energy dispersive spectroscopy

ELI ─ Extra low interstitial

FCC ─ Face-centered cubic

FEM ─ Finite element method

FESEM ─ Field emission scanning electron microscope

FO ─ Focus offset

GAN ─ Generative adversarial networks

GP ─ Gaussian process

Grad-CAM ─ Gradient-weighted class activation maps

HCP ─ Hexagonal close-packed

HV ─ Vickers hardness

KNN ─ K-nearest neighbours

MAPE ─ Mean absolute percentage error

ML ─ Machine learning

MLP ─ Multilayer perceptron

OFAT ─ One-factor-at-a-time

OM ─ Optical microscopy

PBF ─ Powder bed fusion

PCA ─ Principal component analysis

PMP ─ Process-microstructure-property

PSD ─ Particle size distribution

ReLU ─ Rectified linear unit

RF ─ Random forest

RGB ─ Red-green-blue

RMSE ─ Root mean square error

RNN ─ Recurrent neural networks

RSM ─ Response surface method

SE ─ Secondary electron

SEBM ─ Selective electron beam melting

SEM ─ Scanning electron microscope

SF ─ Speed function

SHS ─ Self-sustaining high-temperature synthesis

SL ─ Sheet lamination

SLM ─ Selective laser melting

SMA ─ Shape memory alloy

SME ─ Shape memory effect

SS ─ Stainless steel

SVM ─ Support vector machine

TL ─ Transfer learning

UTS ─ Ultimate tensile strength

VAE ─ Variational autoencoder

WD ─ Working distance

XRD ─ X-ray diffraction

YS ─ Yield strength

Chapter 1 Introduction

This chapter provides the background, research motivation and objectives. The organization of the thesis in the form of a brief outline of the contents is also presented at the end of the chapter.

1.1 Background

Additive manufacturing (AM) is a disruptive digital manufacturing technology. It is defined as a process of joining materials to make objects from 3D model data, usually layer upon layer, as opposed to subtractive manufacturing methodologies [1]. Compared to conventional manufacturing technologies, it has the advantages of fabricating intricate parts with complex geometries and designs, unique microstructure and properties, as well as reduced lead time and lower cost (e.g. ~ 30% - 50% cost saving for aerospace titanium structural components in F-35 airframe [2]). Therefore, in recent years, AM has attracted wide research interest in both academic research and industrial applications worldwide.

Metals and alloys are important engineering materials with unique advantages such as a good combination of strength and ductility, high thermal and electrical conductivity. Metal AM can be classified into three broad categories, namely powder bed fusion (PBF), directed energy deposition (DED) and sheet lamination (SL), as summarized in Figure 1.1. PBF can be further categorized into laser or electron beam-based process and sinter-based process. PBF AM system excels in resolution, accuracy, and the ability to create intricate internal passages and geometries. DED consists of two sub-systems, namely powder-fed system and wire-fed system, depending on how the raw material is supplied. DED process can typically create large-scale components with high deposition rate, despite its poor surface finish and low resolution (~ 2 - 2.4 mm [3]). It can also be used for repairing damaged parts. As for SL system, it uses ultrasonic vibration to join dissimilar materials for specific properties and reducing additional cost for post-processing [4].

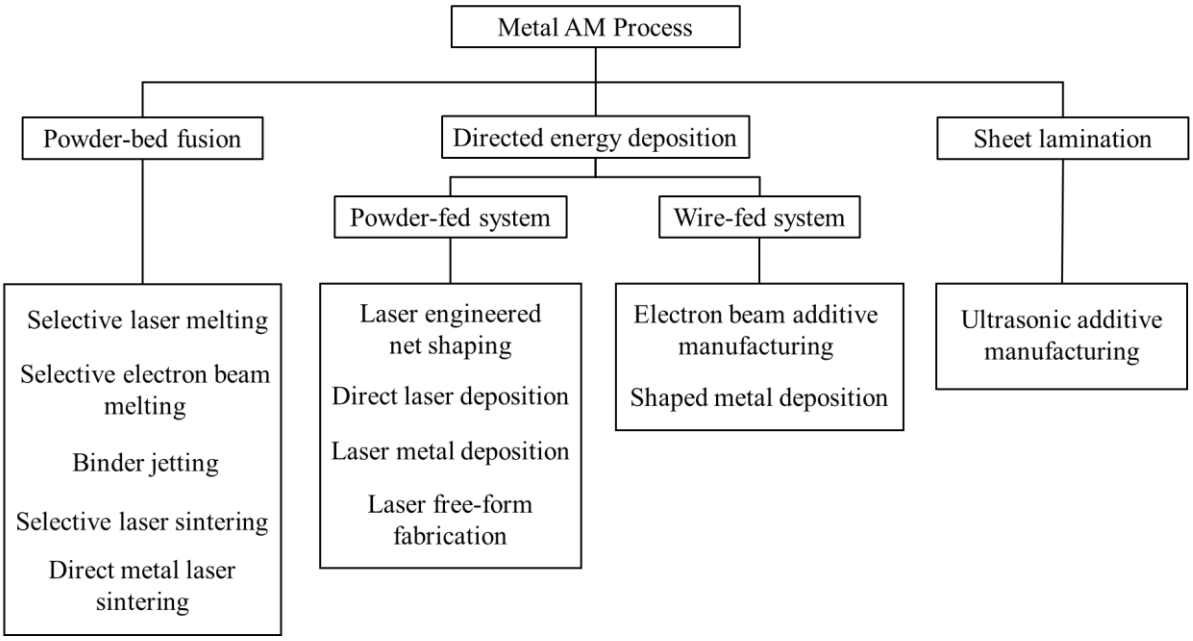

Figure 1.1 Three broad categories of metal AM process.

Electron beam melting (EBM) AM, also known as selective electron beam melting (SEBM), is a representative PBF technology that uses electron beam as the energy source to process metallic powder feedstocks in vacuum environment (~ 10^{-4} - 10^{-5} mbar) at elevated temperatures (~ 500 - 1100 °C). The electron beam can be focused and precisely controlled by electro-magnetic lenses contained in the electron beam unit. The inertial-free movement in SEBM enables the electron beam to travel transversely with a speed up to 10^5 mm/s [5], which implies a relatively higher build rate as compared to selective laser melting (SLM) process. The absorptivity of electron beam for most of the metals and alloys is higher than that of laser beam, as less energy is reflected away from the surface of the metallic powder particles (e.g. 80% in SEBM as compared to 2% in SLM when processing pure copper), which makes it more energy efficient. The large penetration depth of ~ 3 - 4 times of layer thickness using electron beam can mitigate layer defects such as lack of fusion and un-melted powders by a few rounds of re-melting. Moreover, the vacuum environment ensures that almost no oxidation would happen during processing, which is particularly important for processing materials with high affinity to oxygen, such as titanium alloys [5]. Last but not least, the high build temperature can serve as in-process annealing heat treatment, which can help to minimize residual stresses and cracking that resulted from the rapid cooling rate during AM processing [6]. With these unique advantages, SEBM could fabricate orthopaedic implants with minimized impurities, reduced support structures, and high throughput (e.g. 108 acetabular cups per build [7]) as the

parts could be stacked efficiently in a single build. Besides, SEBM can also process high strength-to-weight ratio and heat-resistant but crack-prone materials such as TiAl, which is desirable for jet engine blades. Hence, SEBM technique is favored in fabricating biomedical implants and aerospace components that are subject to stringent requirements and high added value, as demonstrated in Figure 1.2.

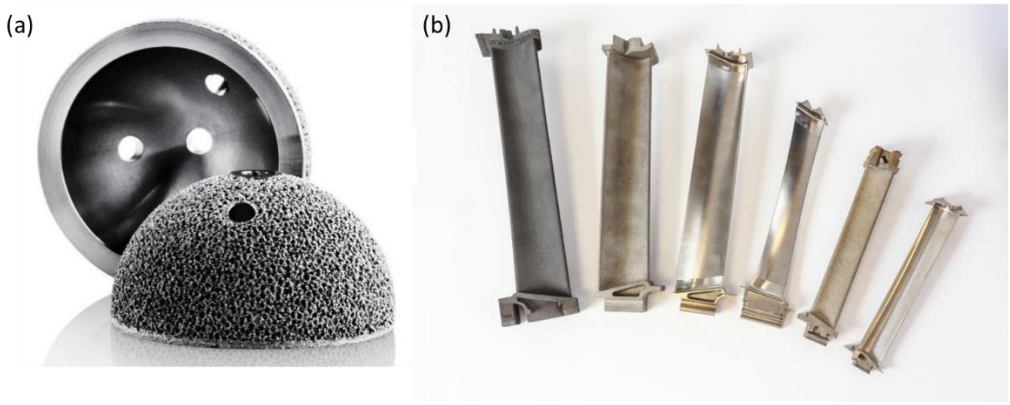

Figure 1.2 EBM-built (a) acetabular cup from Ti-6Al-4V ELI for orthopaedic implantation [8] and (b) TiAl used in low-pressure blades for jet engines [9].

In principle, all kinds of metals and alloys can be processed by SEBM. In this study, three different engineering alloys with a wide variety of industrial applications were chosen, i.e. Ti-6Al-4V, stainless steel 316L (SS316L) and NiTi. The other considerations for the selection of these materials will be explained in section 2.4.1. The three materials used are briefly introduced following the order in terms of their importance. Ti-6Al-4V alloy is reputable for its high specific strength, corrosion resistance and biocompatibility. It is one of the most important lightweight engineering materials in decades with extensive applications in many industry sectors such as aerospace, marine and offshore, and biomedical implants and devices [10]. Despite the potential issue of aluminum loss due to evaporation during processing, SEBM is still a preferred route to process Ti-6Al-4V as titanium has high affinity to oxygen. Although it is an extensively investigated material for SEBM, in this work, a novel machine learning (ML) method will be used to conduct process parameter study for this material. SS316L is an austenitic stainless steel with a face-centered cubic (FCC) crystal structure, exhibiting high strength and ductility. It is also advantageous in weldability, corrosion resistance and biocompatibility. Hence it is widely used in marine and offshore sectors, biomedical devices, automobile industry, petrochemical plants [6]. Despite its wide applications as a structural material, the process parameters were not optimized for SS316L, not to mention two different powder size distributions are used. Lastly, NiTi is the most popular

type of shape memory alloy (SMA) that can recover its original shape through thermal-induced or stress-induced stimuli repeatedly. It is an attractive material for biomedical implants such as bone plates, bone screws and stents [11]. NiTi is a new functional material for SEBM. Besides, high-quality NiTi parts are expected to be fabricated by SEBM, as the vacuum processing environment could minimize the oxidation, and the high build temperature could dissolve the unwanted secondary phases. To additively manufacture any material by any AM technology, process parameter optimization is always the very first step to proceed. Considering the importance and potentially wide applications of the three materials mentioned above, it is of interest to carry out process parameter study firstly in order to fabricate high-performance parts using SEBM technique in the next stage.

Unfortunately, the available materials that can be processed by SEBM are still limited, which has become an obstacle to wide applications of SEBM in metals and alloys. Moreover, the conventional method to obtain the optimized SEBM process parameter is by design of experiments (DoE) which involve a lot of trials and errors, thus is expensive and time-consuming. Numerical simulation may reduce the process optimization time and reveal the underlying physics during processing. However, there is a tradeoff between computational cost and accuracy, depending on the scale and complexity of the models. It is thus imperative to develop a new method that is more efficient and cost-saving to conduct process parameter optimization for SEBM process. ML is a branch of artificial intelligence (AI) that allows a system to learn from data (i.e. in the form of numerical, categorical or image data under the context of AM), identify patterns and make decisions without being explicitly programmed. In recent years, ML has gained increasing attention in AM due to its unprecedented performance in data tasks such as classification, regression and clustering [12]. Therefore, it is meaningful to explore the applications of data-driven ML techniques in SEBM processing, which will aid the development of new ML-assisted method for process parameter optimization on top of the conventional DoE method.

1.2 Research Motivation and Objectives

The overall aim of the current Ph.D. thesis is to carry out process parameter optimization of different metallic materials in order to fabricate metal parts with superior mechanical properties via SEBM. The motivation of this research is to investigate the most

effective way to optimize the process parameters and establish the process-microstructure-property (PMP) relationships, which will expedite the materials development for SEBM in the long run.

There will be two main objectives for the current Ph.D. work. The first objective is to use the conventional DoE method to optimize process parameters for SS316L via SEBM and conduct a qualitative study of the PMP relationships. The second objective is to develop a ML method for fast and precise process parameter optimization for Ti-6Al-4V and SS316L and quantitatively map the PMP relationships with high accuracy.

The property herein refers to tensile property. The term process parameter optimization is used interchangeably with process development in this thesis.

1.3 Organization of Thesis

- Chapter 1 introduces the research background, motivation and objectives of this study.
- Chapter 2 reviews the literature on the mainstream metal AM technologies and SEBM process. The detailed processing and key process parameters of SEBM are highlighted. The powder feedstocks and the current research status on materials development for SEBM are summarized. Particularly, the classification of the materials that can be processed by SEBM is described and justified. The materials used in the current Ph.D. study, including Ti-6Al-4V, NiTi and SS316L alloys, are introduced. The various methods applicable to SEBM process parameter optimization are elaborated. Moreover, the principles and state-of-the-art applications of DoE and ML techniques in AM process parameter optimization are comprehensively reviewed. Lastly, it concludes with the scope as well as research roadmap to achieve the stated research aim and objectives of this Ph.D. study.
- Chapter 3 describes the experimental procedures and methods used in this study.
- Chapter 4 investigates the DoE-based process parameter optimization, microstructure characterization and mechanical properties of SEBM-built SS316L alloys using both fine and coarse powders.
- Chapter 5 demonstrates the ML method for fast and precise process optimization with a small dataset and mapping of the complex PMP correlations for SEBM-processed Ti-6Al-4V alloy.

- Chapter 6 validates the generalization ability of the ML method by using the pre-trained weights from Ti-6Al-4V baseline models to predict the process window for SS316L alloy with an even smaller data through transfer learning (TL).
- Chapter 7 discusses the in-chapter and cross-chapter links of the various studies conducted in this thesis. Specifically, the efficiency of using DoE and ML methods is quantitatively assessed and compared. The contributions of this work to both academic advance and industrial relevance in the global picture of AM are elaborated.
- Chapter 8 concludes the present Ph.D. work, discusses the limitations and recommends the future works.

It should be noted that the work for process parameter study for pre-mixed NiTi powders using SEBM is placed in Appendix A due to its general lack of success. Nevertheless, it is still a part of the thesis. It comprehensively reveals the mechanism accounting for the phenomena described, which will be useful for the investigators who are inclined to attempt this.

Chapter 2 Literature Review

Based on the aim, motivation and objectives, a literature review is conducted to systematically and comprehensively overview the processing, materials and methodology aspects of AM. This chapter presents the literature published pertaining to this area. More specifically, the four mainstream powder-based metal AM processes are introduced. A comprehensive understanding of SEBM processing at different stages are reviewed. The scanning strategy and the two key process parameters are elaborated. The requirements of the powder feedstocks that are suitable for SEBM processing are explained. The classification of the materials processable for SEBM is justified and summarized afterwards, emphasizing the need for materials development. The crystal structures, phases, microstructures, mechanical properties and applications of the three materials studied in this Ph.D. work are discussed. Next, the prevailing methods adopted for SEBM process parameter optimization are summarized. The next two sections comprehensively review the principles and applications of the state-of-the-art DoE and ML methods in optimizing the AM process parameters. Lastly, the research gap is analyzed, and a detailed research roadmap is presented to achieve the proposed research aim and objectives.

2.1 Metal Additive Manufacturing

The mainstream metal AM techniques that have been adopted for industrial applications include directed energy deposition (DED), selective laser melting (SLM), selective electron beam melting (SEBM) and binder jetting (BJ). In powder-based DED process, a continuous powder stream is injected from the deposition nozzle into the molten pool and is simultaneously melted by a focused laser to fabricate net-shape parts [13]. SLM also employs laser to selectively melt the powder bed which is uniformly distributed by re-coater in a layer-wise manner [14]. SEBM uses high energy electron beam to selectively melt metallic powder bed in vacuum environment and at elevated temperatures [6]. Instead of using laser or electron beam as an energy source, BJ creates 3D objects by selectively depositing liquid binder droplets to join the metal powder particles to form near-net-shape 'green' parts, which are subsequently sintered in a furnace or infiltrated with a low melting-point metal [15]. The schematics of the above four processes are shown in Figure 2.1.

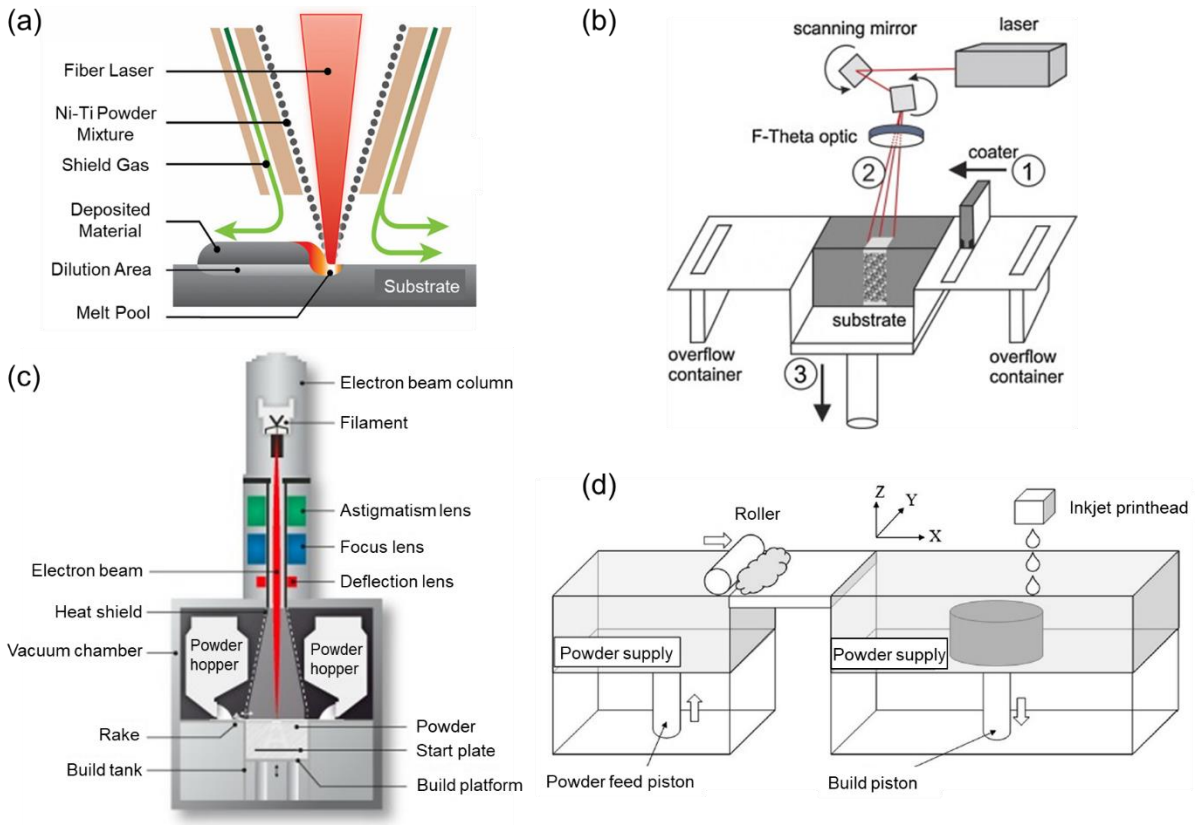

Figure 2.1 Schematic illustrations of (a) DED process [16], (b) SLM process [17], (c) SEBM process [18] and (d) BJ process [15].

A general discussion of the advantages and disadvantages of the above-mentioned four metal AM processes is as follows. The data used here are extracted from the machine specifications of SLM250HL [19] from SLM Solutions, Arcam EBM A2X [20] from Arcam AB, Magic 800 with 24V× deposition head [3] from BeAM and X125Pro [21] from ExOne. They are representative machine systems from reputable machine suppliers in SLM, SEBM, DED and BJ process, respectively. The data that cannot be found from the datasheets are cited from literature. It should be noted that as the technologies in metal AM are advancing rapidly, the data provided herein are updated by the time of writing. SLM and SEBM processes are compared as these two PBF techniques have many commonalities except for the energy source and build environment. SLM typically creates parts with higher accuracy (± 0.02 to 0.1 mm for SLM and ± 0.2 mm for SEBM [22]) and smoother surface finish (Ra ~ 10 - 12 for SLM and ~ 25 - 35 for SEBM [23]), due to the smaller particle size used (typically ~ 15 - 45 µm or 20 - 63 µm for SLM and ~ 45 - 106 µm for SEBM) and smaller beam spot size (≥ 75 µm for SLM and ≥ 250 µm for SEBM). SEBM processes materials in vacuum environment (10^{-4} to 10^{-5} mbar) with higher penetration depths (~ 3 - 4 times of layer thickness) and faster scanning speeds (up

to 8,000 mm/s) during melting, as well as elevated temperature (up to 1100 °C), which results in low impurity, faster build rate (up to 80 cm^3/hr [24]) and minimized residual stress. Nevertheless, its accuracy and surface roughness are still inferior to SLM process. Despite the poor surface finish and low resolution (~ 2 - 2.4 mm), DED is believed to offer a higher build rate (~ 90 - 130 cm^3/hr) and can build large-scale parts (up to 1 m level). BJ is a beamless process where thermal processing is not involved during printing, so it does not face issues such as residual stress and warping [25]. Besides, it can be adopted to process a wider variety of materials, including metals, ceramics and polymers. However, BJ suffers from either high porosity (~ 4%) or high shrinkage (~ 15% in the case of printing SS316L) after sintering, which is a tradeoff [26]. These disadvantages can be minimized through the infiltration of a lower melting point material during sintering. Nevertheless, the mechanical properties of the BJ-built parts after post-processing are still inferior to those fabricated by laser or electron beam AM techniques.

2.2 Selective Electron Beam Melting

SEBM, as depicted in Figure 2.1 (c), is an important type of powder-bed fusion metal AM technology developed and patented by Arcam AB in Sweden, where their first unit was sold in 2002. SEBM uses a high-energy electron beam to selectively melt the metallic powders layer by layer directed by computer-aided design (CAD) models [27, 28]. SEBM process is performed in vacuum environment (10^{-4} - 10^{-5} mbar) with a typical power of up to 3 - 6 kW. Electrons are generated from a tungsten filament or a lanthanum hexaboride LaB_6 cathode and then focused and accelerated to approximately half of the speed of light through electromagnetic fields [29]. When the high-speed focused electron beam impacts on metallic powder, the kinetic energy is converted to local heating of high temperature, which melts the metal powder granules [30]. Comparing to its laser-based AM counterparts, such as SLM and DED, SEBM has the advantages of building parts with superior comprehensive tensile properties, i.e. a good combination of strength and ductility (as for examples in the case of fabricating Ti-6Al-4V alloys in Table 2.1), low residual stress and low impurity [31]. Despite the extensive advantages against conventional manufacturing methods, SEBM still exhibits some process deficiencies, including process instability, poor surface finish and dimensional accuracy [31, 32].

Table 2.1 Comparison of yield strength (YS), ultimate tensile strength (UTS) and elongation among SEBM-built Ti-6Al-4V samples and their laser metal AM-processed counterparts found in literature.

Sample	YS (0.2% offset) (MPa)	UTS (MPa)	Elongation (%)
SEBM (as-built) [33]	870 ± 8.1	971 ± 3.1	12.1 ± 0.8
SLM (as-built) [34]	1093 ± 64	1279 ± 13	6 ± 0.7
DED (as-built) [35]	976 ± 24	1099 ± 2	4.9 ± 0.1

One particular issue associated with SEBM processing is the chemistry control for alloys with elements of widely different boiling and vaporization characteristics, such as Ti-6Al-4V and TiAl alloy. Since the powder feedstocks are heated to a very high temperature under vacuum environment, evaporation loss of the constituting elements with high vapor pressure needs to be considered [5]. As a result, the chemical composition of the SEBM-processed parts will be altered, thus affecting the microstructure and mechanical properties. It is therefore necessary to minimize the evaporation loss during processing via careful selection of process parameters. Juechter et al. [36] have systematically probed into the evaporation loss of aluminum (up to ~ 30 wt.%) in SEBM processing of Ti-6Al-4V as a function of process parameters. Schwerdtfeger et al. [37] have adopted suitable beam parameters and process strategies to minimize the aluminum loss to ~ 0.5 at.% during SEBM processing of Ti-48Al-2Nb-2Cr.

2.2.1 Overview of Selective Electron Beam Melting Building Process

The overall SEBM building process consists of four steps, namely start-plate heating and outgassing, sintering of powder under start-plate, layer melting, and cooling down. A typical time-temperature graph is presented in Figure 2.2.

In the context of SEBM processing, sintering refers to employing a defocused electron beam to rapidly scan the entire area of the start-plate in order to bind the loose powder particles over and under the start-plate. By sintering, the thermal and electrical conductivity of powder bed can be enhanced, thus improving the melting stability. In the melting stage, the focused electron beam with a high energy density is used to fully consolidate the powder bed selectively. After the build is completed, if heat treatment is required, the defocused electron beam can

continue to input energy to allow the powder bed to achieve the desired temperature, which effectively provides solution, aging and annealing heat treatment in the vacuum environment.

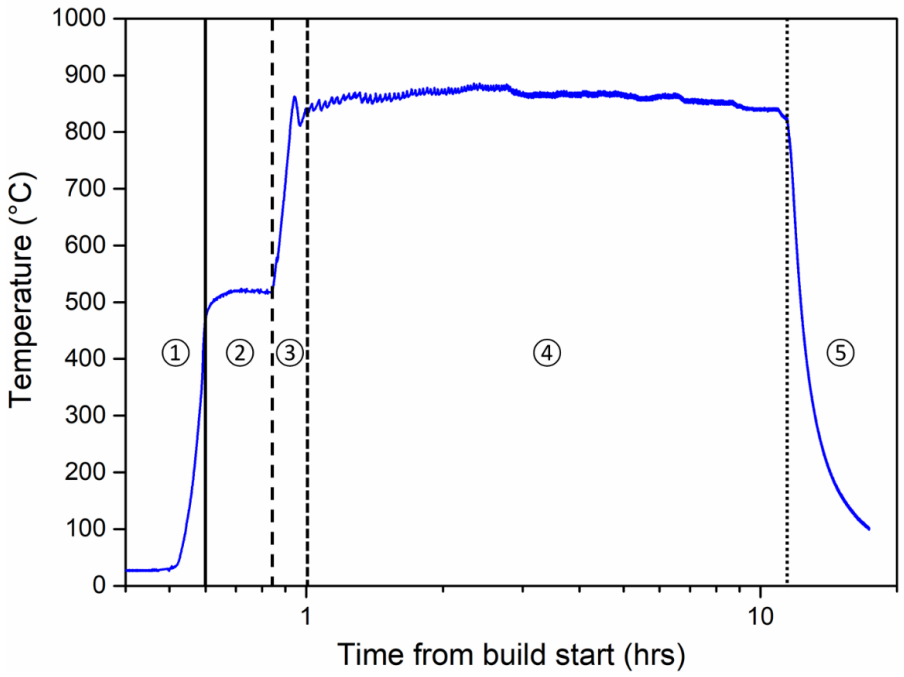

Figure 2.2 A typical time-temperature curve during SEBM process with the steps including 1. initial heating; 2. outgassing; 3. sintering; 4. layer melting; 5. cooling down.

At start-plate heating step, a defocused electron beam rasters rapidly over the entire area of start-plate to heat it up. Afterwards, the electron beam increases the energy input to the start-plate until it reaches the desired temperature. This temperature is measured by the thermocouple placed underneath the start-plate. This heating process ensures that the start-plate can be secured in the powder bed, so that it will not be shifted by the moving rake in the layer melting process. In this step, the desired temperature is defined by the user, which primarily depends on the material properties. This temperature is typically around 300 °C for Cu, 600 °C for Ti, 730 °C for Ti-6Al-4V, 850 °C for CoCr, 1100 °C for TiAl and some Ni-based alloys [5, 38, 39]. It should be noted that sintering test should be carried out to determine the desired temperature for new materials.

Layer melting is the most important step where the parts are built by SEBM, which will be detailed in the next section. After the build is completed, the entire powder bed is cooled down. The cooling down stage can be modified by the user. The default mode allows the parts to cool down via conduction and radiation mode until it reaches below 200 °C, then helium is pumped into the build chamber to provide convection to facilitate cooling. The chamber door

is only allowed to be opened when the build is cooled below 100 °C. Alternatively, in-situ heat treatment can be opted with a defocused electron beam [40].

2.2.2 Layerwise Melting Process

Layerwise melting is the most crucial stage of SEBM process, as it directly determines the success of the build. For each layer of the build, it is iterated through raking, preheating I, preheating II, contouring, preheat post-heating, hatching, and melt post-heating (see Figure 2.3).

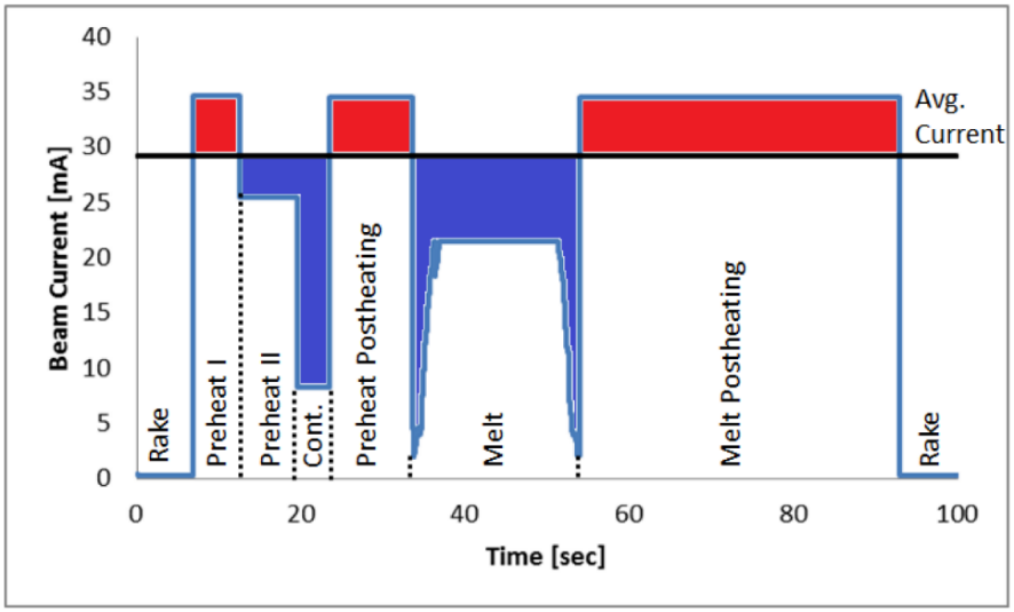

Figure 2.3 A representative graph of each stage in layered melting with the corresponding beam current [40].

After the build table moves one step downwards, the powder is uniformly distributed on the start-plate by the rake blade. This process is termed as raking.

Preheating (see Figure 2.4 (a)) is used to sinter the new layer of powder distributed over the start-plate in order to increase the thermal and electric conductivity of powder bed, so that a powder explosion will not occur due to the repulsive force of electrically charged powders. In addition, the negative charges from the powder bed can also be dissipated by the positively ionized He atoms supplied by the inflow helium of up to 2×10^{-3} mbar under Control Vacuum mode [38]. Meanwhile, the sintered powder bed can also provide mechanical support for the parts during the building process. In preheating I, a defocused electron beam rapidly

scans the entire area of the start-plate several times, so that the new layer of applied powder can be sintered. Preheating II is a localized heating process which selectively heats the area that closely corresponds to the geometry of the part, which enhances the sintering of powder bed, although this step is optional.

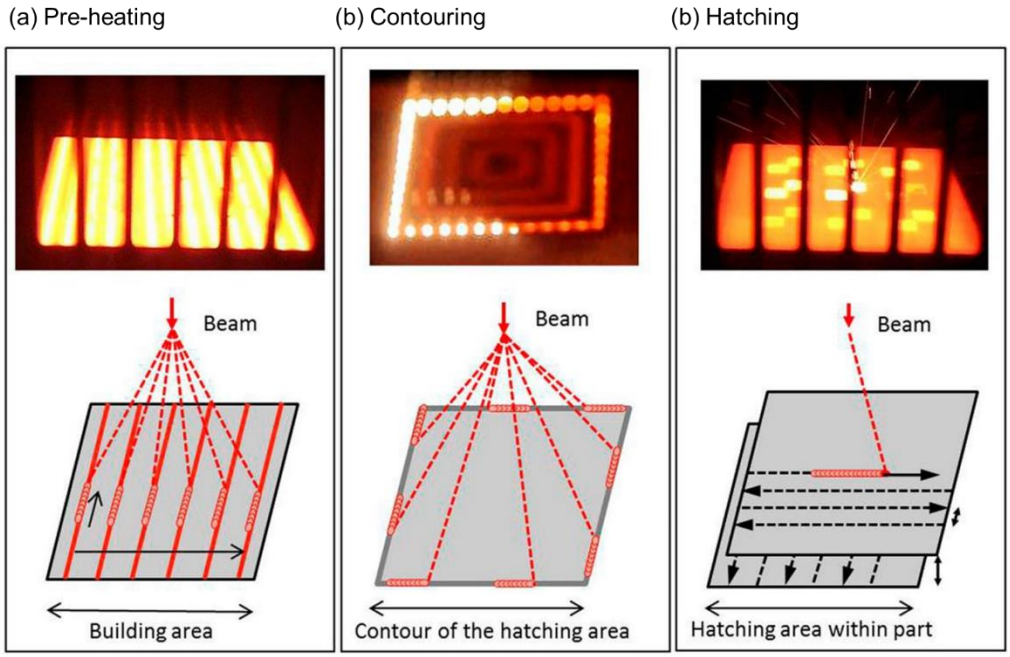

Figure 2.4 The real melting process with the corresponding schematic illustration on the movement of the electron beams. The three basic steps are (a) pre-heating, (b) contouring and (c) hatching [5].

In preheat I and II stages, a few important parameters are line order, line offset, beam speed, focus offset (FO) and beam current. Line order defines the order that electron beam travels along scan lines, as schematically illustrated in Figure 2.5. In this manner, the time between adjacent scan lines can be maximized. Increasing line order decreases energy input for sintering the powder bed [41]. Line offset is the distance between two hatch lines. Increasing the line offset decreases energy input as well. Arcam's EBM requires the relationship below to be satisfied when setting the abovementioned parameters (see Eq. 2.1). Size refers to the size of the reference square; it is the effective zone where the electron beam scans on start-plate. Beam current can be further divided into max/min and average current. When the auto-calculation is enabled (i.e. EBM Control software automatically adjusts the beam current and bean speed on the fly to ensure a constant surface temperature during melting), which is highly recommended for EBM process, it will be the max/min current for the reference square set in EBM Control. Usually, max current is equal to min current. Average current is the mean current for the entire layer melting process, which is used for energy balancing. To

achieve this, the area of preheating I and preheat post-heating above the average must be equal to the area below for preheating II and contouring, and the area of preheating I and melt post-heating above the line must match that below for preheating II, contouring and melting, as indicated in Figure 2.3. Increasing the average current will prolong the post-heating process in order to achieve the target average value, which also effectively increases the build temperature. However, an excessively high build temperature may make the removal of sintered powder cake difficult and is bad for the mechanical properties of some materials.

$$\frac{size}{line\ order \times line\ offset} = even\ number \qquad \text{Eq.2.1}$$

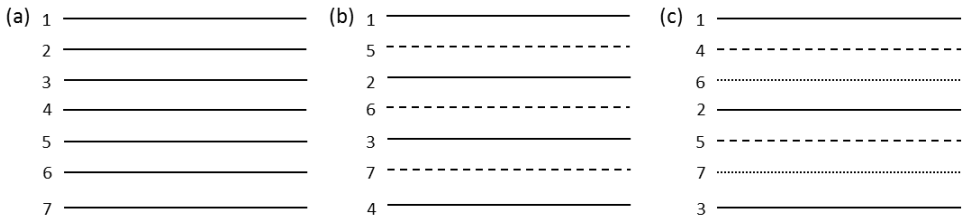

Figure 2.5 Schematic of (a) a line order of 1 (b) a line order of 2 (c) a line order of 3. The numbers represent the order that electron beam travels along the path.

Preheat post-heating and melt post-heating are utilized to compensate for the energy loss which takes place in preheat II, contouring and melt steps. Hence, similar to preheating I, the heat input in post-heating process is also applied to the entire area of the start-plate. It is noteworthy that once the start-plate temperature reaches the desired temperature in the sintering stage, the temperature feedback is no longer used for the remainder of the process. Therefore, an auto-calculation for energy balance is done by the EBM Control algorithm to maintain a constant surface temperature of the parts. A more stable temperature can be achieved if post-heating is performed after each individual part is melted.

Melting consists of two processes, namely contouring (see Figure 2.4 (b)) and hatching (see Figure 2.4 (c)). The beam is at its most focused position for contouring and slightly defocused for hatching. The order of contouring can be swapped with hatching. During contouring, similar to preheating, the beam current and speed do not deviate from the values input by the user [42]. In contouring process, a focused electron beam is used to melt the borders of the parts, where three contours are typically used. This process determines the side surface quality of the as-built parts [40].

In melting process, the default scanning strategy (see Figure 2.6) is interlayer cross snake-shaped scan line [36]. As the melt pool width is larger than hatch spacing, on the same layer, the previously melted and solidified melt pool was partially re-melted by the subsequent scan line. The adjacent melt pool was partially overlapped, thus forming the wavy melt track morphology when observed along the scan line direction. The scanning direction rotates by 90° after each layer [43], and the electron beam drives the melt pool to move along scanning directions, thus producing smooth melt tracks when observed normal to the scan line direction. Such scanning pattern helps to produce more uniform microstructure with less residual stress [44]. It should be noted that the melt pool shape of layer n is askew to the left, while it is askew to the right for layer (n-2). This is owing to the algorithm of scanning strategy in Arcam software, which rotates the scanning start position anticlockwise between layers. One cycle of rotation completes in every four consecutive layers.

In laser PBF processing, the important process parameters include power input, scanning speed, hatch spacing and layer thickness, which determine the volumetric energy density [45]. In SEBM processing, the power input is fixed at 3 kW, and the scanning speed is controlled by speed function (SF), which will be detailed below. Hatch spacing and layer thickness significantly affect the quality of fusion between adjacent melt tracks and layers. The two parameters are usually set at 0.1 mm for hatch spacing and 50 μm for layer thickness by Arcam and other EBM users, which are determined from the practical experience of balancing the quality of fusion and build speed. There is an additional parameter which determines the spot size of the electron beam, namely focus offset (FO). Hence, considering the abovementioned factors, to develop parameters for new materials in SEBM processing, the key parameters for melting process include FO and SF, as also suggested by Arcam.

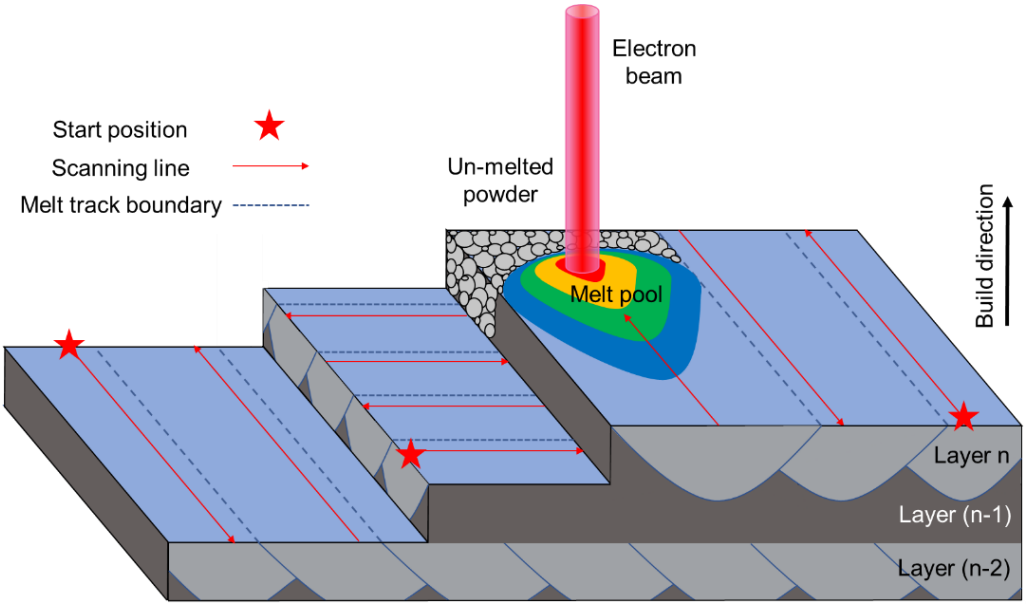

Figure 2.6 Relationship between interlayer cross S-shape scanning strategy and melt track morphology for SEBM as-built samples in three consecutive layers. Scanning direction is indicated by the red arrow [6].

Focus Offset (FO)

FO is the additional current running through the respective coil and can be translated into an offset of the focal plane from its zero position [46]. It can be set to zero, positive or negative values, where the focal plane is on, above or below the melt surface, respectively (see Figure 2.7). Al-Bermani [41] has discovered that the electron beam is not symmetric about the focal point. More specifically, a negative FO is more defocused than its equivalent positive value. Different SEBM systems may require different optimum value for FO. A change in beam diameter of around 50 µm can be achieved by changing FO in the range of ±10 mA, according to Schwerdtfeger et al. [47]. In general, a larger FO produces a wider but shallower melt pool, provided that the energy is sufficient to melt the powder. The depth of melt pool is essential to ensure good bonding between layers.

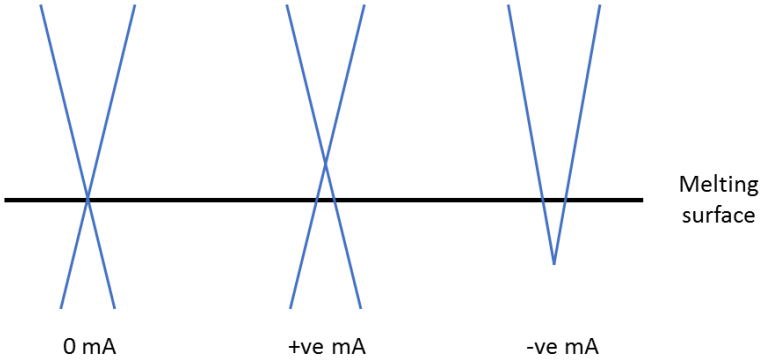

Figure 2.7 Schematic of focus offset (FO) at zero, positive and negative values.

Speed Function (SF)

In the melting process, beam current and beam speed cannot be directly set by the user. Instead, it is automatically calculated by EBM Control software. During hatching, beam current varies linearly with the length of hatching line, so a lower beam current is applied to shorter hatching line in order to avoid over-heating. This is termed as current compensation in EBM algorithm. A change in beam current is accompanied by a change in SF in order to maintain a constant melt pool size and depth [42]. For example, an increase in beam current is accompanied by an increase in beam speed, so that the effect of an increase in beam power can be negated [41]. From Figure 2.8 (a), it can be observed that SF is nonlinear. As its value increases, the nonlinearity becomes more pronounced. Conversely, at a given current, the beam speed increases linearly with SF, as shown in Figure 2.8 (b). In general, when other parameters are fixed, a higher SF corresponds to a lower energy density and smaller melt pool size.

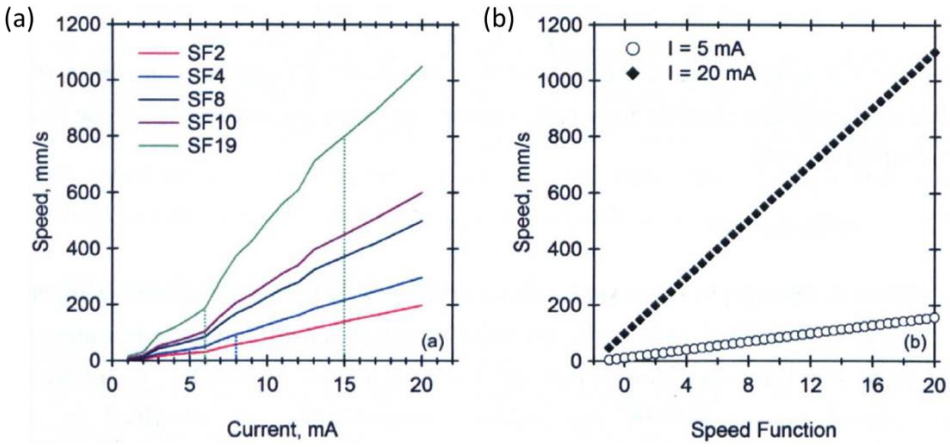

Figure 2.8 An illustration of the relationship between (a) speed and current; (b) speed and speed function at a given current [41].

2.3 Powder Feedstock for Selective Electron Beam Melting

SEBM is a layer-wise fusion process where the quality of the powder feedstock plays an important role in powder spreading, hopper dosing and bulk packing performance. These factors affect the material deposition and part densification, thus determining the final part quality. Smooth flowability and high packing density are desirable attributes of powder feedstock in SEBM process. The critical powder characteristics, such as particle morphology, particle size distribution (PSD), packing density and flowability, are dependent on the powder production routes. Table 2.2 adopted from Dawes et al. [48] summarizes the commonly used manufacturing processes for metal powder production with the corresponding powder characteristics. The comparison of the particle morphology can be found in Figure 2.9. In general, water atomisation process yields low manufacturing cost but produces metal powders with irregular particle morphology and high oxide content. In contrast, plasma atomisation and plasma rotating electrode processes can produce highly spherical powders with minimum satellite particles, but at a high cost. Typically, gas atomised powders are adopted in metal AM due to the balance in quality and cost.

Table 2.2 List of powder production routes (adopted from Dawes et al. [48]).

Manufacturing process	Particle size (μm)	Advantages	Disadvantages	Common uses
Water atomisation	0 - 500	High throughput Range of particle sizes Only requires feedstock in ingot form	Post-processing required to remove water Irregular particle morphology Satellites present Wide PSD Low yield of powder between 20 - 150 mm	Non-reactive
Gas atomisation/ Electrode induction gas atomization	0 - 500	Wide range of alloys available Suitable for reactive alloys Only requires feedstock in ingot form High throughput Range of particle sizes Use of electrode induction gas atomization allows for reactive powders to be processed Spherical particles	Satellites present Wide PSD Low yield of powder between 20 - 150 mm	Ni, Co, Fe, Ti, Al
Plasma atomisation	0 - 200	Extremely spherical particles	Requires feedstock to either be in wire form or powder form High cost	Ti (Ti64 most common)
Plasma rotating	0 - 100	High purity powders Highly spherical powder	Low productivity High cost	Ti Exotics

electrode process				
Centrifugal atomisation	0 - 600	Wide range of particle sizes with very narrow PSD	Difficult to make extremely fine powder unless very high speed can be achieved	Solder pastes, Zinc of alkaline batteries, Ti and steel shot

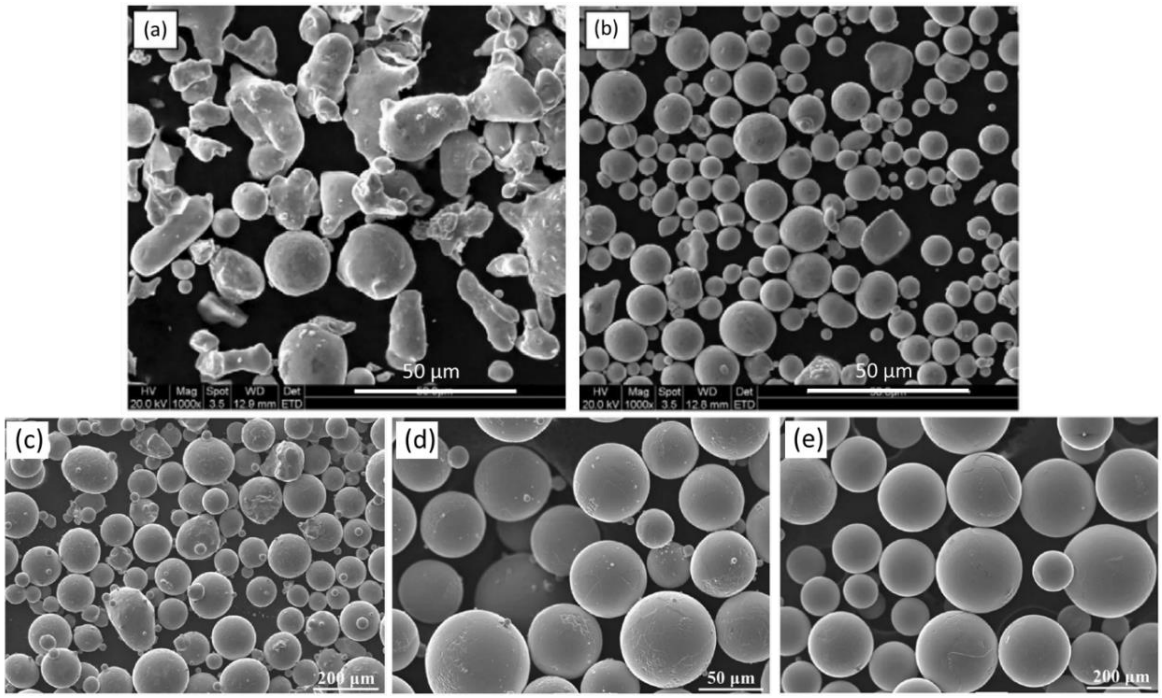

Figure 2.9 (a) Water atomised and (b) gas atomised SS316L powders [49]; (c) gas atomised, (d) plasma atomised and (e) plasma rotating electrode processed Ti-6Al-4V powders [50].

The powder characteristics are significant to AM processing. Regarding powder morphology, the spherical particles can arrange and pack more efficiently, leading to higher final part density. Hence spherical particles are favored in PBF. The PSD affects the minimum layer thickness and resolution of the part. A wide size distribution and high content of fine particles tend to exhibit high packing density, as the void interstices in coarse powder matrix can be occupied by fine powders. Nevertheless, fine particles smaller than 30 µm are likely to experience agglomeration, which may reduce the flowability due to the powder cohesion and inter-particle forces [51]. Moreover, powders with a higher packing density are less free-flowing than those with a lower packing density [48]. The typical powder feedstocks roughly follow Gaussian or bimodal/multimodal distribution. It was reported that bimodal Ti-6Al-4V powders have poor flowability when containing an excessive amount of fine particles as compared to Gaussian model powder [52]. The commercial feedstocks in PBF typically follow a Gaussian distribution.

In addition to the general requirements of powder feedstock for metal PBF, the particle size for SEBM should range from 45 μm to 106 μm without internal pores, and the quantity of ultra-fine particles < 10 μm should be as low as possible.

2.4 Materials for Selective Electron Beam Melting

2.4.1 Current Research Status on Materials Development for Selective Electron Beam Melting

To date, Arcam's EBM (now under GE Additive) [53] and QBEAM's EBSM (developed at Tsinghua University) [54] are the two major SEBM machines. Some companies such as Sailong [55] and Freemelt AB [56] are developing their open-source commercial EBM machines. The commercially metallic powder materials supplied by GE Additive include Ti-6Al-4V (Grade 5 and 23 ELI), Cp-Ti (Grade 2), CoCr, TiAl, IN718, highly alloyed tool steel and pure copper for different machine models [53].

However, as compared to other metal AM processes such as SLM and DED, the materials that can be processed by SEBM are still very limited mainly due to the following two reasons: Firstly, SLM and DED are more widely adopted AM processes than SEBM, hence more efforts have been dedicated to materials research; secondly, the patents of the key technologies in SEBM are still under protection by Arcam, so the in-house developed SEBM machines are still rare, if not impossible, as compared to SLM and DED machines. Therefore, only a few research institutes have access to SEBM facilities, which hinders the expansion of the processable materials for SEBM.

Table 2.3 summarizes the materials investigated for SEBM process from literature. In general, most of the materials investigated are alloys because of their wider applications as compared to pure metals.

Table 2.3 Classification of the bulk metallic materials that have been processed by SEBM.

Material group	Materials	Class	Reference standards	Refs
Ti-based	Ti-6Al-4V Grade 5	I	ASTM F1108	[57]
	Ti-6Al-4V Grade 23 (ELI)	I	ASTM F136	[58]
CoCr-based	Co-26Cr-6Mo-0.2C	I	ASTM F75	[59]
Ni-based	IN718	I	International specification AMS 5597	[60]
	IN625	III	-	[61]
	713ELC	II	International specification AMS 5377F	[62]
	CMSX-4	III	-	[63]
	Rene142	III	-	[64]
TiAl	Ti-47Al-2Cr-2Nb	III	-	[65]
	Ti-48Al-2Cr-2Nb	I	Cast counterparts [66]	[67]
	Ti-45Al-7Nb-0.3W	III	-	[68]
High-entropy Alloys	AlCoCrFeNi	II	Cast counterparts	[69]
	$Co_{1.5}CrFeNi_{1.5}Ti_{0.5}Mo_{0.1}$	II	Cast counterparts	[70]
Fe-based	SS316L	III	-	[30]
	Fe-18Cr-2W-0.5Ti-0.3Y_2O_3	III	-	[71]
	CrMnNi steel	II	Cast counterparts [72]	[73]
Pure metals	Ti	I	ASTM F67	[39]
	Cu	I	International specification CC040A	[73]
	Nb	II	Wrought counterparts	[74]
	Fe	III	-	[75]
Others	35 wt.% NiBSi + 64 wt.% WCp metal matrix composites	III	-	[76]
	Cu-25Cr composites	III	-	[77]
	NiTi shape memory alloys	III	-	[78]

The materials listed in this table are categorized into three classes. The benchmark for classification applied herein is that the SEBM as-built samples have flat top surface, relative density of ≥ 99%, and tensile strengths (YS and UTS) that can exceed while the elongation is at least half of their conventional cast or wrought counterparts. The rationale for this benchmark is that firstly, the top surface condition is an indicator of the suitability of the process parameters. The macro defects, such as unevenness, warping and porousness, can be directly observed on the top surface. Secondly, the relative density is an implicit way to measure the level of microstructural defects. The voids, lack-of-fusion and keyhole defects are reflected on the relative density. Although it is challenging to achieve 100% density, the samples with a relative density of ⩾ 99% are considered highly dense, and this value is widely accepted in metal AM community [45, 79, 80]. Finally, as the first tier mechanical properties, the tensile properties should match or exceed those of conventional cast or wrought counterparts. However, the elongation to fracture may not be comparable, mainly due to the fast cooling rate and refined grains during processing. Hence, this criterion is relaxed for SEBM as-built parts. Besides, tensile testing result is also an indicator of the existence of interlayer bonding defects and cracks.

According to the proposed benchmark, the materials listed in Table 2.3 can be broadly categorized into three classes. Note that the room temperature tensile data of SEBM as-built samples were used for classification in this table, except for TiAl which was subjected to additional hot isostatic pressing (1260 °C under 1700 bar for 4 hrs) and subsequent heat treatment (1320 °C for 2 hrs). Class III are the materials that can be processed by SEBM to form solid parts, but with one or more characteristics that are missing or unable to meet the benchmark criteria. Class II are those who can meet all the criteria stated above. If the class II criteria are satisfied and the materials are demonstrated to produce parts with complex geometry other than simple cubes, rectangular bars or cylinders (which is usually the case of class II materials), they are categorized as class I. In general, class I materials were developed by Arcam, and they are commercially available materials for EBM.

Nevertheless, this is just a preliminary classification of the processable materials for SEBM. Some other characteristics, such as chemical control, heterogeneity and anisotropy for microstructure and tensile properties [81], fatigue and fracture toughness properties are out of the scope of this work, although they are also important factors in industrial applications. Besides, the class I materials are also required to go through a series of stringent tests before

meeting the qualification standards for intended industrial applications [82]. Finally, this table is not exhaustive, as the research in SEBM materials development is evolving rapidly.

This Ph.D. work focuses on three materials: pre-alloyed Ti-6Al-4V, pre-alloyed SS316L and in-situ alloyed NiTi. Although these materials are listed in Table 2.3, they are studied due to the following reasons:

As a proof of concept, a ML method will firstly be applied to Ti-6Al-4V for process parameter optimization. The optimal process window will be compared with Arcam's default parameters which are known to be developed by DoE. The potential of ML in establishing the quantitative and all-round PMP interlinkages will be exploited. Next, the baseline models built for Ti-6Al-4V will be transferred to a different material (i.e. SS316 in this work) for faster and cheaper process parameter optimization for SEBM. The SEBM-built SS316L alloy reported by Zhong et al. [30] is categorized as class III material. This is mainly because the tensile strengths are inferior to their cast counterparts, indicating that their process parameters were not optimized. Hence, it is worth the effort to upgrade it to class II due to the high industrial value of this material. The pre-alloyed NiTi material has been processed by SEBM. However, the in-situ alloying of pre-mixed NiTi powders has not been attempted, which should be explored considering its flexibility to control the shape memory characteristics by tuning the Ni:Ti ratio, and the lower production cost as compared to pre-alloyed powders.

The detailed review of the three chosen materials is conducted in the following sub-sections.

2.4.2 Ti-6Al-4V Alloy

The microstructure of Ti-6Al-4V alloys is rather complex as compared to single-phase alloys, especially in metal AM which involves a lot of phase transformations. Hence, to understand the complex microstructure of Ti-6Al-4V alloys with different phases, we can start with pure titanium. Below ~ 860 - 890 °C (referred to as the β transus temperature), pure titanium exists in the form of a hexagonal close-packed (HCP) crystal structure, which is the α phase. Above the transus temperature, α phase is transformed into a body-centered cubic (BCC) crystal structure called β phase. In general, the densely packed HCP α phase is harder and stronger while the BCC β phase is more ductile in pure titanium.

Ti-6Al-4V is an α+β dual phase titanium alloy which has a weight percent composition of 90% Ti, 6 % Al and 4 % V, as the name suggests. Specifically, Al can improve the strength of the material and serve the α stabilizer, which promotes the formation of α phase by decreasing the β transus temperature, which is ~ 980 °C. It should be noted that α phase normally precipitates in β phase matrix. V can increase the room temperature ductility and serve as the β stabilizer, which promotes the formation of β phase by increasing the β transus temperature, thus helping achieve balanced mechanical properties. As a result, the duplex α+β Ti-6Al-4V has improved strength and formability than pure α phase. The extra low interstitial (ELI) grade of Ti-6Al-4V has improved ductility and better fracture toughness but slightly reduced tensile strength, mainly due to its low level of oxygen [83]. Ti-6Al-4V ELI material is used in this Ph.D. work.

Figure 2.10 shows a portion of the Ti-6Al vs. V pseudo-binary phase diagram. Above β transus temperature (~ 980 °C), the microstructure is pure BCC β phase. Between β transus temperature and martensite transformation temperature (~ 800 °C), it is a mixture of α+β dual phase. Below this temperature it is pure HCP α phase. In general, after Ti-6Al-4V solidifies from liquid state, the β to α solid state phase transformation occurs if it is cooled to below the β transus temperature. A slow cooling from above transus temperature to ambient temperature makes β phase completely transform into lamellar α phase by diffusion-controlled transformation, while a fast cooling makes it form some very fine needle-like martensitic α' phase by diffusionless martensitic transformation.

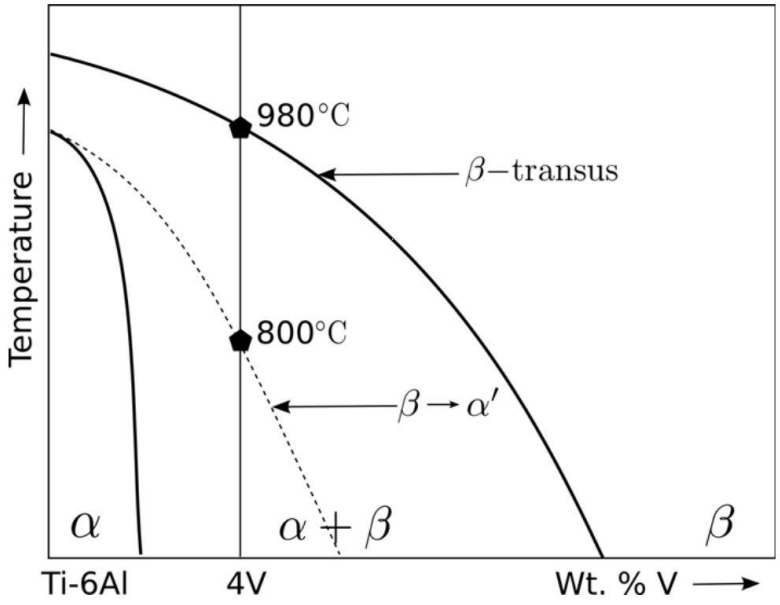

Figure 2.10 A portion of the Ti-6Al vs. V pseudo-binary phase diagram [84].

Ti has high affinity to oxygen, hence SEBM is a preferred metal AM technique due to its vacuum environment in processing. In SEBM processing, the thermal history is very complicated, which involves rapid unidirectional solidification, repeated melting and cyclic heating and cooling. Hence, the SEBM as-built Ti-6Al-4V alloys have gone through multiple stages of phase transformations and possess complex microstructures and phases. As shown in Figure 2.11, according to Tan et al. [58], the typical microstructure of SEBM as-built Ti-6Al-4V alloys consists of columnar prior β grains which are delineated by grain boundary α. The columnar grains are formed due to unidirectional rapid solidification after melting. The prior β matrix contains transformed α+β structures with both lamellar colony and basket-weave morphologies. In the continuous α phase, the retained discrete β phases are rod-like. The presence of high-strength and low-ductility α′ martensite is possible if the cooling rate is very high and it is not decomposed in the long-time annealing heat treatment after printing. This phase has numerous twin-like or/and stacking-fault structures that can significantly strengthen the material [85]. Note that as α phase is etched out by Krolls' reagent, and it is darker in contrast to brighter β phase when observed under the scanning electron microscope (SEM).

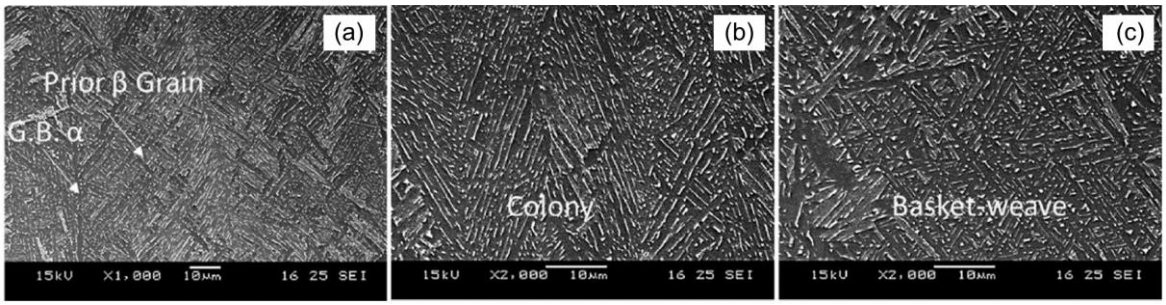

Figure 2.11 SEM images of Ti-6Al-4V showing (a) columnar prior β grains delineated by grain boundary α, and transformed α+β structures with (b) lamellar colony and (c) basket-weave morphology [58].

It is particularly of interest to investigate the underlying mechanism that accounts for the formation of such microstructure in SEBM processing of Ti-6Al-4V. Tan et al. [58] have proposed that 4 steps are involved in the SEBM-built Ti-6Al-4V alloys (see Figure 2.12): (i) the molten pool is rapidly solidified into prior β phase after the scanning of the electron beam; (ii) prior β phase is transformed into martensite α′ phase when cooled down rapidly from above β transus temperature to the build temperature of ~ 650 °C; (iii) martensite α′ phase is decomposed into colony and basket-weave-like α + rod-like β phase during the prolonged near-isothermal annealing. α continues to grow and ejects V, which allows β to appear and embed

into the continuous α phase [85]; (iv) the slow cooling makes the top build layers undergo the same decomposition process as elaborated in (iii). It should be noted that martensite α′ phase can be well retained if the build temperature is close to ambient temperature, such as in SLM processing of Ti-6Al-4V [86].

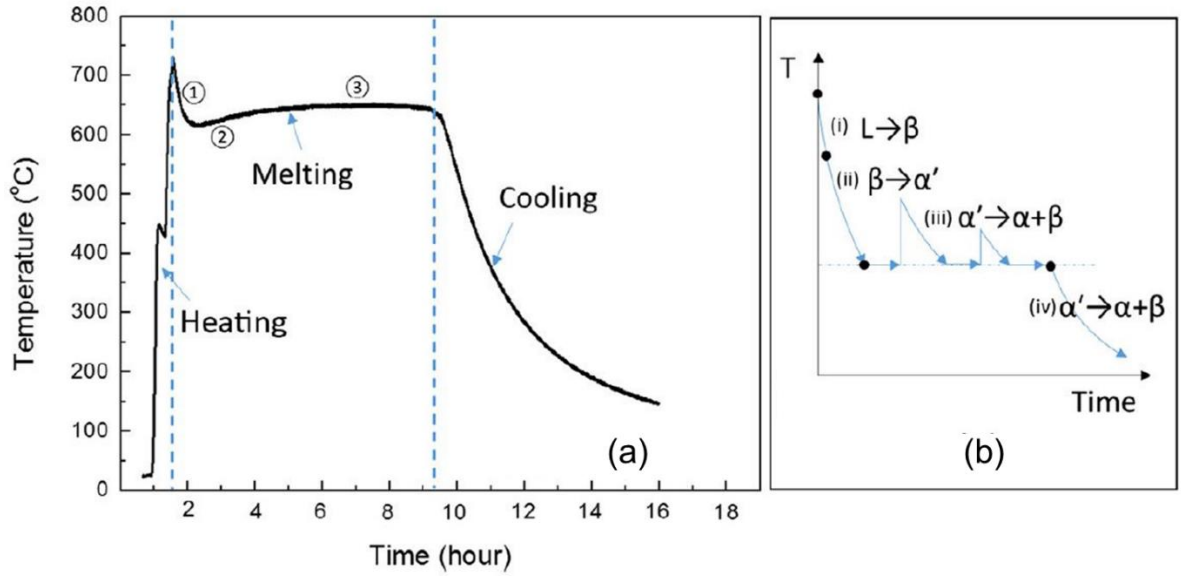

Figure 2.12 (a) Time-temperature curve during SEBM processing. (b) Schematic illustrating of the possible phase transformation steps involved during processing [58].

2.4.3 Stainless Steel 316L Alloy

Stainless steels have been traditionally classified based on their microstructures at room temperature, which are controlled by the specific amounts of alloying elements. According to American Welding Society [87], stainless steels can be divided into five groups: ferritic, martensitic, austenitic, duplex and precipitation hardening stainless steel.

Ferritic stainless steel is a magnetic grade which mainly consists of ion-chromium alloy with BCC crystal structure. It is relatively cheaper, due to the low amount of nickel addition. However, their corrosion resistance and ductility are limited. Martensitic stainless steel has a body-centered tetragonal crystal structure with high carbon content to improve the strength and hardenability, but its ductility and toughness are sacrificed. Austenitic stainless steel is the most popular group with a face-centered cubic (FCC) crystal structure, which is widely used in many industries and consumer applications. It is non-magnetic with good corrosion resistance, ductility and weldability. Duplex stainless steel has approximately equal amounts of ferritic and austenitic microstructure, which has high strength and stress corrosion

cracking resistance. Finally, precipitation hardening stainless steel is chromium-nickel stainless steel, which is hardened by the formation of precipitates within the microstructure.

SS316L is a grade of austenitic stainless steel with a low carbon content (< 0.03 wt.%), which makes it more resistant to sensitization, namely grain boundary carbide precipitation of chromium-rich carbides so that the intergranular cracking can be minimized. According to UNS S31603, the chemical composition ranges for SS316L are listed in Table 2.4.

Table 2.4 Chemical composition ranges for SS316L.

Element	C	Mn	Si	P	S	Cr	Mo	Ni	N	Fe
wt.%	≤0.03	≤2.00	≤1.00	≤0.04	≤0.03	16.00 - 18.00	2.00 - 3.00	10.00 - 14.00	≤0.10	Balance

Amongst the metallic alloying elements of stainless steel, Cr is the most important element that gives stainless steel robust corrosion resistance. It is noteworthy that when the Cr content is > 12 wt.%, steel becomes stainless steel because the chromium oxide layers are formed on the surface to prevent corrosion [88]. Ni generally increases the ductility and toughness. Mo can also significantly increase its pitting corrosion resistance. Mn is added to improve hot ductility. For the non-metallic alloying elements, Si increases resistance to oxidation, while N can significantly increase its mechanical strength. It should be noted that although C is a strong austenite former and can significantly increase mechanical strength, it reduces the intergranular corrosion resistance by the formation of carbide.

The classical Schaeffler diagram shown in Figure 2.13 (a) can predict the phase evolution of stainless steel based on the equivalent amount of Cr (Cr_{eq} = %Cr + %Mo + 1.5×%Si + 0.5%Nb) and Ni (Ni_{eq} = %Ni + 0.5×%Mn + 30×%C) in weight percentage. However, the cooling rate of metal AM is much higher than conventionally fabricated steels, meaning that the solidification is out of equilibrium condition [89]. Therefore, a pseudo-binary predictive phase diagram [90] is plotted in Figure 2.13 (b). SS316L undergoes a few phase transformation steps. After melting, the liquid state is cooled down to form δ-ferrite phase first, followed by the presence of γ-austenite phase which co-exists with δ-ferrite phase at around 1400 °C. As the temperature further goes down, δ phase is transformed into γ phase via solid phase transformation. Finally, the material becomes full γ phase. However, some detrimental precipitates such as carbides $M_{23}C_6$ and σ phase might be formed if the SS316L is subject to

prolonged heat treatment at certain temperatures [91], which should be avoided as they negatively affect the mechanical properties.

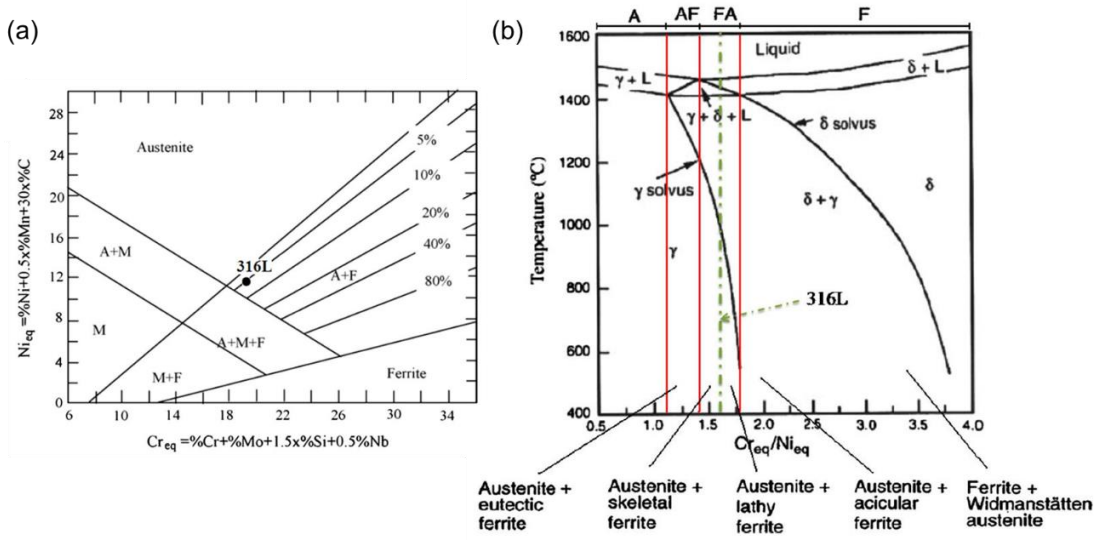

Figure 2.13 (a) Schaeffler diagram and (b) pseudo-binary phase diagram [90] in steels.

Due to the broad applications of SS316L and its high weldability, it is one of the most widely studied metallic material in metal AM. Sun et al. studied how to significantly improve the build rate while maintaining a high relative density for SLM-built SS316L parts [45]. Miranda et al. employed various combinations of process parameters to analyze their effects on density, hardness and shear strength of SLMed SS316L parts [92]. Cherry et al. investigated the effects of SLM energy density by varying point distance and exposure time, on the microstructural and physical properties of SS316L parts [93]. Tsopanos et al. evaluated the influence of SLM process parameters, particularly for laser power and laser exposure time, on the performance of SS316L microlattice structures in aerospace applications [94]. Moreover, Zhong et al. performed mechanical tests and microstructural characterization on SEBMed SS316L parts at both room and elevated temperatures [30].

Recently, researchers have made significant advancements to manufacture SS316L with superior mechanical properties, which has solved the longstanding dilemma of strength-ductility tradeoff. Wang et al. [95] used SLM to manufacture SS316L parts with hierarchical structures of different scales (see Figure 2.14). The cellular structures induced during rapid solidification, the nano inclusions that precipitated at cellular walls, low-angle grain boundaries and dislocation formed during processing have contributed to the high strength. The prolonged steady work hardening regulated by a hierarchically heterogeneous microstructure significantly

improves its ductility. Sun et al. [96] implemented high laser power and multi-scan strategy using SLM to obtain large melt pool, which formed <011> crystallographic texture with fine grains as compared to the typical <001> texture in SLMed SS316L (see Figure 2.15 (a) to (d)). This texture promotes nano-twinning during plastic deformation, which could enhance both strength and ductility of the alloy, as shown in Figure 2.15 (e).

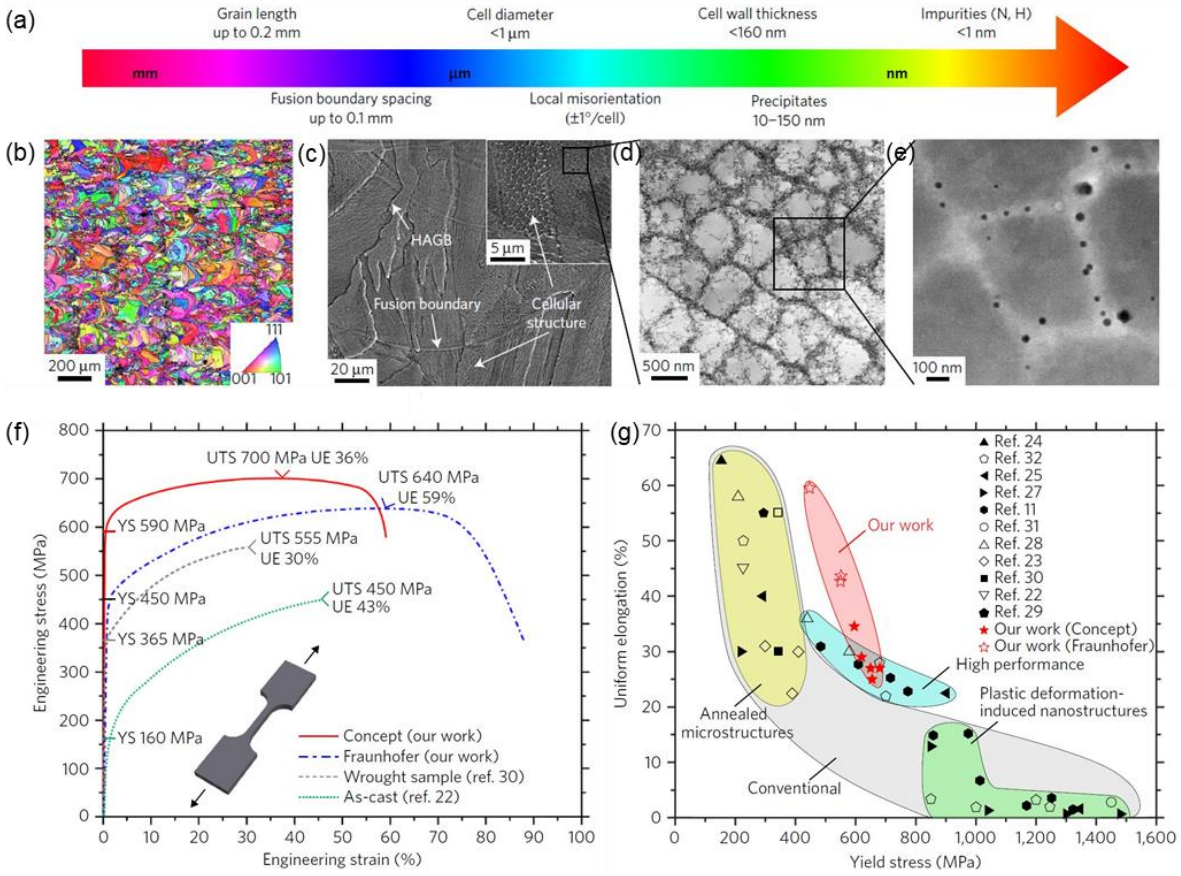

Figure 2.14 Hierarchical microstructure of SS316L with an exceptional combination of strength and ductility manufactured by SLM [95]. (a) The scale of the structures ranges from nanometer-sized precipitated to millimeter-size grains. (b) Electron backscatter diffraction (EBSD) mapping shows a ripple pattern instead of the columnar grains observed in most SLMed SS316L along the build direction. (c) The microstructure with cellular structures which contain nano inclusions along the walls shown in (d) and (e). (f) The parts exhibit superior strength and high ductility, as compared to (g) their counterparts manufactured by conventional manufacturing and other metal AM processing.

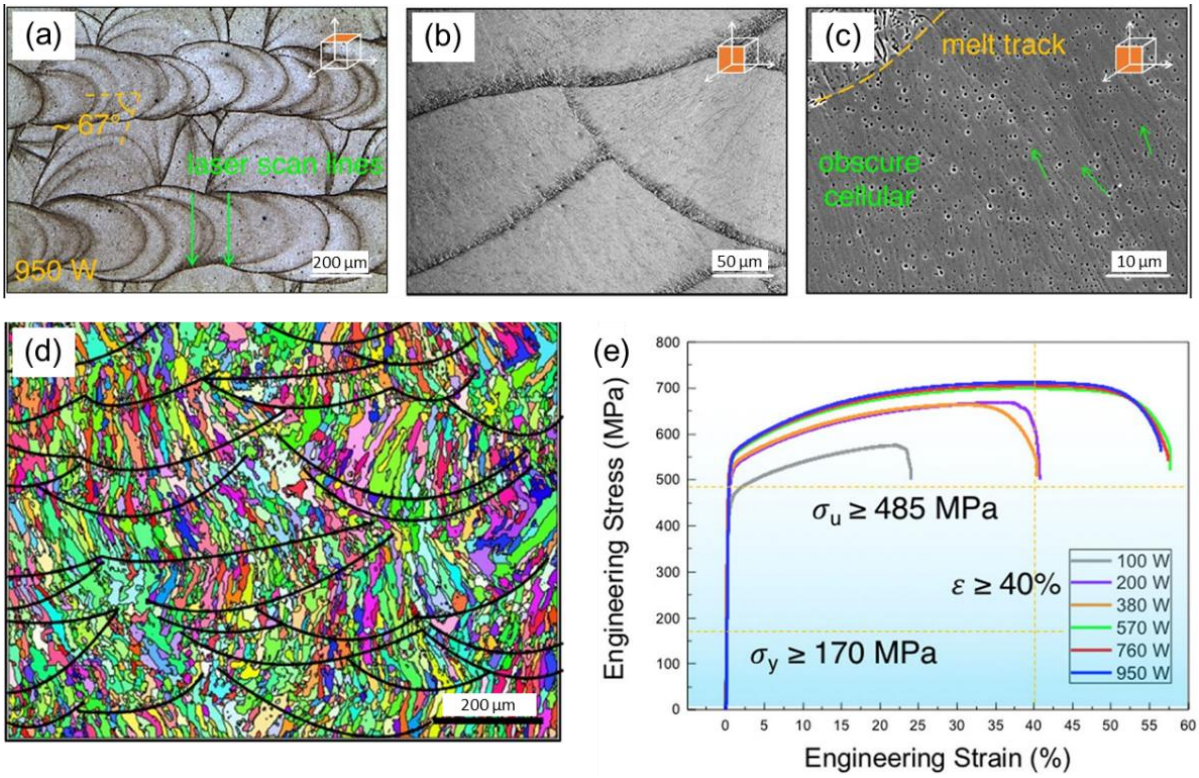

Figure 2.15 (a) Top view and (b, c) side view of the microstructure of SS316L alloys fabricated by SLM with high 950W laser power and multi-scan strategy. (d) EBSD mapping shows strong <011> texture is obtained. (e) This material with engineered <011> texture has enhanced strength and ductility [96].

2.4.4 NiTi Alloy

Shape memory alloys (SMAs) can recover its original shape through various stimuli [97, 98]. The reversible phase transformation (i.e. B19' martensite product phase ↔ B2 austenite parent phase) can be achieved via thermal-induced shape memory effect (SME) during heating or via stress-induced superelasticity during unloading [99]. More specifically, at a temperature below M_f (martensite finish) and in the absence of mechanical loading, the martensite phase is called twinned martensite. When the material is forced by mechanical loading, the twinned martensite transforms into another phase called detwinned martensite. This process starts at the stress level of σ_s (detwinning start) and completes at σ_f (detwinning finish). The detwinned martensite remains unchanged after unloading, as the material is permanently deformed. Figure 2.16 (a) shows that the SME behavior happens when applying heat at a temperature above A_s (austenite start). The material starts to recover to its original shape by transforming from detwinned martensite into full austenite phase, which finishes at A_f (austenite finish). On the other hand, Figure 2.16 (b) shows that superelasticity behavior happens at the temperature above A_f, where the twinning-to-detwinning martensite phase

transformation can be induced by mechanical loading and unloading. The normal elastic behavior of the material stops at the stress level of σ_{Ms}, after which the stress-induced martensite transformation starts and finishes at σ_{Mf}. At this stage, the material experiences large deformation with little increase in stress, which is also called pseudoelasticity. Upon unloading, the material transforms into the original shape in austenite phase without permanent deformation, which starts at σ_{As} and finishes at σ_{Af}.

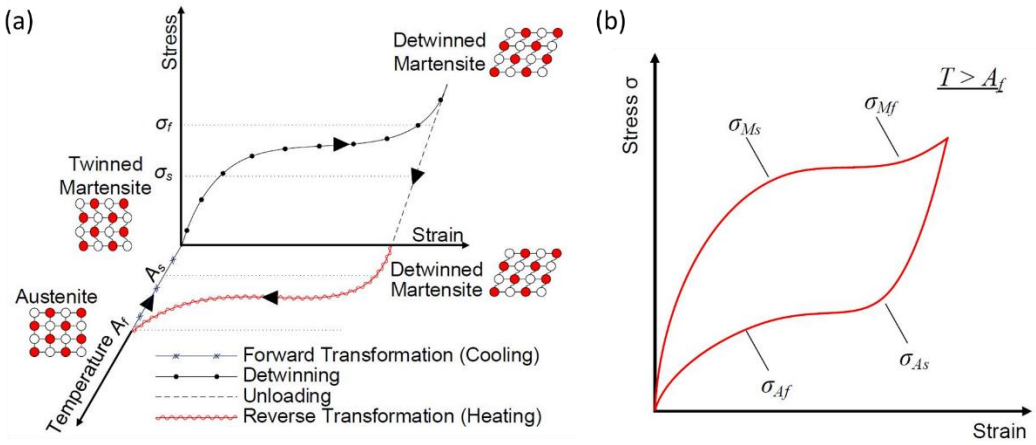

Figure 2.16 Typical (a) SME behavior and (b) superelasticity behavior of an SMA [100].

NiTi is one of the most popular SMAs. The Ni-Ti phase diagram in Figure 2.17 (a) shows that Ni-Ti can form a variety of intermetallic phases such as NiTi, Ti_2Ni, $TiNi_3$ and Ti_3Ni_4, depending on the atomic ratio of the two constituent elements. In general, Ti_2Ni and $TiNi_3$ are undesirable intermetallic phases which embrittle the materials and are detrimental to the mechanical properties [16]. Ti_3Ni_4 phase usually appears as precipitates after heat treatment, which affects the phase transformation temperature of the material [101]. The phase diagram shows that the NiTi phase only exists in a very limited region with Ni at.% ranging from 49% to 55%. The existence of secondary phases is very common for many NiTi alloys.

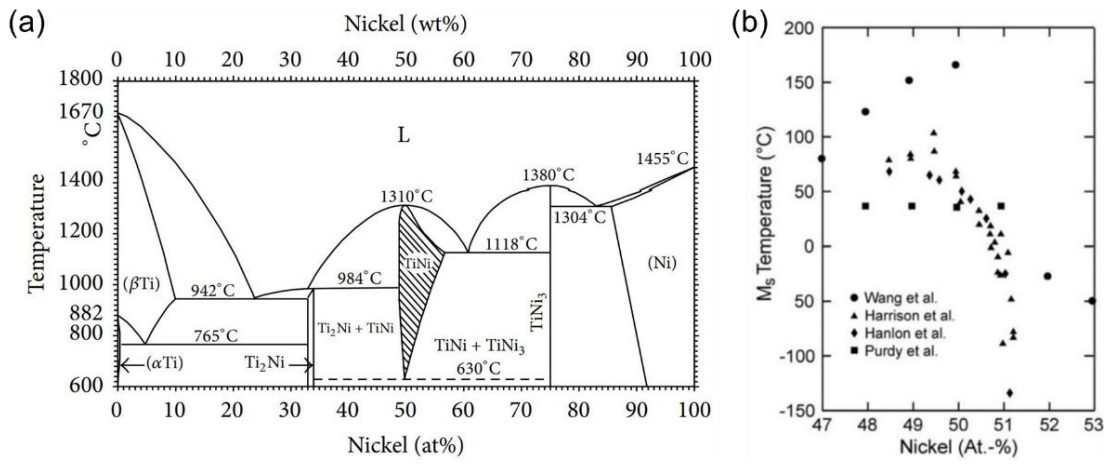

Figure 2.17 (a) Equilibrium Ni-Ti phase diagram. [102] (b) The effect of Ni content on the phase transformation. [103]

Figure 2.17 (b) shows that the phase transformation temperature of NiTi alloy is highly sensitive to the atomic ratio of the two elements. An increment of Ni content by 0.1 at.% will result in a sharp drop of M_s temperature by ~ 20 °C, leading to a drastic change in SME and SE characteristics [104]. Hence, chemistry control is of critical importance when processing NiTi alloy. In general, SME is the dominant SMA regime for Ti-rich NiTi alloys, in contrast to SE which is dominant for Ni-rich products [105]. However, fabricating NiTi through thermo-mechanically conventional manufacturing methods, such as powder metallurgy and casting, can introduce contaminants and degraded functional properties [106]. In addition, machining NiTi alloys is also challenging due to its spring back effects, which could result in excessive tool wear [107].

Significant efforts were devoted to developing metal AM processing of NiTi alloys. Krishna et al. systematically studied the influence of laser power and scanning speed on phase formation, compressive strength and phase transformation temperature of fully dense equimolar NiTi parts produced by DED [108]. Marattukalam et al. also employed DED to manufacture Ni-rich NiTi samples which were subsequently subject to annealing in order to investigate the effect of heat treatment on microstructure, shape memory characteristics and corrosion resistance of this alloy [109]. Li et al. designed a re-entrant auxetic structure which was fabricated by SLM from Ti-rich NiTi powders with the optimized parameters for reusable armour applications [105]. Moreover, by varying the hatch distance and thus differing the thermal history at various locations within the same part, Ma et al. innovatively adopted SLM to create a NiTi structure with multi shape-recovery stages activated at different temperatures [110]. The study of NiTi fabricated by SEBM is still rare. Hayat et al. utilized SEBM to print

NiTi samples, which exhibited limited tensile strain despite the vacuum environment and high build temperature during processing [111]. To improve its properties, Zhou et al. optimized the beam current and scanning speed of SEBM and successfully fabricated the NiTi samples with predominantly B2 austenite phase and minor Ti_3Ni_4 precipitates, which exhibit excellent SE at room temperature, as shown in Figure 2.18 [78].

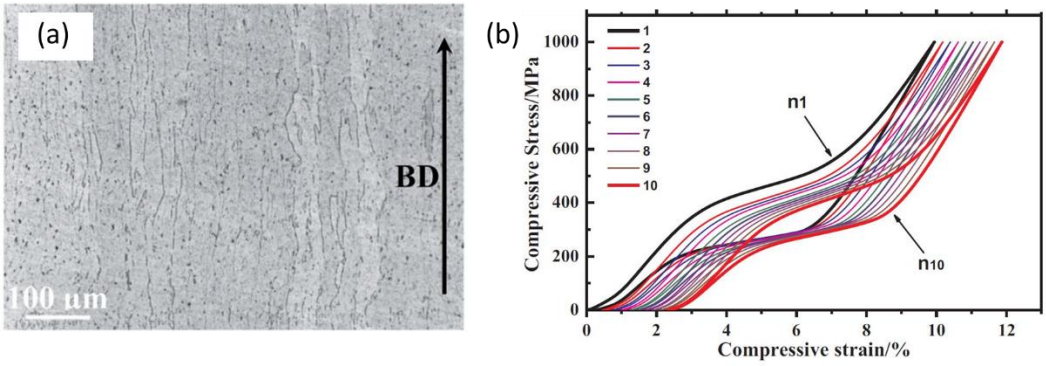

Figure 2.18 (a) The microstructure of SEBM as-built NiTi alloy with predominantly B2 phase and some Ti_3Ni_4 precipitates in dark contrast. (b) the corresponding SE behavior in cyclic compressional test [78].

2.5 Methods for Process Parameter Optimization for Selective Electron Beam Melting

In general, the mainstream methods applied to the optimization of SEBM process parameters can be categorized into two groups: data-driven methods and physics-based methods (see Figure 2.19). Data-driven methods are based on empirical experimental data and statistical/intelligence learning methods, which are further divided into DoE and ML methods. The physics-based methods herein refer to numerical simulation, which relies on differential equations that govern the underlying thermo-mechanical process. A few innovative methods have been proposed by various researchers, such as leveraging the experimental data from similar prior studies to accelerate the process optimization for the current study [112], and translating the optimal process parameters from one material to another [113]. However, they are neither well established nor adopted by SEBM processing yet. Thus they will not be elaborated in the literature review.

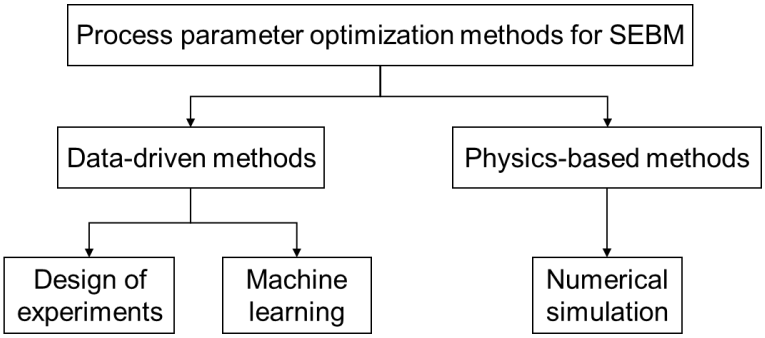

Figure 2.19 Classification of the methods applied to process parameter optimization for SEBM.

2.5.1 Design of Experiments Methods

Most of the data-driven methods for SEBM center on DoE. Overall, screening designs are used to identify the significant parameters with the aid of analysis of variance (ANOVA) as a statistical tool to evaluate their influences on the response in the initial stage of experimentation [114]. Response surface designs are employed to cover a range of process parameters in order to locate the optimal process window [36, 115]. More details of the applications of DoE methods in metal AM will be covered in section 2.6.2.

2.5.2 Machine Learning Methods

Despite the increasing effort to adopt ML in process parameter optimization for metal AM, its application in SEBM processing is still at a nascent stage [116]. To the best of the author's knowledge, only Aoyagi et al. [117] have leveraged ML to assist process parameter optimization for SEBM. In their work, a ML technique was used to construct a process map to classify the top build surface conditions. Nevertheless, the accuracy of the model could not be evaluated due to the lack of test set. More details will be discussed in section 2.7.2. Hence, it is desirable to explore the potential of ML in the context of SEBM process parameter optimization.

2.5.3 Numerical Simulation Methods

Numerical simulation is another widely used method in SEBM that can reduce the process optimization time and reveal the underlying physics accounting for some phenomena. According to Galati and Luliano [18], the numerical simulation for SEBM process can be grouped into three classes, namely black box models, grey box models and white box models according to their physical meaning (from low to high) and level of approximation (from high to low), as shown in Figure 2.20. The accuracy of the simulation improves as the model incorporates more mechanics that describe the process but at the cost of increasing computing time and power. In reality, the grey box models are more feasible and commonly practiced by researchers.

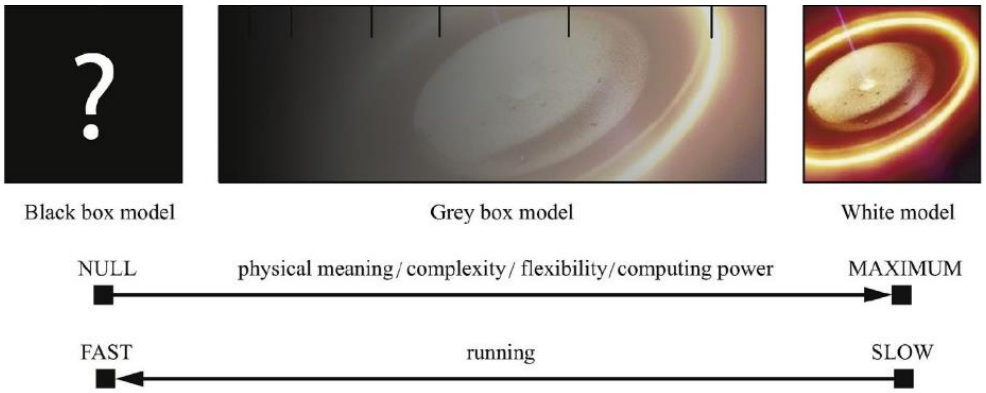

Figure 2.20 Classification of numerical simulation models for SEBM according to their physical meaning and level of approximation [18].

Depending on how the powder bed is modelled, the grey box models can be further classified into mesoscopic method and finite element method (FEM). The mesoscopic method considers the numerical behavior of a single powder particle. It simulates the sequential addition of powder layers, which involves discrete element method (DEM) for particle spreading and computational fluid dynamics (CFD) for thermal convection, as shown in the work of Yan et al. [118]. The mesoscopic method can accurately predict the morphology and size of the melt tracks from the preset process parameters. However, it is not suitable for large-scale simulation due to its high complexity and high cost in computational resources.

To counter this obstacle, the powder bed can be treated as a continuum so that FEM could be used to balance the calculating time and accuracy. Simulations can also be grouped into uncoupled and coupled methods, depending on how the thermal dynamics are modelled.

The uncoupled models are simplified methods that only consider the main phenomena that cause heat transfer, such as heat conduction and radiation, with many assumptions. Conversely, the coupled models are further divided into thermal-fluid flow model and thermo-mechanical model. The former includes the effect of flow convection on the temperature distributions and the molten pool geometry, while the latter incorporates the mechanical properties of the bulk material.

2.6 Design of Experiments

2.6.1 Principles of Design of Experiments

DoE is a powerful statistical approach used to plan and conduct experiments, as well as analyze and interpret the experimental data [119]. It is a prevalent scientific method in but not limited to medicine, engineering, biochemistry, physics and computer science. DoE allows multiple input factors to be included and can determine the significance of their effects on the desired outputs (also termed as responses). It can also determine the direction of adjustment for effective factors to maximize or minimize the responses. DoE is much more efficient and can identify the important interactions of different factors which are neglected in the one-factor-at-a-time (OFAT) method.

DoE can investigate all the possible combinations of factors (full factorial design), or only a portion of it (fractional factorial design) to reduce the time and cost, especially when the factors investigated are numerous. A good fractional factorial design should preserve the key information of main effects and discard the insignificant information of higher-order interactions. Usually, the usage of DoE is accompanied by analysis of variance (ANOVA), which is an important statistical tool to decide whether and which factors or interactions have significant effects on the response [120]. One variant of DoE called Taguchi's Method can also help reduce the number of experimental runs using orthogonal arrays and help reduce the variations of responses (i.e. robust design) caused by the uncontrollable factors [121].

After identifying the significant factors, response surface method (RSM) can be used to optimize the results. Based on the dataset obtained from DoE, RMS uses a response surface function $\boldsymbol{f}$ to perform regression using the least-squares method, where $\boldsymbol{f}$ can be a linear function for first-order model or a quadratic function for second-order model, depending on

the complexity of relationships between the input variables and the output responses. Hence, a 2-D or 3-D contour plot can be constructed to visualize the relationships. The optima can be therefore determined, as for examples shown in Figure 2.21.

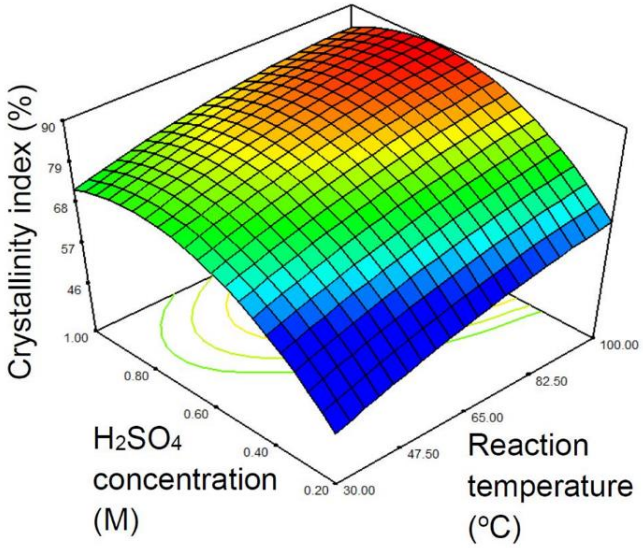

Figure 2.21 A 3D-contour plot of response surface method (RSM) used in materials synthesis with two design factors [122].

2.6.2 Design of Experiments in Process Parameter Optimization for Additive Manufacturing

In the context of process development for metal AM, depending on the objectives, DoE methods can be broadly classified into two types: preliminary screening and optimization. Due to the numerous process parameters involved in each AM process, a preliminary screening is paramount to narrow down the long list of potentially important parameters to only a few. It usually requires fewer experimental runs that involve many factors in order to reduce the cost. Fractional design or full factorial design with a limited number of levels are typically used as screening methods. In contrast, in the later stage of experimentation after the significant parameters are identified, a small number of factors with a range of continuous values are used. The commonly practised optimization methods are full factorial design in conjunction with RSM, which can model the curvature in the relationships between the parameters and the target response. With this visualization tool, the setting of the parametric combinations can be found to either maximize (e.g. tensile strength, density) or minimize (e.g. surface roughness, defects) the responses. Some representative prior studies that involve DoE are summarized in Table 2.5.

Table 2.5 Selected prior studies with DoE applied in process parameter optimization for metal AM.

Objectives	DoE methods	ANOVA used	AM process	Materials	Process parameters	Responses	Refs
Preliminary screening	Full factorial design	No	SEBM	Ti-6Al-4V	Scanning speed, beam current, focus offset	Surface roughness, critical pitting temperature, density	[123]
Preliminary screening	Full factorial design	Yes	SEBM	Ti-6Al-4V	Sample orientation, location, height	Dimensional accuracy, repeatability	[124]
Optimization	Full factorial design	No	SEBM	Ti-6Al-4V	Scanning speed, beam power	Top surface condition, aluminum evaporation loss	[36]
Optimization	Full factorial design	No	SEBM	Ni-based superalloy CMSX-4	Scanning speed, beam power, build temperature	Binding faults, crack density	[63]
Optimization	Full factorial design	No	SEBM	Ti-6Al-4V	Scanning speed, beam current	UTS, elongation	[125]
Preliminary screening	Full factorial design	Yes	SLM	Ti	Scanning speed, laser power, lattice structure design	Dimensional accuracy, elastic constant	[126]
Preliminary screening	Full factorial design	Yes	SLM	Maraging steel	Scanning speed, laser power	Relative density, UTS, hardness, surface roughness	[127]
Preliminary screening, optimization	Fractional design, RMS	Yes	SLM	AlSi10Mg	Scanning speed, laser power, hatch spacing, island size	Porosity	[128]
Optimization	Full factorial design	No	SLM	Maraging steel	Scanning speed, laser power, pitch, spot diameter	Relative density, top surface morphology	[129]
Optimization	Full factorial design	No	SLM	Ti-6Al-4V	Scanning speed, laser power	Melt pool geometry of single beads	[130]
Preliminary screening	Fractional design	No	DED	Ti-6Al-4V	Substrate thickness and initial temperature, interlayer dwell time, hatch pattern, number of layers	Porosity, hardness	[131]

Optimization	Full factorial design	No	DED	Inconel 719	Scanning speed, laser power, powder feed rate	Single track geometrical characteristics	[132]
Preliminary Screening, optimization	Taguchi design	Yes	BJ	SS402	Layer thickness, printing saturation, heater power ratio, drying time	Surface roughness, shrinkage rate	[133]

The studies for the preliminary screening of process parameters simply follow the standard DoE guidelines, which will not be elaborated in this section. In the optimization stage, two approaches are commonly leveraged to discover the optimal process window. The first approach can be termed as DoE chart representation, which illustrates the evolution of the responses that involve image data, such as melt pool morphology by Gong et al. [130] (see Figure 2.22) and Bax et al. [132]. However, the relationships between the parameters and response are not quantified.

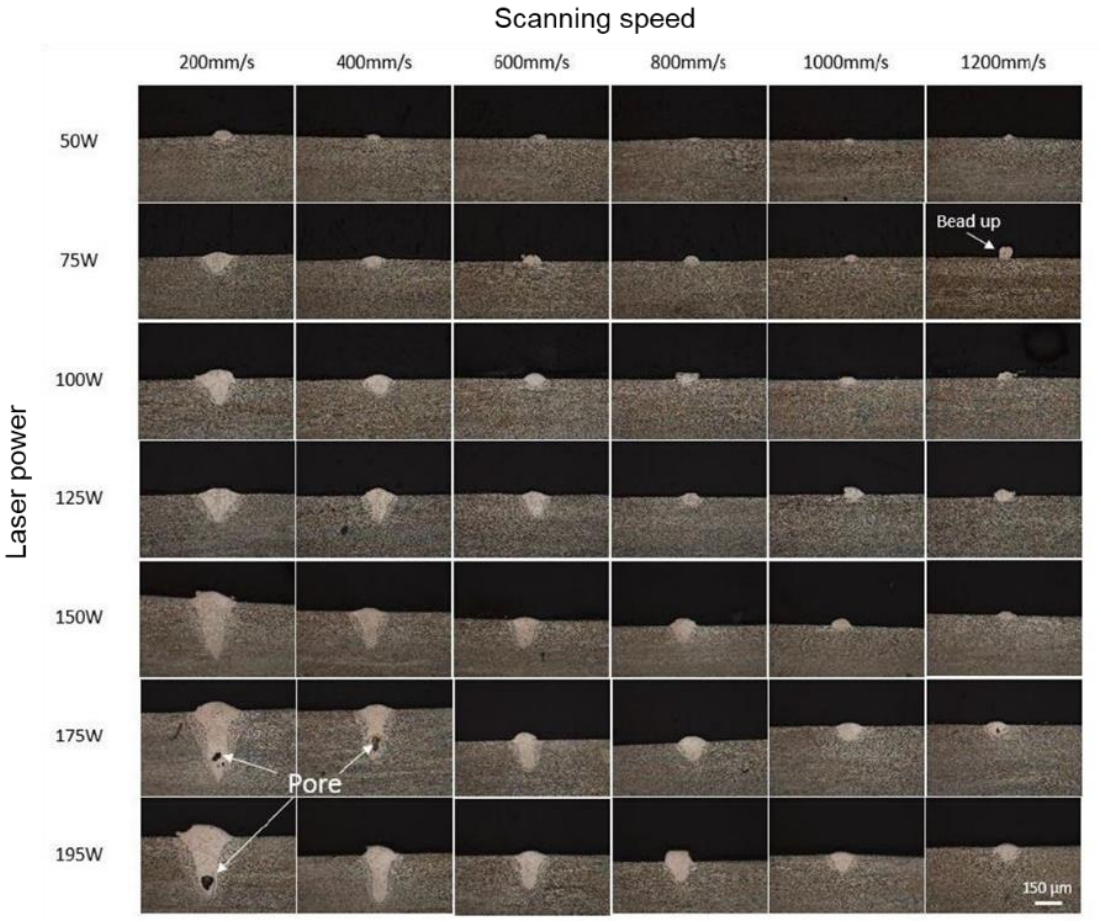

Figure 2.22 DoE chart representation to illustrate the evolution of melt pool with varying scanning speed and laser power in SLM processing [130].

The second approach is the process map where the response can be easily quantified by numerical or text labels, such as relative density and top surface morphology classification by Mutua et al. [129] and Kirchner et al. [125], and aluminum evaporation loss by Juechter et al [36]. The process maps can be constructed in either 2D (see Figure 2.23 (a)) or 3D (see Figure 2.23 (b)) so that the effects of each process parameter are visualized clearly, and the optimal process window can be selected. Nevertheless, constructing a process map requires numerous parametric combinations associated with high cost in sample fabrication.

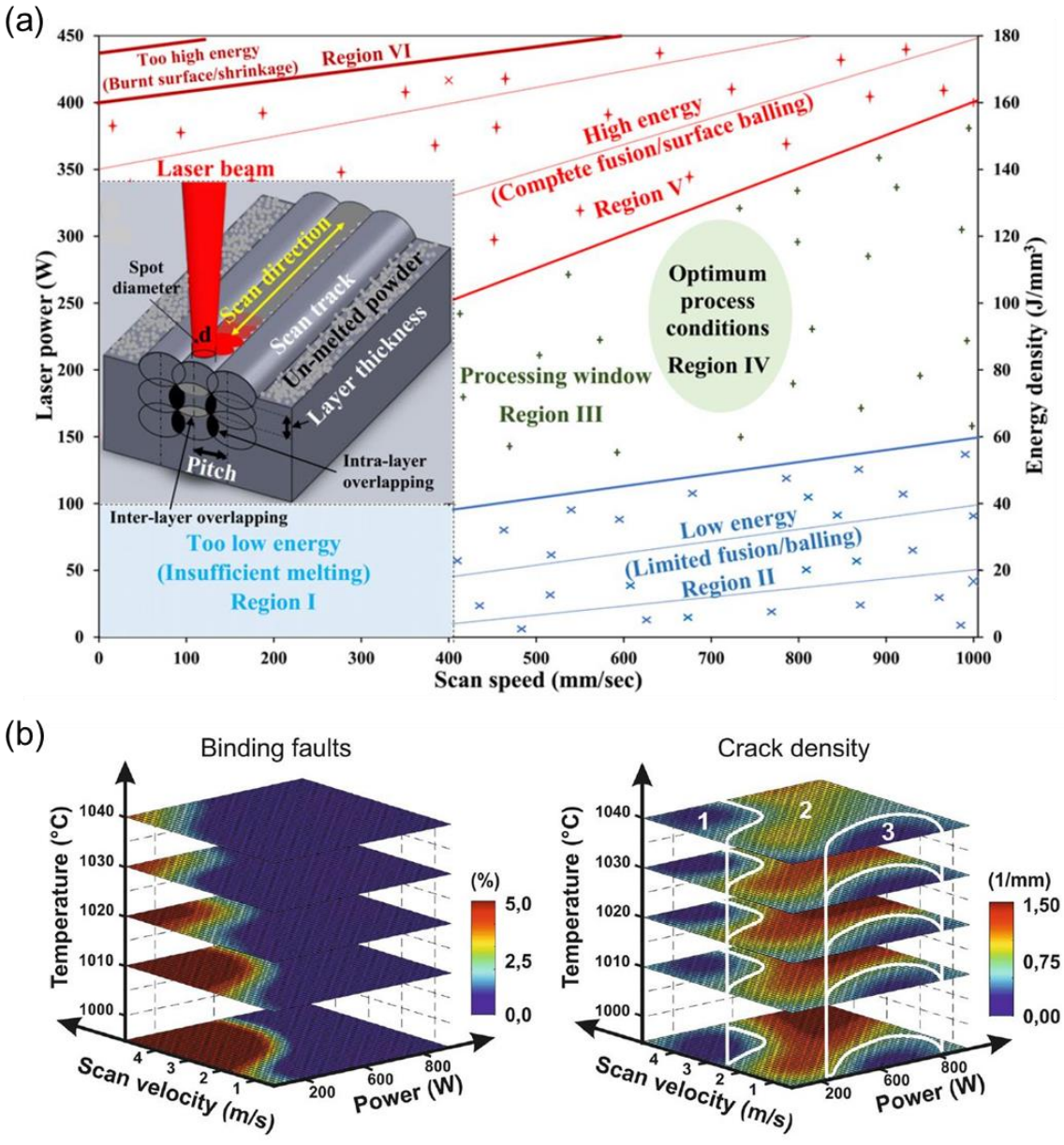

Figure 2.23 (a) 2D process map considering the effects of scanning speed and laser power on the relative density and top surface morphology in SLM processing [129]. (b) 3D process map integrated with three process parameters and their combined effects on binding defaults and crack in SEBM processing [63].

In addition to the high cost in process mapping, another drawback of DoE is the knowledge pertaining to the prior studies cannot be translated to a new context. When the experimental conditions (e.g. materials, machines, laser calibration) change, new sets of experiments are required, thus leading to even higher experimentation cost.

2.7 Machine Learning

2.7.1 Principles of Machine Learning

ML is an artificial intelligence (AI) technique that allows a machine or system to learn from data automatically and make decisions or predictions without being explicitly programmed. In research, ML is gaining popularity in medical diagnostics, material property prediction, smart manufacturing, autonomous driving, natural language processing and object recognition [116]. ML algorithms are commonly categorized as supervised, unsupervised and reinforcement learning. As the majority of the ML works applied in metal AM are supervised learning, the concepts of unsupervised and reinforced learning are not elaborated here. The details can be referenced from our recent review article [116].

Supervised learning enables a computer programme to learn from a set of labelled data in the training set so that it can identify unlabelled data from a test set with the highest possible accuracy [134]. The datasets can be in a variety of forms including forms of images, audio clips or text. There is an objective function known as cost function, which calculates the error between the predicted output values and the actual output values. In the training process, the parameters (or weights) between neurons in adjacent layers are updated in order to reduce the cost function after each iteration (or epoch) [135]. In the testing process, the previously unseen new data, i.e. test set, is introduced to provide an unbiased evaluation of the model's accuracy.

In this work, only supervised ML algorithms are used. Within this context, the most common ML tasks include classification and regression, as summarized in Table 2.6. In fact, many of the algorithms below can be used for both classification and regression tasks. For simplicity, we just present the tasks that the authors aimed to achieve in their respective works.

Table 2.6 Different types of ML algorithms for supervised learning applied for AM process parameter optimization.

ML algorithms	Concepts	Tasks	Refs
Decision trees (DT)	A hierarchical tree-shape model that classifies instances by sorting them based on feature values	Classification	[136]
Random forest (RF)	A model consisting of a large number of individual decision trees that operates as an ensemble, where the class with the most votes from each decision tree becomes the model's output	Classification, regression	[137]
Support vector machine (SVM)	A model that maps the input points into high-dimensional feature space in order to find a separating hyperplane that maximizes the margin between the two classes	Classification, regression	[138]
Gaussian process (GP)	A probability distribution over possible function	Regression	[139]
Multi-layer perceptron (MLP)	A typical neural network with interconnected neurons which can approximate extremely non-linear functions	Classification, regression	[140]
Adaptive network-based fuzzy inference system (ANFIS)	A hybrid model that implements a fuzzy inference system in the framework of adaptive neural networks	Regression	[141]
Recurrent neural network (RNN)	A deep learning neural network popular for processing sequence data	Time series prediction	[142]

2.7.2 Machine Learning in Process Parameter Optimization for Additive Manufacturing

Conventionally, process parameter development and optimization are implemented by DoE or simulation methods to additively manufacture new materials. Nevertheless, the DoE method requires time-consuming and costly experimentation, particularly for metal AM where numerous process parameters are investigated [6, 45, 143, 144]. The physical-based simulation can reveal the underlying mechanism for the formation of specific features during processing, e.g. melt pool geometry, keyhole, microstructure. Nevertheless, macro-scale simulations, e.g. FEM, may suffer from discrepancies with experimental results due to the simplified assumptions [145]. The increasingly more sophisticated techniques, e.g. computational fluid dynamics (CFD), usually focus on single tracks [146] or a minimal number of tracks and layers [118]. This makes it challenging to predict the mechanical properties of the parts at a macro scale or continuum. Therefore, many researchers have explored the feasibility of introducing

ML methods to solve the abovementioned challenges in process optimization of metal AM, as summarized in Table 2.7. It is found that under the various AM processes, ML was mainly used to link their key process parameters to the quality indicators at two levels, namely mesoscale level (i.e. porosity or relative density, melt pool geometries) and macroscale level (i.e. mechanical properties). Moreover, some researchers applied ML to construct process maps, which could serve as an excellent visualization tool to identify the process windows.

Table 2.7 ML methods used to optimize AM process parameters.

AM processes	Materials	Inputs	ML methods	Outputs	Purposes	Refs
Powder-bed fusion						
SLM	SS316L	Laser power, scan speed, layer thickness, post-processing temperature, tensile properties	ANFIS	High cycle fatigue life	To predict high cycle fatigue life with 'process-based' and 'property-based' models	[147]
SLM	Bronze	Laser power, scan speed, hatch distance	MLP	Relative density, microhardness	To predict porosity and microhardness	[148]
SLM	SS316L	Laser power, scan speed	GP	Melt pool depth	To construct a process map and predict melt pool depth	[149]
SLM	SS17-4 PH	Laser power, scan speed	GP	Porosity	To model and predict porosity at any combination of process parameters from a small dataset	[150]
SLM	In718	Part orientation, part position, fraction of recycled powder	RF	Porosity, median pore diameter and spacing	To link the process parameters to pore formation	[151]
SLM	Ti-6Al-4V	Spreader translation and rotation speed	MLP	Powder bed Surface roughness, spread speed	To construct a spreading process map to optimize surface roughness and spreading efficiency for powder bed	[152]
EBM	CoCr	Beam current, scan speed	SVM	Energy density	To construct a process map from a small dataset	[117]
EBM	–	Presence of core support, support density and angle	DT, Bayes classifier	Classification of part quality	To investigate the influence of support structure parameters on part quality	[153]

Directed energy deposition						
DED	Copper-coated steel wire	Wire feed rate, welding speed, arc voltage, nozzle-to-plate distance	MLP	Bead width, height	To predict bead width and height	[154]
DED	Copper-coated steel wire	Welding speed, welding voltage	MLP	Offset distance between the center of weld bead and fed wire	To model the relationship between the bead's geometry and the offset distance	[155]
DED	2020 Al alloy powder	Laser power, scan speed, powder feeding rate	MLP	Melt pool width, depth and height	To estimate the process parameters required to obtain a specified melt pool geometry	[156]
DED	–	Laser power, scan speed, scan strategy, build size and shape	RNN	Thermal history	To predict the high-dimensional thermal history of complex parts during printing	[145]
DED	SS316L	Laser power, scan speed, powder feeding rate	MLP, SVM	Depositing height	To predict and control depositing height	[157]

At the mesoscale, single tracks act as the fundamental building blocks of high-energy AM processes. The melt pool morphology, such as geometry, continuity and uniformity, can largely influence the final product quality. Therefore, multilayer perceptron (MLP) was utilized to predict the melt pool geometry (particularly width, depth and height) for powder-based [156] and wire-based [154, 155] DED processes based on limited experimental datasets. The melt pool geometries were hence closely linked to the process parameters. This implies that a specified melt pool geometry is achievable by controlling the process parameters in a reverse way. To better visualize the linkage, Tapia et al. [149] introduced a Gaussian process-based (GP) surrogate model to construct 3D response maps of melt pool depth versus process parameters, as illustrated in Figure 2.24 (a)-(c). The process window can therefore be determined to avoid the undesirable keyhole mode melting. It should be noted that the 139 data points used in the study were obtained from a combination of their own one experimental dataset and two additional datasets from the published literature. Moreover, a few ad hoc filters were put in place to remove outliers, leading to a total of 96 valid data points. Their prediction

error of 6.023 μm is acceptable as they were comparable to the errors occurred in data collection process.

Another critical concern at mesoscale is the porosity of AM-built parts. In metal AM, achieving full density is the primary objective, as the internal voids and pores significantly affect the mechanical performance of parts, especially fatigue properties [158]. MLP is able to model complex nonlinear relationships while hardly interpreting how it makes the prediction. Moreover, GP usually can estimate the uncertainties in prediction results, but the process is more computationally expensive given the same amount of input data as MLP. Hence, MLP [148], as well as GP coupled with Bayesian methods [78], were adopted to predict the porosity based on the combinations of process parameters in SLM, as depicted in Figure 2.24 (d)-(e). Moreover, open porosity is required in some cases such as auxetic structures for energy absorption and porous structures for medical implants.

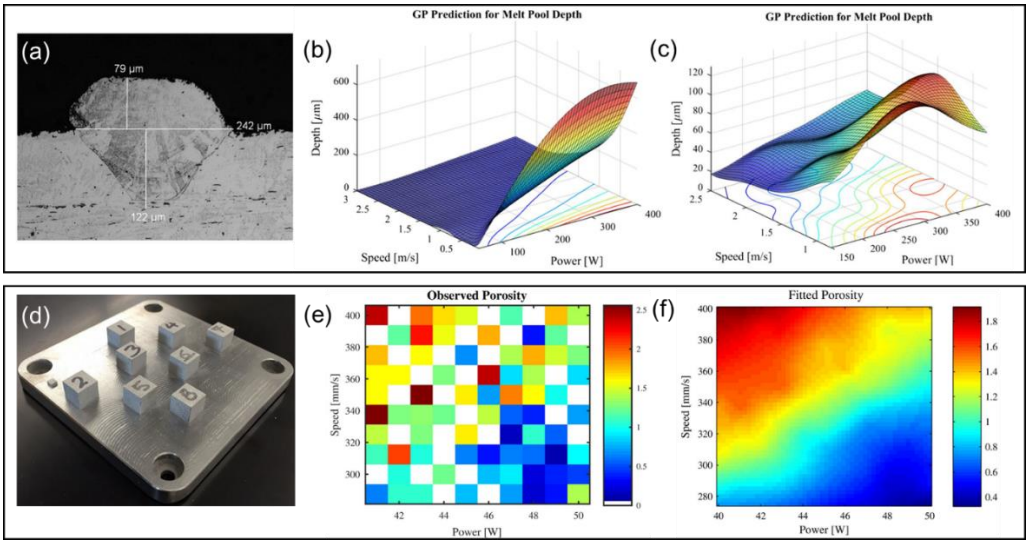

Figure 2.24 GP-based model for mesoscale characteristics prediction of the parts fabricated by SLM. SS316L samples [149]: (a) Optical micrograph of the single track. (b) Melt pool depth prediction from experiments and (c) the simulation. SS17-4 PH samples [150]: (d) As-built test coupons. (e) Spatial behavior of the observation across the grid of process parameters (white values mean no test coupons in that location). (e) Porosity prediction at any desired power-speed combinations.

The macro-scale properties of AM-built parts can also be analyzed by the ML method. Adaptive-network-based fuzzy inference system (ANFIS) usually can model uncertainties as a probability distribution. Hence it is good for the assessment of fatigue properties due to many uncertainties involved in fatigue process. Zhang et al. [147] collected 139 fatigue data from SS316L parts processed by the same SLM machine under a total of 18 varying processing conditions. They successfully applied ANFIS to predict the high-cycle fatigue life with root

mean squared errors of ~ 11 - 16% using two models: the ‘process-based’ model (printing process parameters and heat treatment temperatures) and the ‘property-based’ model (UTS and elongation). However, their models' performance was downgraded when they attempted to use the trained model to predict fatigue life using the 66 data points collected from published literature data, which was mainly due to the machine-to-machine variability. Hence, it is suggested to incorporate both experimental and literature data in model training in order to improve its generalization capability. According to Wang et al. [6], observing the top build surface condition can help to narrow down the process window for EBM. Support vector machine (SVM) performs well particularly when the margin of separation between classes is clear, while the drawback is that it is easy to overfit. Aoyagi et al. [117] proposed a simple method to construct process maps for EBM out of only 11 samples. The SVM classifier was trained to correlate process parameters (beam current and scan speed) to surface conditions (see Figure 2.25). However, it should be noted that SVM in their work was only used for data fitting in order to plot the decision boundaries. It was challenging to allocate a test set to evaluate the accuracy of the entire model as their dataset was too small. Recurrent neural networks (RNN) is used for times series forecasting. Therefore, considering the temporal dependency of the input data, RNN was used to train FEM data in order to predict the high-dimensional thermal history of complex parts in DED process, as demonstrated by Mozaffar et al. [145]. Moreover, Lu et al. [157] attempted both MLP and SVM to predict depositing height of thin walls for DED.

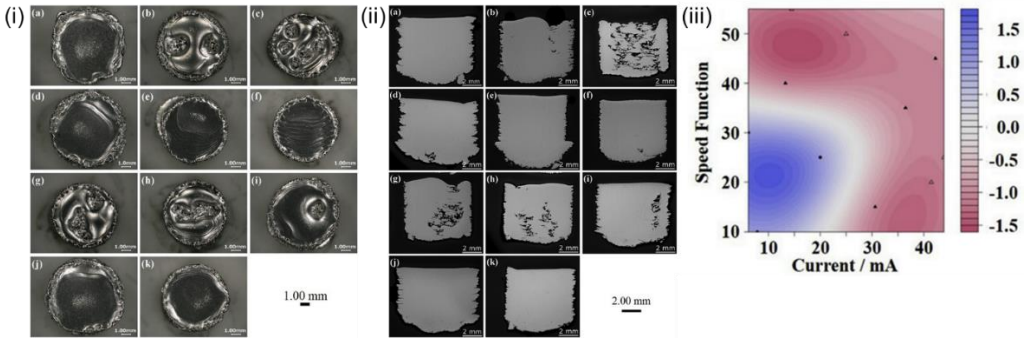

Figure 2.25 SVM used for predicting macro-properties of EBM-built parts [117]. (i) Top surface conditions the samples printed under 11 different process parameters. (ii) The corresponding cross-sectional micrographs of each sample. (iii) A process map was constructed to optimize process parameters to print parts with low porosity and good surface.

Despite its increasing popularity in AM community, ML is also faced with challenges in process development. Firstly, since ML is data-driven, its performance highly relies on the amount of accessible data. However, constructing a big database is not practical from economic

considerations in AM. There is a tradeoff between the size of dataset and performance of ML models. Secondly, the interpretability of the ML models is generally poor, especially for neural networks. As a result, ML models are sometimes treated as a “black box” and the way they make predictions is often questioned. Thirdly, the generalization ability of the ML models needs to be validated, as the models which perform well for one process or material may deteriorate when the factors such as processing techniques, machine models and material characteristics change. The abovementioned challenges will be addressed in Chapter 6 and 7.

2.8 Research Gap and Scope

From the literature review, it is found that the processable materials for SEBM are still very limited, not to mention the class I materials, which implies the necessity for materials development for SEBM processing. Besides, the conventional methods to optimize process parameters include DoE and simulations, both of which are deficient in terms of efficiency, reliability and cost. More importantly, it may also lead to a sub-optimized or incomplete process window over the entire parameter space. Furthermore, the full-scope relationships of PMP for SEBM processing are still less known. Therefore, it is necessary to develop a more effective method to optimize the process parameters and depict the relationships of PMP under SEBM from a complete and explicit process window based on the deployed process parameter optimization work.

To address the abovementioned concerns and fill the research gap, the first part of the present Ph.D. study involves developing optimal process parameters for pre-alloyed SS316 and in-situ alloyed NiTi by SEBM. In the second part of the Ph.D. work, a ML method will be attempted for fast and precise process parameter optimization for pre-alloyed Ti-6Al-4V and SS316L with a small dataset. A high-fidelity ML-centered tetrahedral framework is proposed to map the full-scope PMP relationships by state-of-the-art deep learning (DL) algorithms.

2.9 Research Roadmap and Approach

The research roadmap is shown in Figure 2.26. The framework outlines the key steps taken to achieve the aim and objectives of this Ph.D. study, which include the traditional parametric investigation using DoE and a novel ML method to optimize SEBM process

parameters. Firstly, a literature review was done to systematically and comprehensively understand the SEBM processing and the key process parameters involved. The three materials that have high industry added-value but were processed by SEBM with underperformed mechanical properties were identified. In the first part of the Ph.D. study, DoE method was employed to conduct process parameter optimization for SEBM-built SS316L alloys using both fine and coarse powders. Their microstructure and mechanical properties were studied, and the effects of varied powder size distribution on these three aspects were discussed. Process parameters were studied for an equimolar NiTi alloy using pre-mixed elemental Ni and Ti powders. This allows the author to understand the feasibility and mechanisms of processing the alloys which may be subject to exothermic reactions using SEBM (see Appendix A). In the second half of the Ph.D. study, the author proposed a ML method to optimize process parameters quickly and precisely with a small dataset. Ti-6Al-4V alloy was used to verify the effectiveness of this new method. Moreover, comprehensive and quantitative PMP relationships were established by DL over the entire parameter space. This method was further extended to SS316L alloy with an even smaller dataset through transfer learning (TL) in order to prove its generalization ability for process parameter optimization. Finally, the efficiency of the two methods was compared and discussed. Eventually, the joint efforts in materials and methods development presented in this thesis will expedite the adoption of SEBM at a larger scale as an industrial manufacturing technique in the long run.

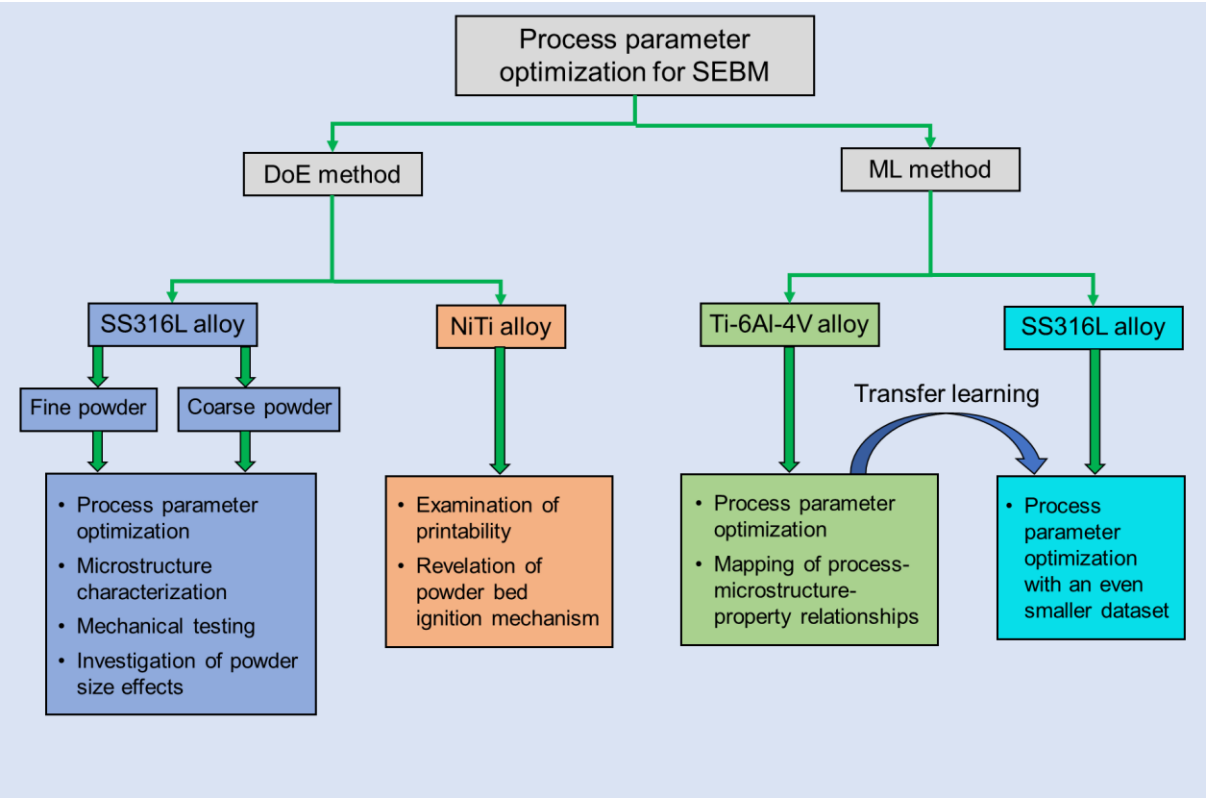

Figure 2.26 Research roadmap for the present Ph.D. study.

Chapter 3 Materials and Methods

This chapter describes the material characteristics and the equipment used to conduct the experiments in order to achieve the proposed research objectives: using both DoE and ML methods for SEBM process parameter optimization, as well as establishing the PMP relationships.

More specifically, the preparation and examination of the powder feedstocks are presented. The SEBM sample fabrication and preparation steps are detailed. The top surface condition, relative density and tensile properties are the benchmark criteria to determine the level of success that a material can be processed by SEBM. Hence, a series of post-process characterization and testing techniques are explained: Archimedes method for density measurement; optical microscopy (OM) for preliminary microstructure observation and relative density measurement using image analysis; laser confocal microscopy for top surface topography examination; scanning electron microscopy (SEM), backscatter diffraction (EBSD) and X-ray diffraction (XRD) for detailed microstructural characterization; tensile and hardness testing for the evaluation of mechanical properties. The equipment used is listed in the flowchart diagram shown in Figure 3.1.

Finally, the DoE and ML methods, both of which are adopted for process parameter optimization in this Ph.D. work, are elaborated.

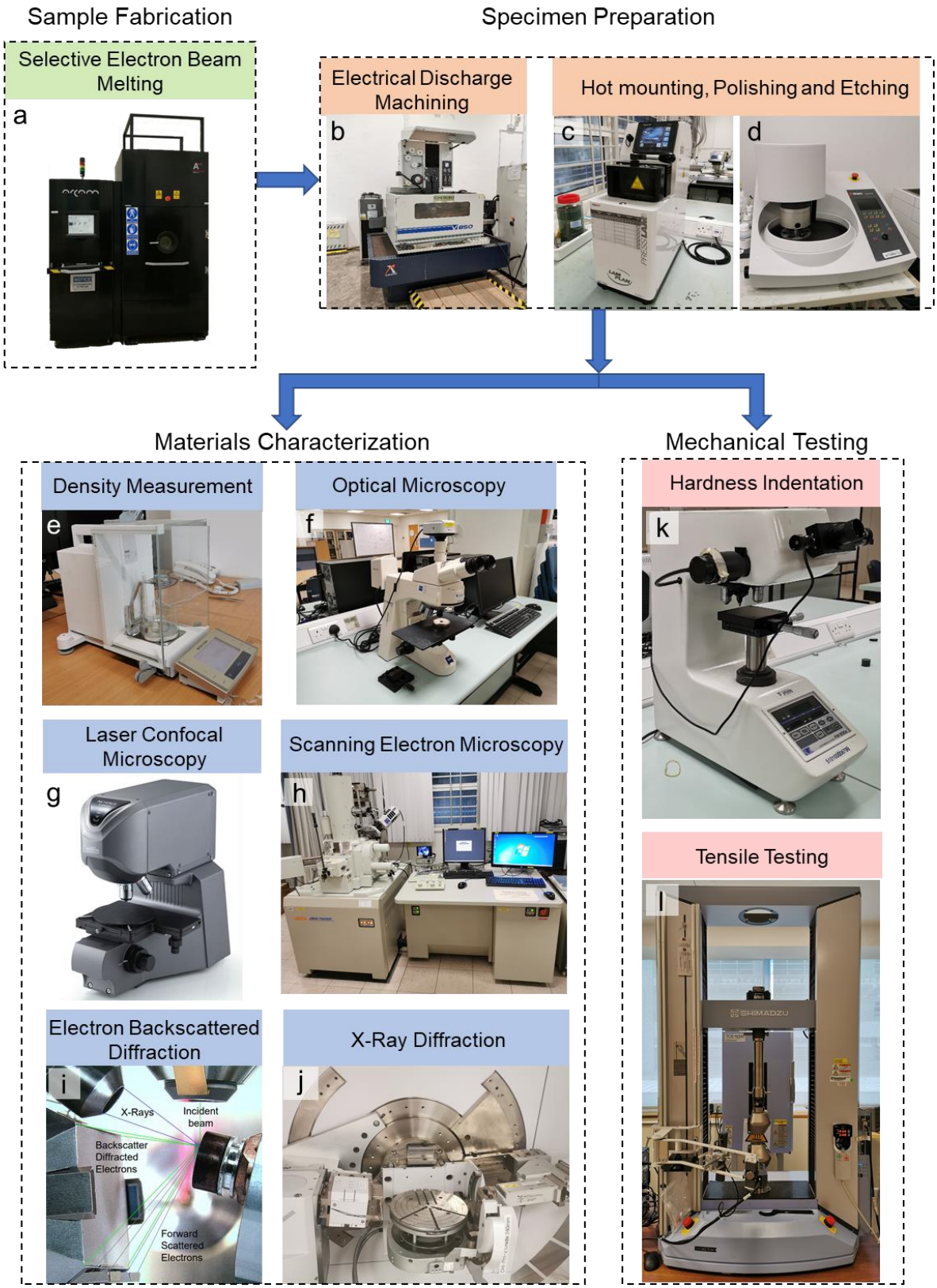

Figure 3.1 The flowchart diagram depicting the equipment used for experimentation: (a) Electron beam melting (EBM, Arcam A2XX) machine housed at SC3DP, NTU; (b) Wire-cut electrical discharge machining (EDM, ICHI SEIKI) system used to cut SEBM-built samples; (c) Hot mounting machine (PRESSLAM®1.1); (d) Automatic polishing machine (Struers Tegramin-25); (e) Density measurement apparatus (Mettler Toledo XS204) based on Archimedes principle; (f) Optical microscope (OM, ZEISS

Axioskop 2 MAT); (g) 3D laser confocal microscope (Keyence VK-X series) [159]; (h) Field emission scanning electron microscope (FESEM, JEOL JSM-7600F) with (i) the auxiliary electron backscatter diffraction (EBSD) detector; (j) X-ray diffraction (XRD, PANalytical Empyrean) apparatus; (k) Microhardness tester (Future Tech FM-300e) for Vickers hardness (HV) indentation; (l) Uniaxial tensile testing machine (Shimadzu AGX).

3.1 Powder Feedstocks

Three types of powder feedstocks with distinctive chemical and physical properties were used in this Ph.D. work. The pre-alloyed SS316L and Ti-6Al-4V powders are commercial ones purchased from renowned suppliers. The Ni-Ti powder mixture was prepared by the author at lab in an argon gas-purged container.

3.1.1 Pre-alloyed Stainless Steel 316L Powders

Two types of inert gas-atomized spherical SS316L pre-alloyed powders (TLS Technik GmBH, Germany) were used in this work, with a nominal size range of ~ 20 - 63 μm for fine powders (Figure 3.2), and a nominal size range of ~ 45 - 106 μm for coarse powders (Figure 3.3). The datasheet given by the supplier shows that the chemical composition of the powder includes 0.02 wt.% C, 0.8 wt.% Si, 0.4 wt.% Mn, 17.1 wt.% Cr, 2.3 wt.% Mo, 11.8 wt.% Ni, and Fe for the balance. For both SS316L fine and coarse powders, they are spherical overall, with small satellites attached to some larger particles, which were formed during the gas atomization process where the small liquid droplets were attached to larger ones.

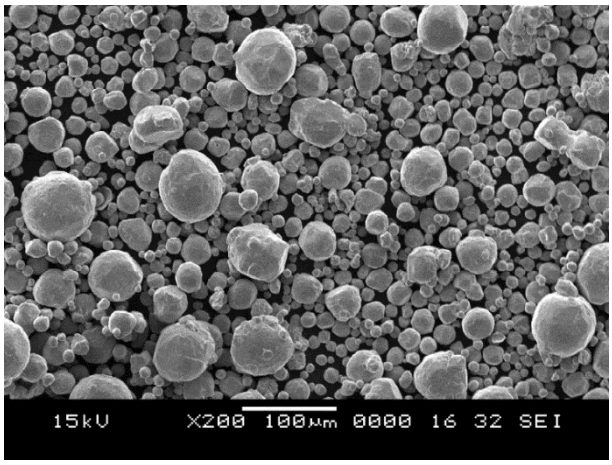

Figure 3.2 SEM micrograph of fine SS316L precursor powders.

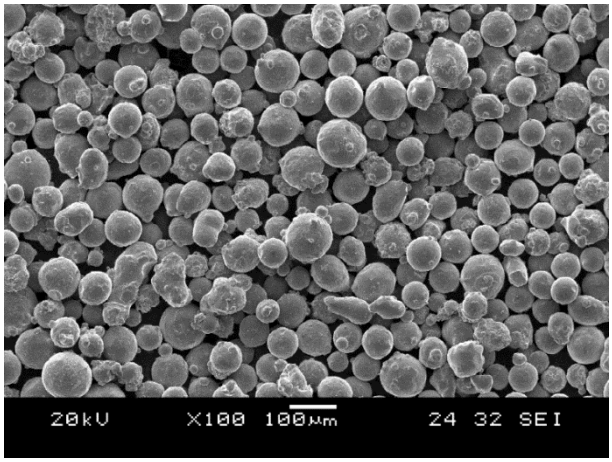

Figure 3.3 SEM micrograph of coarse SS316L precursor powders.

The actual PSD of the two types of SS316L precursor powders was measured by a laser particle size analyzer (Malvern Panalytical, Mastersizer 3000; measurable size range ~ 0.01 - 3500 µm) [160]. It uses the technique of laser diffraction to conduct the measurement. The powder sample was first loaded to a hopper and then vibrated slowly into the channel feeder. The feed rate was set to be 10%, and the air pressure was 4 bar. The PSD is shown in Figure 3.4. Both fine and coarse powders roughly follow a slightly skewed Gaussian distribution, where the median (D_{50}) is smaller than the mean diameter in both cases. The actual size for fine powders ranges from 7 µm to 140 µm, with D_{50} ~ 44 µm and mean diameter ~ 75 µm, while the actual size for coarse powders ranges from 40 µm to 165 µm, with D_{50} ~ 72 µm and mean diameter ~ 95 µm.

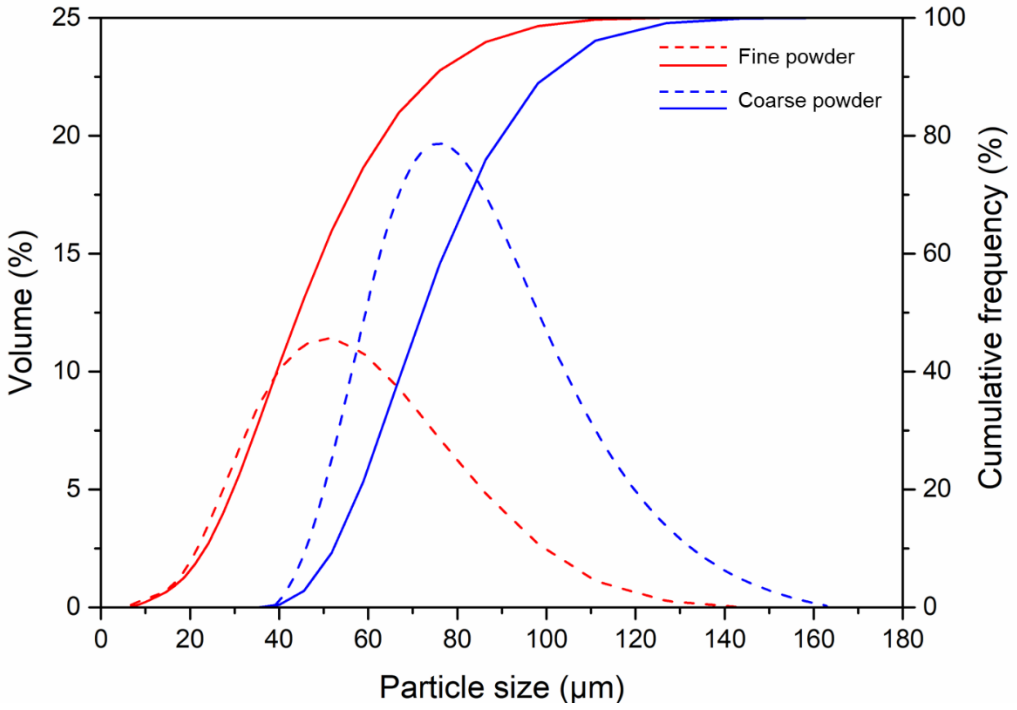

Figure 3.4 Particle size distribution (PSD) plot for SS316L fine and coarse powders.

3.1.2 Pre-alloyed Ti-6Al-4V Powders

Ti-6Al-4V ELI (Grade 23, Arcam AB) with a size range of ~ 45 - 106 μm was used to fabricate the samples. The datasheet given by the supplier shows that the chemical composition of the powder includes 6 wt.% Al, 4 wt.% V, 0.03 wt.% C, 0.1 wt.% Fe, 0.1 wt.% O, 0.01 wt.% N, 0.003 wt.% H, and Ti for the balance. This type of powder is already commercialized by Arcam, hence the morphology of the powder is almost perfectly spherical with a very small amount of satellites. The powders used in this work have been recycled for a few times by powder recovery system. Figure 3.5 shows that the recycled powders can still maintain spherical morphology after many builds.

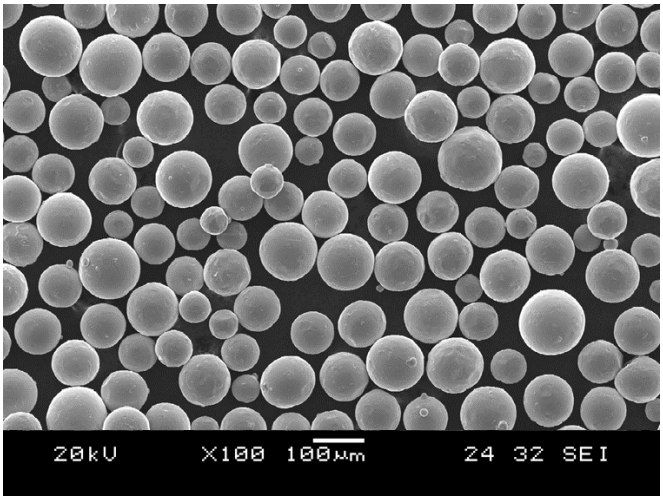

Figure 3.5 SEM micrograph of Ti-6Al-4V precursor powder.

3.1.3 Pre-mixed Ni-Ti Powders

Inert gas-atomized elemental Ni powders (Apphia Advanced Materials, Singapore; size range of ~ 20 - 63 µm) and Ti powders (Grade 2, Arcam AB, Sweden; size range of ~ 45 - 106 µm) were blended in equimolar contents. A tumbling mixer (Inversina 2L, Switzerland) was used to mix the powders in an 1 L argon gas-purged container with a 50% filling ratio. The results in Figure 3.6 show that a 2-hr mixing time is sufficient to achieve a relatively high-level homogeneity, which is testified by energy dispersive spectroscopy (EDS) mapping. It should be noted that Ni-Ti powder mixtures were not recycled, otherwise the composition of the mixed powder would be changed significantly. Hence, newly prepared Ni-Ti mixture powders with equimolar ratio were used for each build.

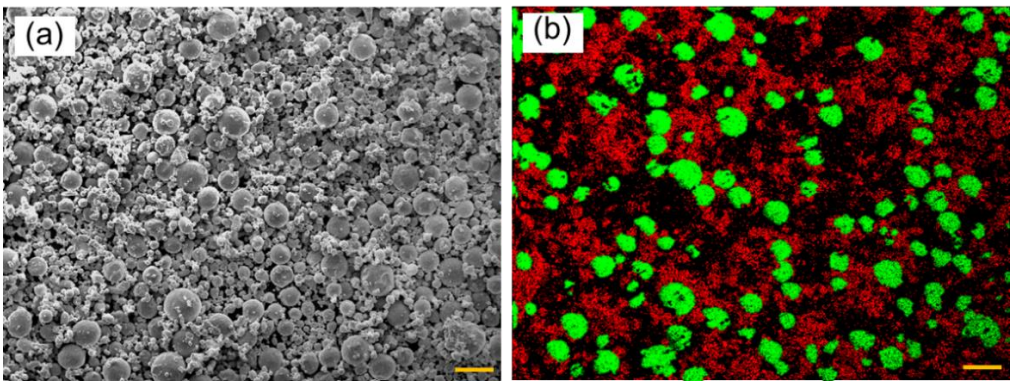

Figure 3.6 (a) SEM micrographs of Ni-Ti powder mixtures with a blending time of 2 hrs. (b) Energy dispersive spectroscopy (EDS) results show that red color denotes Ni powders and green color for Ti powders. All the scale bars are 100 µm.

3.2 Selective Electron Beam Melting Process

All the samples were fabricated by an EBM A2XX system (Arcam EBM, Sweden), as shown in Figure 3.1 (a). It is the largest EBM machine model available currently, which offers a build envelope of Ø 420 × 380 mm^3.

Firstly, the substrate was heated up to the desired temperature set by the user and then the layer-wise fusion process started. During the heating stage, the powder surrounding and underneath the start-plate was sintered to tightly secure the start-plate, preventing it from being shifted by the moving of rake blade. After the first layer of powder was uniformly distributed on the start-plate by the rake blade, the preheating step started. In this stage, the fast-moving defocused electron beam rapidly rastered the start-plate to maintain the elevated temperature. The FO and beam current for preheating were optimized, so that the so-called "smoke" phenomenon, i.e. charged powders are pushed away, could be prevented and the sintered powder encapsulating the built parts could be easily blasted away by the powder recovery system after the build was completed. The melting process started by using the focused electron beam to fully melt the powder. Contours of the parts were traced, followed by in-fill hatch melting of the interior parts. Thereafter the build table was lowered by 50 μm, then powder distribution, preheating and melting process were repeated. The parts were built consecutively to the final height defined by the CAD model, followed by slow cooling, albeit helium gas was pumped into the build chamber to facilitate the cooling process. The detailed process parameters for melting will be provided in each subsequent result chapter.

3.3 Specimen Preparation Techniques

3.3.1 Electrical Discharge Machining

Electrical discharge machining (EDM, ICHI SEIKI) was used to remove the samples built on the stainless steel start-plate, as shown in Figure 3.1 (b). This material removal process is achieved by applying a pulsating electrical charge of high-frequency current to the workpiece from the electrode. Here, the wire-cut EDM uses a continuous-travelling spool of tungsten wire (~ 0.18 mm in diameter) under tension as the electrode, causing the resulting spark discharge to erode the workpiece to form a desired final shape. The dielectric fluid will be circulating to dissipate the heat and flush away the metal particles generated. As the high-temperature cutting

process affects the original microstructure of the sample, a rough polishing to ~ 100 µm depth with sandpaper of grit #320 is usually required to remove the wire-cut surface. It should be noted that Ti-6Al-4V samples do not require EDM mainly due to the dissimilarity in thermal expansion coefficient with the stainless steel start-plate. Instead, they could be removed manually by hands or via knocking the other side of the start-plate by a hammer.

3.3.2 Hot Mounting, Polishing and Etching

To conduct microstructural characterization and crystallographic texture analysis which requires mirror-like surfaces, the samples were hot mounted in thermoset epoxy by a hot mounting machine (PRESSLAM®1.1) as shown in Figure 3.1 (c) and subsequently mechanically polished. For the current Ph.D. work, all samples were polished using Struers Tegramin-25 (see Figure 3.1 (d)). They were first ground with SiC paper of grit #320 and followed by MD-Largo (DiaPro Largo 9 µm suspension). Afterwards, Ti-6Al-4V samples were treated by a chemical polishing process with a MD-Chem disc and OP-S active oxide polishing suspension, followed by flushing water to clean the samples and the rotating disc thoroughly. The polishing step for Ti-6Al-4V samples was completed here.

For NiTi and SS316L samples, this chemical polishing process was not applied. Instead, they were polished with MD-Dac (DiaPro Dac 3 µm suspension) and MD-Nap (DiaPro Nap 1 µm suspension). When these processes were completed, mirror-like surfaces were obtained for porosity examination.

To reveal the microstructures for both OM and SEM observation, Kroll's reagent (2 ml HF, 6 ml HNO_3, 92 ml distilled water) was adopted to etch the polished samples by immersion of 5 mins, 20 mins and 10 sec for NiTi, SS316L and Ti-6Al-4V, respectively.

For EBSD studies, the chemical etching step was not applied. Instead, the as-polished samples were taken out from the epoxy sample holder. Subsequently, they underwent the chemical polishing process using a MD-Chem disc and OP-S active oxide polishing suspension. It should be noted that the size requirement for EBSD study is $10 \times 10 \times 3$ mm^3.

3.4 Materials Characterization Techniques

3.4.1 Density Measurement

The density of the samples was determined by both Archimedes method and image analysis method. For Archimedes method, the samples cut by EDM were only polished by sandpaper of grit #320 to remove the wire-cut surface. Based on Archimedes principle, the density of samples can be calculated by using the equation of $\frac{w_{in\ air} \times \rho_{ethonol}}{w_{in\ air} - w_{in\ ethonol}}$, where $w_{in\ air}$ and $w_{in\ ethonol}$ are the weights of samples measured in air and ethanol, and $\rho_{ethonol}$ is the density of ethanol. Three repetitive measurements were taken for each sample using a density balance (Mettler Toledo XS204), as shown in Figure 3.1 (e). Besides, density measurement could also be implemented by image analysis using microscope, which will be detailed in the next section.

3.4.2 Optical Microscopy

Optical microscopy (OM; ZEISS Axioskop 2 MAT with a magnification range from ×50 to ×500) was used as the first step to briefly examine the microstructure of the chemically etched samples (see Figure 3.1 (f)). Under OM, the sub-millimeter features such as melt tracks, layer boundaries and grains can be observed.

OM could also be used for density measurement on the mirror surface of mechanically polished samples before they were chemically etched. The images showing pores were captured by OM and then processed by ImageJ software [161] by converting it to a 16-bit image. A default threshold was applied to convert the image to black and white. ImageJ could calculate the fraction of the porous areas over the entire image to obtain the relative density value. Ten images were taken in random areas for each sample.

3.4.3 Laser Confocal Microscopy

Laser confocal microscopy is an optical technology that enables the reconstruction of 3D structures based on the stack of cross-sectional images obtained from the specimen. It offers

several major advantages over the conventional widefield optical microscopy, such as eliminating or reducing the out-of-focused background information, collecting serial cross-sectional views of the thick specimen to reconstruct the 3D structure. When measuring the surface topography of solid samples, the height of features can be represented by different colors.

Keyence VK-X series 3D laser confocal microscope (see Figure 3.1 (g)) was used in this Ph.D. work. For material studies of Ti-6Al-4V alloys, the top build surfaces of the samples were captured using the magnification of ×50 and z-depth resolution of 5 μm under high-speed mode. 88 images were captured for each sample, which were then stitched by the auxiliary software to create the topography image of the entire 10 × 10 mm^2 surface. The mirror-like cross-sectional surfaces were taken but with a reduced area of 3.75 × 3.75 mm^2 in the same manner to show the pore microstructure.

3.4.4 Scanning Electron Microscopy

The maximum magnification of optical and laser microscopy typically ranges from ×500 to ×1500. Its resolving power is limited by the light wavelength and the numerical aperture of the objective lens. Hence, to reveal more delicate details of the samples, scanning electron microscopy (SEM) is used, which can provide magnifications higher than ×160,000, as shown in Figure 3.1 (h).

When electrons impinge on the matter, different types of signals are generated. In SEM, two types of electrons are detected primarily, namely secondary electrons (SE) and backscattered electrons (BSE). SE is the result of inelastic interaction between the beam and the sample, which happens at the surface or near the surface of the sample. It has relatively lower energy and can inspect the surface topography of the samples. In contrast, BSE is the result of elastic collisions with atoms, which happens in a broad region within the interaction volume. The atoms with a larger atomic number can scatter more electrons and produce higher signals. Hence, based on this principle, BSE can identify different atoms, phases and even crystallographic textures of the samples. Moreover, when electron beam displaces an inner shell electron that is replaced by an outer shell electron of the atom, characteristic x-ray is emitted as the energy difference between outer and inner electron shells of an element is unique.

Hence, energy dispersive spectroscopy (EDS) affiliated to SEM can detect the elements of the sample.

In this Ph.D. work, the morphology of the powder, microstructure and fracture surface of tensile coupons were observed under a field emission scanning electron microscope (FESEM; JEOL JSM-7600F, Japan). Microstructures were observed only after chemical etching. Powders were observed in the as-received state, while the fracture surfaces were observed directly without polishing or etching. Since the magnification needed was below ×10,000 for microstructure observation in our case, we used an accelerating voltage of ~ 15 kV, probe current of ~ 9 mA and working distance (WD) of ~ 20 mm in SE mode. In BSE mode, the same accelerating voltage was used but with a higher probe current of ~ 15 mA and smaller WD of ~ 10 mm. In EDS mode, the setting was the same as SE mode except that a higher accelerating voltage of ~ 20 kV was applied. The chemical compositions of some particular particles or phases were detected by at least ten measurements using EDS. Besides, it could also obtain 2D composition maps with a resolution of 1024 × 1024 pixels and a pixel dwell time of 50 ms.

3.4.5 Electron Backscattered Diffraction

Electron backscatter diffraction (EBSD) is widely used in materials science to identify phases, crystalline defects and crystallographic orientations. Figure 3.1 (i) illustrates the working principles of EBSD. The sample is placed at an inclined angle of ~ 70° with respect to the normal incidence of the electron beam. As the accelerated electrons interact with the sample, some electrons are diffracted away according to the Bragg's angle and subsequently impinge on a phosphor screen of a highly sensitive EBSD detector to form the Kikuchi bands. These patterns can provide information about the geometry of the lattice planes in the crystal. The Aztec software affiliated to JEOL 7600F FESEM can process the Kikuchi lines and index the patterns by comparing the measured angles between different bands with the theoretical values in the database. In this technique, phases and crystallographic orientations can be determined.

3.4.6 X-Ray Diffraction

X-ray diffraction (XRD) technique can be used to identify phases and analyze crystallographic textures (see Figure 3.1 (j)). Based on the Bragg's Law ($\lambda = 2d\sin\theta$), when a crystal structure with a lattice constant of d is irradiated by an x-ray beam with a wavelength of λ, diffraction peaks can be observed at angles of 2θ if the constructive interferences are generated. Hence, by using a goniometer to measure 2θ, d can be determined. In our work, the PANalytical Empyrean XRD model (detection limit ~ 3 vol% [58]) was used at room temperature to identify the phases of the powder feedstocks and SEBM as-built SS316L samples. The X-rays were generated from Cu Kα source. It was operated under 40 kV and 40 mA with a step size of 0.01°. The XRD peaks were obtained over a 2θ range of 30° - 100° for each test. The raw data were processed using the HighScore software.

3.5 Mechanical Testing

3.5.1 Vickers Hardness Indentation

Vickers hardness (HV) indentation is used to measure the hardness of a material, which is calculated by the size of an impression produced under load by a square-based pyramid-shaped diamond indenter. The HV is calculated by the formula:

$$HV = 1.854(F/D^2) \qquad \text{Eq. 3.1}$$

where F is the applied load (in kgf) and D is the indentation area (in mm^2).

In this Ph.D. work, the Future Tech FM-300e microhardness tester was used (see Figure 3.1 (k)). The indentation was performed on as-polished mirror-like sample surfaces with a load of 1 kgf and holding time of 15 s. Five measurements were taken along the vertical midplane of each sample, with a spacing of 1 mm between adjacent indentation impressions.

3.5.2 Tensile Testing

Tensile testing provides a comprehensive examination on the mechanical properties of a material in terms of strength, elongation and modulus. The strain rate and load cell are two

critical factors that will affect the accuracy of testing. In practice, for metallic tensile coupons in plate shape, the strain rate should be within the range of 10^{-5} /s - 10^{-3} /s. Ultimate tensile strength (UTS) of testing materials should not be less than 5% of the load cell used. In this Ph.D. work, a uniaxial mechanical testing machine (Shimadzu AGX, Japan) with a non-contact digital video extensometer was used (see Figure 3.1 (l)).

For SS316L samples, the plate-type tensile coupons were first machined by EDM from the SEBM as-built blocks to a dimension of 30 × 10 × 3 mm^3 for horizontal tensile coupons and 15 × 10 × 3 mm^3 for vertical tensile coupons, with the respective gauge lengths of 10 mm and 5 mm, as illustrated in Figure 3.7. The coupons were polished with #320 grit sandpapers to remove the wire-cut surfaces. The tensile properties of samples were tested under a constant loading speed of 0.2 mm/min, which is equivalent to a strain rate of 3.33×10^{-4} /s at room temperature with a load cell of 10 kN. Four tensile coupons were tested for each set of samples.

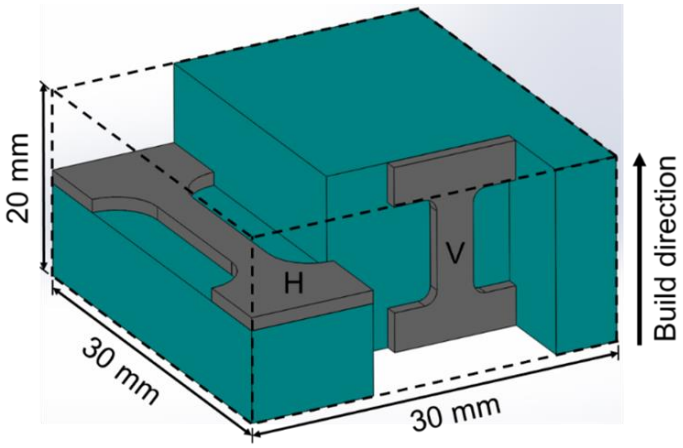

Figure 3.7 Schematic showing how tensile coupons were machined from the SEBM as-built SS316L solid cuboids. H denotes horizontal tensile coupons, and V denotes vertical tensile coupons.

The near-net-shape Ti-6Al-4V coupon samples were first polished with #320 sandpaper to remove the partially melted powders attached to the surfaces. They were subsequently tested with the same machine model except that a 50 KN load cell was used. The testing speed was set to be 0.5 mm/min, which is equivalent to a strain rate of 8.33×10^{-4} s^{-1}. The elongation was also measured by a non-contact digital video extensometer. Three specimens were tested for one set of samples.

3.6 Design of Experiments

3.6.1 Full Factorial Design

To optimize the process parameters for SS316L, a three-step strategy was adopted as recommended by Arcam, which included top surface morphology examination, density measurement and tensile property testing. Specifically, a low energy level produces samples with porous surfaces due to insufficient fusion of powder granules. In contrast, a high energy level causes the surfaces to warp due to localized heat accumulation. A preliminary screening of the process parameters could be achieved by visual examination of the top surface morphology. Next, density measurement was required because some samples with seemingly flat surface might have minor porosity with a relative density < 99.0%, below the minimum criteria for density. After the process window was further narrowed down by the secondary screening, tensile testing was done to select the fully dense samples with desirable tensile properties.

The rationale for this strategy aligns with the benchmark criteria required for SEBM material classification justified in section 2.4.1. DoE methods were carried out for the first two steps. SF and FO are two independent factors that play critical roles in process parameter optimization according to Arcam. Full factorial designs were selected to investigate the effects of all possible parametric combinations on the response.

The line offset and layer thickness was fixed at 0.1 mm and 50 µm, respectively. In the preliminary screening for fine powder samples, FO had 4 levels, ranging from 8 mA to 14 mA; SF had 8 levels, ranging from 130 to 300. This design resulted in 32 parametric combinations. After the process window was narrowed down by observing the top build surface conditions, both FO (8 mA to 12 mA) and SF (150 to 190) were set at 3 levels. The DoE table for fine powder samples is shown in Table 3.1, where the digits in the matrix are sample numbers. Likewise, the DoE table for coarse powder samples is shown in Table 3.2.

Table 3.1 Full factorial DoE design for SEBM-built samples using fine powders. The samples built within the shaded region are used for relative density measurement.

FO \ SF	130	150	170	190	210	230	250	300
8 mA	1	5	9	13	17	21	25	29
10 mA	2	6	10	14	18	22	26	30
12 mA	3	7	11	15	19	23	27	31
14 mA	4	8	12	16	20	24	28	32

Table 3.2 Full factorial DoE design for SEBM-built samples using coarse powders. The samples built within the shaded region are used for relative density measurement.

FO \ SF	70	90	110	130	150	170
5 mA	1	8	15	22	29	36
6 mA	2	9	16	23	30	37
7 mA	3	10	17	24	31	38
8 mA	4	11	18	25	32	39
9 mA	5	12	19	26	33	40
10 mA	6	13	20	27	34	41
12 mA	7	14	21	28	35	42

3.6.2 Analysis of Variance

As a statistical tool, ANOVA was used to carry out a rigorous and quantitative analysis of the effects of the two process parameters on the relative density of the SEBM-built SS316L samples. The sum of squares, degree of freedom and mean squares were calculated for SF and FO, respectively. As only one sample was produced under each parametric combination (i.e. no replication), the sum of squares for the errors was estimated by the interaction of SF and FO. This is based on the assumption that SF and FO have no strong interactions. The validity of this assumption needs to be checked by Tukey's test for additivity [162].

3.6.3 Response Surface Method

RSM is a combination of statistical and mathematical method for modelling and analyzing engineering problems. In this work, RSM was adopted for optimizing the response surface of relative density, namely finding the parametric combinations of FO and SF that could yield a high relative density. The least-squares method was used to minimize the error when establishing the response surface function $\boldsymbol{f}$. The order of the polynomials that constituted $\boldsymbol{f}$ was determined empirically so that the response surface could fit the data points well while overfitting was prevented.

In the case of fine powder samples, the degrees of FO and SF were set to be 1 and 2, respectively. The equation is expressed as:

$$\boldsymbol{f}_{fine} = p_{00} + p_{10}x + p_{01}y + p_{11}xy + p_{02}y^2 \qquad \text{Eq. 3.2}$$

where p_{ij} is the coefficient for each polynomial term, x represents FO and y represents SF. Similarly, the degrees of both FO and SF were set to be 2 for coarse powder samples, where the equation is expressed as:

$$\boldsymbol{f}_{coarse} = p_{00} + p_{10}x + p_{01}y + p_{20}x^2 + p_{11}xy + p_{02}y^2 \qquad \text{Eq. 3.3}$$

3.7 Machine Learning Models

This section provides a general description of the ML models that are applied in this work. The technical details of each model can be found in Appendix B. As various models were used to process different types of data with distinctive predictions, the inputs and outputs provided to the ML models are summarized in Table 3.3 for clarity.

Table 3.3 List of input and output data for various ML methods used in this work.

ML methods		Input data	Output data
Traditional machine learning models	Support vector machine (SVM), k-nearest neighbors (KNN), decision trees (DT)	Process parameters	UTS
			Relative density
Deep learning models	Multilayer perceptron (MLP)	Process parameters	UTS
			Relative density
			Surface condition classification
	Convolutional neural networks (CNN)	3D surface topography images	UTS
			Relative density
		Surface morphology images	UTS
			Relative density
		Pore microstructure images	UTS
	Multimodal learning	Process parameters, 3D surface topography images, surface morphology images, pore microstructure images	UTS
	Variational autoencoder (VAE)	Surface morphology images, pore microstructure images, SEM α/β microstructure images	Latent space representation
	Conditional generative adversarial network (cGAN)	Process parameters	Surface morphology images
			Pore microstructure images
			SEM α/β microstructure images
	Transfer learning (TL)*	Process parameters	Relative density
			Surface condition classification
			Vickers hardness

* denotes that the technique is specifically applied in Chapter 6.

3.7.1 Traditional Machine Learning Models

Support Vector Machine

Support Vector Machine (SVM) classifies data points by finding a hyperplane (or decision boundary) in an N-dimensional space (namely the number of input features) that can maximize the margin [163]. SVM is one of the most widely used ML algorithms. It performs well especially with a small dataset that is coupled with high dimensional features, thus can solve complex problems. However, its performance declines with a large dataset, and it is prone to overfitting mainly because the margins heavily rely on the support vectors (i.e. the data points closer to the hyperplanes). Hence it is not robust to outliers.

K-nearest Neighbors

K-nearest neighbors (KNN) is a straightforward ML algorithm which assumes that similar things exist in proximity. It identifies the nearest neighbours to a query example and uses those neighbours to determine the class of the query [164]. KNN makes predictions rapidly as it does not require training. Nevertheless, it does not perform well with large datasets and high dimensional input features.

Decision Trees

Decision trees (DT) makes predictions by learning decision rules derived from the original data. It sorts the data by creating a tree-like structure. The nodes are further split into sub-nodes, and decisions are made based on whether the data can satisfy the conditions provided by these nodes [165]. The most salient advantage of DT algorithm is the simplicity to interpret and visualize. It does not require much data pre-processing such as data normalization or scaling. On the other hand, DT is susceptible to overfitting and unstable. It is also more computationally expensive to train the model.

However, the capability of traditional ML techniques is limited when processing the raw data in natural form such as raw images, which usually require domain expertise to perform feature engineering and extraction in order to transform them into suitable representations.

3.7.2 Deep Learning Models

Deep learning (DL) models are empowered by neural networks, which consist of multiple processing layers that can learn representations of data with multiple levels of abstraction [166]. DL can discover intricate patterns of high dimensional data and is widely applied in many areas such as object detection, speech recognition, drug discovery and genomics.

Multilayer Perceptron

Multilayer perceptron (MLP) is a typical type of neural networks that consists of 3 types of layers, namely the input layer, the hidden layers and the output layer (see Figure 3.8). The elements of each layer are neurons. In the training phase, the coefficients of connectivity between neurons (termed as weights) are updated iteratively by an algorithm called backpropagation to calculate the gradients so that the cost function can be minimized [166]. MLP can represent highly complicated relationships with non-linearity between inputs and outputs. In general, training neural networks requires a large dataset to prevent overfitting.

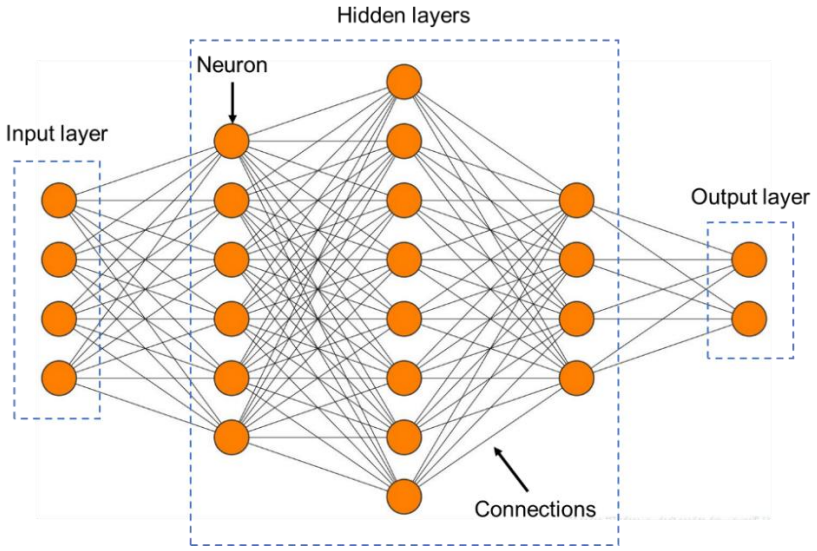

Figure 3.8 Schematic representation of an MLP with 3 hidden layers [12].

Convolutional Neural Networks

Convolutional neural networks (CNN) are composed of a series of convolutional layers with filters and pooling layers followed by fully connected layers and the output layer, as

illustrated in Figure 3.9. When processing the data with high dimensional input features, such as images, it can extract important features automatically. It is also more computationally efficient due to the convolution and pooling operations as well as parameters sharing. Hence, CNN is very prevalent in but not limited to image-related tasks such as image classification, object detection, face verification and so on.

Despite the above-mentioned advantages of CNN that created a resurgence of DL in the past few years, the intermediate layers of CNN are highly abstract and hard to interpret. Besides, the hyperparameters (i.e. the parameters used to control the learning process) involved in CNN are numerous, making the models hard to be tuned.

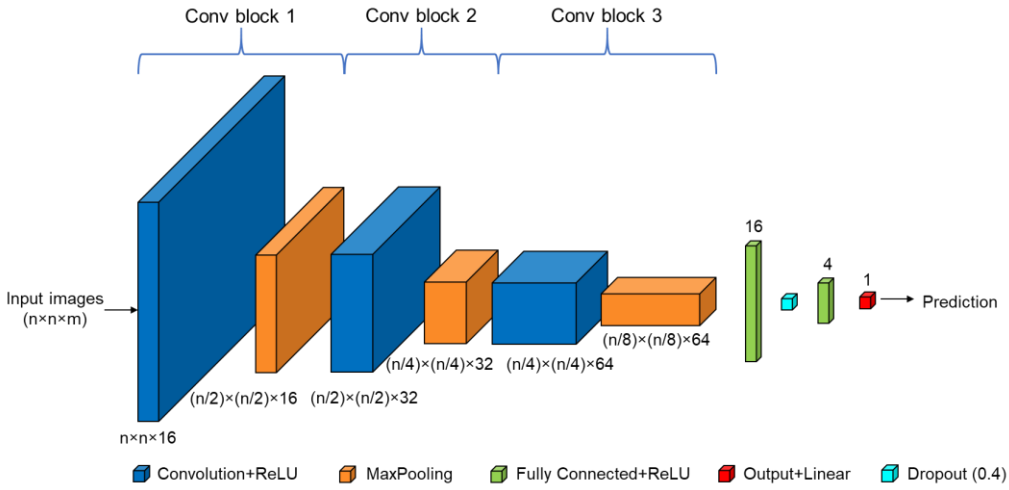

Figure 3.9 Schematic illustration of the architecture of the CNN model used in this work.

Multimodal Learning

Multimodal learning combines different sources of information to improve the overall prediction performance. In this work, the numerical data and image data could provide complementary information to each other. Hence, they were combined to produce more robust predictions, as schematically shown in Figure 3.10. Nevertheless, the model complexity and computational cost would increase using this technique.

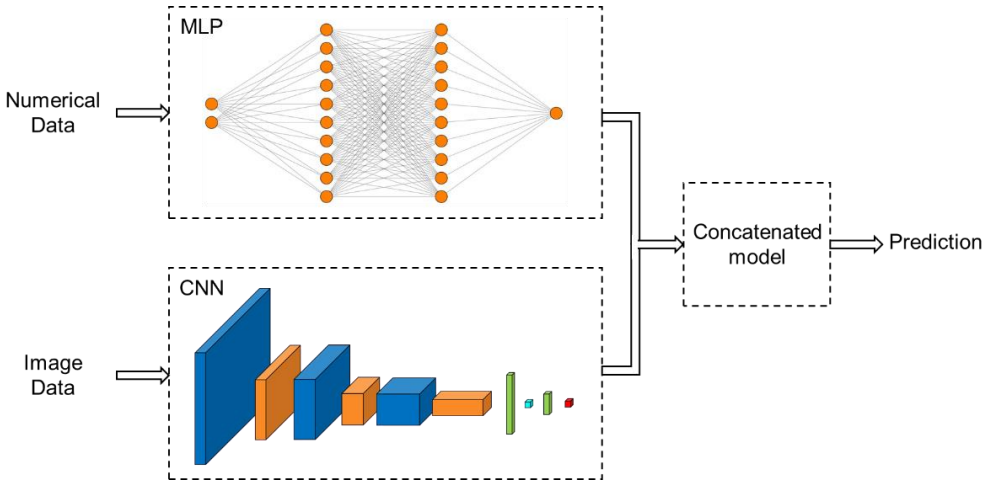

Figure 3.10 A DL model that combines MLP and CNN models using a mixed form of data from different modalities (image and numerical data) as inputs.

Variational Autoencoder Architecture

Variational autoencoder (VAE) is a generative model which consists of an encoder model and a decoder model, as shown in Figure 3.11. The encoder processes the input data by dimensionality reduction, which can be interpreted as data compression. The decoder restores the original data in a reverse process. The bottleneck-shape region that connects the encoder and decoder is called latent space, which preserves the key information of the data structure in the reduced dimensional representation. Compared with the classical autoencoder, VAE has a regularization technique imposed in the latent space to avoid overfitting [167].

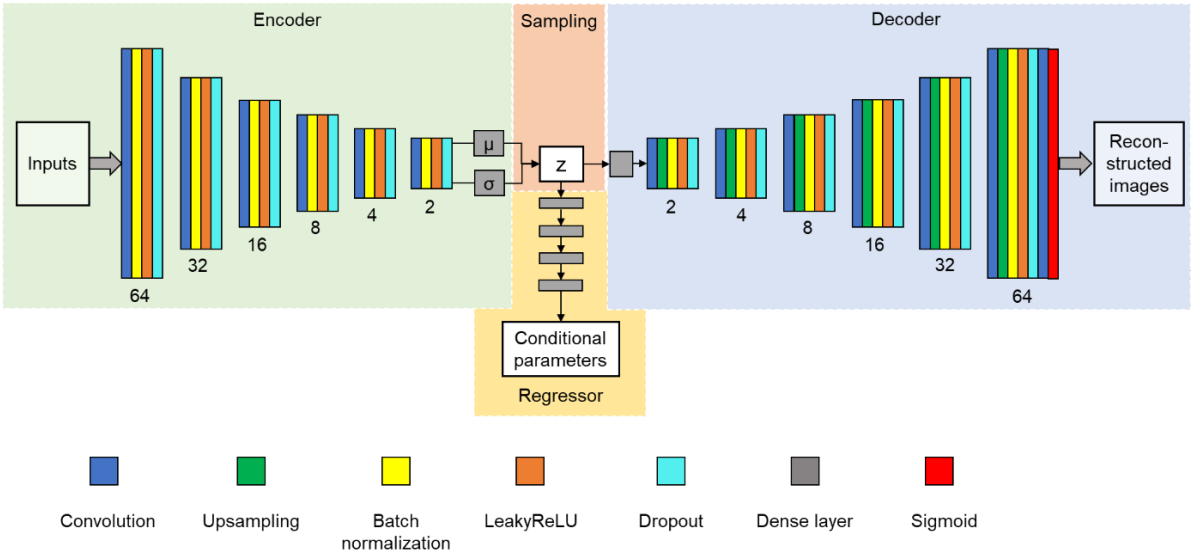

Figure 3.11 Architecture of the VAE model used in this work. The numbers below each block indicate the size (i.e. width and height) of the output image.

Conditional Generative Adversarial Networks

Generative adversarial networks (GAN) is able to automatically discover and learn the patterns from input data, and generate new examples that are hardly differentiable from the original dataset. The basic GAN model has two networks, a generator and a discriminator, as shown in Figure 3.12. In the case of generating images, the generator is responsible for producing plausible fake samples to fool the discriminator, while the discriminator is responsible for classifying whether these samples are real (i.e. from the training dataset) or fake (i.e. generated) [168].

However, it is difficult to train GAN due to the two typical failure modes: it may fail to converge, thus generating poor images that can be easily identified by the discriminator; and it is prone to mode collapse, meaning that only one or a few subsets of identical images are produced, which fool the discriminator easily but lack diversity. To counter these problems, conditional generative adversarial networks (cGAN) was introduced with the conditional parameters as additional input data. Besides, the target images of a given type can be generated by the conditional parameters.

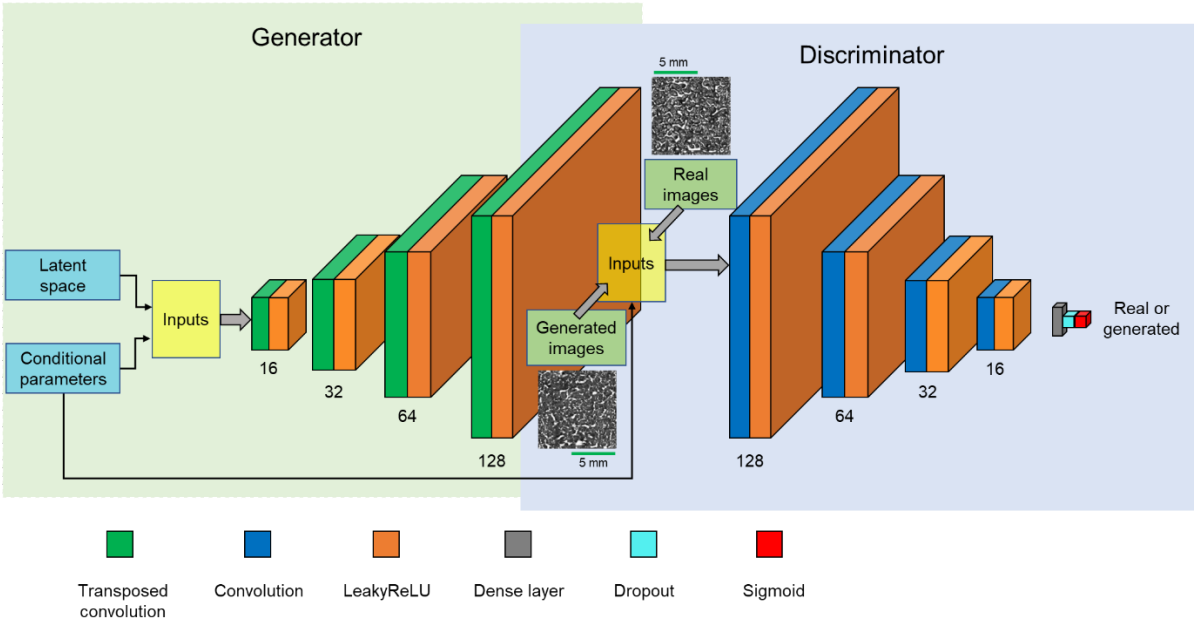

Figure 3.12 Architecture of the cGAN model used in this work. The numbers below each block indicate the size of the output image (width and height). The surface morphology images were used as an example.

Transfer Learning

Transfer learning (TL) is a new paradigm that extracts the knowledge from one or more source tasks and applies the knowledge to a target task, without the need to train a new learning system from scratch [169]. In TL, the knowledge is leveraged from the previously trained models to tackle a different task with higher accuracy, faster training and even a smaller dataset. Therefore, TL can improve the model's generalization ability to solve complex real-world problems. In this thesis, the pre-trained weights from Ti-6Al-4V baseline model were transferred to SS316L model to expedite the process development by TL. The technical details for TL implementation will be elaborated in Chapter 6 for the sake of clarity.

Chapter 4 Process Parameter Optimization for Stainless Steel 316L by Design of Experiments

In this chapter, the process parameters are optimized for SS316L fabricated by SEBM using two types of powder feedstocks, namely fine powders and coarse powders. The PMP relationships are qualitatively studied. More specifically, DoE methods are used for preliminary and secondary screening of the process window by evaluating the top build surface conditions and relative densities, respectively. The microstructure and tensile properties of the samples built within the process window are tested and analyzed. Finally, the effects of powder size distribution on the process window, microstructure and tensile properties are investigated.

4.1 Introduction

One of the challenges that AM faces is the lack of material varieties. This is especially true for metal AM, as many materials that can be processed by conventional manufacturing are not applicable to AM. For example, the metallic AM feedstocks with poor weldability are susceptible to solidification cracks after they are processed by high-energy laser or electron beam. The discovery of materials with good processability and desired properties for AM is therefore a pressing mission. As SS316 has a wide range of applications, it is of great research interest in metal AM.

However, before the start of this Ph.D. work, the majority of the SS316L samples were built by SLM or DED. Very limited studies were conducted on the influence of process parameters on mechanical properties of SS316L parts produced by SEBM. Though Rännar et al. explored the potential of increasing the layer thickness of SEBM process to improve the manufacturing productivity of SS316L parts, their process parameters were not optimized [43].

Moreover, as powder-bed fusion metal AM process builds parts layer by layer, the resulting microstructural heterogeneities, as well as defects between adjacent layers, may cause strong anisotropic mechanical properties. Therefore, many research works reported that their mechanical properties, especially tensile strengths, were deteriorated when tested along build direction due to the lack-of-fusion defects among layers [170-179]. However, due to the vacuum environment, deeper energy penetration and elevated build temperature of SEBM

process, the eliminated lack-of-fusion defects and in-situ heat treatment may change the anisotropic properties of SEBM as-built parts, as compared to the laser-based metal AM processes.

In order to address the above two questions, the two major process parameters in melting (i.e. FO and SF) were investigated. Besides, as the powder particles are loosely in contact with one another, the particle size distribution (PSD) can affect the packing density of powder bed. This may further affect the melting parameters and potentially influence the microstructure and mechanical properties. Therefore, it is of interest to investigate the powder size effect in SEBM processing. The fine powders with the nominal size of ~ 20 - 63 μm were selected, as it is commonly used for SLM processing. Similarly, the coarse powders with the nominal size of ~ 45 - 106 μm were selected following Arcam EBM's recommendation. The actual PSD slightly differs from the nominal value, which is shown in Figure 3.4.

4.2 Results

4.2.1 Process Parameter Optimization for SS316L Fine Powders

Using SS316L fine powders, the parametric combinations with FO from 8 mA to 14 mA and SF from 130 to 300 were used to print cuboids of 30 × 30 × 5 mm^3 samples for preliminary screening of top build surface conditions. The DoE results are shown in Table 4.1. To maintain a build temperature of ~ 850 °C so that the SS316L powders could be well sintered, the size of the start-plate cannot be too large otherwise the build temperature will drop rapidly, leading to the build failures. Hence, due to the constraint on the size of the start-plate (150 × 150 × 10 mm^3), only 6 samples under different sets of process parameters could be printed in each build, which resulted in 6 trials of builds in total.

Table 4.1 DoE table of SEBM parameters for the fabrication of SS316L samples using fine powders. The relative densities shown here are measured by Archimedes method.

Sample No.	Speed Function	Focus Offset (mA)	Response 1: Top surface conditions	Response 2: Relative density (%)
1	130	8	Over-melted	–
2	130	10	Over-melted	–
3	130	12	Slightly over-melted	–
4	130	14	Slightly over-melted	–
5	150	8	Slightly over-melted	99.020 ± 0.016
6	150	10	Slightly over-melted	99.057 ± 0.030
7	150	12	Well-melted	99.045 ± 0.058
8	150	14	Slightly porous	–
9	170	8	Slightly over-melted	99.032 ± 0.024
10	170	10	Well-melted	99.003 ± 0.021
11	170	12	Slightly porous	98.995 ± 0.016
12	170	14	Slightly porous	–
13	190	8	Slightly porous	98.890 ± 0.074
14	190	10	Slightly porous	98.794 ± 0.095
15	190	12	Slightly porous	98.857 ± 0.033
16	190	14	Porous	–
17	210	8	Slightly porous	–
18	210	10	Porous	–
19	210	12	Porous	–
20	210	14	Porous	–
21	230	8	Porous	–
22	230	10	Porous	–
23	230	12	Porous	–
24	230	14	Porous	–
25	250	8	Porous	–
26	250	10	Porous	–
27	250	12	Porous	–
28	250	14	Porous	–
29	300	8	Porous	–
30	300	10	Porous	–
31	300	12	Porous	–
32	300	14	Porous	–

The preliminary screening results of the process window concerning the top build surface conditions are illustrated in Figure 4.1. FO is the additional current running through the

respective coil and can be translated into an offset of the focal plane from its zero position [46]. An increased value of FO will result in a less focused beam and reduced energy density. SF is an index that determines the relationship between transverse beam speed and beam current, which also varies along build height during SEBM process [180]. The purpose of adopting SF is to ensure that constant melt pool size is maintained along the entire build process [41]. Despite the complicated SF algorithm protected by Arcam, at a single build height, an increase in SF linearly increases the beam speed [180]. In general, high SF coupled with high FO yields a low energy density, producing porous top surface on the sample, due to insufficient fusion of powder granules. Conversely, low SF coupled with low FO generates a high energy density, causing over-melted top surfaces, due to localized heat accumulation. Hence, by examining the morphology of the top build surface, the range of the above-mentioned two parameters was narrowed down to 8 - 12 mA for FO and 150 - 190 for SF in order to carry out the secondary screening of the process window. The samples were labelled from F1 to F9 as given in Figure 4.1.

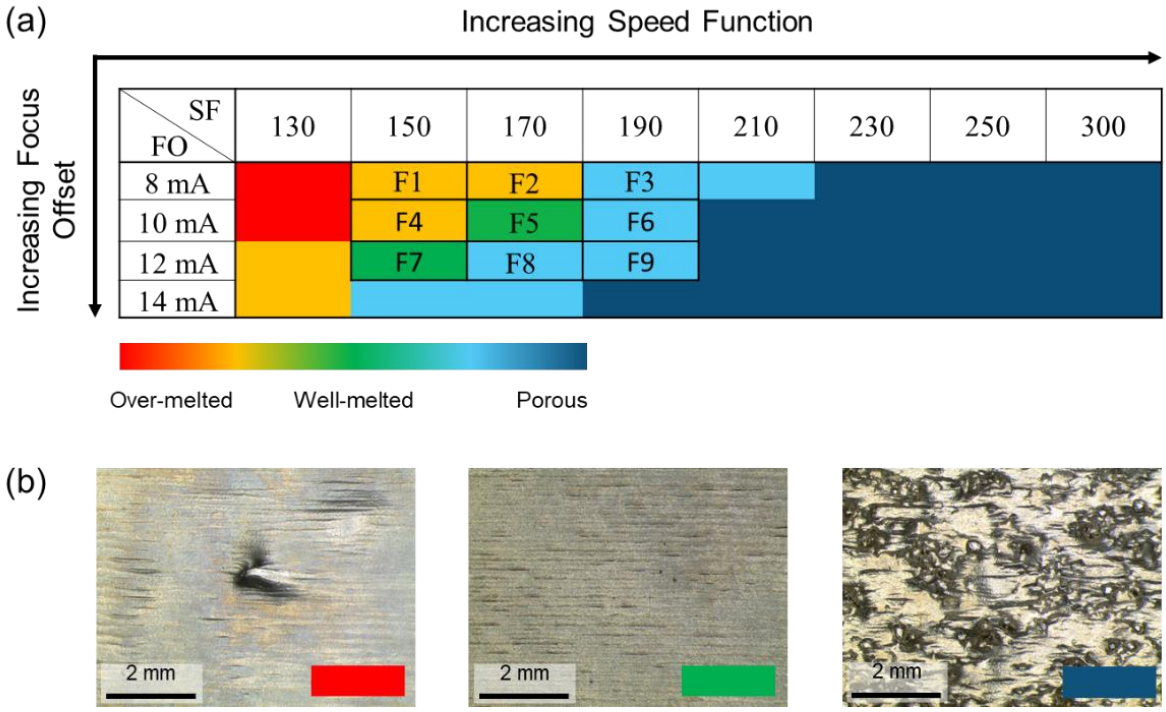

Figure 4.1 (a) DoE chart of process parameter optimization for SEBM fabrication of SS316L samples. After narrowing down the process parameter range, samples F1 to F9 were selected for a detailed parametric study. (b) Representative OM images reveal the over-melted, well-melted and porous top build surfaces that were also illustrated using different colors shown in the color bar above.

The respective densities for sample F1 to F9 were measured by both Archimedes method and image analysis method. Despite the minor over-melted surfaces for F1, F2 and F4,

both results show that a high density of > 98.8% was obtained in all these nine SEBM as-built samples, as illustrated in Figure 4.2. Although image analysis method records a relatively higher value, the overall trend is well aligned with Archimedes method. It is noteworthy that the true density may lie between the aforementioned two curves.

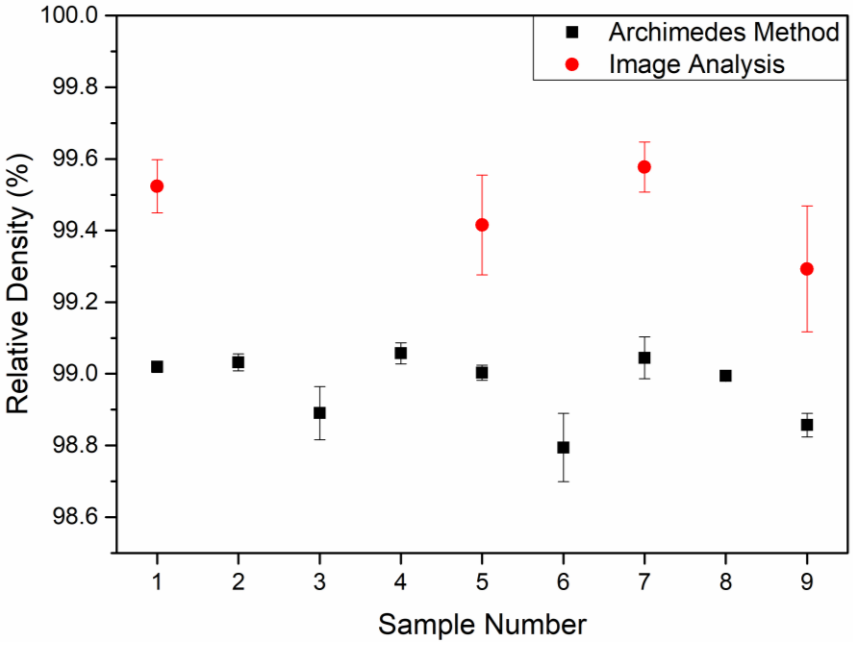

Figure 4.2 Density graph for the SEBM-built SS316L cuboids (F1 - F9) using fine powders with varying process parameters shown in Figure 4.1. The relative density data were obtained from both the Archimedes and image analysis methods.

Using the data obtained from the Archimedes method, ANOVA was employed to investigate the effects of FO and SF on the relative density. The results in Table 4.2 are based on the assumption that the interaction between FO and SF does not have significant effect on the response, which needs to be validated later, as mentioned in section 3.6.2. The probability of Type I error where the null hypothesis H_0 (i.e. the factor investigated is not significant) is rejected was set at 0.05, making the control limit $F_{0.05,2,4}$ equal to 6.94. It can be concluded that only SF has significant effect on the response as its F value is larger than the control limit. Tukey's one degree of freedom test for additivity shows that the F_{Tukey} value for the interaction between FO and SF is 9.81, lower than the control limit of $F_{0.05,1,3} \sim 10.13$. It can be concluded that the previous assumption is valid.

Table 4.2 ANOVA table for relative density of the samples built by SEBM using fine powders.

Factors	Sum of squares	Degree of freedom	Mean square	F value	Control limit $F_{0.05,2,4}$	Significant effect
FO	0.0013	2	0.0006	0.51	6.94	No
SF	0.0648	2	0.0324	26.05		Yes
Interaction between FO and SF	0.0050	4	0.0012	–	–	–
Total	0.0710	–	–	–	–	–

The main effects plot and 3D response surface on relative density are illustrated in Figure 4.3 (a) and (b). It shows that density decreases as SF increases, which was also verified by previous studies [180]. However, FO has negligible effects on part density, as proven by ANOVA. Gong et al. have reported that FO below 16 mA did not significantly affect part density [181]. Therefore, by considering top build surface conditions and bulk density, the process parameters for samples F5 and F7 were selected as the provisionally optimized parameters for SEBM processing of SS316L alloy.

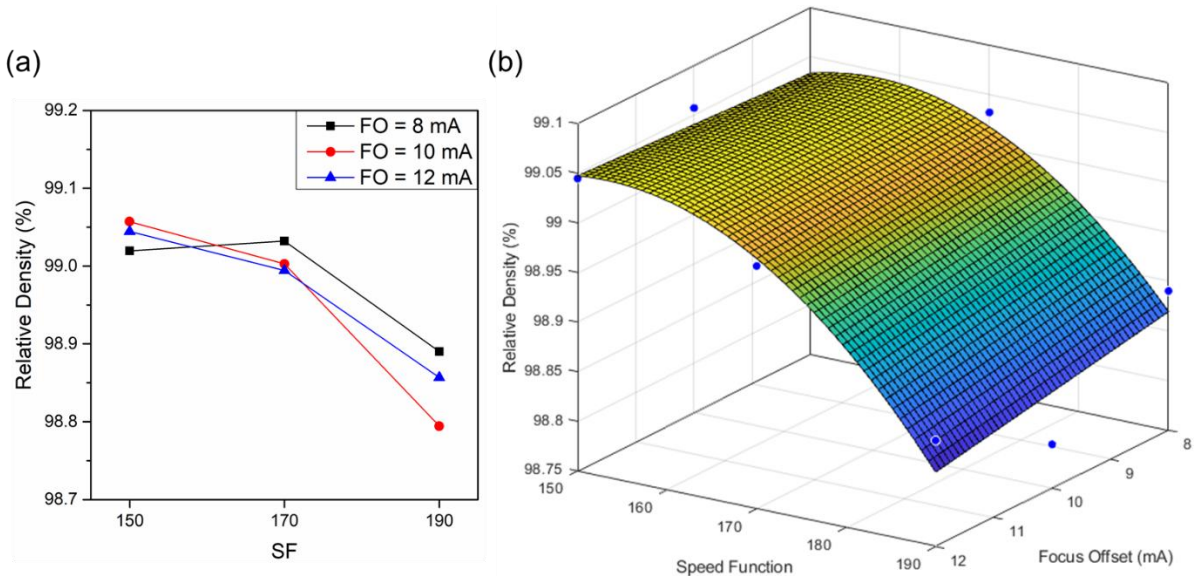

Figure 4.3 (a) Main effects plot and (b) response surface plot showing the effects of SF and FO on the relative density for the SEBM-built SS316L cuboids using fine powders.

4.2.1.1 Phase Identification

XRD (detection limit ~ 3 vol% [58]) patterns of the fine precursor powder and the SEBM as-built SS316L samples are shown in Figure 4.4. It reveals that the precursor powder consists of two phases, i.e. FCC austenite (γ phase) and BCC ferrite (δ phase). After high-temperature processing, δ phase disappeared, thus making solid samples F5 and F7 comprise of pure γ phase. Moreover, <200> texture became the dominant crystallographic texture in SEBM-built samples, indicating that the grains were primarily columnar grains with the [002] orientation.

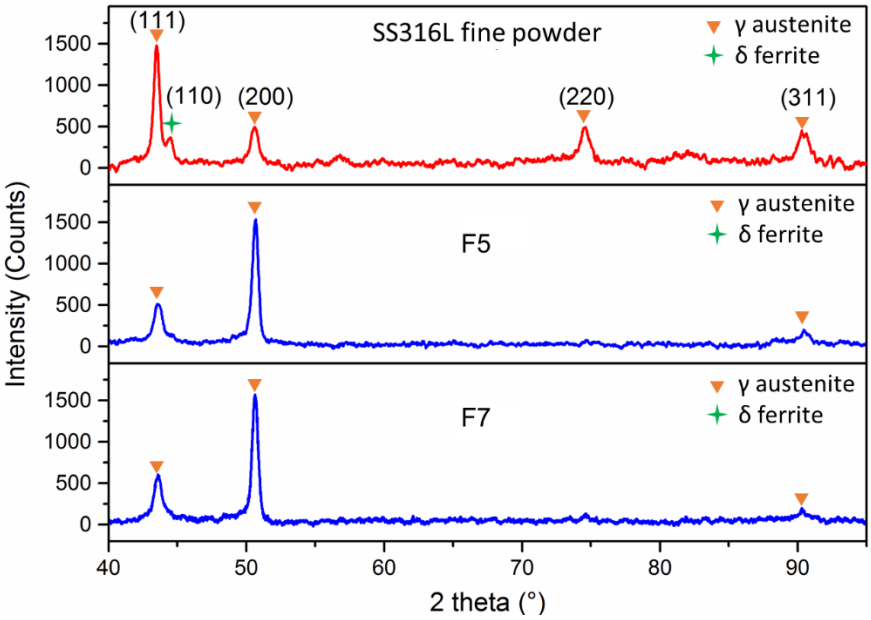

Figure 4.4 XRD profiles for SS316L (a) precursor powder, and SEBM-built samples (b) F5 and (c) F7.

4.2.1.2 Microstructural Observation

Figure 4.5 and 4.6 comprehensively reveal the microstructure of sample F5 at various scales. The pseudo-3D micrograph, which is constructed by combining OM images captured from the three different planes, is illustrated in Figure 4.5. The layered feature on the side surfaces can be clearly observed, which is a typical characteristic of AM process. Very few defects are found at layer boundaries, proving that electron beam energy is sufficient to ensure complete fusion of adjacent layers and the process parameters are suitable. Melt tracks are revealed on both top and side surfaces. It is noted that two types of melt-track morphologies, i.e. wavy melt tracks and smooth melt tracks, repeat at alternative layers. The formation of this

morphology has been schematically explained in Figure 2.6. The grains are columnar-shaped parallel to build direction due to the largest z-axis thermal gradient during the building process [30].

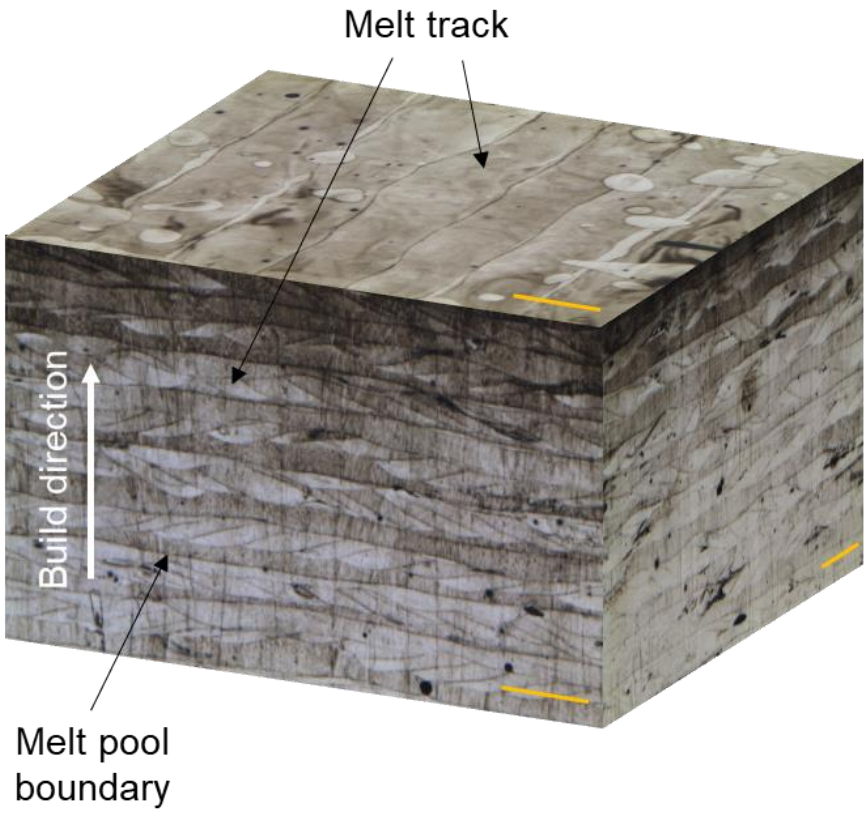

Figure 4.5 Pseudo 3D micrograph of the top 16 layers of SEBM-built SS316L under OM. All the yellow scale bars are 200 μm.

Figure 4.6 (a) shows the melt tracks clearly from the top plane. The spacing of two adjacent melt pool boundaries yields ~ 100 μm, which is consistent with the adopted hatch spacing of 100 μm in this work. The typical intragranular cellular sub-grains can be observed at a higher magnification shown in Figure 4.6 (b). The average cell size is determined to be ~ 1 μm. However, the size of cellular sub-grains located in the overlapping zone of melt tracks is larger, which is attributed to the coarsening effects of re-melting.

Figure 4.6 (c) displays the melt pool boundaries and columnar grain boundaries for the side view of the region near the top surface. The actual layer thickness is smaller than the pre-defined value of 50 μm, as the previously solidified melt pools were partially re-melted when the electron beam scanned upon the subsequent layer [30]. Due to this re-melting process, grains can grow upwardly across layer boundaries, i.e. epitaxial growth and form into columnar

shape. The width of columnar grains is ~ 35.9 ± 9.0 μm. In general, the columnar grains exhibit a strong <001> texture, which implies the evident anisotropy in mechanical properties. In addition, Figure 4.6 (d) clearly presents intragranular dendrites which grow in the same direction of columnar grains. The average width of dendrites is ~ 1 μm, which is the same as cellular sub-grains in Figure 4.6 (b), since cellular sub-grains are the cross-sectional view of dendrites.

From the cross-sectional view of middle region and longitudinal view of bottom region, as revealed in Figure 4.6 (e)-(f) and Figure 4.6 (g)-(h), it can be seen that the cellular sub-grains become rarely visible below the top region. Moreover, the melt pool boundaries also become less visible. Such longitudinal heterogeneity of microstructure for SEBM as-built samples will be discussed in the following sections. The discontinuous pits shown in Figure 4.6 (e) are anticipated to be precipitates that were etched away from the grain boundaries, which will be investigated subsequently.

The columnar grain boundaries of sample F7 in Figure 4.7 (a) are evidently thicker than those of sample F5 in Figure 4.6 (h). In addition, discontinuous precipitates are found to occur along grain boundaries, as depicted in Figure 4.7 (b). Figure 4.8 shows EDS mappings that were performed on the grain boundary areas of columnar grains in sample F7, as depicted by the bounding box in Figure 4.7 (b). The EDS point detection reveals that the precipitates are rich in Cr (27.1 ± 1.0 wt.%) and Mo (9.0 ± 0.7 wt.%).

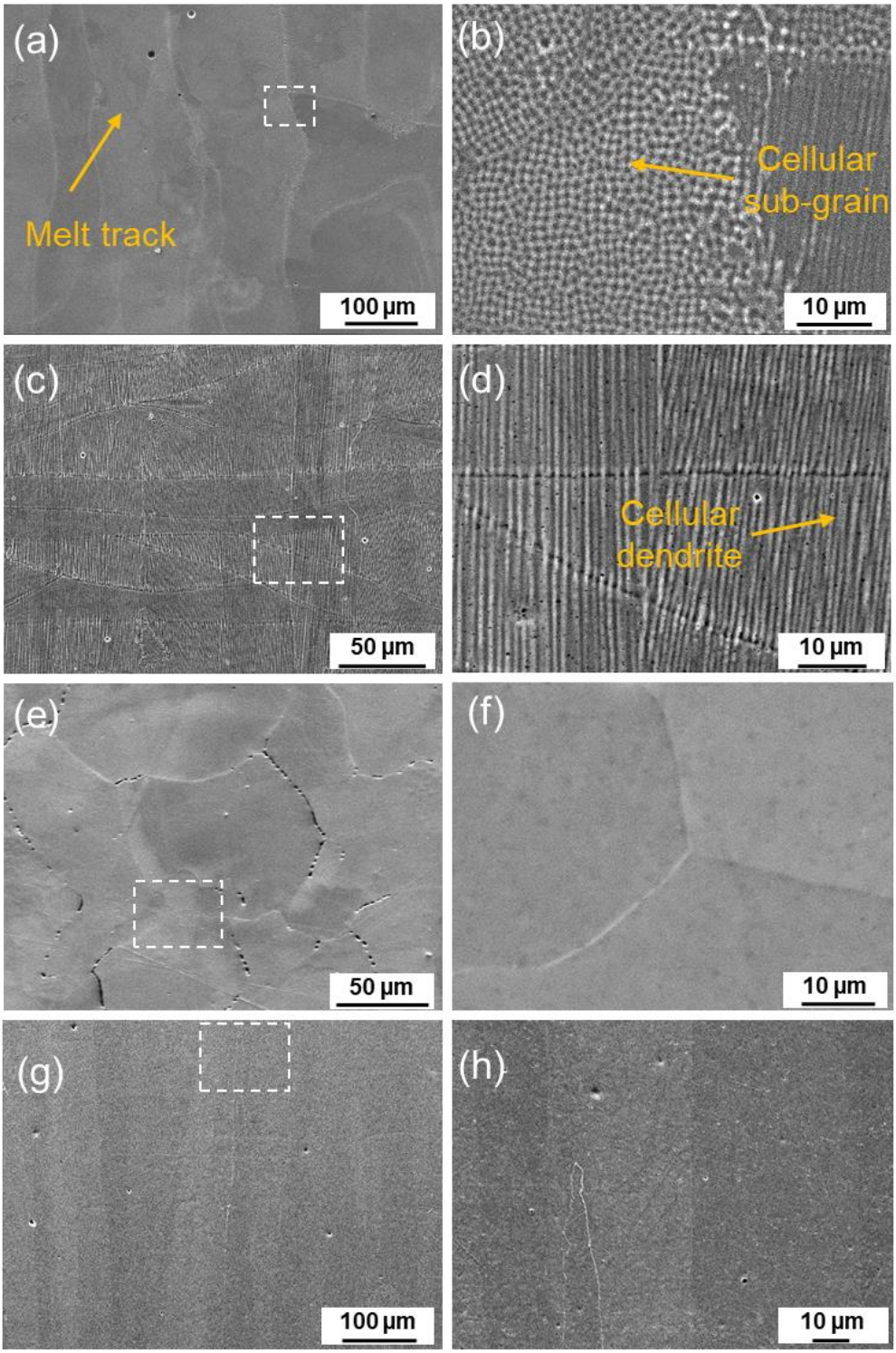

Figure 4.6 Microstructure of SEBM-built SS316L sample F5: (a) Low and (b) high magnification SEM images of X-Y plane at the top region revealing the melt track and the cellular sub-grains, respectively. (c) Low and (d) high magnification SEM images of X-Z plane at the top region revealing the columnar grains with fine dendrites. (e) Low and (f) high magnification SEM images of X-Y plane at the middle region showing no visible sub-grains. (g) Low and (h) high magnification SEM images of X-Z plane at the bottom region revealing the columnar grains with invisible dendrites.

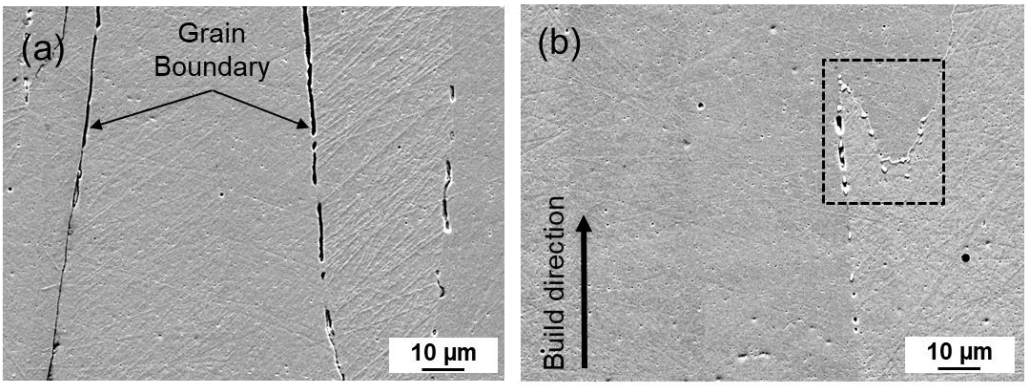

Figure 4.7 (a) SEM image of X-Z plane for sample F7 showing thick grain boundaries after etching. (b) SEM image of σ phase particles precipitating at grain boundary and inside grains.

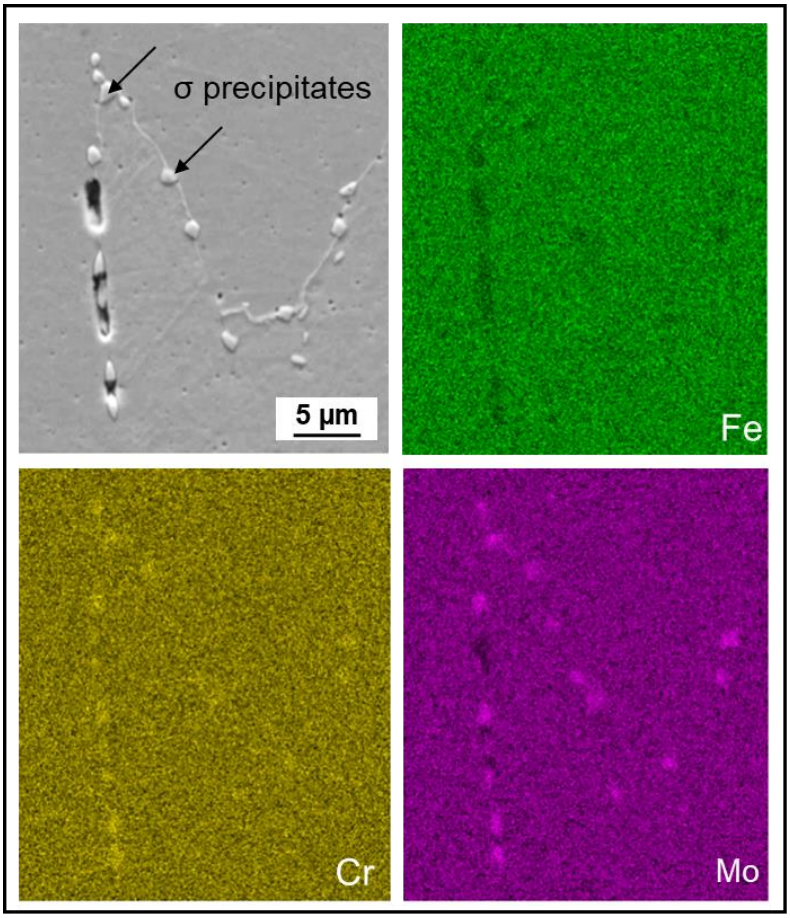

Figure 4.8 EDS mappings showing element depletion of Fe and enrichment in Cr and Mo for sample F7.

4.2.1.3 Tensile Properties and Fractography

Figure 4.9 shows the stress-strain curves of samples F5 and F7 respectively at two different orientations. Table 4.3 compiles the yield strength (YS), ultimate tensile strength

(UTS) and elongation of SEBM-built SS316L samples and the as-cast [182] and wrought counterparts [183]. It is found that all the values of tensile strengths, except for F7-H, are higher than those of conventional cast and wrought SS316L, while the elongation is lower. More specifically, F5-V has the highest tensile strength of 651.7 ± 8.5 MPa, which is even superior to many SLM [172, 178, 179, 184] and DED [182, 183, 185] processed counterparts. By contrast, the tensile properties of F7-H are inferior to most metal AM processed SS316L parts.

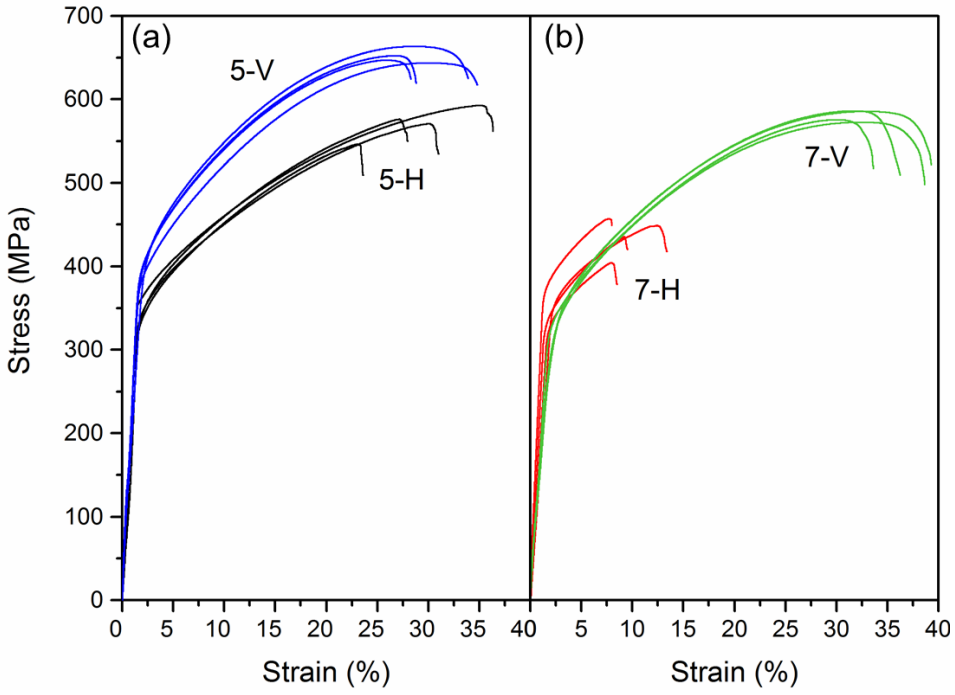

Figure 4.9 Engineering stress vs engineering strain curves of SEBM-built SS316L samples (a) F5 and (b) F7 tested along horizontal and vertical directions.

Table 4.3 Comparison of tensile properties between SEBM-built SS316L samples and conventional cast [182] and wrought [183] counterparts. The gauge length used is 10 mm for sample F5-H and F7-H, and 5 mm for sample F5-V and F7-V.

SEBM-built samples	Young's modulus (GPa)	YS (0.2% offset) (MPa)	UTS (MPa)	Elongation (%)			Reduction of area (%)
				Total strain (%)	Uniform strain (%)	Non-uniform strain (%)	
F5-H	112.4 ± 1.7	334.2 ± 15.5	571.8 ± 19.3	29.7 ± 4.6	28.9 ± 4.4	0.9 ± 0.2	40.3 ± 2.4
F7-H	97.1 ± 12.5	342.9 ± 22.8	436.5 ± 23.2	9.9 ± 2.1	9.3 ± 1.9	0.5 ± 0.3	25.6 ± 3.0
F5-V	101.2 ± 2.7	395.8 ± 9.0	651.7 ± 8.5	31.5 ± 2.9	27.7 ± 1.5	3.8 ± 1.5	51.7 ± 1.7
F7-V	64.1 ± 8.0	315.7 ± 10.0	580.2 ± 6.8	37.0 ± 2.2	32.1 ± 1.2	4.9 ± 1.1	63.5 ± 1.9
Cast	–	262	552	55	–	–	–
Wrought	–	170	480	40	–	–	–

In general, anisotropic mechanical properties with respect to the build direction are shown in various metal AM parts [4]. In this work, the tensile coupons machined in vertical direction exhibit significantly higher UTS and elongation than those prepared in horizontal direction. This is contradictory to the common understanding that tensile testing performed along build direction yields the worst tensile properties of AM processed samples. Moreover, the most notable finding is that F5 has better tensile properties than F7 in both directions, despite its slightly lower build density as compared to F7. More specifically, F7-H exhibits brittle fracture behavior in tensile testing. The possible reasons for its weak tensile properties will be discussed later.

Fracture surfaces of the tensile tested samples were observed by SEM, as shown in Figure 4.10 for sample 5 and Figure 4.11 for sample 7. Samples F5-H, F5-V and F7-V show a combination of ductile and brittle surfaces, whereas F7-H shows an obvious brittle feature. The average size of small ductile dimples is less than 1 μm in diameter. The defects, specifically the voids and partially melted powders (indicated by arrows) can be observed in samples F5-H (Figure 4.10 (a)) and F5-V (Figure 4.10 (c)). However, the fracture morphology of sample F7-H (Figure 4.11 (a)) exhibits intergranular fracture features, as evidenced by the brittle surfaces and the large gaps left over after tensile testing. In sample F7-V (Figure 4.11 (c)), many large craters can be seen, which might be formed due to the peel-off of columnar grains tips. On the whole, sample F5 suffered a bit more defects than sample F7, which is in agreement with the lower build density of F5.

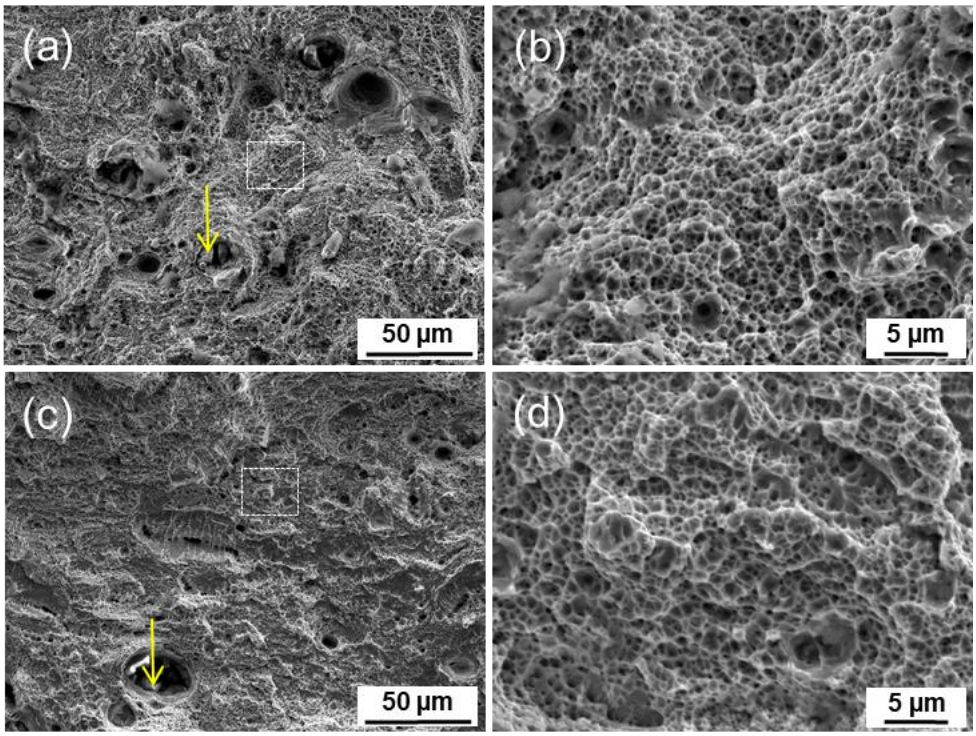

Figure 4.10 SEM fractographs of sample 5. (a and c) Low magnification images of mixed ductile and brittle fracture surfaces for tensile coupons F5-H (a) and F5-V (c). (b and d) High magnification images of ductile fracture surfaces with fine dimples for F5-H (b) and F5-V (d). The yellow arrows indicate un-melted powders.

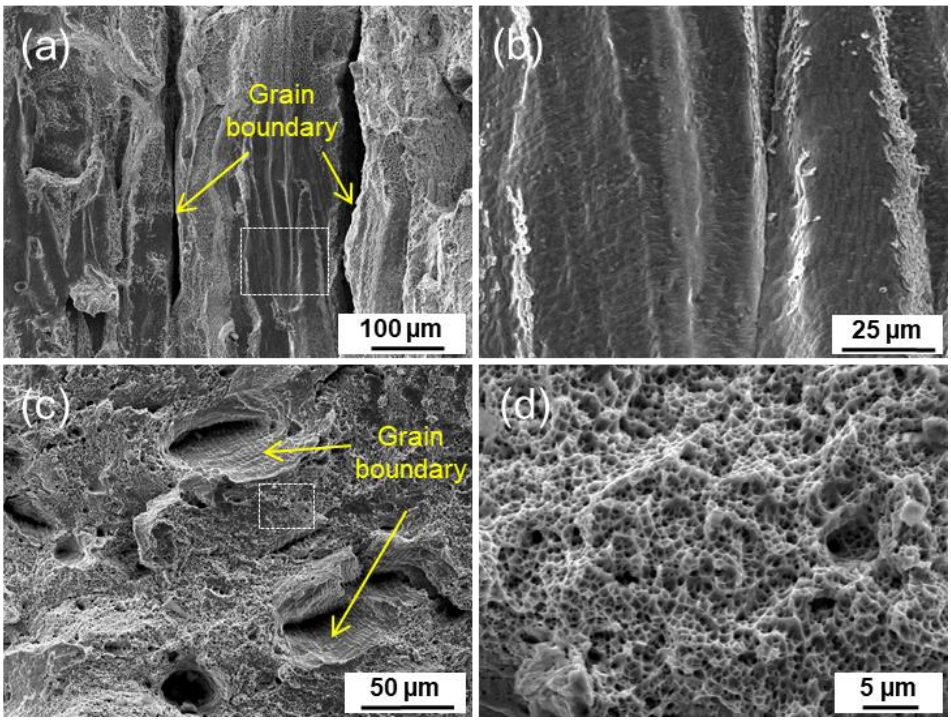

Figure 4.11 SEM fractographs of sample 7. (a and c) Low magnification images of intergranular brittle fracture surface for F7-H (a), and mixed ductile and brittle fracture surfaces for tensile coupons F7-V (c). (b and d) High magnification images of intergranular fracture surface with smooth facets for F7-H (b), and ductile fracture surfaces with fine dimples for F7-V (d).

4.2.2 Process Parameter Optimization for SS316L Coarse Powders

To study the effects of powder size on the process window, microstructure and mechanical properties of the SS316L parts fabricated by SEBM, the same pair of process parameters were studied with the coarse powders. The process parameters range from 70 to 170 for SF and 5 to 12 mA for FO. The 30 × 20 × 20 mm^3 samples were fabricated for preliminary studies. The cross-sectional area of the samples was reduced as compared to parameter studies for fine powders, so that 9 samples could be built each time. The full list of parameter studies is shown in Table 4.4, which implies that only 5 trials were possible with this build.

Table 4.4 SEBM parameters for the fabrication of SS316L samples using coarse powders. The relative densities shown are measured by Archimedes method.

Sample No.	Speed Function	Focus Offset (mA)	Response 1: Top surface conditions	Response 2: Relative density (%)
1	70	5	Over-melted	–
2	70	6	Over-melted	–
3	70	7	Over-melted	–
4	70	8	Over-melted	–
5	70	9	Over-melted	–
6	70	10	Over-melted	–
7	70	12	Over-melted	–
8	90	5	Over-melted	–
9	90	6	Over-melted	–
10	90	7	Over-melted	–
11	90	8	Over-melted	99.410 ± 0.017
12	90	9	Slightly over-melted	99.482 ± 0.013
13	90	10	Slightly over-melted	99.462 ± 0.017
14	90	12	Slightly over-melted	–
15	110	5	Over-melted	–
16	110	6	Over-melted	–
17	110	7	Over-melted	–
18	110	8	Slightly over-melted	99.456 ± 0.015
19	110	9	Slightly over-melted	99.454 ± 0.014
20	110	10	Slightly over-melted	99.450 ± 0.015
21	110	12	Slightly over-melted	–
22	130	5	Over-melted	–

23	130	6	Over-melted	–
24	130	7	Slightly over-melted	–
25	130	8	Slightly over-melted	99.393 ± 0.018
26	130	9	Well-melted	99.418 ± 0.016
27	130	10	Well-melted	99.403 ± 0.007
28	130	12	Slightly porous	–
29	150	5	Slightly porous	–
30	150	6	Slightly porous	–
31	150	7	Slightly porous	–
32	150	8	Slightly porous	–
33	150	9	Slightly porous	–
34	150	10	Slightly porous	–
35	150	12	Porous	–
36	170	5	Slightly porous	–
37	170	6	Porous	–
38	170	7	Porous	–
39	170	8	Porous	–
40	170	9	Porous	–
41	170	10	Porous	–
42	170	12	Porous	–

As stated in the experimental studies for SS316L fine powders, insufficient energy produces porous parts, while excessive energy results in overly-melted parts. Hence, following the rationale of examining the top surface topography to determine the suitability of the energy level, the process window could be narrowed down to 8 - 10 mA for FO and 90 - 130 for SF in order to carry out a more detailed study. The samples were labelled from C1 to C9 as given in the DoE chart in Figure 4.12.

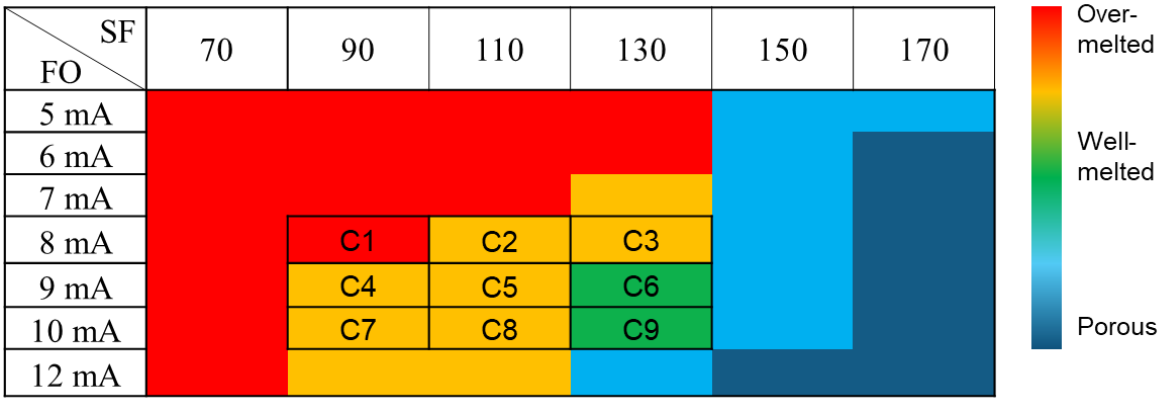

Figure 4.12 DoE chart of process parameter optimization for SEBM fabrication of SS316L samples using coarse powders. A preliminary classification of the build surfaces was illustrated using different colors shown in the right color bar. After narrowing down the process parameter range, samples C1 to C9 were selected for a detailed parametric study.

The respective densities for sample C1 to C9 were measured by both Archimedes method and image analysis method. As illustrated in Figure 4.13, both results show that an even higher density of > 99.3% was obtained in all these nine SEBM as-built samples. Although image analysis method records a relatively higher value, the overall trend is consistent with the Archimedes method. Again, the true density may lie between the aforementioned two curves. Although C2 to C9 have shown a generally flat surface, a more detailed examination reveals that some samples have subtle humps on the surfaces. The slightly overly-melted samples are highlighted in yellow according to Figure 4.13, which are denser as compared to the well-melted samples (i.e. C6 and C9). This is because a slightly excessive input energy could ensure better fusion of the adjacent layers and eliminate the existence of un-melted powder granules. However, it is not favored as this produces uneven top surfaces and negatively affects the mechanical properties, as discovered in the previous section for SS316L fine powder studies. However, the overly excessive input energy, as in the case of C1, may result in a lower relative density due to keyhole effects, as also commonly reported in electron beam welding [186].

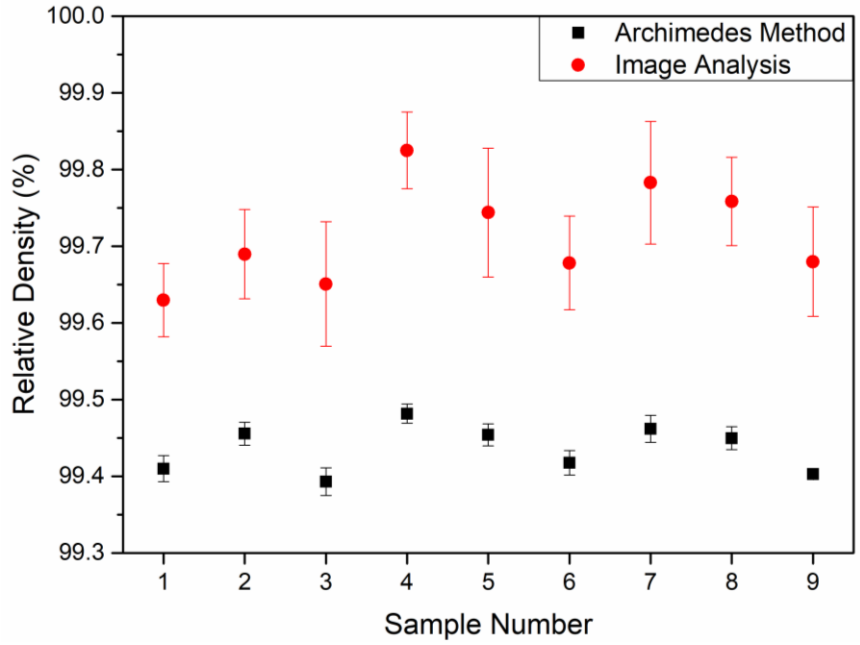

Figure 4.13 Density graph for the SEBM-built SS316L cuboids (C1 - C9) using coarse powders with varying process parameters. The relative density data were obtained from both the Archimedes and image analysis methods.

Following the same methodology implemented for fine powder samples, the results of ANOVA (Table 4.5) show that only SF has significant effect on the relative density. The Tukey's test for additivity validates that the interaction of FO and SF is also negligible. The main effects and 3D response surface are plotted in Figure 4.14 to illustrate how to tune the process parameters in order to increase the response. In general, density increases as SF decreases, except for C1 (FO = 8 mA and SF = 90), which has a low relative density due to keyhole defects as explained before. The conclusions drawn here are consistent with the results for fine powder samples.

Table 4.5 ANOVA table for relative density of the samples built by SEBM using coarse powders.

Factors	Sum of squares	Degree of freedom	Mean square	F_0	Control limit $F_{0.05,2,4}$	Significant effect
FO	0.0012	2	0.0006	2.16	6.94	No
SF	0.0049	2	0.0024	8.76		Yes
Interaction between FO and SF	0.0011	4	0.0003	–	–	–
Total	0.0072	–	–	–	–	–

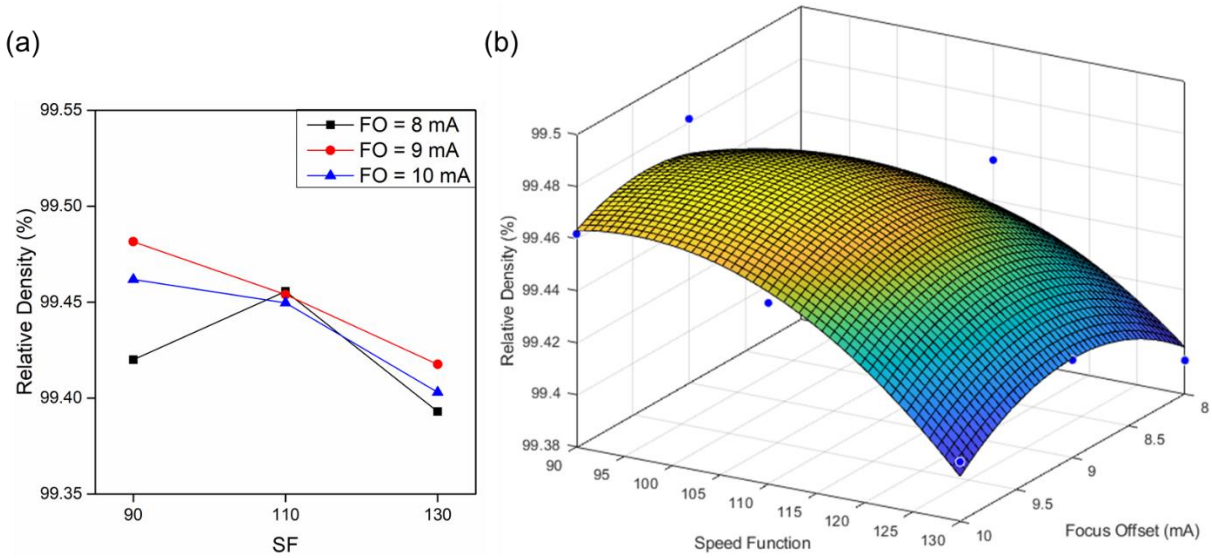

Figure 4.14 (a) Main effects plot and (b) response surface plot showing the effect of SF and FO on the relative density for the SEBM-built SS316L cuboids using coarse powders.

Although SF = 90 and FO = 9 mA could yield the highest density within this window, by considering the top surface, the process parameters for samples C6 and C9 were selected as the provisionally optimized parameters for SEBM processing of SS316L alloy. However, the final choice is also determined by tensile properties.

4.2.2.1 Microstructural Observation

A pseudo-3D micrograph was constructed by the assembly of the OM images from the three different planes, as shown in Figure 4.15 (a). The input energy is sufficient to well fuse the adjacent layers and powder granules, as the defects are nearly negligible. The melt tracks and layer boundaries are clearly visible near the top regions of the sample, and they become progressively invisible when the observation moves down along the build direction. The dendrites or sub-grains are hardly visible from the sample, in contrast to the SS316L samples fabricated from fine powders in the previous section.

The SE image mode micrograph in Figure 4.15 (b) shows that the grains are non-columnar. The dendrites are rather obscure as compared to melt tracks and layer boundaries. In Figure 4.15 (d), the melt track and layer boundaries are dissolved as a result of prolonged in-situ heat treatment during SEBM processing. The grain morphology is still non-columnar. The black dots enclosed by bright rings might be introduced by pitting corrosion during the

chemical etching [187]. The pitting corrosions mostly occurred at the grain boundaries if precipitates are present for austenitic steels. However, an in-depth investigation of this phenomenon is not the focus of this work.

The BSE mode in SEM can distinguish between different phases and provide information on grain orientation of metallic samples. Here, the BSE mode micrographs shown in Figure 4.15 (c) and (e) reveal that the grains are confirmed to be non-columnar, which is contradictory to the reports from various literature on SEBM as-built SS316L parts where the grains grew epitaxially along the build direction [30, 188, 189]. To the best of the author's knowledge, this grain morphology for SS316Lis also rare even in other metal AM processes such as SLM and DED, except for the two works from Wang et al. [95] and Sun et al. [96]. The grains in the top layer are finer than the grains in the layers below. This is because the last layer did not undergo re-melting after the rapid solidification, hence the grains retained their original size and shape without being coarsened.

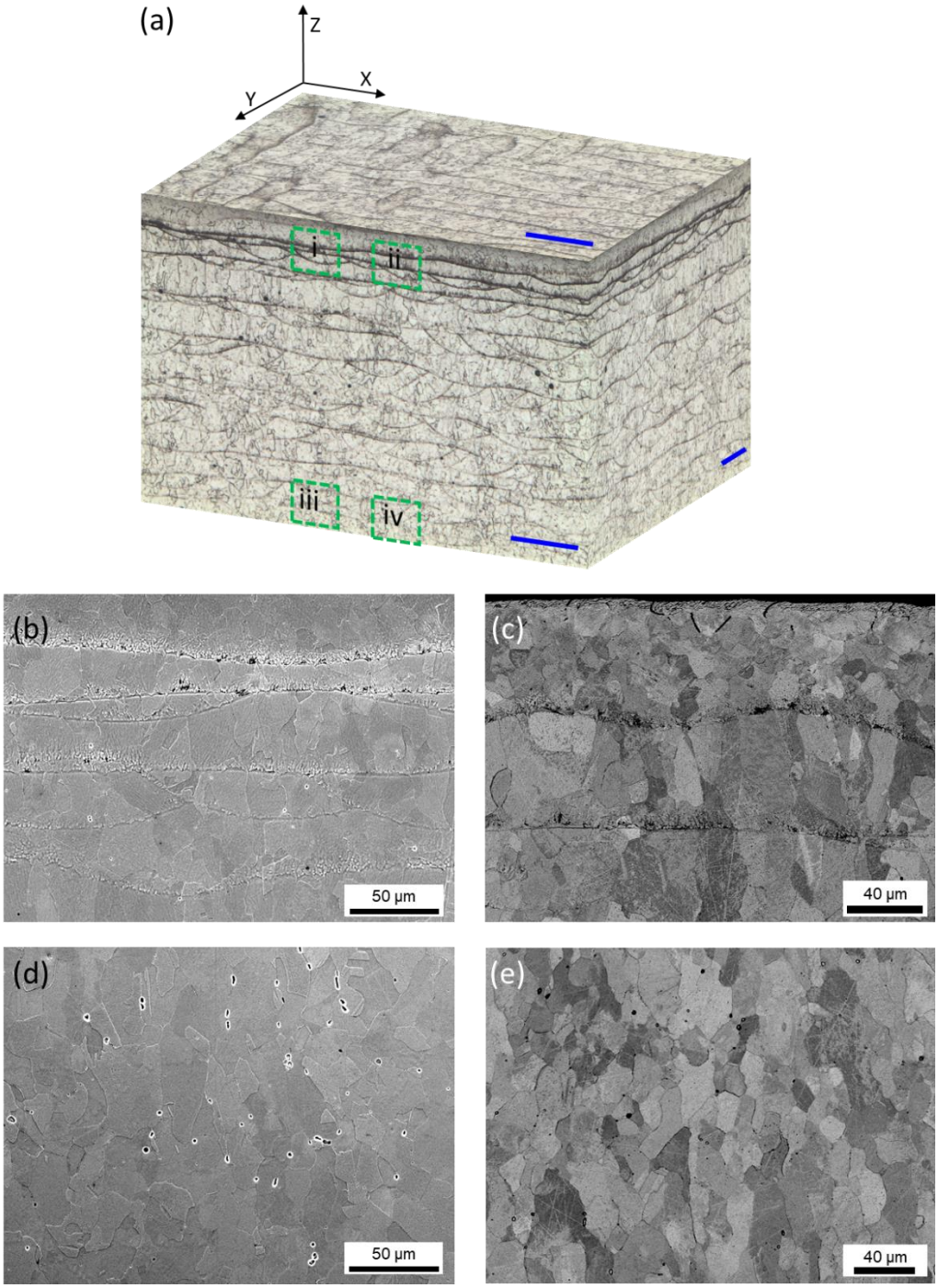

Figure 4.15 Microstructure of SEBM-built SS316L sample C6 (fabricated at the right-middle position of the start-plate) using coarse powders: (a) Pseudo 3D micrograph of the top 18 layers examined under OM. The areas i and ii near the top regions of the sample are examined of the (b) SEI mode and (c) BSE mode, respectively. (d) SE image mode and (c) BSE mode were also employed to reveal the microstructure for area iii and iv near the bottom region. The blue scale bars in (a) are 200 µm.

To further examine the crystallographic texture and average grain size of this sample, EBSD studies were carried out. An area of ~ 1.2 × 0.9 mm^2 was scanned on X-Z plane. The results are shown in Figure 4.16 (a) with an inset to highlight the enclosed area at a higher

magnification, as displayed in Figure 4.16 (b). The normalized orientation intensity along the <001>, <011> and <111> orientations can be visualized by the pole figures below in Figure 4.16 (c). The results show that the grains do not have a preferred orientation, proving that the grains are nearly equiaxed. This crystallographic texture also indicates that the sample may exhibit isotropic tensile properties if the interlayer defects are negligible. The EBSD sampling covers ~ 3800 grains, and the measured average grain size is ~ 14.8 ± 7.7 μm.

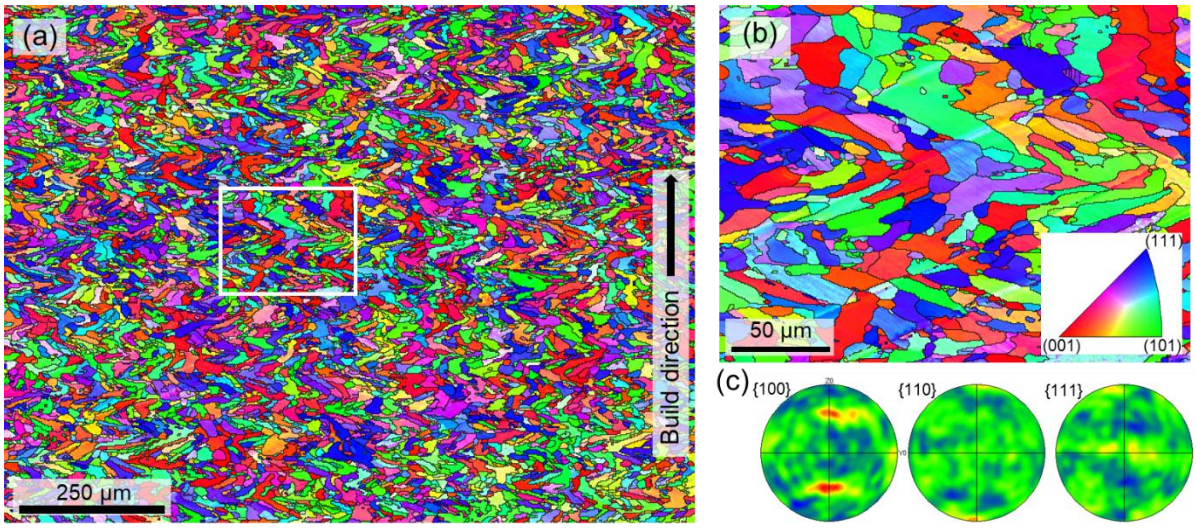

Figure 4.16 (a) EBSD inverse pole figure map in X-Z plane along build direction. (b) Enlarged view of the white rectangular region in (a). (c) Pole figures for the entire mapping of (a).

4.2.2.2 Tensile Properties and Fractography

The stress-strain curves of samples C6 and C9 at two different orientations are shown in Figure 4.17. Their YS (0.2% offset) values are almost the same despite different testing directions. The tensile curves for each sample coincide with one another in the elastic region, proving their isotropy before plastic deformation happens. When tested in horizontal direction, C6-H and C9-H have similar values in UTS and elongation%. In the vertical direction, these two values for C6-V are slightly lower but still close to C6-H. The shapes of the tensile curves for C6-H and C6-V are similar, proving their near-isotropy in tensile properties. However, the UTS and elongation values for C9-V are significantly lower than C9-H, implying that an early fracture might have happened. This is because a larger FO was used to fabricate C9, meaning that a lower input energy was applied. Hence, C9 may suffer more from interlayer defects during the testing, which is also evidence by its lower relative density as compared to C6.

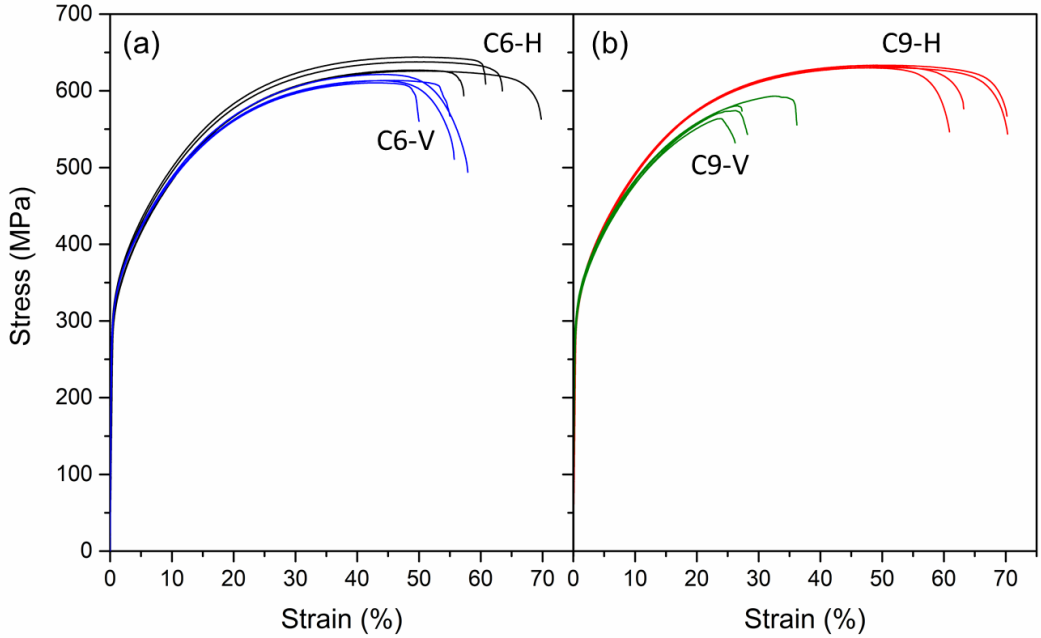

Figure 4.17 Engineering stress vs engineering strain curves of SEBM-built SS316L samples (a) C6 and (b) C9 tested along horizontal and vertical directions.

Table 4.6 summarizes the tensile properties of the SEBM-built SS316L samples using coarse powders, their laser metal AM-built counterparts with the best tensile properties, and their cast and wrought counterparts reported in literature. Our samples have higher YS, UTS and elongation as compared to their cast and wrought counterparts, except for C9-V which experienced an early fracture. To the best of our knowledge, our samples exhibit better tensile properties than all the SEBM-built samples found in literature. However, our YS and UTS are still lower than the best values reported in DED and SLM processing, although our elongation is generally higher.

Table 4.6 Comparison of tensile properties among SEBM-built SS316L from the current study, and their SLM [95], DED [190], conventional cast [182] and wrought [183] counterparts found in literature. Samples C6-H and C9-H were machined with a gauge length of 10 mm while C6-V and C9-V with a gauge length of 5 mm. The gauge lengths for DED and SLM samples from literature are 2.5 mm and 6.5 mm, respectively.

Sample	Young's modulus (GPa)	YS (0.2% offset) (MPa)	UTS (MPa)	Elongation (%)			Reduction of area (%)
				Total strain (%)	Uniform strain (%)	Non-uniform strain (%)	
C6-H	109.8 ± 9.9	304.4 ± 4.0	634.1 ± 8.6	62.8 ± 4.6	50.4 ± 0.6	12.5 ± 4.2	54.7 ± 5.0
C9-H	110.6 ± 6.6	304.0 ± 2.4	631.9 ± 1.6	66.2 ± 4.2	49.2 ± 1.3	17.0 ± 3.4	60.7 ± 2.2
C6-V	143.6 ± 16.1	297.0 ± 4.1	614.8 ± 4.9	54.7 ± 2.9	44.1 ± 1.2	10.6 ± 2.6	55.6 ± 6.6
C9-V	158.0 ± 5.6	297.0 ± 3.0	578.0 ± 12.3	29.5 ± 3.9	27.4 ± 3.3	2.1 ± 1.0	40.6 ± 2.3
DED (as-built)	–	576	776	33	–	–	–
SLM (as-built)	–	590	700	58	–	–	–
Cast	–	262	552	55	–	–	–
Wrought	–	170	480	40	–	–	–

Fracture surfaces of samples C6-H and C6-V after tensile testing were examined by SEM in Figure 4.18 and Figure 4.19, respectively. Both samples exhibit a typical ductile fracture with fine dimples of < 1 μm in diameter. The is no significant difference in the fractography in these two samples. This finding is consistent with their near-isotropic tensile properties. Very few un-melted powders could be observed, proving that the input energy density is suitable to fully melt the powder feedstocks. The craters shown in Figure 4.19 (b) and (c) were formed when the grains were pulled out during tensile testing.

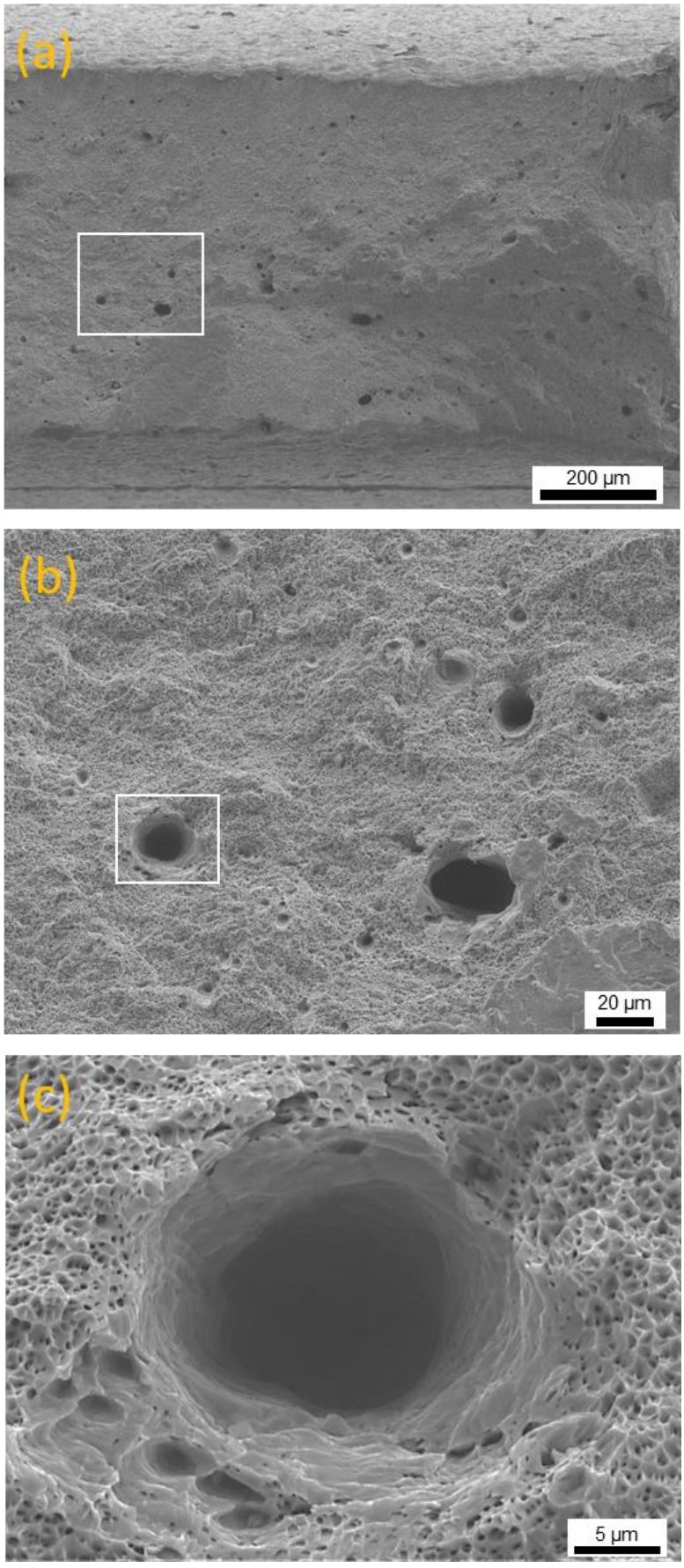

Figure 4.18 SEM fractographs of sample C6-H with increasing magnification to reveal the voids.

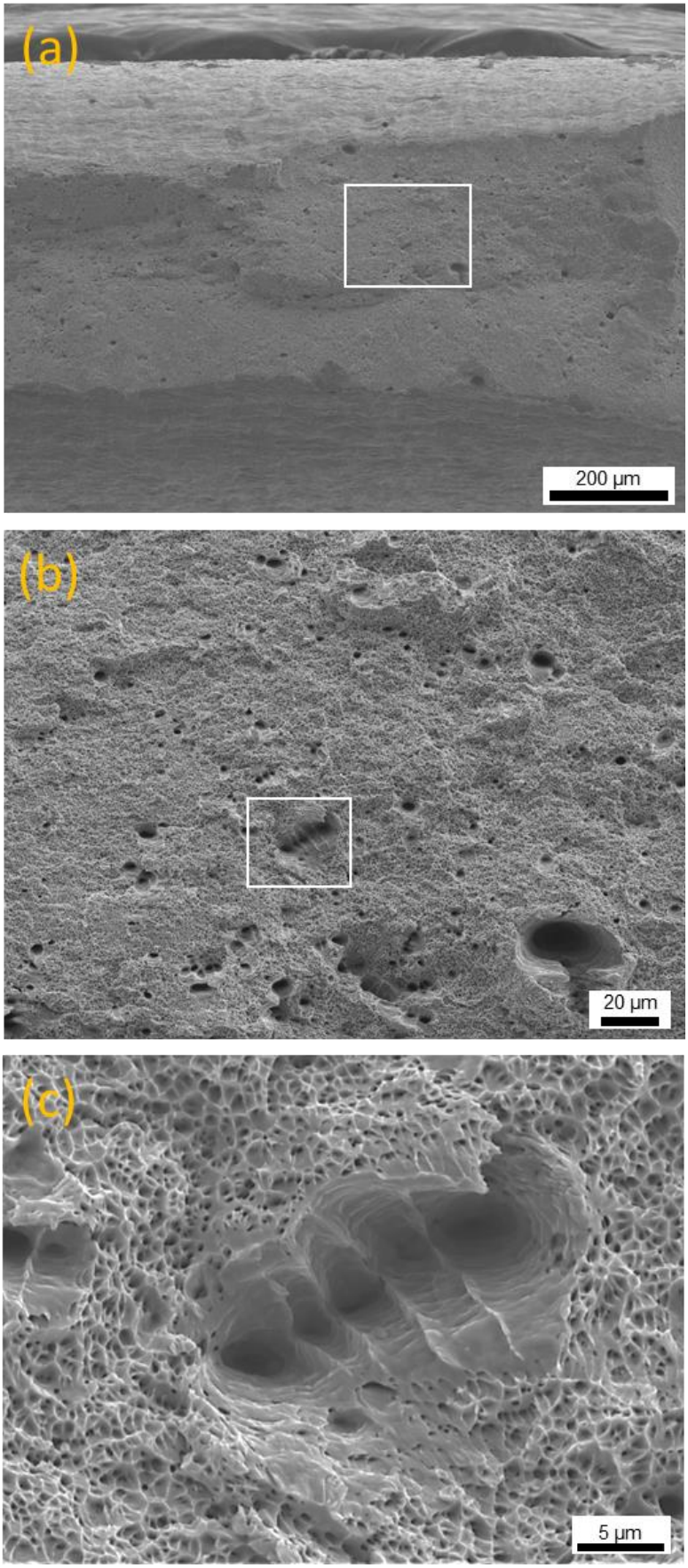

Figure 4.19 SEM fractographs of sample C6-V with increasing magnification to reveal the craters.

4.3 Discussions

4.3.1 SS316L Samples Using Fine Powders

4.3.1.1 Microstructural Analysis

Intragranular cellular sub-grains are only observed near the top build surface. This morphology has also been discovered in previous studies of SLM and SEBM as-built SS316L samples [30, 43, 45, 178, 184, 191]. The formation of cellular sub-grains is ascribed to the insufficient time for larger and heavier Mo atoms to completely diffuse during rapid solidification, as evidenced by the enrichment of Mo at sub-grain boundaries [191]. Therefore, the appearance of cellular microstructure is preferred when cooling rate is high [178]. On the other hand, the local enrichment of misaligned large Mo atoms induces numerous crystal lattice distortions, which in turn increases the hardness of SLM as-built samples [191]. The intragranular cellular sub-grain boundaries can also act as reinforcement elements which would retard or even prohibit crack propagation, thus enhancing the material's strength without sacrificing its ductility [178, 179].

The middle and bottom regions present rarely visible cellular dendrites and melt pool boundaries. Moreover, only grain boundaries can be observed after chemical etching. The similar phenomenon has been reported in previous studies which investigated the effects of heat treatment on the microstructure of laser-based AM processed SS316L samples [182, 184]. However, their samples were post heat-treated, and they did not exhibit any visible spatial microstructure heterogeneity. Differently, SEBM is a high-temperature material deposition process with in-situ heat treatment capability. During the layer-wise build process, the bottom section near the start-plate experienced significantly longer heat treatment period than the section near the top build surface. Therefore, the elemental segregation at cellular sub-grain boundaries was eliminated through elemental diffusion under elevated build temperatures, resulting in the vanishing of cellular dendrites in the lower region of the sample. Furthermore, due to the homogenizing effects of the in-situ heat treatment, the melt track boundaries were also dissolved. Thus, the SEBM as-built SS316L sample is characterized by longitudinal graded microstructure along build direction [58].

With regard to the distinctly different mechanical performance of the two samples F5 and F7 that have a close build density, of particular note is that the columnar grain boundaries in sample F7 appear significantly thicker as compared to those in sample F5. More specifically, the groove-like grain boundaries can be observed after chemical etching in sample F7 (Figure 4.7 (a)). It is owing to the fact that the heavy elements segregated at grain boundaries were etched away, thus creating the groove-like elemental depletion zone. In general, thick grain boundaries may lead to inferior mechanical properties, especially when grain boundaries are weakened by brittle precipitates. Furthermore, Cr and Mo are found to be enriched in precipitates congregating at grain boundaries (Figure 4.8). The chemical composition detected by EDS is close to σ phase (FeCr) [91, 192]. Austenite SS316L contains relatively high contents of Cr and Mo to improve its corrosion resistance. However, at elevated temperatures, the austenitic matrix can be decomposed, and the chromium carbides ($M_{23}C_6$) and intermetallic phases may occur [91]. Previous studies have discovered that σ phase appears only after $M_{23}C_6$ is formed, which causes Cr-depletion zone at grain boundaries. Hence, a higher temperature or a longer period of exposure to heat treatment is required for Cr to diffuse from grain interior towards grain boundaries to achieve a critical value, so that the formation of σ phase can take place, as Cr is its main forming element [193]. During the SEBM process, the build temperature was kept at ~ 820 - 870 °C in this work. Moreover, the samples were built under this temperature range for ~ 10 h, followed by ~ 7 h of slow cooling to reach below 100 °C. According to the time-temperature-precipitation diagram of SS316L determined by Weiss et al. [91], it is suggested that those precipitate particles congregating at grain boundaries in sample F7 are σ phase. σ phase is hard and brittle, and it may create local embrittlement and microcracks during loading [193]. Therefore, the formation of large amounts of σ phase should be avoided, as it reduces the material's toughness and ductility, which is detrimental to mechanical performance [194].

4.3.1.2 Mechanical Properties and Fracture Analysis

Microstructure determines the mechanical properties of SEBM as-built parts. When densification rate reaches near full density, the two neighboring layers become well bonded, thus the effects of metallurgical defects on tensile properties may become negligible [79]. In addition, the in-situ heat treatment in SEBM process enabled the layer boundaries to be dissolved (seen in Figure 4.6 (h)), making the samples less prone to fracture due to interlayer

defects. Hence, the anisotropy in tensile properties of SEBM processed parts is mainly due to the directional growth of columnar grains in solid samples, in contrast to their laser-based AM counterparts that are often due to the lack-of-fusion defects between layers.

More specifically, in SEBM processed SS316L parts, the tensile properties are directly linked to the amount of grain boundaries exposed to tensile opening modes, when the grain boundaries are weakened due to brittle precipitates. When load is applied perpendicular to build direction, the long axes of columnar grains are loaded in tension, making the entire length of grain boundary susceptible to Mode I opening failure; conversely, when applying load along build direction, only the short axes of columnar grains are subjected to Mode I opening tension, which reduces the chance of Mode I opening failure [79]. Furthermore, when columnar grain boundary is parallel to stress direction, dislocations can move more easily and have higher storage capacity, thus increasing its ductility, as evidenced by F5-V and F7-V in Table 4.3. Similar findings have also been reported in other SEBM as-built samples [195, 196].

Sample F7-H has the worst tensile properties, which is attributed to the precipitation of σ phase at grain boundaries. Figure 4.20 schematically illustrates the failure mechanism for sample F7-H. Due to the heat treatment effects of SEBM process, a lot of hard and brittle σ phase precipitates were formed at grain boundaries in sample F7. When the sample is subjected to the load along horizontal direction, the microcracks created by σ phase precipitates at grain boundaries act as main sites for triggering fracture by means of crack initiation and propagation, which may force grain boundaries to open and separate the neighbouring grains. The big gaps in Figure 4.11 (a) and the craters in Figure 4.11 (c) were the detached grain boundaries of sample F7 after intergranular fracture, though they were tested under different loading directions. Furthermore, the smooth fracture surface of sample F7-H can indicate that the detrimental σ phase precipitation will cause local embrittlement.

Samples F5 and F7 underwent the same heat treatment time of SEBM process as they were fabricated in one build. However, the tensile properties of sample F7 were much deteriorated. This is ascribed to the slower scanning speed and larger FO to build sample F7. The increasing FO enlarged the melt pool size, and the decreasing scanning speed caused localized heat accumulation, thus making F7 exposed to higher temperatures during building process. As a consequence, more σ phase precipitates were formed, which deteriorates the mechanical properties of sample F7 particularly normal to build direction. Therefore, a larger SF coupled with a smaller FO, i.e. the process parameters of sample F5, is recommended for

SEBM process of SS316L. In addition, it can be concluded that apart from the top build surface condition and relative density, the build temperature governed by SF and FO is also a key to SEBM processing of high-performance metals and alloys. Future experiments will be focused on further optimizing the process parameters to minimize the formation of detrimental σ phase and improve the mechanical performance of SEBM as-built SS316L parts.

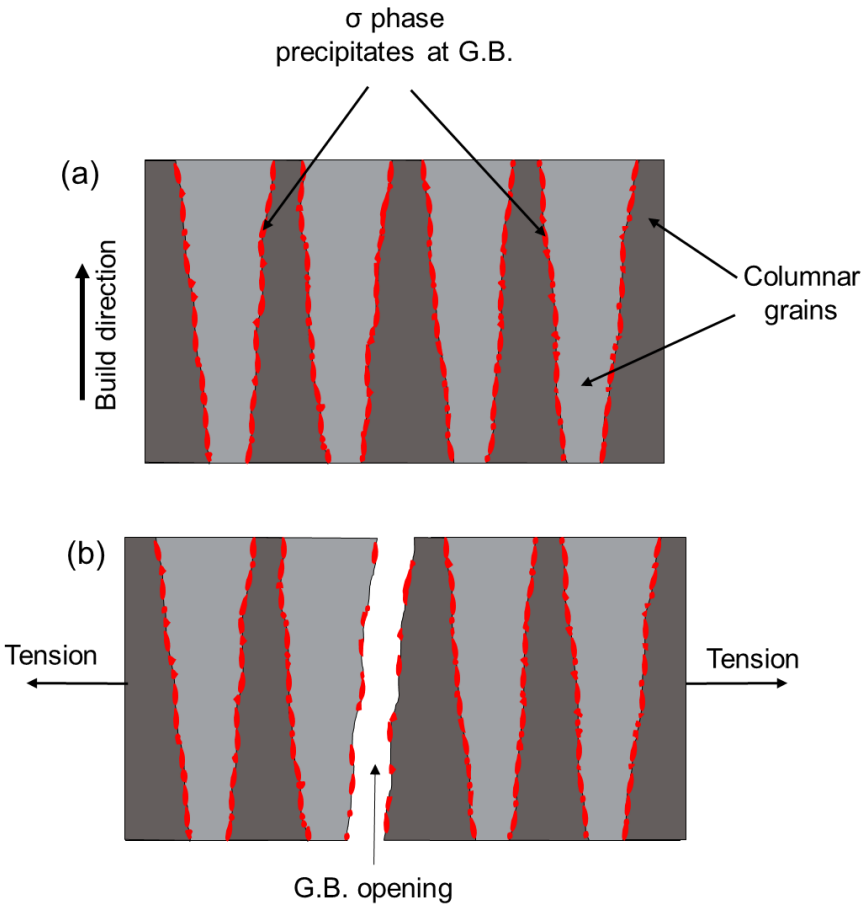

Figure 4.20 Schematic illustrations of (a) side view of sample F7 with σ phase precipitates congregating at grain boundaries (G.B.), and (b) intergranular fracture when subjected to a horizontal load.

4.3.2 SS316L Samples Using Coarse Powders

In this section, the discussions will be carried out by comparing the process window, micrographs, crystallographic textures and tensile properties with the SS316L samples fabricated using fine powders. A comparative study will be more effective in revealing the powder size effects and the possible mechanisms.

4.3.2.1 Process Window

As illustrated in Table 4.7, the powder size has a significant influence on the optimized window to process the material using SEBM. The coarse powder requires a lower SF and smaller FO, meaning that a higher energy input is demanded to fabricate fully dense SS316L alloys. From the EBM log, the beam current for C and F is 8.1 mA and 11.37 mA. By referring to the beam current and SF matrix provided by Arcam, the scanning speed for C and F is determined to be 1594.8 mm/s and 3894.8 mm/s, which is equivalent to a line energy of 0.305 J/mm and 0.175 J/mm. The line energy for C is 74.3% higher than F. This is expected as the powders with larger size are more difficult to be fully melted.

Table 4.7 DoE chart for comparison of the respective optimized process window to fabricate SS316L samples using fine powders (denoted by F) and coarse powders (denoted by C).

FO \ SF	110	130	150	170	190
8 mA					
9 mA		C			
10 mA				F	
11 Ma					
12 mA					

The time-temperature curve in Figure 4.21 shows the temperature recorded by a thermocouple placed underneath the start-plate during SEBM processing. Although the start temperature of 850 °C is the same for coarse and fine powders, coarse powders experienced a significantly higher average temperature, particularly in the first half of processing. This finding is consistent with the effect of higher energy input for coarse powders. The processing time for coarse powders is longer mainly because the sample build height is 5 mm taller and the scanning speed is lower for C.

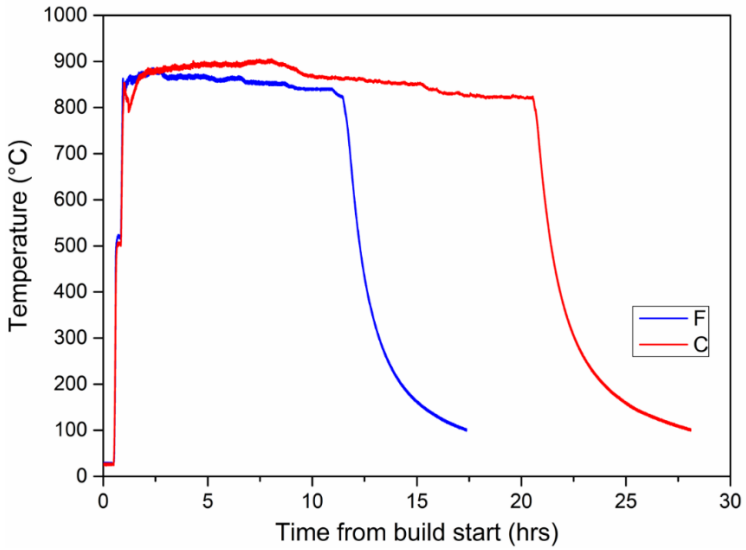

Figure 4.21 Time-temperature curve of SEBM processing of C and F samples.

4.3.2.2 Microstructure Analysis

Figure 4.22 comprehensively compares the microstructures of both C and F samples at different locations observed under OM, SEM and EBSD.

Near the top region, Figure 4.22 (a) and (b) show that the melt tracks of sample C are deep and narrower, in contrast to the shallower and wider melt tracks of sample F. The detailed dimensions for the melt pool morphology of each sample are summarized in Table 4.8. This difference in melt track morphology could be predominantly dictated by input energy level. The dendrites are obscure and nearly invisible for sample C (Figure 4.22 (d)). This could be ascribed to the effect of more prolonged in-situ heat treatment under higher temperature, due to the lower scanning speed and bigger melt pool, as also observed by Sun et al. [96].

The major difference between the two samples is the crystallographic texture. Sample F has a primarily <001> texture shown in EBSD map (Figure 4.22 (e)), which is a widely reported grain morphology in most metal AM as-built samples including but not limited to SS316L. The formation of the columnar-shaped grains parallel to build direction is mainly due to the largest z-axis thermal gradient during the building process [6]. In contrast, the primarily <111> texture is rarely reported in metal AM literature. There are a few published works with similar morphology for the bulk samples (i.e. excluding site specific control): <011> texture zigzag-shaped grains [96] and ripple-shaped grains [95] for SLM-built SS316L alloys, and a mixture of <001> and <111> for SLM-built CoCr alloys [197]. Different mechanisms account

for the formation of the unique microstructures in their respective works. In our context, it might be associated with the higher thermal conductivity of the sintered powdered when building sample C, which made the resultant thermal gradient and liquid-solid interface velocity fall in the equiaxed grain region according to the columnar to equiaxed transition chart [198]. As this work is primarily focused on the process parameter study, the detailed investigation on grain growth was not carried out.

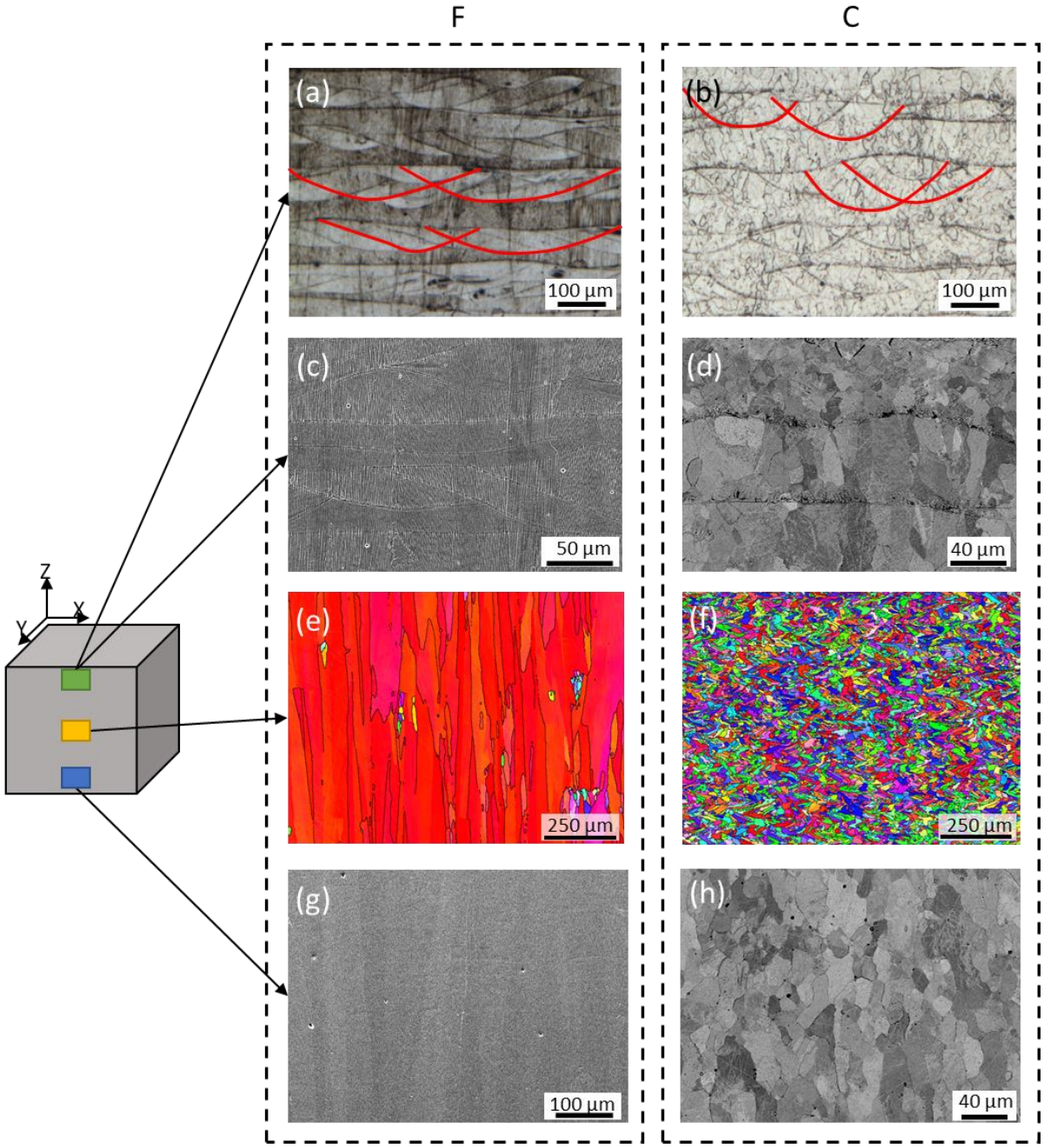

Figure 4.22 Compiled micrographs for both fine and coarse powder SEBM-built SS316L samples examined at different locations under (a and b) OM, (c, d, g and h) SEM, and (e and f) EBSD. The red lines in (a) and (b) outline the representative melt tracks.

Table 4.8 Summary of the melt pool dimensions for F and C samples.

	Width (μm)	Depth (μm)	Aspect ratio (width/depth)
F	277.8 ± 30.5	51.4 ± 5.4	5.4 ± 0.7
C	249.2 ± 27.0	72.0 ± 9.4	3.5 ± 0.4

4.3.2.3 Mechanical Properties

Sample C with equiaxed grains exhibits near isotropic tensile properties (see Figure 4.17), while sample F with columnar grains exhibits obvious anisotropic tensile properties (see Figure 4.9). When both samples are near fully dense, crystallographic texture dominates the respond curves during tensile testing. Their tensile properties are summarized in Table 4.9. Between the two samples, the most eye-catching difference is their uniform strain. The uniform strain of sample C is 74.4% and 59.2% higher when tested along horizontal and vertical directions, respectively. The UTS of sample C is 10.9% higher than sample F when subjected to horizontal tension. The high UTS could be attributed to the refined grains of sample C, while the superior ductility could be ascribed to the early and prolonged work hardening regime which involved deformation twinning during testing. However, the study of the deformation mechanism is not the focus of this work.

Table 4.9 Comparison of tensile properties for samples C and F, which are represented by C6 and F5, respectively.

	UTS (MPa)		Uniform strain (%)	
	Horizontal	Vertical	Horizontal	Vertical
C	634.1 ± 8.6	614.8 ± 4.9	50.4 ± 0.6	44.1 ± 1.2
F	571.8 ± 19.3	651.7 ± 8.5	28.9 ± 4.4	27.7 ± 1.5

4.4 Conclusions

Using fine SS316L powders, solid samples with high relative densities (≥ 99.0%) were fabricated by SEBM under two sets of optimized process parameters using DoE. The tensile properties of the two kinds of SEBM-built SS316L samples were investigated. Low SF coupled with small FO produced over-melted parts, while high SF coupled with large FO created porous parts. ANOVA shows that only SF had significant effect on the part density. The SEBM as-

built SS316L parts generally had a superior tensile strength but inferior ductility compared to their conventionally manufactured counterparts. In particular, the UTS of the best sample produced (i.e. F5-V) was 18.1% and 35.4% higher than the cast and wrought samples respectively, although its elongation was 42.7% and 21.3% lower. In addition, the samples had better tensile properties when tested along the build direction in comparison with the horizontal direction. The SEBM as-built SS316L samples exhibited obvious longitudinal microstructural heterogeneity along the build direction, which featured visible cellular dendrites and melt track boundaries at the top build region and less visible ones at the lower build regions. Severe σ phase precipitation was observed in the SEBM-built SS316L samples fabricated under lower SF and larger FO, due to the prolonged in-situ high-temperature heat treatment of the samples in SEBM process. The σ phase precipitation induced local embrittlement in the samples, which resulted in intergranular fracture of the tested samples. It was found to significantly reduce the ductility of the samples, particularly along the horizontal direction. Hence, a higher SF coupled with smaller FO is recommended to avoid σ phase precipitation, provided that the smooth top build surface and high relative density could still be achieved.

The different PSD in powder feedstock significantly affected the process window, microstructure and tensile properties for SEBM as-built SS316L alloys. The same DoE method was adopted for optimizing the process parameters for coarse SS316L powders. A lower SF with a smaller FO was applied to fabricate solid parts with high relative density, meaning a higher input energy was required. This high input energy resulted in narrower and deeper melt pools. The coarse-powder samples were predominantly composed of nearly equiaxed grains and obscure cellular dendrites. In contrast, the fine-powder samples were primarily made of <001> columnar grains parallel to the build direction and visible cellular dendrites near the top region. Coarse-powder samples exhibited isotropic tensile properties, of particular note is the superior ductility which was comparable with the highest values that could be attained in the literature. However, fine powder samples exhibited strong anisotropy in mechanical properties, as is the case for most AM-processed alloys. This work demonstrates that powder size distribution can significantly affect the optimization of process parameters for SEBM process.

Chapter 5 Process Parameter Optimization and Process-Microstructure-Property Relationships Mapping for Ti-6Al-4VAlloy Using Machine Learning

ML could model complex non-linear relationships between inputs and outputs, process images without domain expertise of feature engineering/extraction, and generate new images that are nearly indistinguishable from the original dataset. In this chapter, a ML method is developed to optimize the process parameters and build the PMP relationships for SEBM-processed Ti-6Al-4V alloy rapidly and precisely. Specifically, the traditional ML techniques are comparatively studied with DL techniques in terms of the performance in predicting tensile strengths and relative densities. The process maps are subsequently constructed using DL to discover the process window. Next, the PMP relationships are quantified over the entire parameter space with the proposed ML-centered tetrahedral framework, where an additional dimension(i.e. surface image) is used to retrieve the PMP data. The prediction power of DL models is demonstrated to build process-to-property, surface/microstructure-to-property, and process-to-surface/microstructure relationships. The microstructure here refers to as-polished pore microstructure and as-etched α/β dual-phase microstructure of the vertical midplane of the samples. CNN feature visualization is implemented to visualize the abstract features of the surface images that contribute to property. Finally, full-scope microstructure/surface maps are generated, which are verified by latent space representation. The structure of this chapter is illustrated in Figure 5.1.

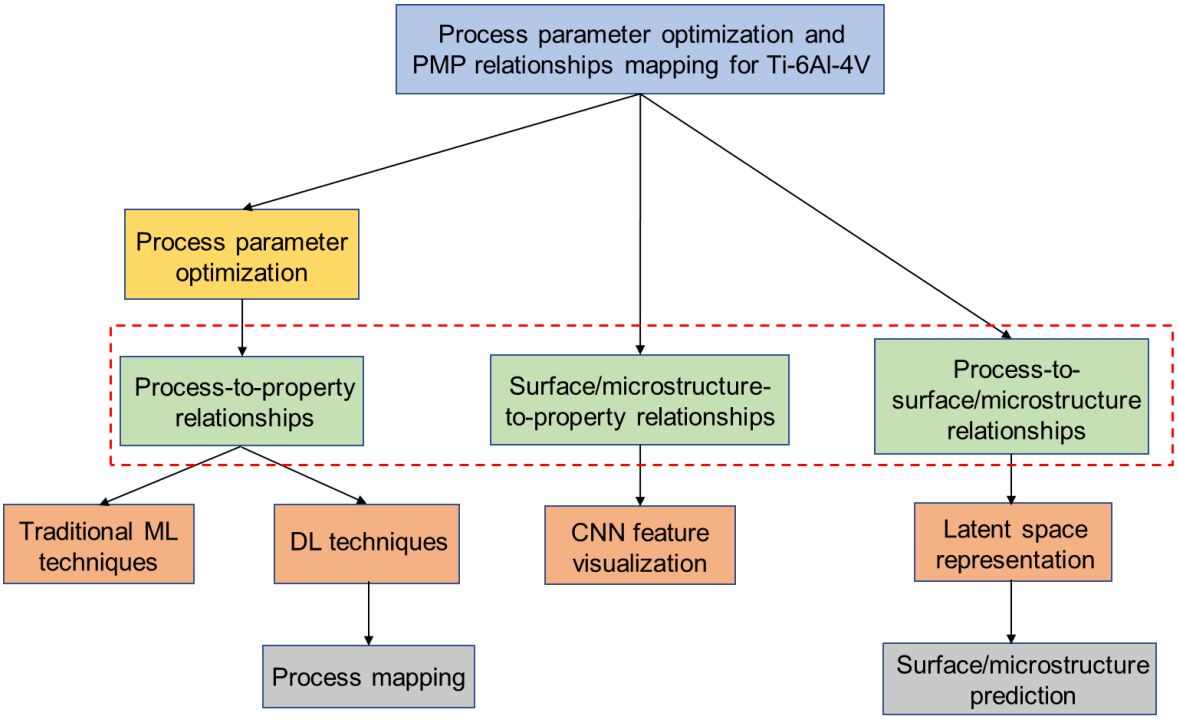

Figure 5.1 Flow chart of the various studies carried out in this chapter. The blocks enclosed by the red dash lines form the ML-centered tetrahedral framework.

5.1 Introduction

Process parameter optimization is essential and also the primary step to additively manufacture any materials. In addition to DoE and simulation methods, ML opens up new opportunities for process optimization. ML-assisted study can model complex nonlinear relationships between process parameters and mechanical properties, and can make accurate predictions in the correlations, which can be leveraged in both experiments and numerical simulations.

Moreover, establishing the PMP relationships is of core interest to material scientists and engineers. Various mathematical models have been developed in the past few decades. A widely accepted model is the Hall-Petch relationship, which well links yield strength of a material to its grain size in microstructure [199]. However, microstructure could be a multi-scale combination of multiple phases or constituents with complex substructures. In the context of metal AM, additional microstructural features like micro-pores, nano-precipitates, sub-grains, anisotropy and heterogeneity may be present due to the rapid, directional but intermittent solidification process [200]. Hence, it is challenging to make predictions solely based on any single microstructural feature, as the properties are also affected by complex

multi-scale physics. Fortunately, some advanced ML techniques can build the entire microstructure-to-property relationships from raw micrographs. A few research works have employed ML methods, particularly CNN to predict ionic conductivity in zirconia ceramics [201], optical absorption for different materials [202], tensile properties in steels [203] and Ti-6Al-4V alloys [204] based on their micrographs.

Therefore, to address the above two problems, we have proposed a ML method to optimize the process parameters and quantify the PMP relationships. The flowchart for the entire ML project is illustrated below in Figure 5.2. Specifically, 56 parametric combinations of SF and FO were generated randomly to build Ti-6Al-4V tensile coupons and witness cubes via SEBM. The tensile properties were evaluated by testing all the tensile samples. The relative density, top surface images, as-polished pore microstructure and as-etched α/β microstructure images were extracted from the witness cubes. The information collected was fed into various ML models to build the interlinkages of each component in order to form the ML-centered tetrahedral framework. To assess the generalization ability and efficiency of our methodology in different materials, based on the baseline models developed for Ti-6Al-4V, transfer learning (TL) technique was applied to SS316L study for process parameter optimization with an even smaller dataset, which will be detailed in the next chapter.

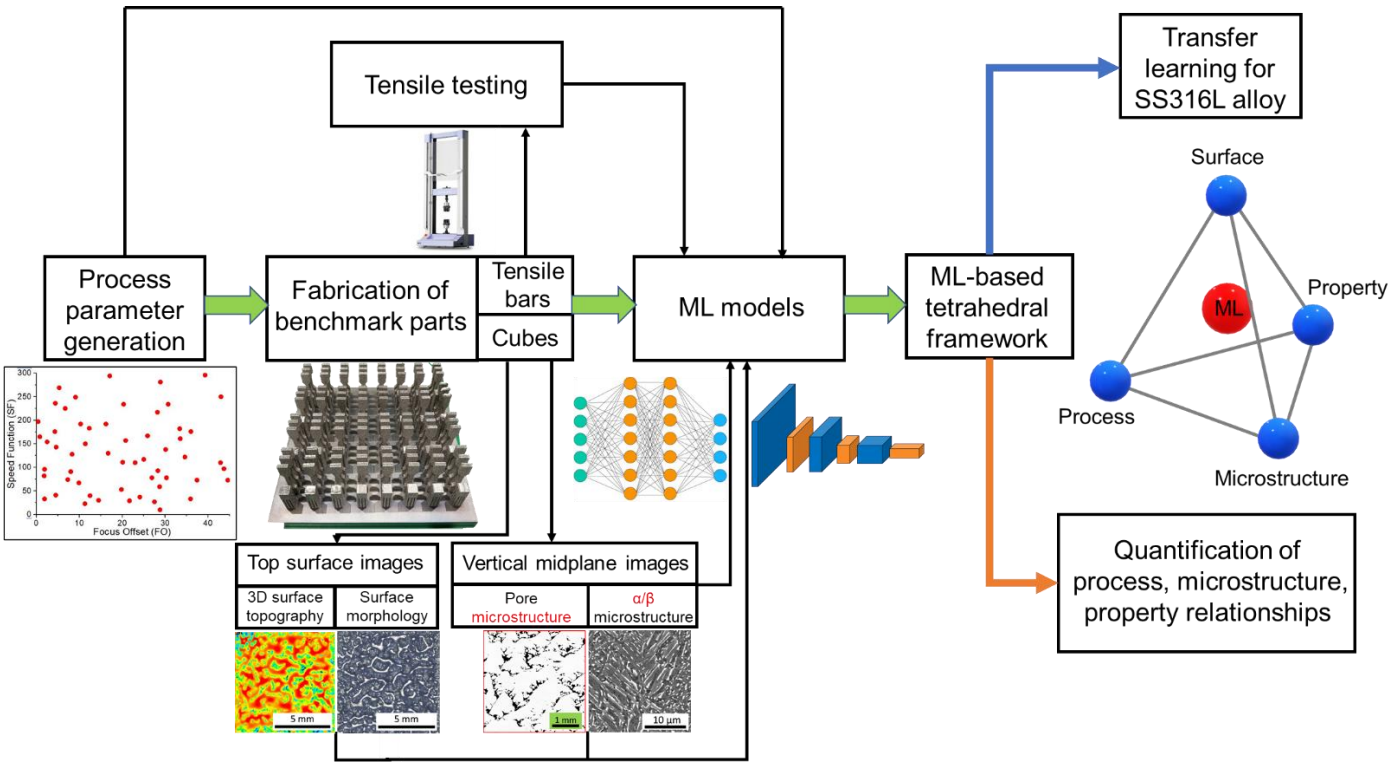

Figure 5.2 Flowchart of the ML-assisted process parameter optimization and the ML-centered tetrahedral framework for the entire ML project. Transfer learning (TL) can be applied to SS316L alloys using the trained weights from Ti-6Al-4V baseline models.

In SEBM, the 3D object is built upon stacking of materials. Different levels of input energy can leave distinctive information on the top build surfaces, as shown in the work of Aoyagi et al. [117]. Inspired by this phenomenon, a ML-centered tetrahedral framework which incorporates surface is proposed to map the paramount PMP correlations in this study. The role of surface is explained in three aspects: firstly, the top surface represents the "skin" of fusion that can be utilized to pre-judge the suitability of the process parameters in the preliminary screening of the process window, as also applied in Chapter 4; secondly, since the features on the surface can implicitly reflect the quality of processing, they can be extracted to predict the microstructure and mechanical properties; thirdly, empowered by DL algorithms, it is a non-destructive way to retrieve the PMP data by simply taking a fusion surface image of the SEBM-built part.

5.2 Sample Fabrication and Data Collection

In Arcam's EBM A2XX model, FO ranges from 0 to 45 mA while SF ranges from 0 to 300. To determine the optimized process window, the study should cover the entire parameter space as widely as possible with a minimum number of trials. As highly complicated multi-physics are involved in the melting process, the process parameters might take effect at some points but remain insignificant at other points, as demonstrated by Gong et al. [181]. Using a systematically full or fractional DoE strategy may fail to find the global optimum in some cases, especially when the number of data points is limited, as schematically illustrated in Figure 5.3. Therefore, inspired by the work of James and Joshua [205] where random search was performed in place of the conventional grid search for hyperparameter optimization for ML models, the random search method for process parameter optimization is proposed for SEBM. It is believed that the random search method can be more efficient in finding out the optimized parameters with higher accuracy.

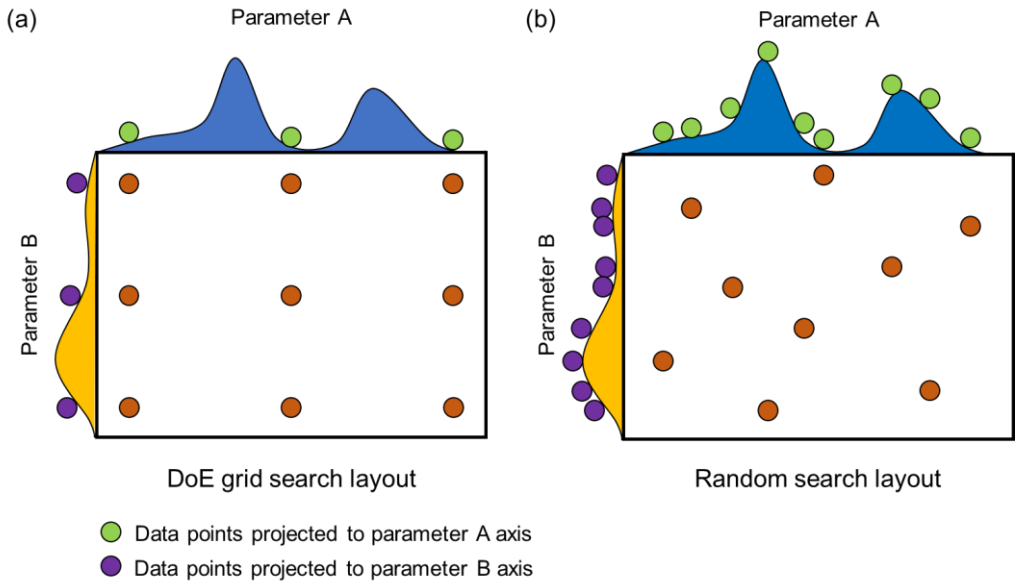

Figure 5.3 Comparison of the efficiency and accuracy of searching the optimal process parameters with 9 data points using (a) DoE grid search method and (b) random search method.

To fabricate Ti-6Al-4V dataset samples, 56 different sets of process parameter were generated randomly to cover the full space of SF and FO map, as shown in Figure 5.4. The layer thickness and line offset were kept constant at 50 µm and 0.1 mm, respectively. Due to the limited number of parameter settings that Arcam's EBM operating software can accommodate, 56 sets of samples were fabricated in two separate builds. The result of one build is shown in Figure 5.5. Under each set of parameters, there are 3 identical near-net-shape tensile coupons built vertically with the dimensions of $4 \times 4 \times 10$ mm^3 for gauge section and one witness cube of $10 \times 10 \times 10$ mm^3. The witness cubes with support structures underneath were placed at the same height of the midplane of gauge section in order to depict the microstructure of tensile coupons, as they both underwent the same thermal history during the printing process.

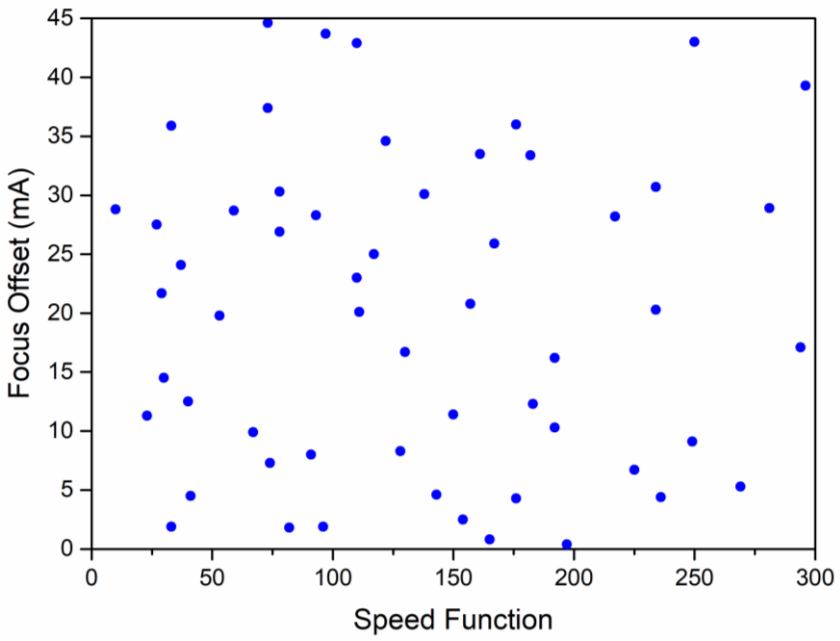

Figure 5.4 Process parameters generated by the random search method for printing Ti-6Al-4V dataset samples using SEBM.

The average UTS value of the three tensile coupons fabricated under the same set of parameters was recorded. Although UTS and elongations are two important elements in tensile properties which usually follow a strength-elongation tradeoff for many metallic materials [96], elongations are not considered in our work. This is because SEBM-built Ti-6Al-4V has a relatively low elongation to fracture ~ 15% [58]. The fluctuation of elongation values even between the identical tensile coupons produced from the same process parameters might be high, as observed from our experimental data. Therefore, it is not very meaningful to predict elongations using ML. Besides, the elongations of the samples with a relative density of $\geq 99.5\%$ are all above 10%, which already satisfies the requirements of ASTM standard for their wrought counterparts [58]. Hence, only UTS is considered as the key tensile property indicator in our work for Ti-Al-4V alloys, if the criterion of relative density of $\geq 99.5\%$ is met.

The support structures of the witness cubes were completely removed. By visual examination, the top build surface conditions could be labelled to three classes, namely porous (P), flat (F) and warping (W). As some cubes have interconnected open pores which can go from top surfaces to the interior regions, using the Archimedes' method may lead to significant errors for density measurements. Hence, the cube samples were cut into halves at midplane along the vertical build direction. The entire as-polished cross sections were examined under

laser confocal microscopy, and image analysis method as described in Chapter 3 was used to compute relative density.

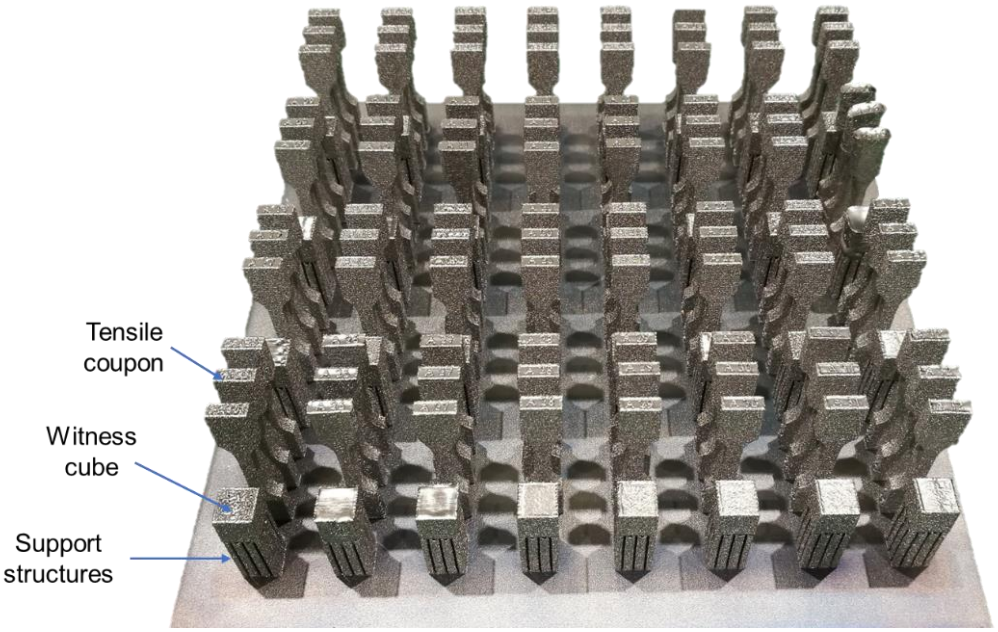

Figure 5.5 Overview of the SEBM-built Ti-6Al-4V samples with random process parameters for melting.

The full dataset is listed in Appendix C. The histograms of the data are plotted in Figure 5.6 to visualize the data distribution of UTS, relative density and classes of top build surface condition. Before feeding the data to ML models, the values for SF, FO, UTS and relative density were normalized to the range between 0 - 1 for better convergence during training.

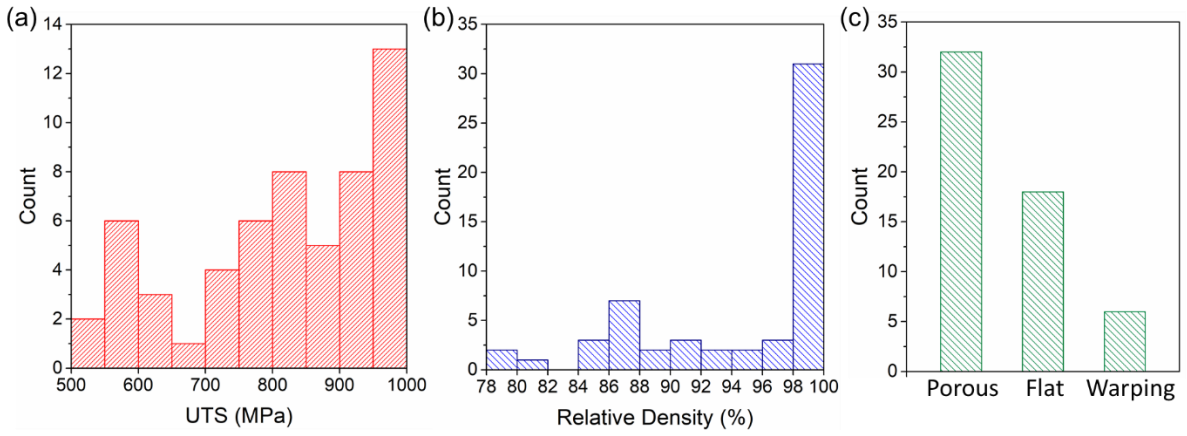

Figure 5.6 Histograms of (a) UTS, (b) relative density and (c) classes of top build surface conditions.

Laser confocal microscopy was employed to acquire the surface and pore image data. 3D surface topography was captured under 3D topography mode as it could include the height information of features. Surface morphology was examined under optical mode. Pore microstructure was captured by laser mode. SEM was used to capture the α/β dual-phase microstructure images. Three representative samples with their top build surface images and corresponding vertical midplane images, including as-polished pore microstructure and as-etched α/β microstructure are shown in Table 5.1. Due to the difficulty in the chemical etching of porous samples, only 23 fully dense samples (relative density of ≥ 99.5%) were etched to reveal their α/β microstructures.

Table 5.1 Top build surface images of three representative samples showing porous (P: sample 02), flat (F: sample 34) and warping (W: sample 51) surface conditions examined by laser confocal microscopy, with the corresponding vertical midplane images of pore microstructure and α/β microstructure of each sample. The SEM α/β micrographs for porous samples are not available. The scale bars for each image are labelled.

	Top surface images		Vertical midplane images	
Sample No.	3D surface topography	Surface morphology	Pore microstructure	α/β microstructure
02	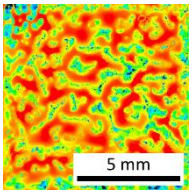	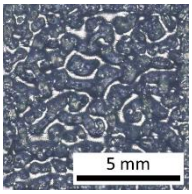	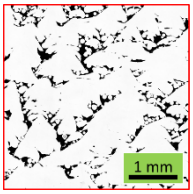	N.A.
34	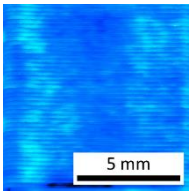	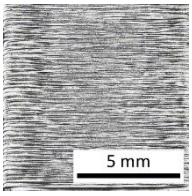	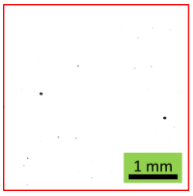	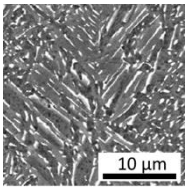
51	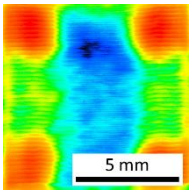	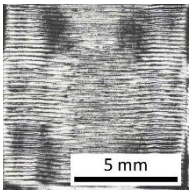	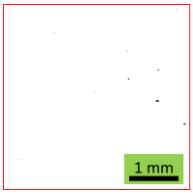	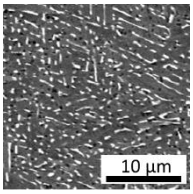

The full dataset for top surface images and vertical midplane images can be found in Appendix D. The details for image data preparation are attached in Appendix E.

5.3 Results and Discussion

To evaluate the performance of a ML model, the overall dataset is usually split into training set and test set. However, this technique may cause bias because the accuracy obtained using one test set can be significantly different from that obtained by another different test set. Hence, the k-fold cross-validation (CV) technique was adopted to provide a robust estimate of the generalization error of the trained model. The k-fold CV is implemented by splitting the dataset near-evenly into k subsets and taking turns to train the model on all (k-1) subsets except the left-out one subset which serves as test set. This process is repeated until all the k subsets are given an equal opportunity to be the left-out test set. As the overall dataset size is small, 5-fold CV is chosen for the models, as illustrated in Figure 5.7.

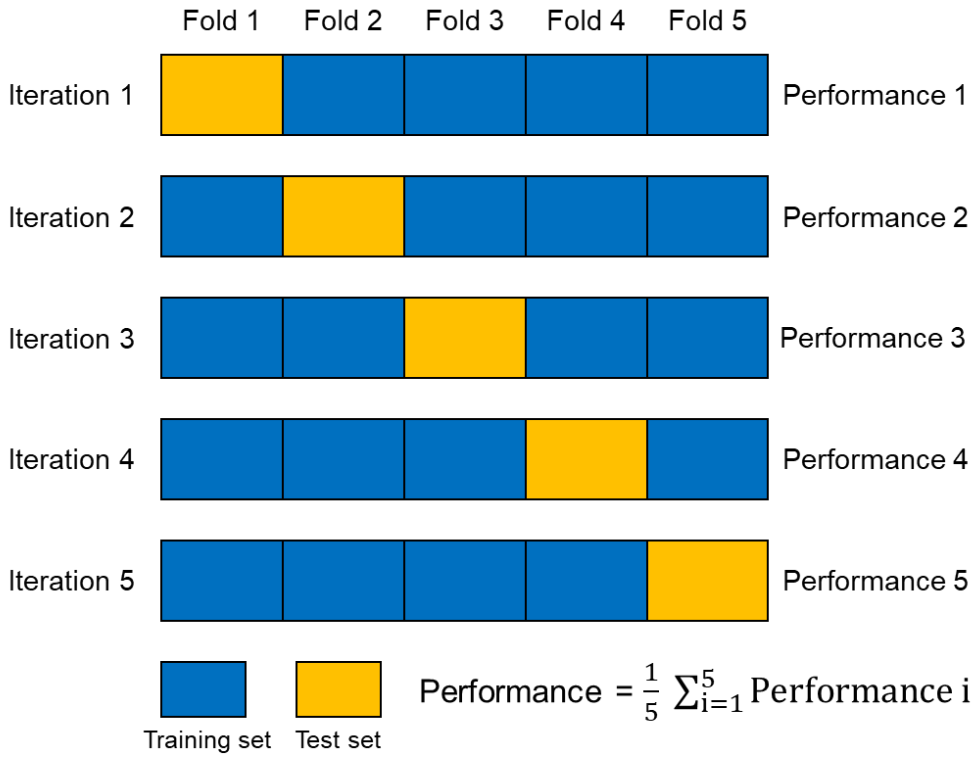

Figure 5.7 5-fold cross-validation (CV) to evaluate the generalization performance of models.

Mathematically, there is an astronomic number of ways to split the dataset into 5 folds. Hence, a random seed was selected to split the 5 folds in the same manner in order to ensure a fair comparison of the performances among different ML models. The dataset was shuffled before splitting in order to minimize the biased data distribution for each fold.

5.3.1 Process-Property Relationships

In this section, the inputs are process parameters, and the outputs are UTS, relative density and classifications for top build surface conditions, respectively. In the end, a comprehensive process map will be constructed to visualize the process window for SEBM processing of Ti-6Al-4V alloy.

5.3.1.1 Model Validation

Totally, 3 traditional ML techniques (i.e. SVM, KNN and DT) were attempted in this Ph.D. work to model the complex relationships between process parameters, relative density and UTS. MLP was also included to compare with the traditional ML models. Boxplots were generated to graphically depict the quartiles of the mean absolute percentage error (MAPE) and root mean square error (RMSE) for predicting UTS (see Figure 5.8) and relative density (see Figure 5.9) by different models.

The boxplots show that among the 3 traditional ML techniques, SVM has better performance for UTS prediction while KNN works better for relative density prediction, as far as the median and interquartile range values are concerned. Overall, MLP could achieve significantly higher performance than the traditional ML methods that were investigated in our work.

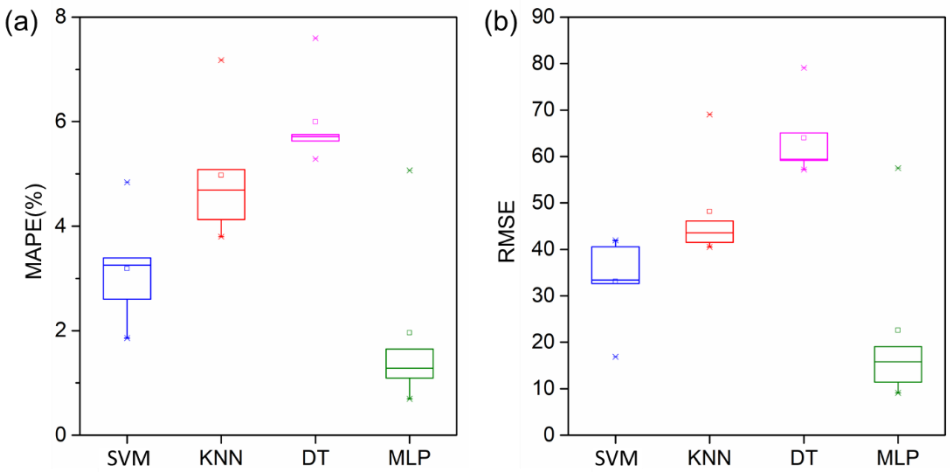

Figure 5.8 Boxplots that depict the quartiles of (a) the mean absolute percentage error (MAPE)% and (b) root mean square error (RMSE) for predicting UTS.

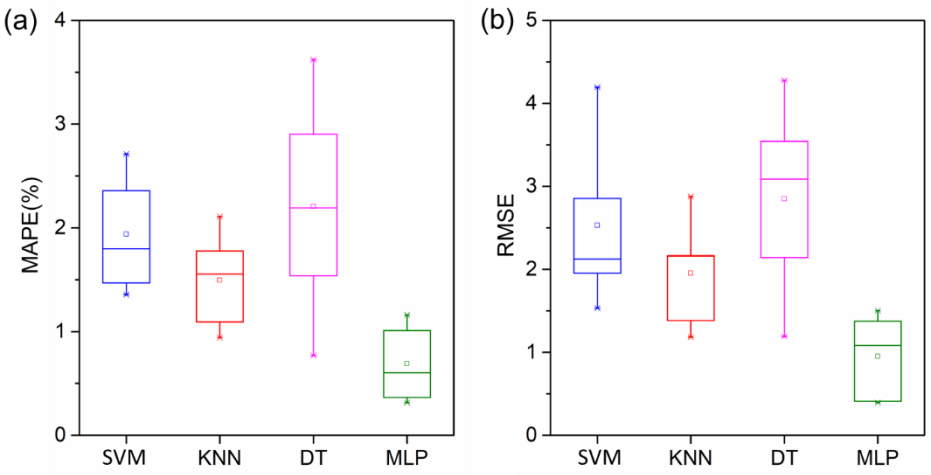

Figure 5.9 Boxplots that depict the quartiles of (a) the mean absolute percentage error (MAPE)% and (b) root mean square error (RMSE) for predicting relative density.

Different from classification tasks which usually require hundreds and thousands of data to achieve a decent accuracy without overfitting, there is no gold standard to know the optimal data size for regression tasks. Hence, it is necessary to investigate the minimum data size required to achieve sufficiently good performance in the context of this work. When the full dataset of 56 data points are used, a train/test split ratio of 80/20 gives 44 train data and 12 test data. There are 2 possible ways to carry out the investigation, either by gradually reducing the entire dataset while keeping the train/test split ratio constant, or by gradually reducing the training data while keeping the test data constant. However, the first way may be unreliable, as it is possible for the model to fit the test data well and produce decent results when the test data size is small with the reduced dataset size. Conversely, this is unlikely to occur when the test data size is large. Hence, the second way can provide a less biased assessment of the data size effect.

To ensure a fair comparison, the random seed was fixed so that the same 12 test data were used in each ML model with the gradually reduced size of training data. The results for UTS prediction are plotted in Figure 5.10. As the training set size increases, the performance of the models also improves until it reaches a plateau at a certain turning point where little improvements can merely be achieved. In general, MLP can produce better performance both in (100-MAPE)% and RMSE, which is consistent with the results obtained in Figure 5.8. It is also observed that the performance curves for most ML models either flatten out or just oscillate after passing their respective turning points. Although it is challenging to precisely quantify the minimum training data to achieve high performance, this figure can at least justify

that a training set of 44 data points is good enough for UTS prediction. Besides, the performance of the regression models also depends on how much deviation from the true value can be tolerated. In this case, a ± 50 MPa (~ ± 5%) error for UTS is commonly seen in tensile testing of Ti-6Al-4V alloys, even for the identical coupons fabricated under the same processing condition. Therefore, a (100-MAPE)% of higher than 98% for UTS prediction is an excellent result with only 56 data points.

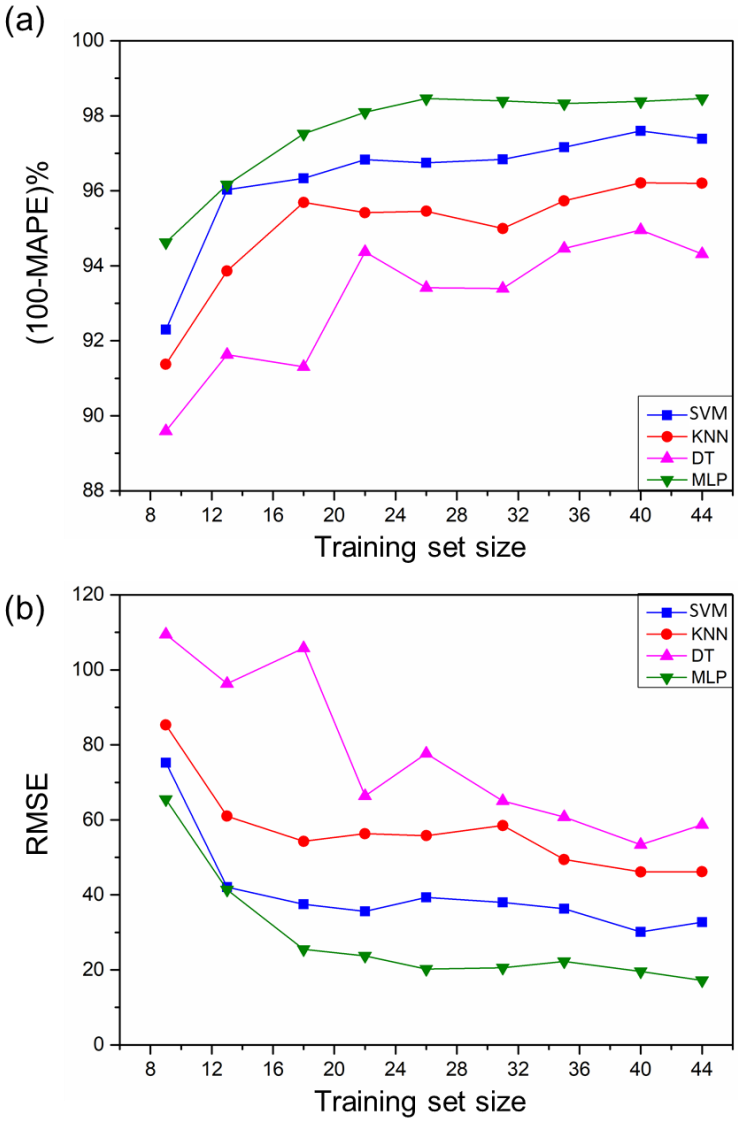

Figure 5.10 Effects of the training set size on the performance of different ML models in terms of (a) (100-MAPE)% and (b) RMSE for UTS prediction.

In summary, it is proven that DL methods demonstrate better performance than tradition ML methods. Besides, it is also more feasible to implement TL for SS316L using DL. Therefore, DL methods are adopted for the following sections.

5.3.1.2 Process Mapping

Process mapping can provide easy and straightforward visualization of the relationships between process parameters, UTS, relative density and top build surface conditions. A random seed was fixed to split training and test set in this section.

To predict UTS from process parameters, a MAPE of 1.51% with a standard deviation (std) of 1.19% and RSME of 18.04 for test data could be achieved using the MLP regression model. A 3D surface plot over the entire parameter space was generated by MATLAB using the trained weights. As shown in Figure 5.11, the plot could fit all the data points well without any odd points that fall far above or below the surface. The 12 test data points, which were previously unseen by the model, could also be well fitted by the regression surface, which further implies that overfitting is not salient in the current case.

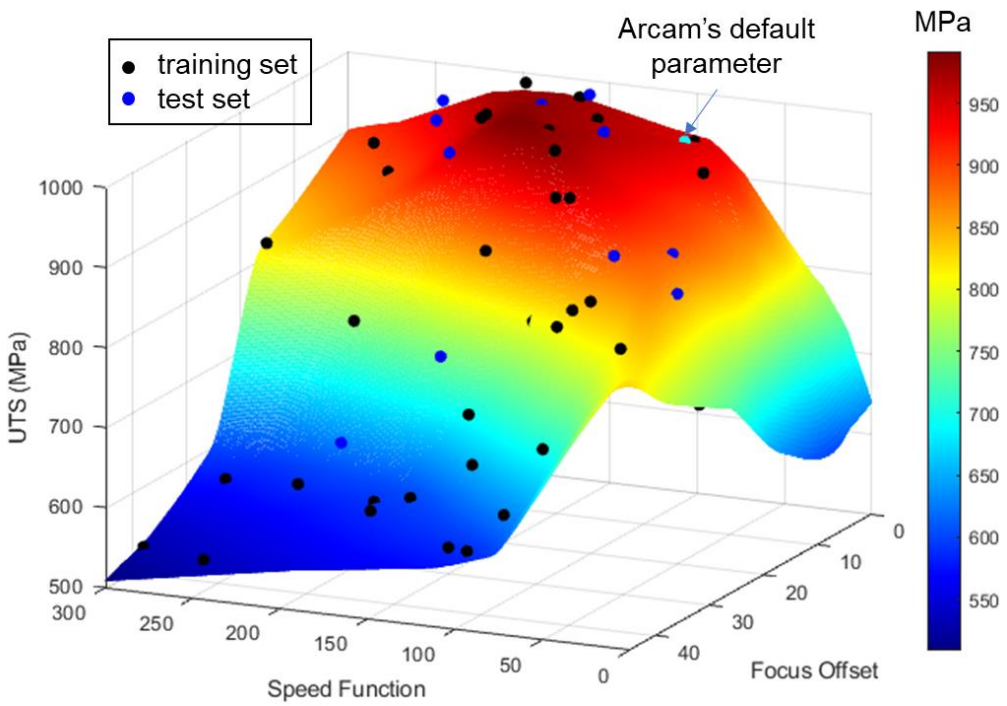

Figure 5.11 3D surface plot of relationships between process parameters and UTS modelled by MLP. Arcam's default parameter setting is labelled by a cyan dot.

The same hyperparameter setting was implemented to map the relationship between process parameters and relative density. The results showed that a MAPE of 0.94% with a std of 0.81% and RSME of 1.14 for test data was achieved. The corresponding 3D surface plot is shown in Figure 5.12.

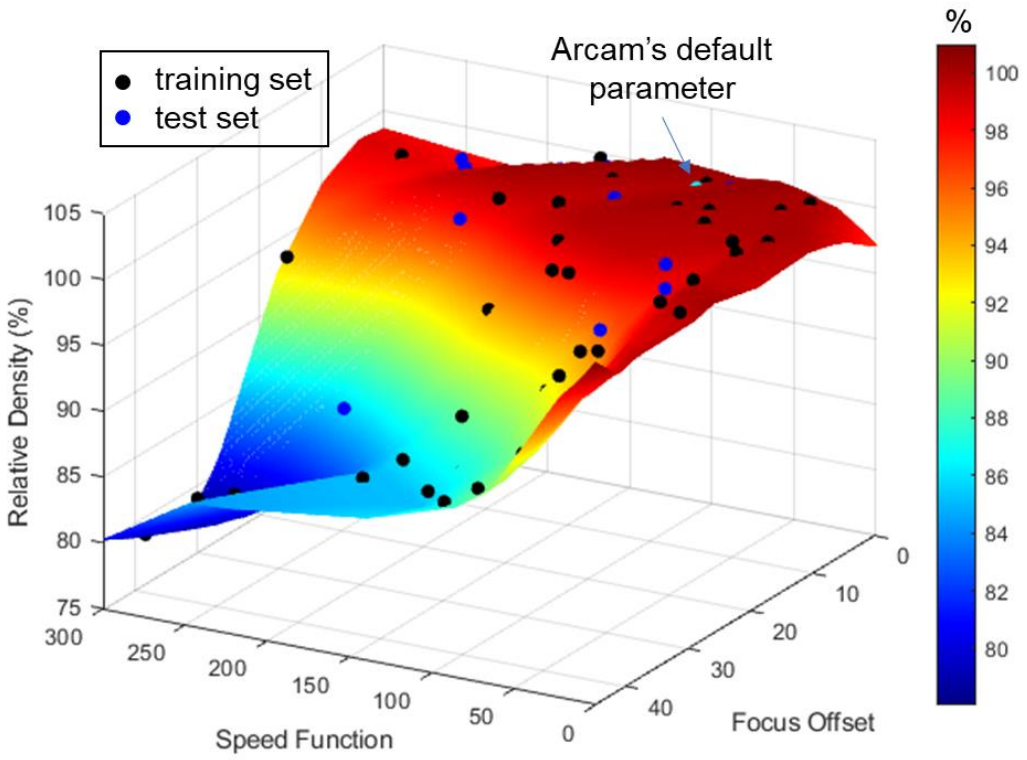

Figure 5.12 3D surface plot of relationships between process parameters and relative density modelled by MLP. Arcam's default parameter setting is labelled by a cyan dot.

To classify the top surface conditions, a classification accuracy of 100% has been achieved for training test and 91.7% for test set using MLP classifier. The decision boundary is visualized for the entire dataset in Figure 5.13. It is seen that all the data points are classified correctly using this model, except for only one flat-surface sample from the test set, which is misclassified as class P. Nevertheless, the misclassification could be more ascribed to the outlier data point rather than the deficiency of the ML model.

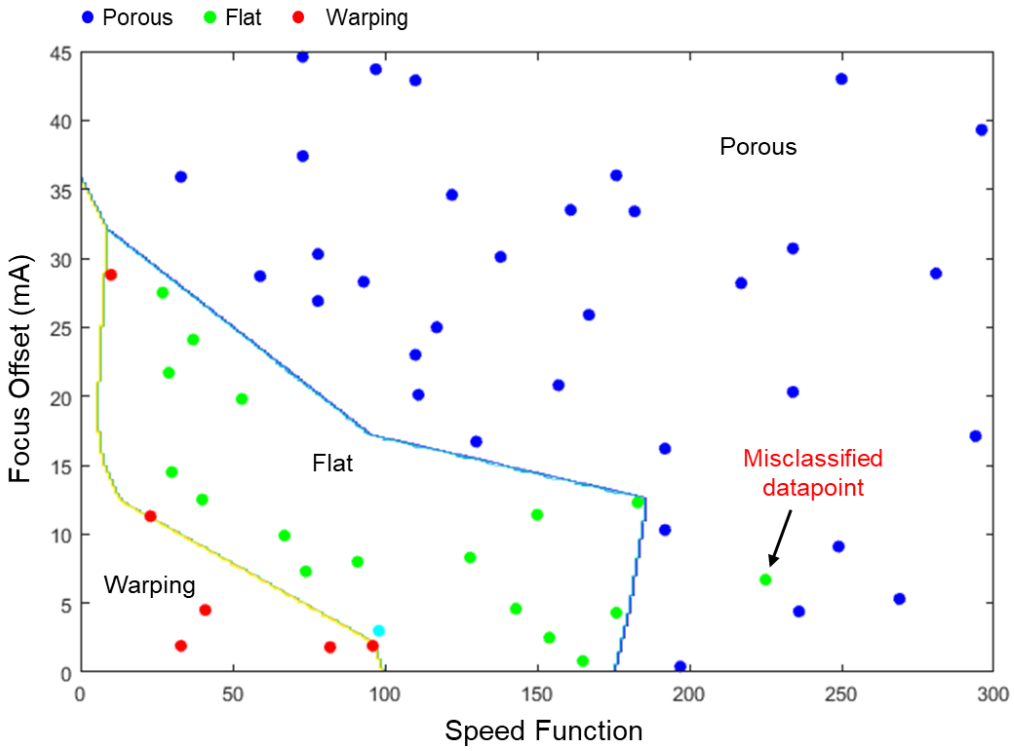

Figure 5.13 The decision boundary lines for surface condition classification divide the entire parameter space into three regions. The blue, green and red dots represent samples with porous, flat and warping surface conditions, respectively. Arcam's default parameter setting is labelled by a cyan dot.

The process window should be determined by three criteria, namely top build surface conditions, relative density and tensile properties, without which the outcome will be deficient. For example, a sample with high UTS and high relative density may have warped surface, while a sample with flat surface and high relative density may yield a low UTS, as demonstrated in our previous work for SS316L alloys in Chapter 4. Hence, an overlaid contour plot which integrates all the three criteria is synthesized in Figure 5.14.

The color-shaded regions represent the corresponding UTS values, while the dark blue lines with texts indicate the relative density values along the line. The lines in magenta are decision boundaries for surface condition classification, which embrace the same shape as shown in Figure 5.13. According to this informative plot, to print flat-surface Ti-6Al-4V samples with the threshold of UTS greater than 950 MPa and relative density larger than 99.5%, the optimal process window is ultimately narrowed down to the region enclosed by the bold red line. It should be noted that a relative density of $\geq$ 99.5% can also ensure an elongation to fracture higher than 10%, as discussed in section 5.2.

This process window is relatively wide. The process parameters recommended by Arcam just lie on the borderline of this optimal process window, as denoted by the cyan dot. The highest UTS predicted by this process window is ~ 5% higher than that from Arcam's default parameter setting (UTS ~ 951.7 MPa), which was also verified by experiments, where the sample with UTS ~ 999 MPa was included in the dataset. As the beam speed increases linearly with SF, the parameters used for this sample also suggest that ~ 87% faster printing speed could be achieved. It is known that the optimal process parameters for Ti-6Al-4V were determined by Arcam EBM using the conventional DoE method, which may lead to sub-optimal results. Therefore, this process map generated by ML is more informative, which assists in decision-making to select the process parameters that can produce parts with superior UTS and faster printing speed while meeting the minimum requirement for elongation.

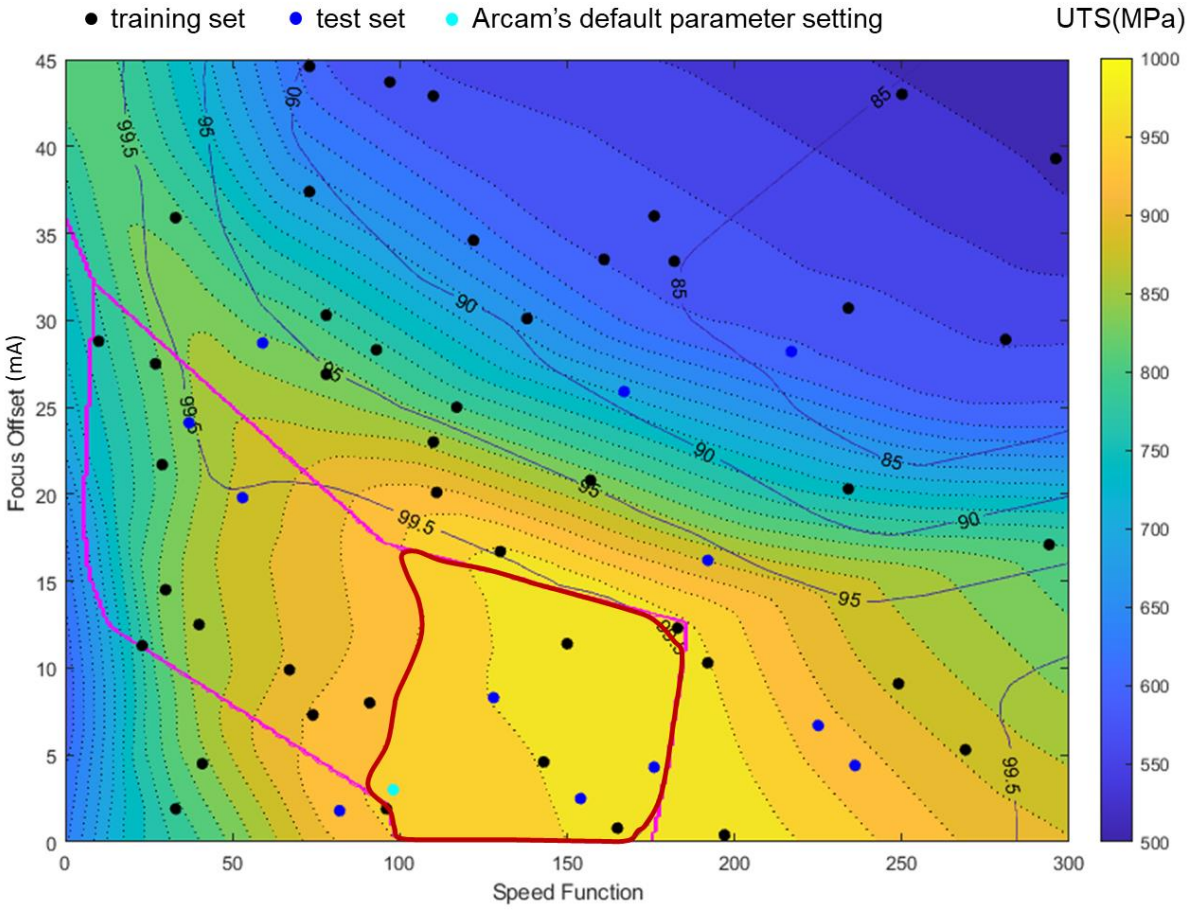

Figure 5.14 The overlaid contour plot reveals the process window for SEBM-processed Ti-6Al-4V alloy by integrating the criteria of top build surface condition, relative density and UTS. The region enclosed by the red line is the optimal process window. Arcam's default parameter setting is plotted in cyan.

5.3.2 Surface and Microstructure-Property Relationships

CNN can extract representative features from raw images while passing through convolutional layers and make predictions on the properties accordingly. It implies that CNN can help to create links from raw images by ruling out human bias with regard to domain knowledge in materials science and skills in hand-crafting features [201]. As the inputs here are surface images and pore microstructure images, CNN will be used for image-related tasks in this section.

5.3.2.1 Model Validation

Here, a 5-fold CV with a fixed random state was implemented to ensure fair comparison among different models.

Different input image sizes were investigated in order to determine the optimal value that could yield the best prediction. As the CNN model reads the image as an array of pixel values with the range of 0 to 255, they were normalized to the range of 0 to 1 for better convergence during training. Each image was labelled by the corresponding values such as UTS and relative density. The hyperparameters for training were the same as the previous MLP models. In addition, as the data size is small, data augmentation was employed to artificially enlarge the training set by random flipping and rotating to the range between ± 10° while preserving the labels. It should be noted that data augmentation was implemented on the fly during training instead of simply expanding the dataset before training. This is to ensure that our model could use new variations of data at each epoch in order to improve its generalization ability to data. Data augmentation was implemented only on the samples with the optimal image size. The inputs were top surface images and pore microstructure images, while the outputs were UTS and relative density. In each CNN model, only one input variable and one output were used. A matrix is constructed to compare the performance of using different types of input images and image sizes, as shown in Table 5.2.

Table 5.2 Effects of image sizes, types of images and data augmentation on the prediction of UTS and relative density with 5-fold CV. Data augmentation was only applied to the samples with the optimal image size.

Image size	Top surface images								Vertical midplane images	
	3D surface topography				Surface morphology				Pore microstructure	
	UTS		Relative density		UTS		Relative density		UTS	
	MAPE%	RMSE	MAPE%	RMSE	MAPE%	RMSE	MAPE%	RMSE	MAPE%	RMSE
128×128	3.86	40.55	0.72	1.08	2.22	21.73	0.60	0.79	3.38	36.56
128×128*	N.A.				2.97	31.81	0.54	0.72	3.99	42.61
64×64	2.47	25.31	0.67	0.92	2.28	23.50	0.96	1.36	3.95	43.23
64×64*	2.63	25.52	0.80	1.22	N.A.				N.A.	
32×32	2.80	28.83	0.92	1.33	2.93	35.18	1.06	1.64	4.93	54.22

* denotes that image augmentation is performed

The image size can affect model performance significantly. Due to the small number of images in the dataset, using a large image size can deteriorate the model performance and slow down the computation as too many features are fed into the model. Conversely, using a small image size may cause loss of important information, leading to the decline of model performance. The table above shows that the image size of 64 × 64 yields the best prediction results of UTS and relative density for 3D surface topography images. In contrast, the surface morphology and pore microstructure images could achieve the best performance with the size of 128 × 128. These results are expected, as 3D surface topography images contain the height information that is represented by color, hence a more compressed size is sufficient to yield decent prediction results. Likewise, the 1-channel surface morphology and pore microstructure images need a larger image size (namely a higher resolution) to provide enough information for the model to make good predictions. It should be noted that when the image used is oversized, the number of features involved increases exponentially, which would cause overfitting and deteriorate the performance. Data augmentation was implemented on the samples with the optimal image size. However, it did not improve model performance as expected.

The prediction accuracy can be further improved by multimodal learning. The underlying motivation is that datasets from different sources can provide complementary

information for each modality involved for a given learning task, thus yielding better performance than using a single modality [206].

The results listed in Table 5.3 show that multimodal learning can indeed boost performance. With multiple data sources and modalities, better prediction can be achieved than using numerical or image data alone. The lowest MAPE of 1.24% for UTS prediction is achieved by combining the process parameters and 3D surface topography images as input data, which could reduce the prediction error by ~ 37% and ~ 44% than using MLP and CNN alone, respectively.

Table 5.3 Comparison of prediction results using the single-modal deep learning models and the multimodal model.

MLP	**CNN**		**UTS**	
	Image types	Image size	MAPE(%)	RMSE
Process parameters	–	–	1.96	22.58
–	3D surface topography	64×64	2.47	25.31
–	Surface morphology	128×128	2.22	21.73
–	Pore microstructure	128×128	3.38	36.56
Process parameters	3D surface topography	64×64	1.24	14.93
	Surface morphology	128×128	1.31	14.77
	Pore microstructure	128×128	1.66	18.86
Relative density	3D surface topography	64×64	2.45	26.55
	Surface morphology	128×128	2.07	22.51

5.3.2.2 CNN Feature Visualization

One of the drawbacks for CNNs is their highly abstract features which lack interpretability. For example, a model was well trained to distinguish buses and cars correctly. However, in the worst-case scenario where all the bus pictures were taken during the daytime, the model's discriminative power may mainly come from the environment rather than the target. This may render bad performance if a bus picture taken at night is fed to the trained model to

make predictions. Hence, it is indispensable to understand the model's behavior and ensure that the model is paying attention to the correct features of the target.

There are three types of visualization techniques, namely activation maximization, saliency maps and class activation maps (CAM). Activation maximization [207] is an inverted process of CNN, which implies it generates the perfect input images for a given class. Saliency maps [207] can visualize the attention of a CNN model by telling the importance of each pixel for generating the class prediction. It could show which part of the image contributes to decision making. CAM [208] can generate heatmaps to visualize where the model is paying attention to in order to make a decision. It takes into account more spatial details than saliency maps. However, CAM requires a global-average-pooling layer in architecture which will change our original CNN model and can only visualize the final convolutional layer. Hence, a more advanced technique termed as gradient-weighted class activation maps (Grad-CAM) [209] was adopted. Here, the gradient of the output class with regards to each channel in the feature map of this layer was calculated. It was then global-average-pooled to obtain the weights of importance of each channel in the feature map. The weighted feature maps were represented by heatmaps.

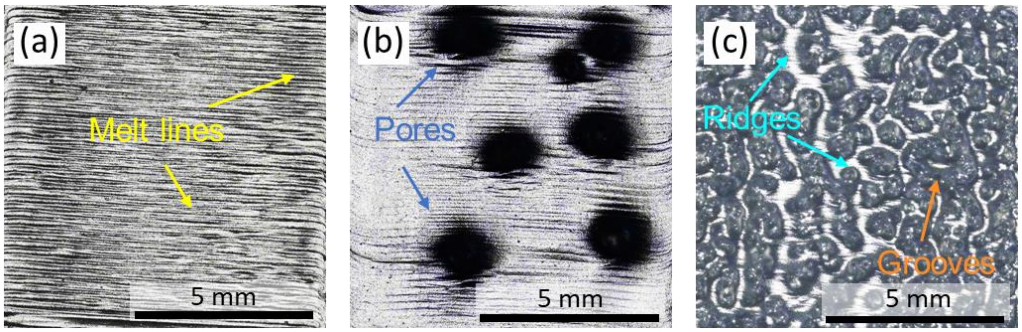

Figure 5.15 Name of the important features on surface morphology images. The images above correspond to (a) well-melted, (b) porous and (c) highly porous samples.

In this work, the last dense layer was visualized. As this is a regression task, the features that correspond to high and low output values are highlighted by Grad-CAM. Figure 5.15 illustrates the naming of the representative features of surface morphology images.

The representative results are shown in Table 5.4, which are arranged from high UTS to low UTS in order. The model weights were adopted from the trained model. The input image size was 128 × 128 pixel as it yielded the lowest MAPE of 2.22% for UTS prediction via 5-fold CV. The columns named Grad-CAM are heat maps that highlight the locations where the

CNN model was paying attention to make predictions. The columns named Overlay superimposed the heat maps with original input images for better visualization of the locations and features.

Table 5.4 Grad-CAM feature visualization of the last dense layer in our CNN model for surface morphology images. T stands for test data and P stands for prediction data for UTS. The original input images and the features that contribute to low and high UTS are visualized, respectively.

No.	UTS (MPa)		Original	Features contributing to low UTS		Features contributing to high UTS		
	T	P		Grad-CAM	Overlay	Grad-CAM	Overlay	
a	984	985	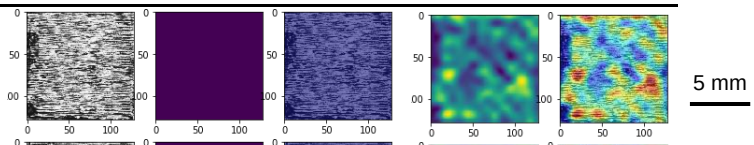					5 mm
b	935	949	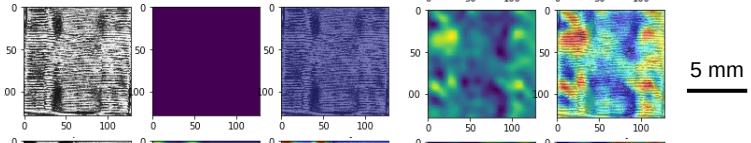					5 mm
c	954	934	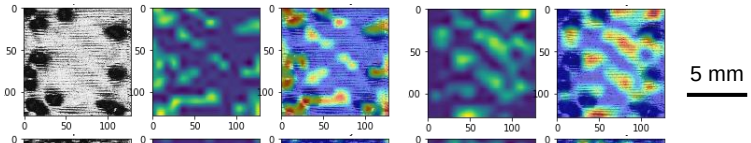					5 mm
d	897	917	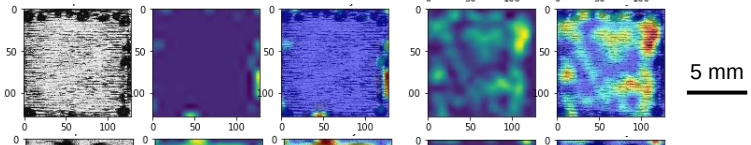					5 mm
e	834	814	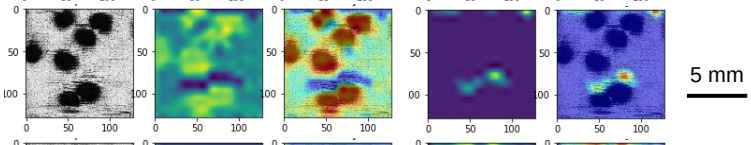					5 mm
f	781	764	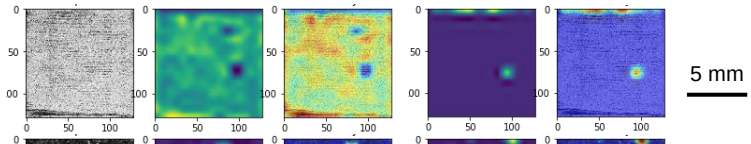					5 mm
g	702	695	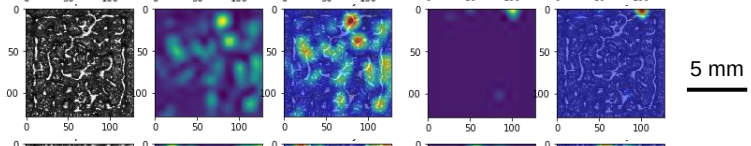					5 mm
h	639	648	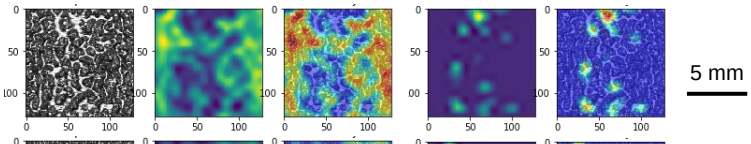					5 mm
i	579	594	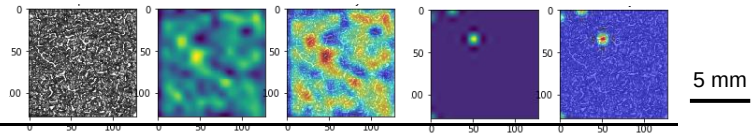					5 mm

From sample a to d, it shows that melt lines are captured as the feature contributing to high UTS, despite the slight warpages on the four corners for sample b and the presence of pores on the surface for sample c and d. Conversely, the flat surface with little melt lines has a relatively low UTS, as shown for sample f. In fact, its overly flat and shiny surface even contribute to low UTS. This observation is consistent with the fact that the presence of melt lines indicates the level of line energy density. An excessively high energy density produces obscure melt tracks as they are re-melted a few times, while an insufficient energy density produces discontinuous melt tracks due to balling effects [210] during printing. Hence the level of line energy density can be reflected by the melt lines on the top build layer of the sample. In sample c and e, Grad-CAM captures pores as the feature that significantly contributes to low UTS, which agrees with the well-known fact that pores can negatively affect tensile properties. Sample g to i are very porous due to the excessively low input energy density. Hence, both grooves and ridges are highlighted by Grad-CAM as indicators of porous surfaces that lead to very low UTS.

In summary, the observations on the results obtained by Grad-CAM prove that our trained CNN model could capture reasonable features when making predictions for UTS.

5.3.3 Process-Surface and Microstructure Relationships

5.3.3.1 Latent Space Representation

Inspired by the work of Banko et al. [211], in this section, the interplays between the two process parameters and the surface/microstructure images can be visualized with the aid of VAE and principal component analysis (PCA). The continuous evolution of the image morphologies can also be illustrated. With this visualization tool, the trends of the morphology evolution from the real experiments will be compared with the images generated by cGAN in the next sub-section.

The full dataset (i.e. 56 samples for surface morphology and pore microstructure images, 23 samples for SEM α/β microstructure images) were used for generating the latent space representation. The latent space representation of the surface morphology images is shown in Figure 5.16. Overall, the images with similar morphologies are well clustered but with a small gap in the middle, which implies that the latent points in this gap cannot generate meaningful

contents. However, this gap is negligible, and the trends of the surface morphology evolution with the variation of process parameters are clearly illustrated. The following discussions are based on Figure 5.16 (a). Fine bright ridges with grooves are formed in the bottom-left region when SF is > 200 and FO is > 30 mA. When SF is increased to 100 - 200, the ridges become larger, as shown in the middle-left region of the diagram. In the top-left region, large ridges are formed when FO is reduced to 20 - 30 mA. The middle-top region shows that the ridges and grooves have disappeared, but large pores are produced when FO is 10 - 20 mA. Flat surfaces are formed when SF is < 50 and FO is 10 - 20 mA, or when SF is 100 - 150 and FO is < 5 mA, as shown in the middle-right and middle-bottom regions. However, when SF is < 100 and FO is < 5 mA, the dents and elevations are visible as seen in the middle region of the diagram. It is observed that flat surfaces can be obtained when SF and FO are balanced, by using either low SF and medium FO or medium SF and low FO. This suggests a relatively wide process window, as proven by Figure 5.14. It is found that FO is more influential on the surface morphologies, as distinctively different clusters representing different levels of FO are formed compared to SF. This is consistent with the finding in the work of Abdeen et al. [123], where they also reported that FO played a more significant role in determining the surface morphologies as compared to beam current and beam speed.

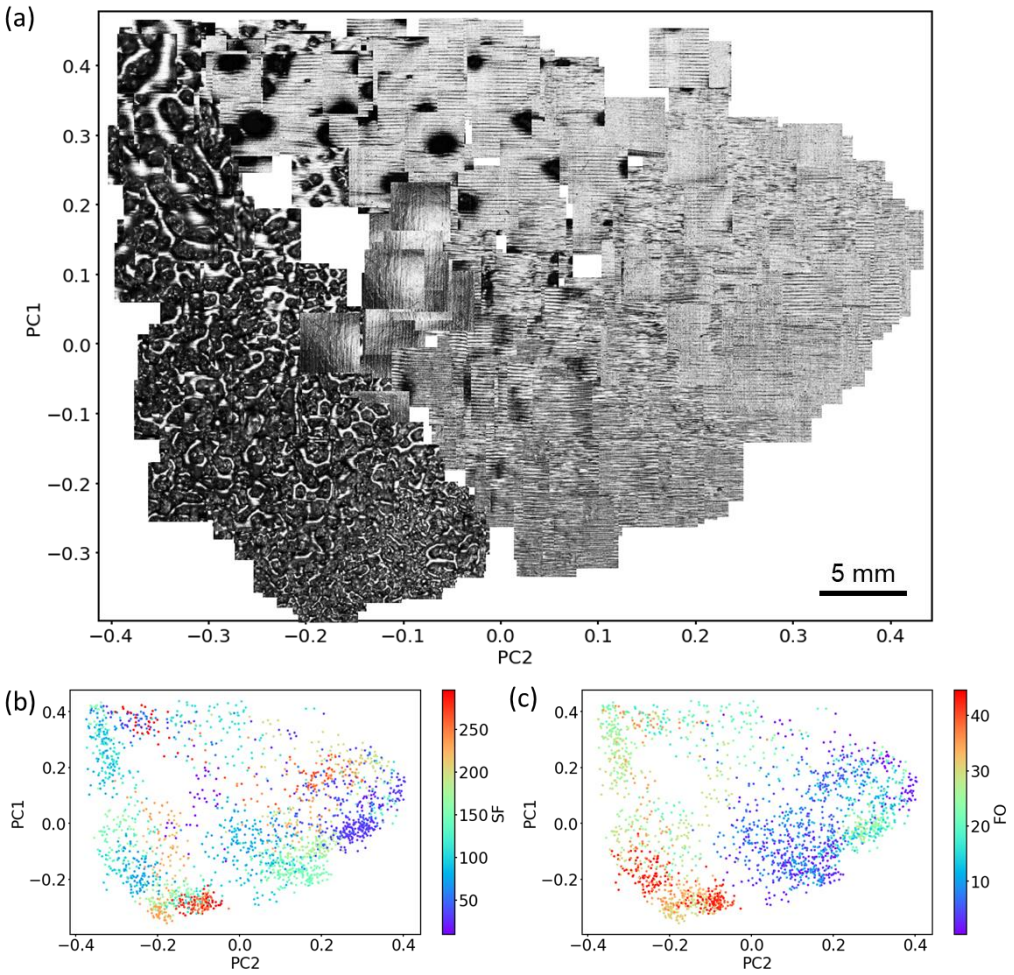

Figure 5.16 Latent space representation of (a) the surface morphology images and their corresponding process parameters, including (b) speed function (SF) and (c) focus offset (FO). The two axes are the two principal components, as denoted by PC.

The latent space representation for pore microstructure images is shown in Figure 5.17. The samples with visible pores are near-uniformly scattered over the latent space, while the samples with high relative density are densely clustered in the mid-left region as indicated. This phenomenon is expected. The images of the fully dense samples are purely white with no distinguishable features, hence the VAE model recognizes them as the same image and clusters them in a small region. Although dense clustering is not preferred for latent space representation, the trends for pore microstructure evolution can still be clearly identified. The discontinuous and uniformly scattered pores with typical lack-of-fusion interlayer defects are formed when SF is > 200 and FO is > 30 mA, as shown in the top-middle region. As SF is reduced to 100 - 200, the pores grow larger (see middle region). When FO is also decreased to 20 - 30 mA, as seen in the bottom-right region, the pores become interconnected and have chimney shape along the build direction. However, the effects of SF cannot be observed in the

mid-left region, where full-density samples are densely clustered (see Figure 5.17 (b)). We can only tell that one necessary condition to achieve high density is when FO is below 5 mA (see Figure 5.17 (c)).

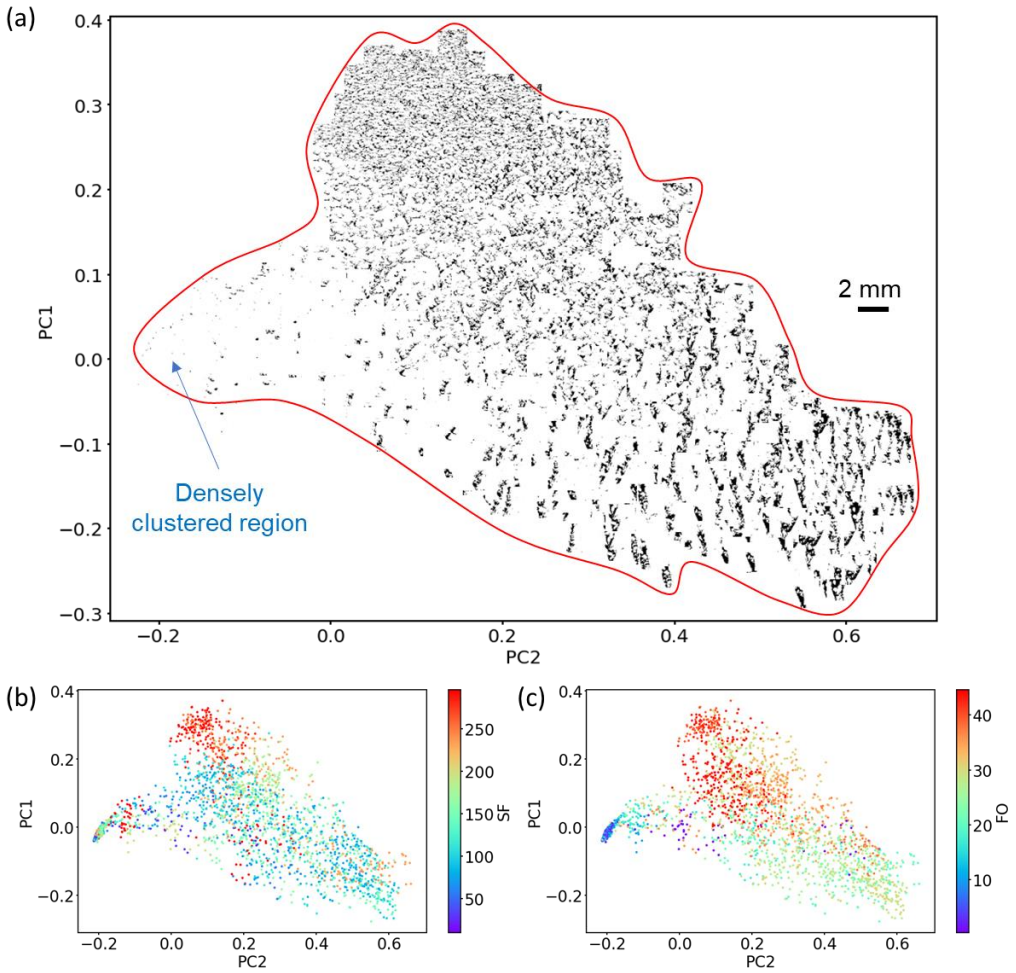

Figure 5.17 Latent space representation of (a) pore microstructure images and their corresponding process parameters, including (b) speed function (SF) and (c) focus offset (FO). The two axes are the two principal components, as denoted by PC. The boundary of the images clustered in (a) is outlined by red line for the ease of illustration, as the background and the samples with high relative density are both white.

Figure 5.18 shows the latent space representation of the Ti-6Al-4V alloy SEM α/β microstructure images and the corresponding process parameters. The α/β microstructure images cluster well based on the similarity of the grain morphologies, which are α and β phases. The effects of SF on the α/β microstructure morphology can be clearly identified in Figure 5.18 (b). Low SF produces α/β microstructures with coarse α/β phases, while high SF produces with colony and basket-weave-like α/β phases or even fine needle-like α′ martensite phases. Of particular note is that when SF is ≤ 40, the α laths become significantly coarsened. This trend

is expected as a higher energy density and longer melting time corresponding to a low SF can coarsen the α/β microstructure of Ti-6Al-4V alloys. Conversely, a high SF results in high cooling rate, which leads to phase refinement. Nevertheless, the effects of the FO shown in Figure 5.18 (c) are not salient, as the points that represent different levels of FO are scattered over the latent space. Prisco et al. [212] have also found that FO does not have significant effects on the α/β microstructure of SEBM-built Ti-6Al-4V alloys, as the change in FO is not enough to obtain differences in cooling rates which could generate phases and grains of significantly different sizes.

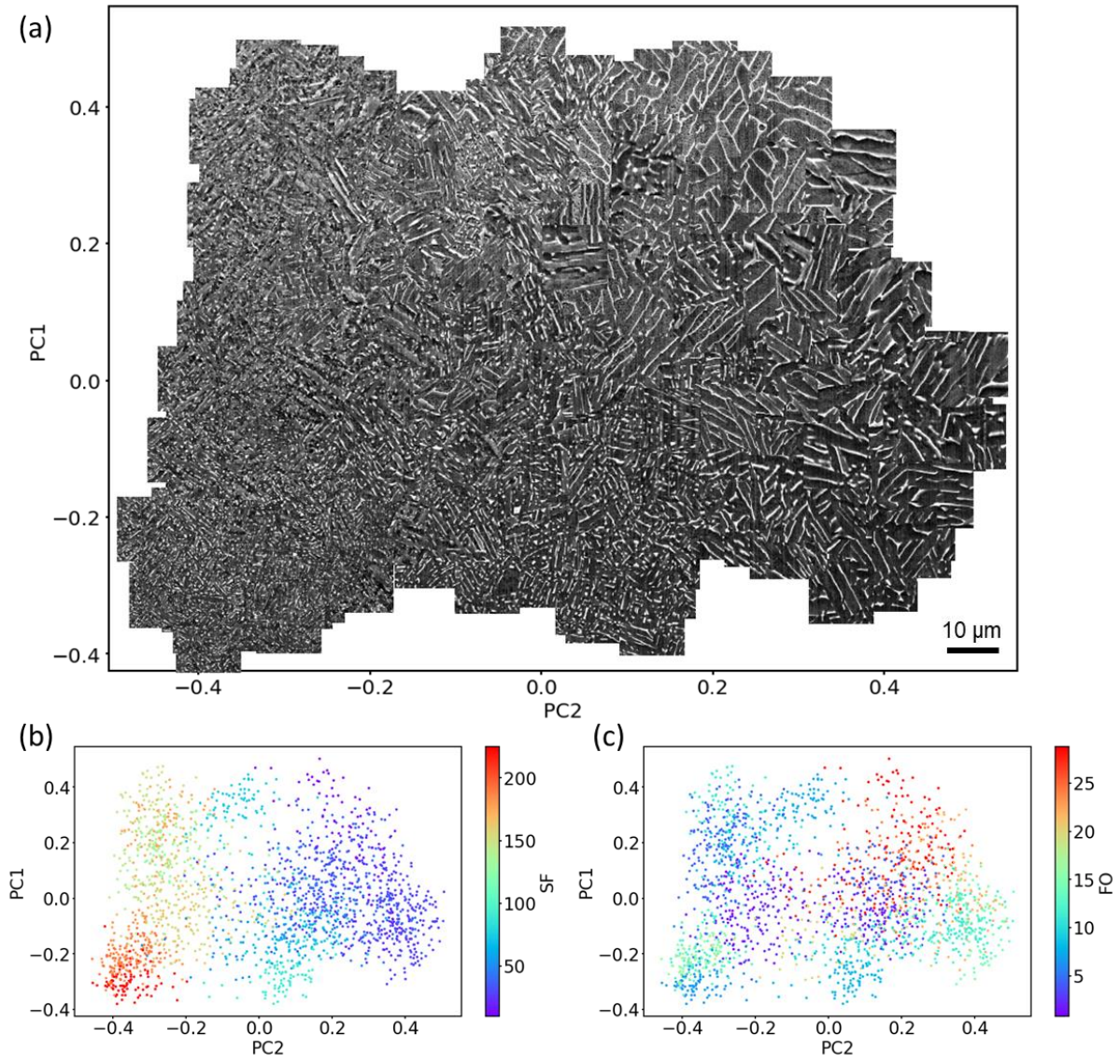

Figure 5.18 Latent space representation of (a) SEM α/β microstructure images and their corresponding process parameters, including (b) speed function (SF) and (c) focus offset (FO). The two axes are the two principal components, as denoted by PC.

5.3.3.2 Prediction of Surface and Microstructure Images from Process Parameters

In this section, cGAN model was trained to reconstruct surface and microstructure (i.e. as-polished pore microstructure and as-etched SEM α/β microstructure) images from the process parameters. The prediction results of surface morphology, as well as pore microstructure images, are compiled in Table 5.5. The 6 test images were from experimental results, but they were removed from dataset before training. Therefore, our cGAN model has never seen the test images, and they can serve as an unbiased evaluation of the model's performance. It should be noted that the sample fabricated under Arcam's default parameter setting, namely sample No. 7, was also included to test the predictive power of the model.

Overall, our cGAN model can well predict the results under different process parameter settings. Although cGAN was not intended to reproduce the exact copy of the original test images, our model could reconstruct images with the feature sizes, shapes and even contrast variations that are almost indistinguishable from their test counterparts. High-quality prediction results are attained for surface morphology (see Table 5.5 (a)) and pore microstructure images (Table 5.5 (b)). The features such as ridges, warpages and clear melt lines can be clearly seen for surface morphology images. The only exception is sample No. 5, which did not reproduce sufficient amount of pores along the borders. The similar problem occurred in the same sample under pore microstructure images, which was supposed to be porous instead of being fully dense. One possible reason is due to the unbalanced training data, where this type of morphologies is the minority as compared to others. Hence, the model could not successfully capture these features.

Table 5.5 Comparison of predicted images and test images of (a) surface morphology and (b) pore microstructure images under different process parameter settings.

	No. 1		No. 2		No. 3		No. 4		No. 5		No. 6		No. 7		
	SF	FO	SF	FO	SF	FO	SF	FO	SF	FO	SF	FO	SF	FO	
	73	37.4	234	20.3	91	8	161	33.5	197	0.4	33	1.9	98	3	
(a) Predict	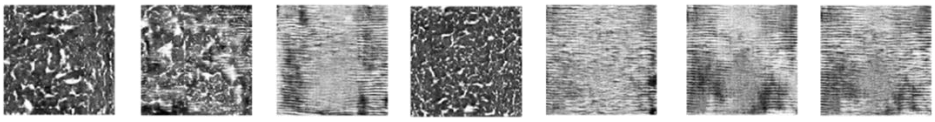														5 mm
Test	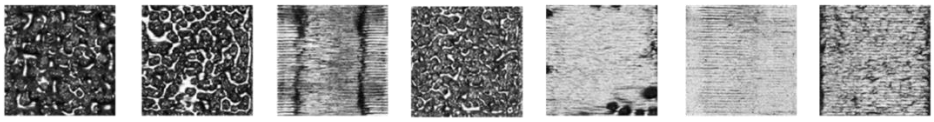														5 mm
(b) Predict	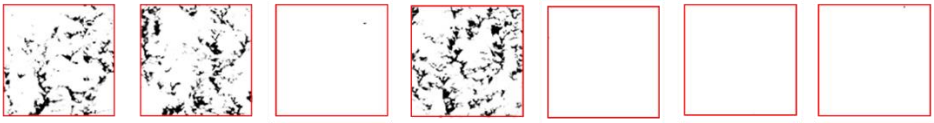														2 mm
Test	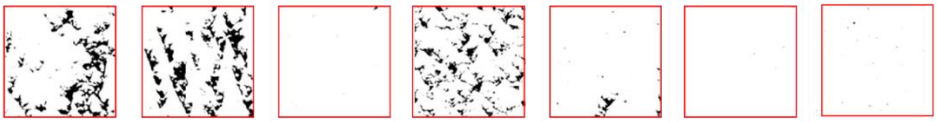														2 mm

By mapping the generated images over the entire parameter space, a representation with the concept similar to structure zone diagram [213] can be obtained. For ease of comparison, the original images of the 56 samples are plotted at positions according to their process parameters, as shown in Figure 5.19 (a) for surface morphology images and Figure 5.20 (a) for pore microstructure images. The generated images occupy the entire parameter space where the image patches of 128 × 128 pixels overlay and appear to be a continuous diagram, as shown in Figure 5.19 (b) and Figure 5.20 (b), respectively. FO is more significant in determining the surface morphology, as shown by the partition line with a low inclination angle of ~ 15° in Figure 5.19 (b). The SF and FO both play important roles in the formation of pore microstructure, as illustrated by the partition line with a high inclination angle of ~ 30° in Figure 5.20 (b). The observations here are consistent with the finding discussed in the VAE latent space representation.

The corresponding positions of the 6 test samples as well as Arcam's sample are highlighted by boxes. With this diagram, we can visualize the evolution of surface and pore microstructure images as the two process parameters vary consecutively. The general trends of the surface morphology and pore microstructure are consistent with the top surface classifications and relative density values depicted in the overlaid plot in Figure 5.14.

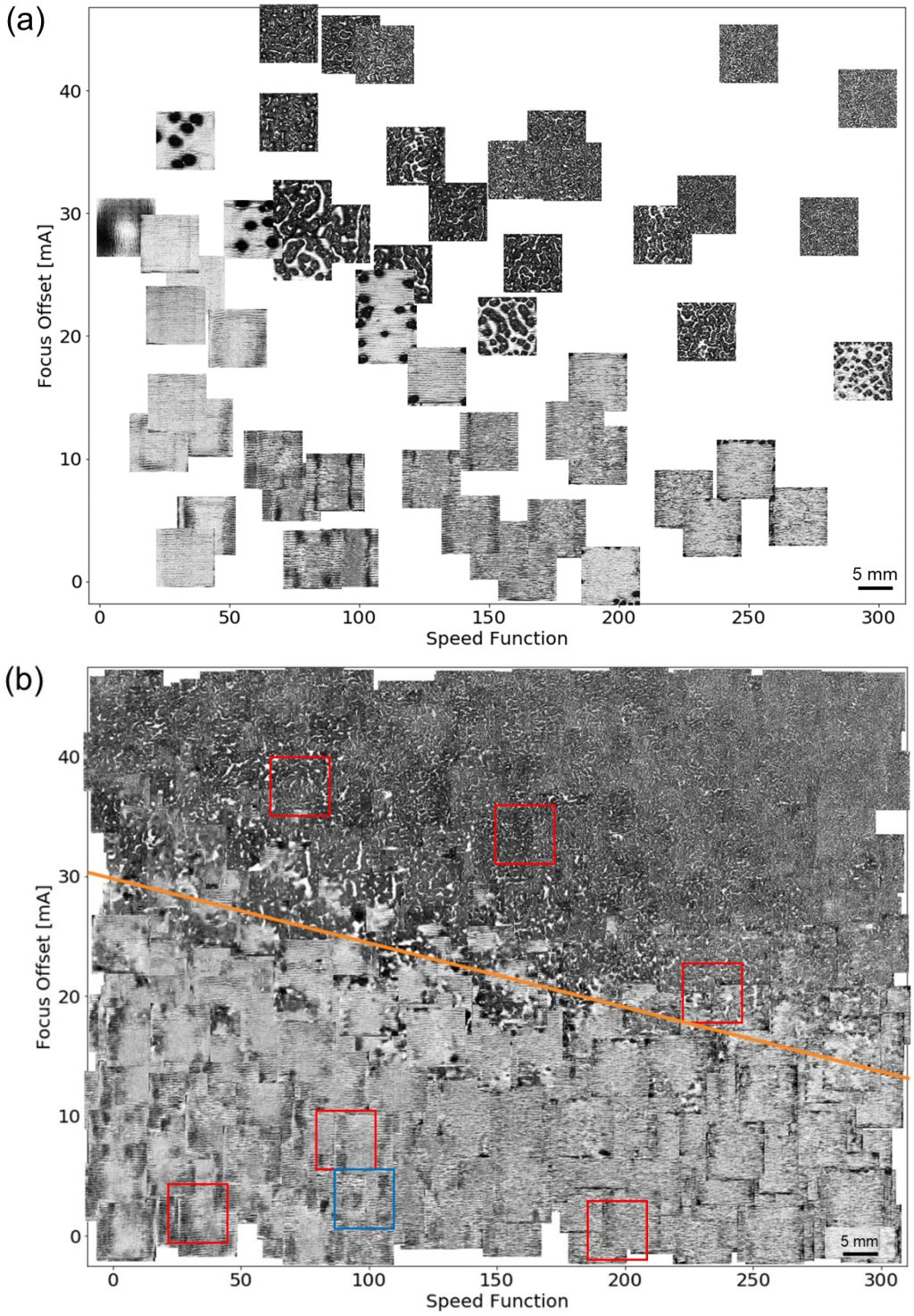

Figure 5.19 (a) Plot of the real surface morphology images of the 56 samples according to their process parameters. (b) The representation of the surface morphology images generated by cGAN model over the entire process parameter space. The positions of the 6 test samples (in red boxes) and Arcam's sample (in blue box) are highlighted. A yellow partition line can roughly divide the diagram into two types of surface morphology images.

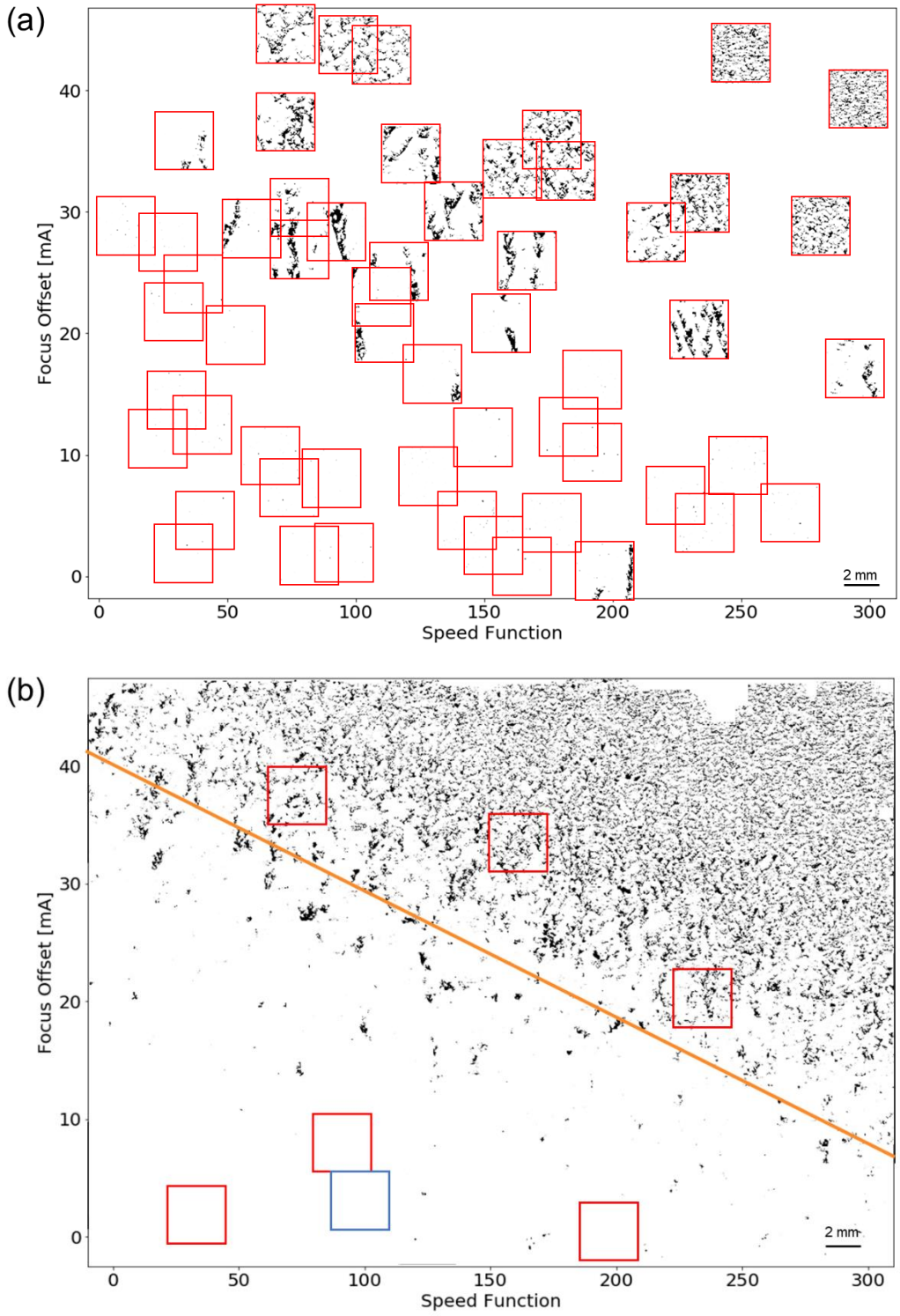

Figure 5.20 (a) Plot of the real pore microstructure images of the 56 samples according to their process parameters. (b) The representation of the pore microstructure images generated by cGAN model over the entire process parameter space. The positions of the 6 test samples (in red boxes) and Arcam's sample (in blue box) are highlighted. A yellow partition line can roughly divide the diagram into two types of pore microstructure images.

For SEM α/β microstructure reconstruction, the 3 test images were removed from dataset before training. The cGAN prediction results and test samples are shown in Table 5.6.

The samples fabricated under Arcam's default process parameters (i.e. sample b) are also included in this synopsis. Overall, the cGAN model could reproduce the α/β microstructure images that resemble their test image counterparts in terms of the size and morphology of the α and β phases. The predicted α/β microstructures are almost indistinguishable from that of the test samples. However, in sample c and d, the rod-like β phases are curved instead of being mostly straight. The reason accounting for the discrepancies from the real images is unclear. A fine-tuning of the hyperparameters in cGAN may improve the results.

The plot of the original SEM α/β microstructure images of the 23 samples that correspond to their process parameters is shown in Figure 5.21 (a). The 23 samples with full density can only cover a limited area over the entire parameter space. Hence, a boundary line that delineates the space allowed to generate the micrographs is plotted. As 9 samples are determined to fall on the border of this space, a simple polynomial regression with 6 degrees of freedom was used to smoothly connect the 9 points in order to plot the boundary line. It is not reasonable to generate micrographs in the region outside the boundary line as it produces porous samples. Based on this rationale, the representation of the micrograph diagram is shown in Figure 5.21 (b). The morphologies of the reproduced α/β microstructures are consistent with the real images. However, discrepancies exist when SF is smaller than 40, where the rod-like β phases are curved, as mentioned earlier. The FO has negligible influence on the α/β microstructure morphology, while SF is much more significant to affect the size and shape of the grains, which is in good agreement with the observation in VAE latent space representation.

Table 5.6 Comparison of predicted and test images of SEM α/β microstructures under different process parameter settings.

	SEM α/β microstructure images	SF	FO	
a	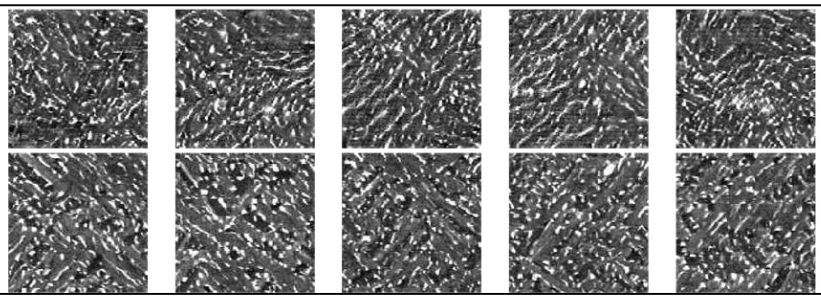	183	12.3	10 μm
b	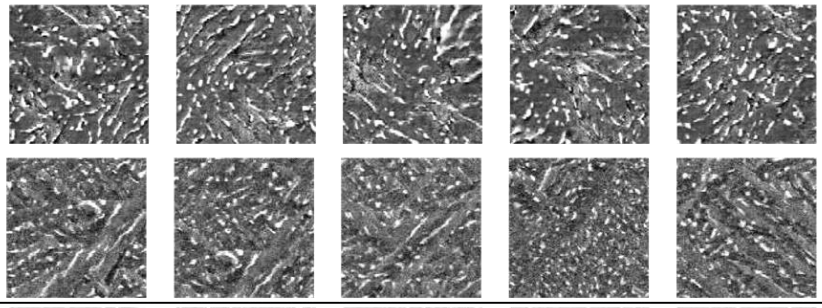	98	3	10 μm
c	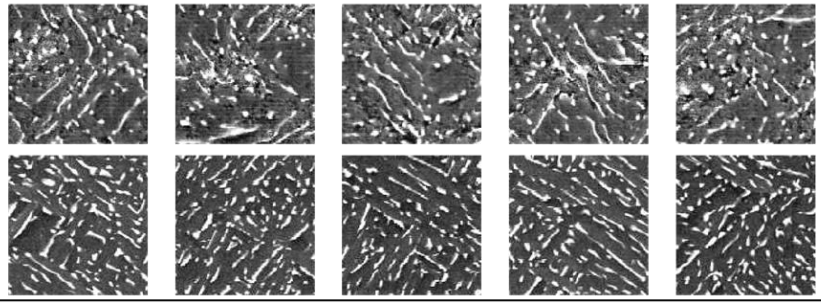	91	8	10 μm
d	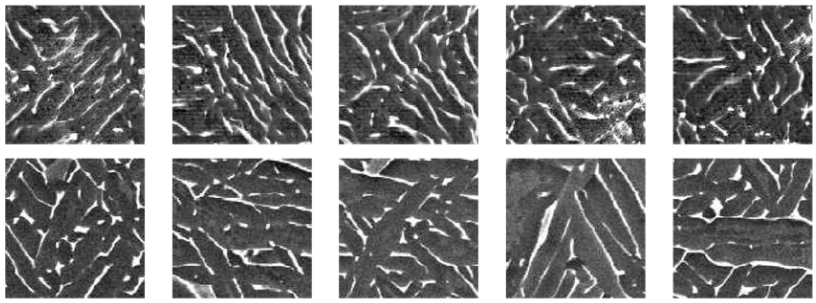	30	14.5	10 μm

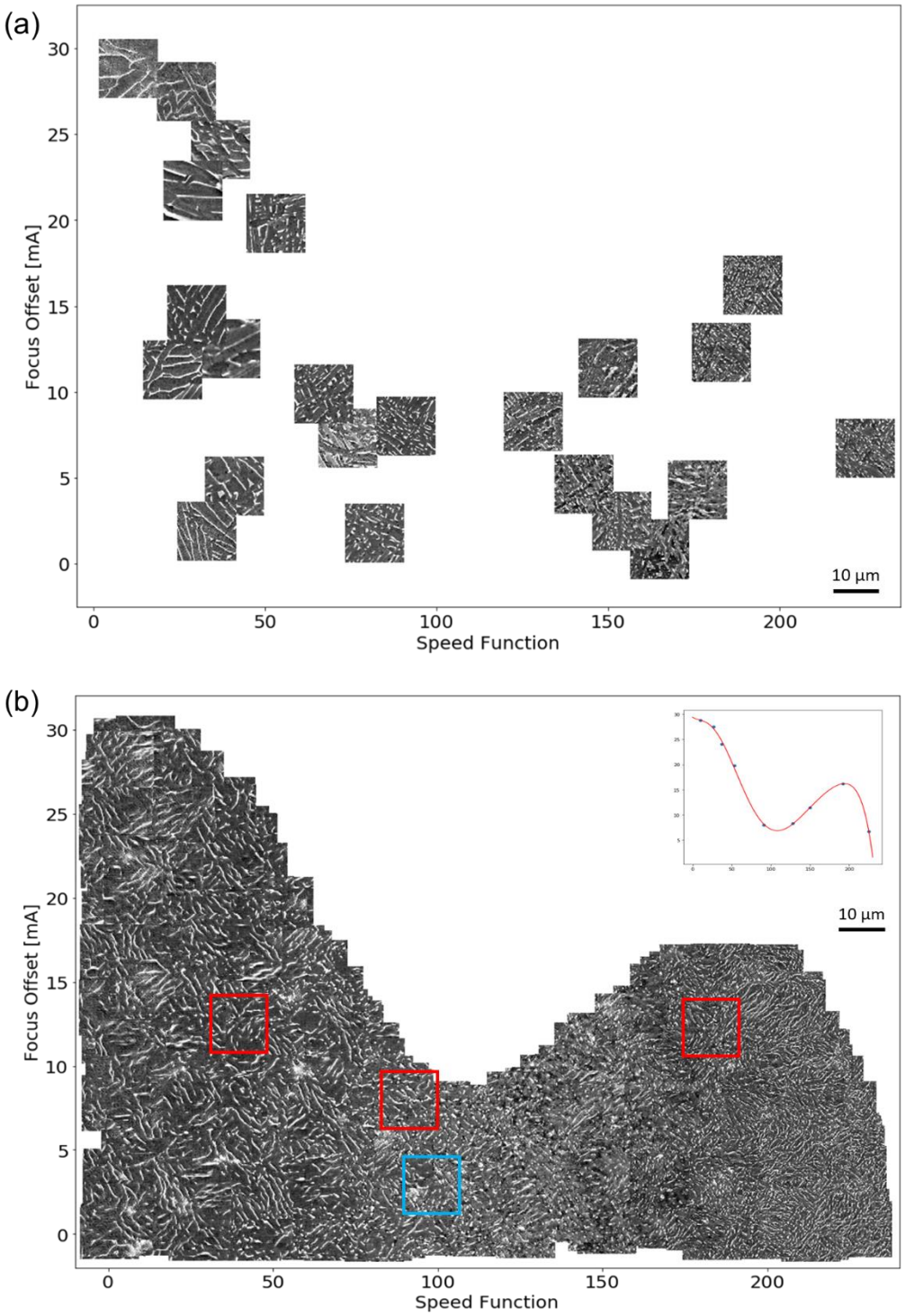

Figure 5.21 (a) Plot of the real SEM α/β microstructure images of the 23 samples according to their process parameters. (b) The representation of the α/β microstructure images generated by cGAN model over the constrained process parameter space. The inset shows the boundary line that constrains the space where the micrographs can be generated. The positions of the 3 test samples (in red boxes) and Arcam's sample (in blue box) are highlighted.

5.4 Conclusions

In this work, a ML method was employed to optimize the process parameters (i.e. SF and FO) for SEBM processing of Ti-6Al-4V and establish the complicated tetrahedral framework to map the PMP relationships with high accuracy, where top build surface served as a medium to correlate the relationships.

A random search technique was adopted to generate 56 different sets of process parameters over the entire parameter space to improve the efficiency and accuracy of finding the process window. MLP outperformed traditional ML methods to predict UTS and relative density from process parameters with 5-fold CV. Considering high UTS (≥ 950 MPa), high relative density (≥ 99.5%) and flat top build surface, an overlaid contour plot was constructed to reveal the relatively wide optimal process window of SEBM-processed Ti-6Al-4V alloys. Arcam's default process parameters merely lie on the border of the process window. The sample fabricated within the predicted process window showed a ~ 5% increase in UTS and ~ 87% increase in printing speed as compared to the Arcam's default parameter setting.

CNN was used to predict tensile properties from top surface images and vertical midplane pore microstructure images. A low MAPE of 2.22% for UTS and 0.54% for relative density could be achieved by using surface morphology images of 128 × 128 pixels. A more powerful multimodal learning method that combined process parameters and 3D surface topography images could reduce the MAPE of UTS prediction to 1.24%. Grad-CAM was applied to visualize the last dense layer of the CNN model. The surfaces with clear melt lines led to a high UTS while the surfaces with obscure melt lines or with pores, grooves and ridges led to low UTS. These observations are consistent with experimental results, proving that our CNN model paid attention to the correct features to make predictions. Using VAE, the interplays of the process parameters, top surface images, pore microstructure images and SEM α/β microstructure images could be visualized by latent space representation. The images with similar morphologies were clustered. Overall, FO is a more significant factor for top build surface morphology, while SF is more influential for the α/β microstructure morphology. SF and FO are both important for determining the pore microstructure. cGAN was adopted to predict surface morphology, pore microstructure and α/β microstructure images from process parameters. The evolutions of morphology were mapped over the entire parameter space for different types of images. The trends are consistent with the observations from the latent space

representation by VAE. The reconstructed images well resemble the real test images that were not previously seen by our model.

Chapter 6 Process Parameter Optimization for Stainless Steel 316L Using Transfer Learning

TL learning is implemented for SS316L with only 24 data points to assess the generalization ability of the ML methodology applied for Ti-6Al-4V. This chapter starts with the investigation of the optimal TL scheme (i.e. weight initialization and feature extraction) for predicting relative density, top surface condition and microhardness. Ti-6Al-4V data is used as a case study to prove the concept of using microhardness as a more economical alternative to predict mechanical properties. Next, the process map for SS316L is constructed and compared with the standalone ML model (a.k.a. without implementing TL). Finally, the results are evaluated with those obtained by DoE.

6.1 Introduction

Our ML models for SEBM-built Ti-6Al-4V alloy can achieve high performance in prediction of the optimal process window. However, there might be two concerns regarding this methodology: firstly, its generalization ability, i.e. whether the models that perform well for this material can also work for a different material with dissimilar physical, chemical and mechanical properties; secondly, its efficiency, i.e. whether the same substantial and expensive data collection steps need to be repeated in order to find the process window for this new material. As mentioned in section 3.7.2, the TL technique can transfer the knowledge learned from the previous source tasks to a new target task for better predictions and with a smaller dataset. To address the above two concerns, TL was implemented by using the trained weights from the Ti-6Al-4V baseline models to SS316L with only 24 data points.

6.2 Sample Fabrication and Data Collection

SS316L samples were fabricated by SEBM using coarse powders as investigated in Chapter 4. A total of 24 sets of different parameter combinations were generated randomly to cover the full space of SF and FO, as shown in Figure 6.1. The other process parameters remained the same as for Ti-6Al-4V fabrication. As it is costly to fabricate and conduct massive

tensile testing, we intended to explore a cheaper alternative (i.e. microhardness testing) to find the process window for SS316L alloys. Here, only 24 cubes of 10 × 10 × 10 mm^3 were fabricated in one build to conduct density measurement, surface condition examination and microhardness testing. The layout of the build is schematically illustrated in Figure 6.2. The data collection of relative density and top surface condition classes followed the same procedures for Ti-6Al-4V samples. Microhardness testing was performed on as-polished mirror-like surfaces along the vertical midplane of the samples. It should be noted that only the samples with a relative density of ≥ 99% were indented, as it is not meaningful to measure the microhardness of porous samples. The full dataset for SS316L can be found in Appendix F.

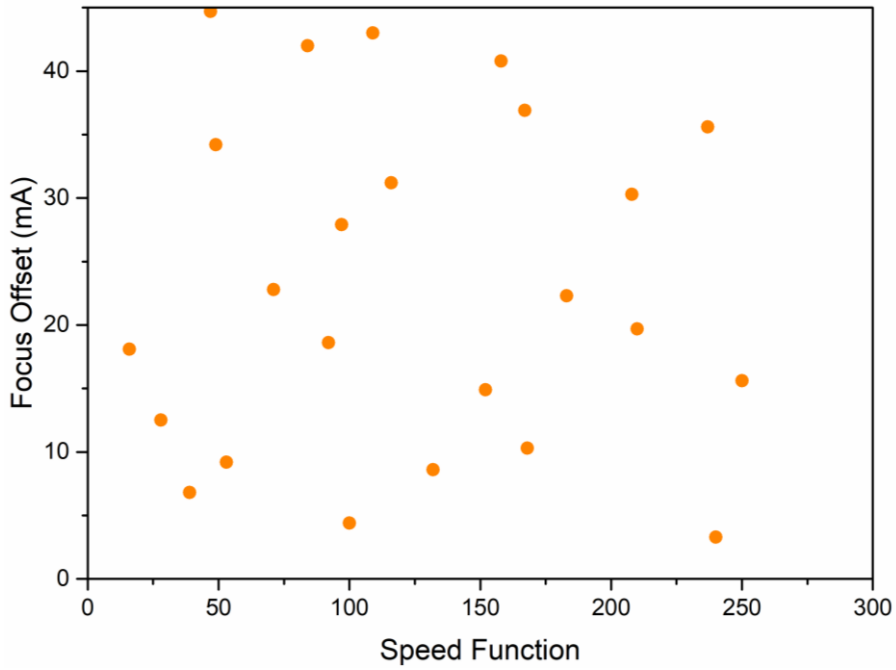

Figure 6.1 Process parameters generated by the random search method for printing SS316L samples using SEBM.

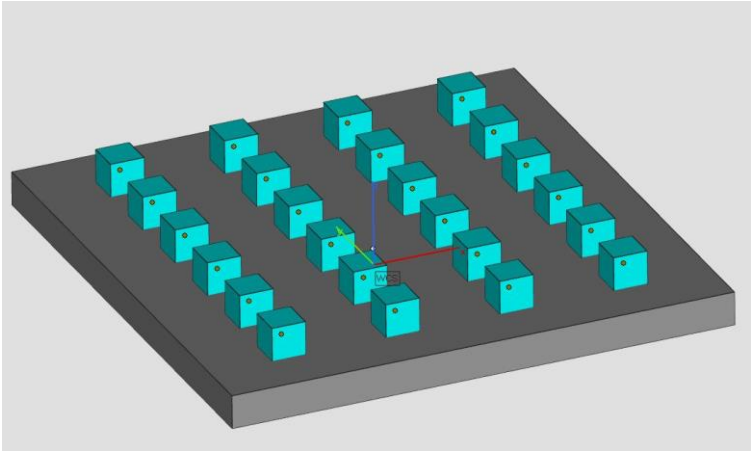

Figure 6.2 Schematic layout of the SEBM-built SS316L samples fabricated for this work.

6.3 Results and Discussion

6.3.1 Transfer Learning Scheme Selection and Model Validation

There are two main approaches to implement TL, namely weight initialization and feature extraction. In the weight initialization scheme, the entire weights of a pre-trained network model are used as the starting point for the training process, which are subsequently adapted to fit the dataset of a new problem. This scheme is useful especially when the first related problem is associated with a much larger labelled dataset than the new problem, and the similarity in the structure of the two problems is high. Feature extraction scheme keeps the first one or more layers fixed, where the unchangeable weights in these layers act as feature extractors. Only the weights in the unfixed layers are fine-tuned to fit the dataset of the new problem. The same MLP architectures, hyperparameters and the corresponding trained weights in the Ti-6Al-4V setting were applied for the new tasks in the SS316L setting.

The standalone model refers to the model that is trained solely based on the SS316L dataset without implementing TL. To compare with the performance of TL using different schemes, the value f refers to the number of the hidden layers that remained fixed during training. Fixing specific layers is achievable, thanks to the fact that the architecture of neural networks is highly configurable. Here, f=0 means that the entire weights were adapted for the new tasks (weight initialization scheme); f=2 means the two hidden layers are fixed and only the output layer of the model was adapted during the training (full feature extractor scheme). Due to the stochastic nature of neural networks, average performance across multiple runs is evaluated to ensure the observed behavior is real instead of a statistical fluke [214]. Here, 20 runs were repeated for each scheme. The scheme that yielded the best performance was adopted for process window prediction.

The performance for the relative density prediction using difference schemes for both training set and test set is summarized in the box plot, as shown in Figure 6.3. The box represents the middle 50% data distribution and the yellow line represents the median. The circles indicate outliers. As compared to the standalone model, the TL (f=0) model shows improvements in terms of the average and the stability of the performance and for both training and test set. The TL (f=2) has the worst performance, which shows severe deterioration in the

median despite its lower variance. Hence, it is concluded that the weight initialization scheme (f=0) can achieve better performance than the full feature extraction scheme (f=2).

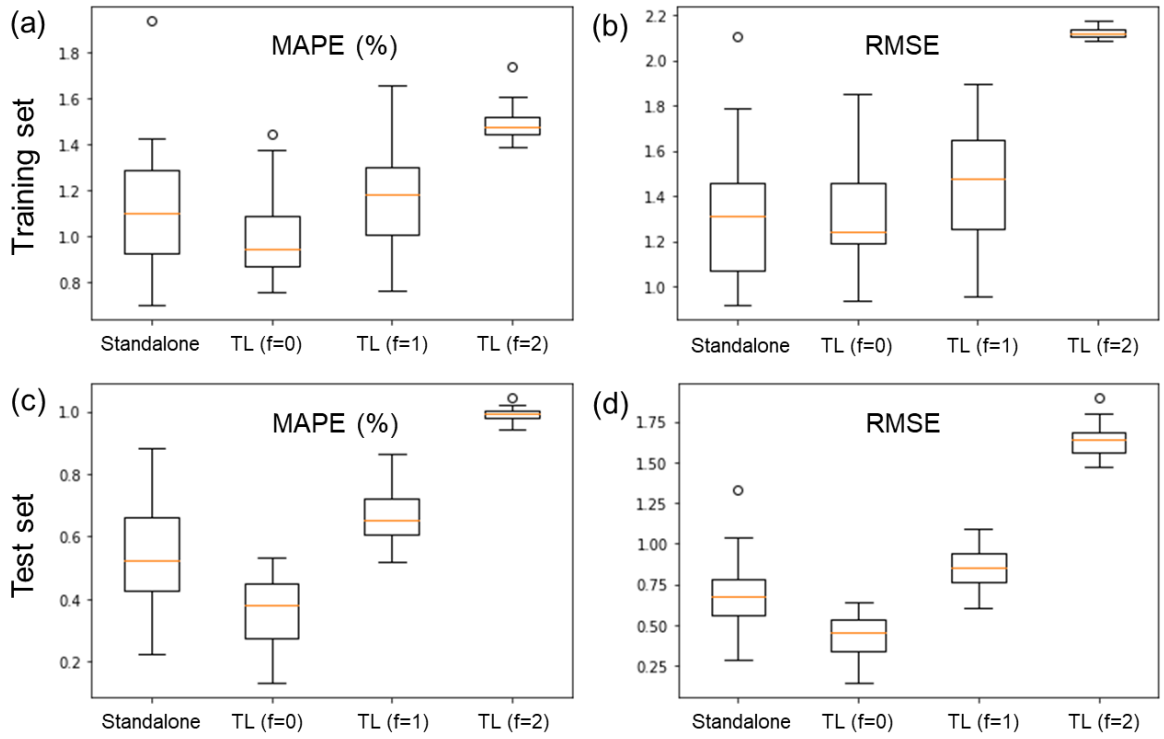

Figure 6.3 Box plot for the density prediction using different schemes. The observed behavior of the training set is measured by (a) MAPE and (b) RMSE, while the test set is also measured by (c) MAPE and (d) RMSE.

The 3D surface plot for the standalone model and TL (f=0) model is shown in Figure 6.4. Two different perspectives are used so that a more holistic view is provided. Overall, the 3D surface plot with TL technique can fit the data better than the standalone model, as most of the data points far from the surface in Figure 6.4 (a) are well fitted or even embedded in the 3D surface plotted in Figure 6.4 (b).

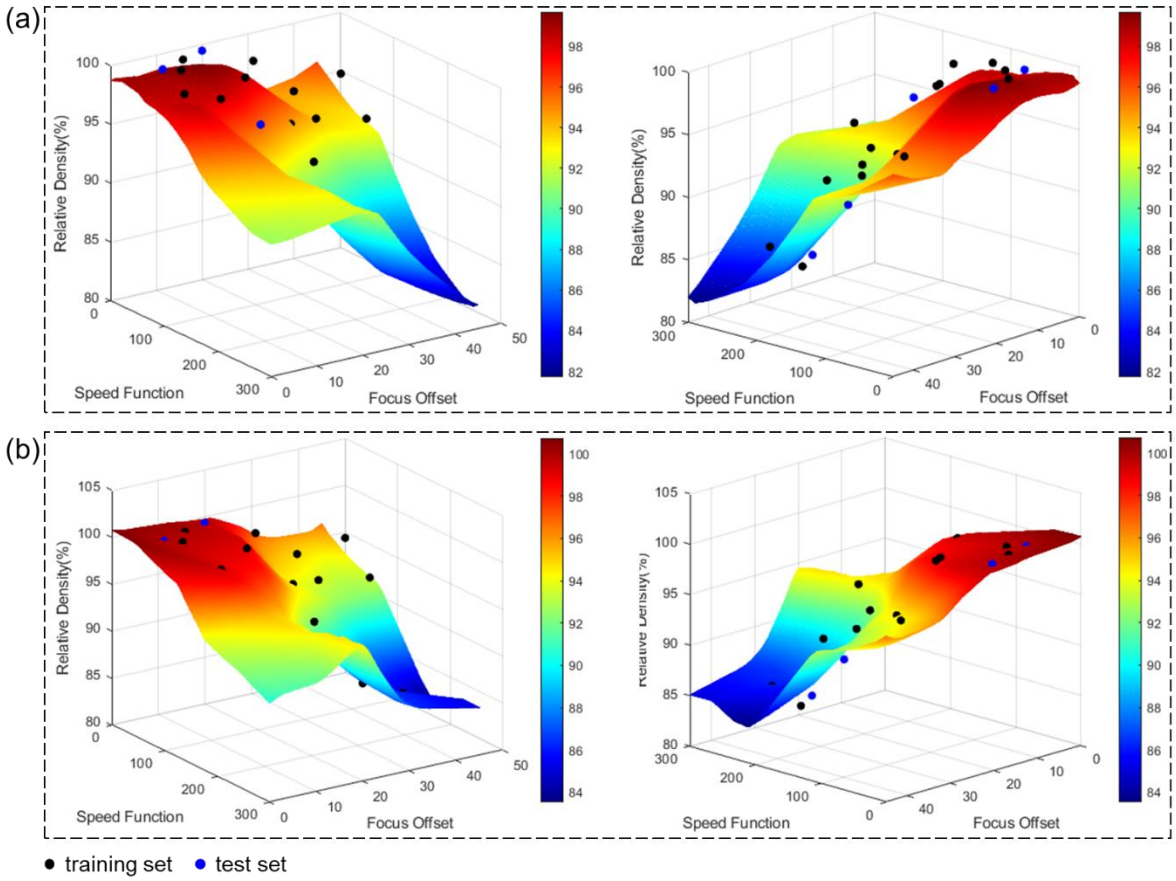

Figure 6.4 Two different perspectives of the 3D surface plot for the relative density prediction using (a) the standalone model and (b) the transfer learning model (f=0).

The results for top surface condition classification using different schemes are shown in Figure 6.5. Although the standalone model can classify all the data points correctly (see Figure 6.5 (a)) with two simple near-straight boundary lines, it is not reliable as the dataset is very small. An increase in the dataset will make the model perform poorly. The shapes of the boundary lines for Ti-6Al-4V shown in Figure 5.13 also proves that two simple near-straight boundary lines are insufficient to classify the data points correctly. Figure 6.5 (b) shows that the TL (f=0) model archives high performance with 100% accuracy in this task, and the shape of the boundary lines are similar to that of Ti-6Al-4V. This is expected as the trained weights for Ti-6Al-4V model were used as the initial weights for SS316L model, which were then adapted to fit the new dataset. Figure 6.5 (c) and (d) show that some data points indicated by black arrows are misclassified, and the shapes of the boundary lines are odd. Therefore, the TL with f=0 is adopted for process window prediction. It should be noted that due to the very limited dataset here, the criterion for surface condition classification determined by the decision boundaries may not be as stringent as the one detailed in Chapter 4. However, within the

predicted flat region, the samples are expected to exhibit generally flat surfaces with negligible humps, if not perfectly smooth.

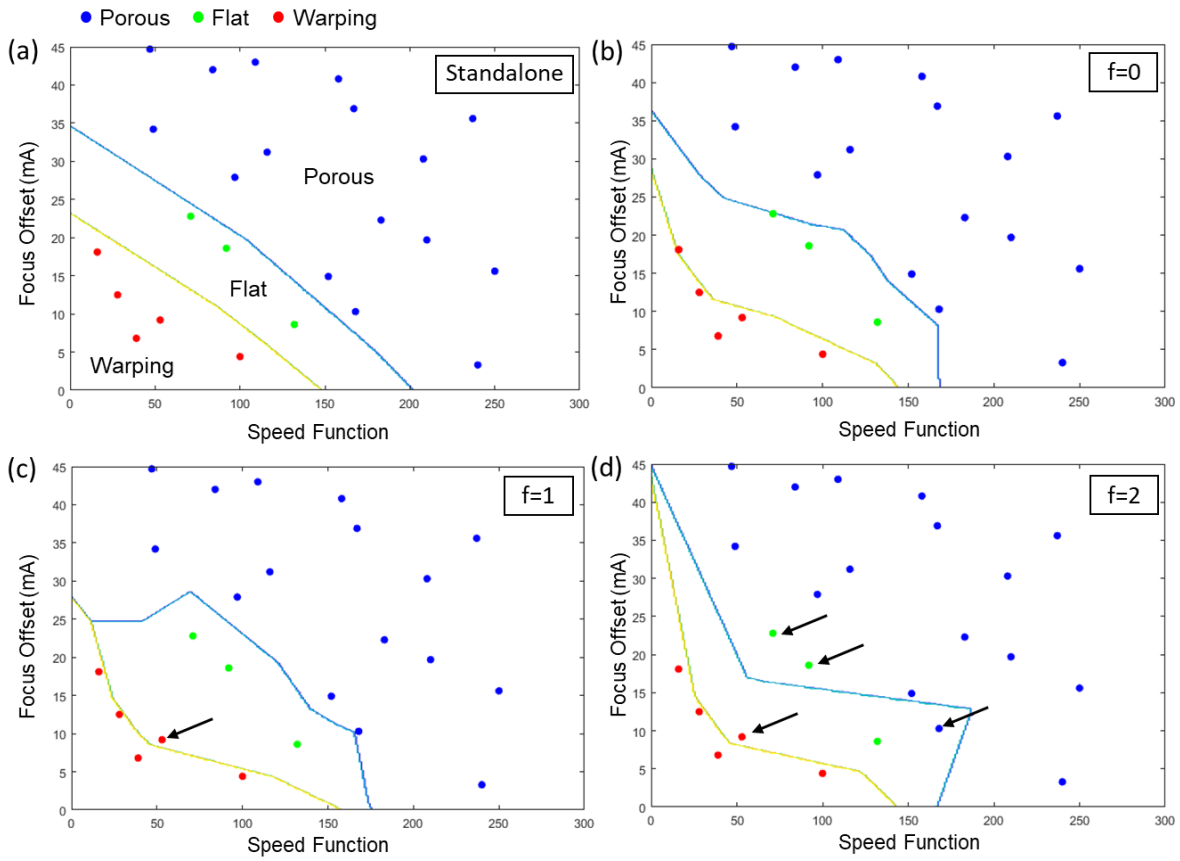

Figure 6.5 The surface classification results for (a) the standalone model, (b) TL (f=0) model, (c) TL (f=1) model and (d) TL (f=2) model. The decision boundary lines for surface condition classification divide the entire parameter space into three regions. The blue, green and red dots represent samples with porous, flat and warping surface conditions, respectively. The misclassified points are indicated by black arrows.

The results for Vickers hardness (HV) prediction are summarized in Figure 6.6. Although the median of the standalone model is close to TL models in the training set, its variance is much higher. Moreover, some outlier points are even far above the box plot. This suggests that on average, the standalone model has acceptable performance, but there is a high chance that it can perform poorly. This result can be explained by the extremely small dataset for HV values, which has only 8 data points. In contrast, the behaviors of TL models are much more stable, as evidenced by the tighter distribution in performance. All the 3 TL models show some improvements in HV prediction, where the TL (f=0) model has a low median and variation in both training and test set. Therefore, TL (f=0) model is adopted for the process mapping.

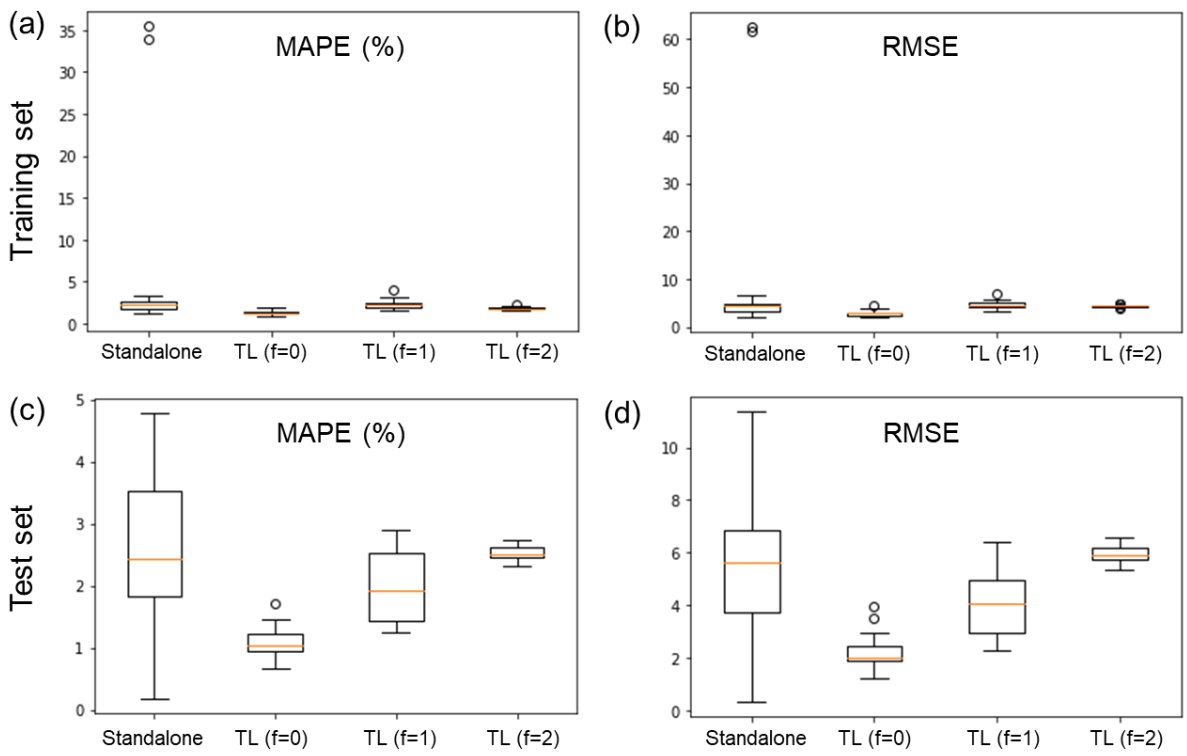

Figure 6.6 Box plot for the microhardness prediction using different schemes. The observed behavior of the training set is measured by (a) MAPE and (b), while the test set is also measured by (c) MAPE and (d) RMSE.

The 3D surface plots for HV prediction using the standalone model and TL (f = 0) models are shown in Figure 6.7. The standalone model has some odd curvatures that deviate from the data points, while the TL model outputs a much smoother surface that can well fit the data points.

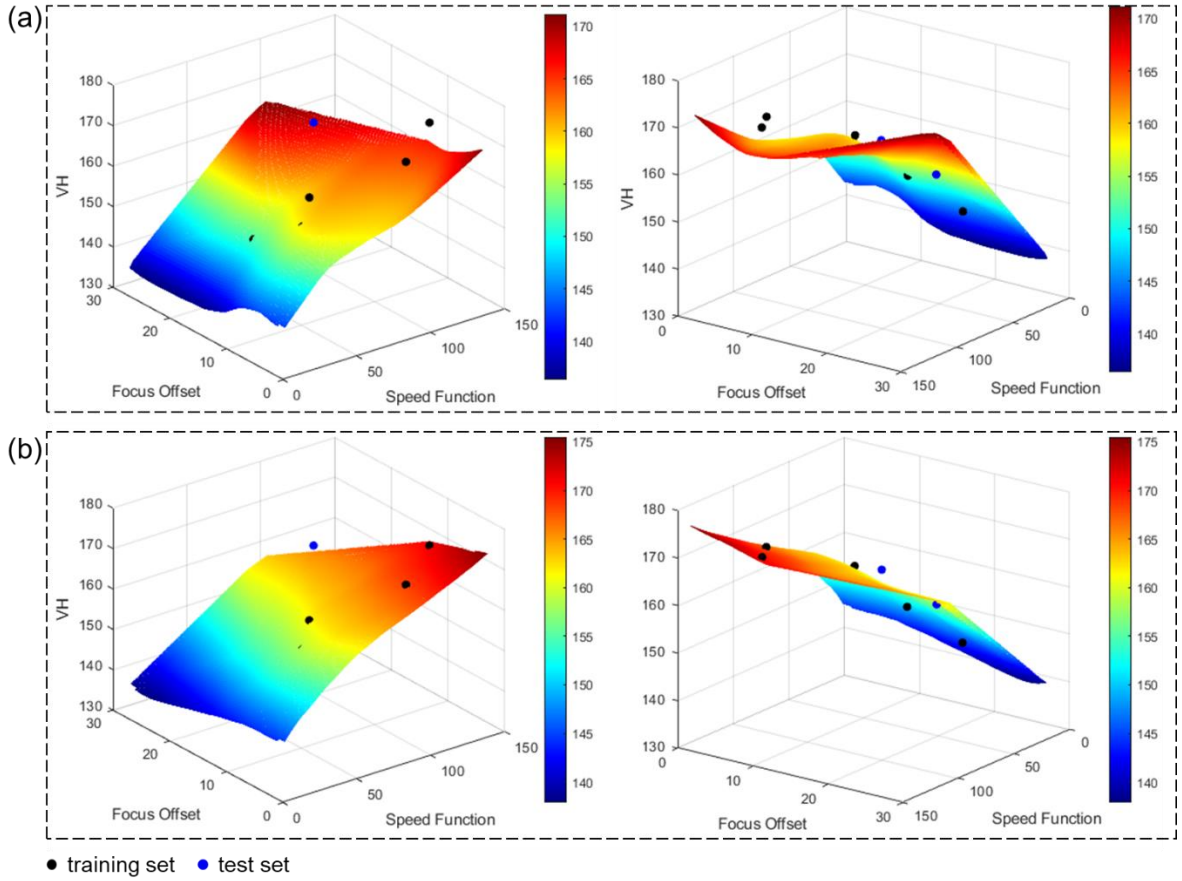

Figure 6.7 The 3D surface plots generated with two different perspectives for the Vickers hardness (HV) prediction using (a) the standalone model and (b) the transfer learning model (f=0).

6.3.2 Process Window Prediction

Based on the three criteria, namely relative density, top surface conditions and tensile properties as proposed in the section for Ti-6Al-4V alloy, the process window for SS316L alloy can be determined in the same manner. However, we intended to explore a more economical alternative to achieve this goal by replacing tensile properties with Vickers hardness. The underlying rationale of this method is that the relationships between microhardness and tensile strength can be estimated roughly as below [215]:

$$HV \approx 3\sigma_{UTS} \qquad \text{Eq. 6.1}$$

where HV is Vickers hardness in MPa and σ_{UTS} denotes UTS. This relationship is valid when the indentation makes the material undergo plastic deformation [216]. It should be noted that a large indent size needs to be created to average the microstructural inhomogeneity. As such, the value is representative of the mean hardness of the bulk sample. In this work, the indent size is ~ 100 - 115 µm while the average grain size of the samples is ~ 15.0 ± 7.6 µm, which

implies that the indentation could cover at least 10 grains. 5 measurements were taken and averaged for each sample. Here, the HV values are only available for samples with a relative density of ≥ 99%. To validate that this streamlined method can also determine the process window correctly, Ti-6Al-4V was used as a case study. In addition, its trained weights can also serve as initial weights to train the SS316L models by TL. 27 HV data points were collected, and a boundary line was generated to enclose the data points within a region, as it is not reasonable to predict the HV values of porous samples that fall out of this region by extrapolation. The HV threshold was set as 345, which is the requirement by ASTM F136 standard for Ti-6Al-4V ELI. The predicted process window is shown in Figure 6.8. Despite the slight dissimilarity in shape, the location and overall size of the process window determined is comparable with the result shown in Figure 5.14, although the Arcam's default parameter setting is outside the enclosed area. The predicted region that can produce the parts with superior mechanical properties is also the same, proving the effectiveness of using HV as a more economical alternative to UTS.

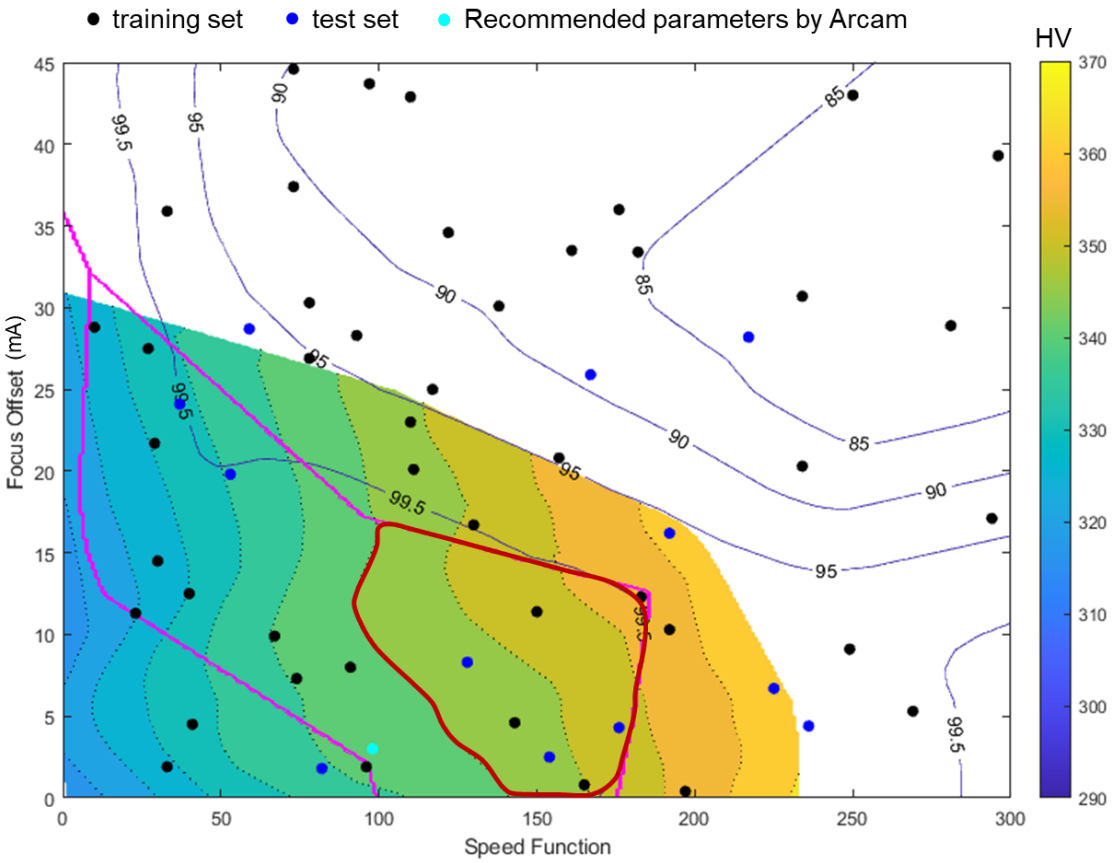

Figure 6.8 Process window prediction for SEBM-processed Ti-6Al-4V alloy by using the streamlined method which replaces UTS with Vickers hardness (HV).

Hence, based on this rationale, the process window for SS316L can be determined. The sample C6 has the best tensile properties with a VH ~ 165 in section 4.2.2 using DoE method. This benchmark value serves as the threshold for HV of SS316L in this work. Only ~ 21% of the SS316L samples have a relative density of ≥ 99.5%, as compared to ~ 38% for Ti-6Al-4V samples. Hence, the threshold for the relative density is relaxed to 99% so that the requirement is not too stringent for SS316L samples. The overlaid contour plots for the standalone model and TL model are compared in Figure 6.9. The predicted process window using the standalone model shows a lath-like shape with a bottleneck region in the middle (see Figure 6.9 (a)). Besides, the near-optimized process window determined by DoE detailed in section 4.2.2 almost falls out of the predicted region, indicating that the standalone model fails to predict the process window correctly as the dataset is too small. In contrast, the shape of the process window predicted by TL model is much more regular, which fully encloses the near-optimized window by DoE (see Figure 6.9 (b)). The odd and sharp corner on the top left of the window might be attributed to the small dataset, which more or less resulted in some errors. However, it does not affect the overall judgement on the optimal process window. This proves that using ML coupled with TL can correctly predict the process window with much less effort. Besides, the black dot outside but near the border of the DoE-determined process window has a HV = 171.6, which implies that the tensile properties of this data point might be even better than C6.

In summary, by implementing TL technique, our ML method could correctly predict the optimal process window for SS316, which generally agrees with the results achieved by DoE, although its size is slightly larger than the latter. Moreover, as mentioned in section 4.2.2, the DoE method required printing 42 samples in 5 trails of build to find the optimized process parameters, while the ML method required fabricating 24 samples with only 1 build. The detailed evaluation of the efficiency in terms of time and cost will be discussed in Chapter 7.

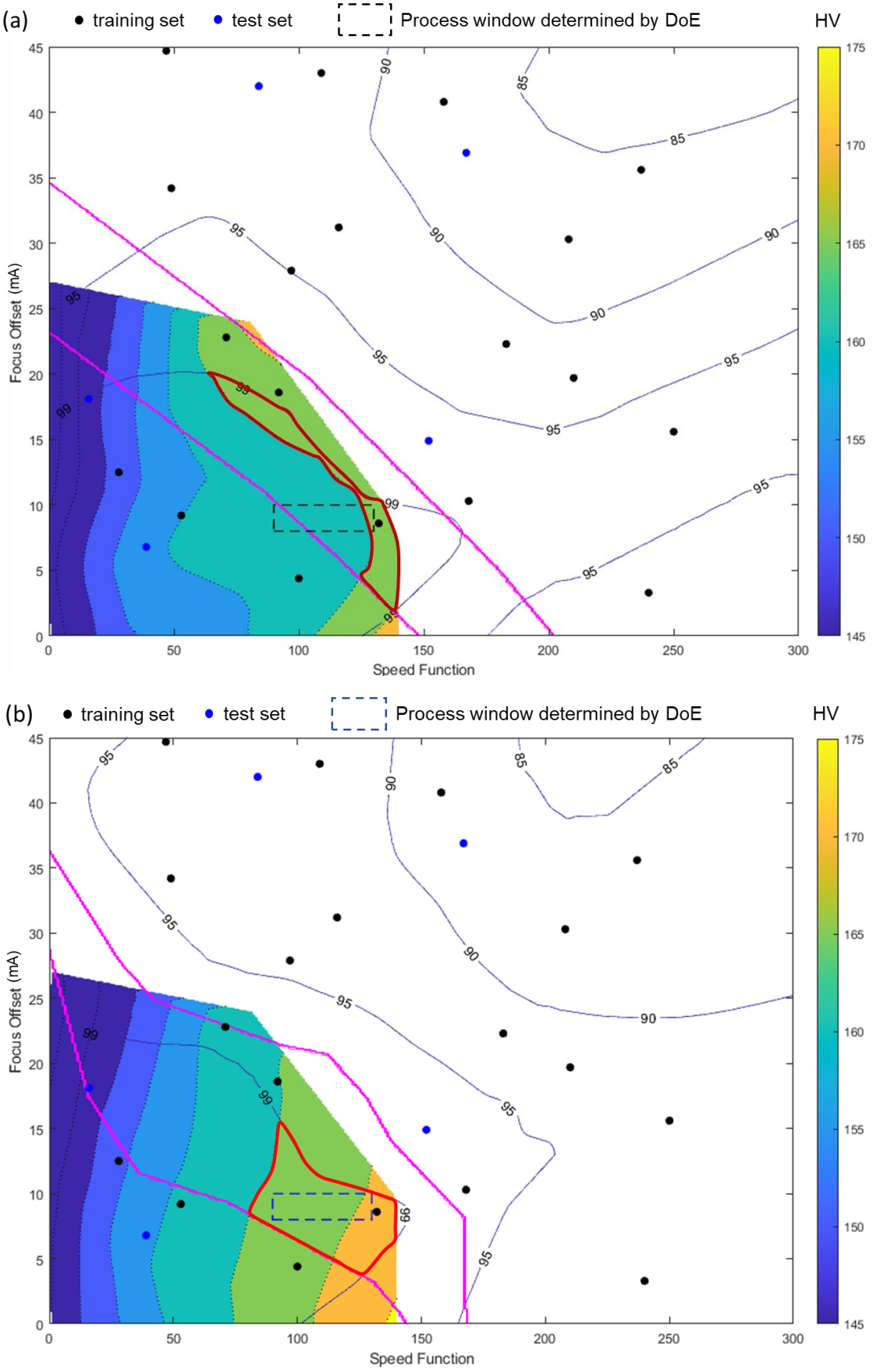

Figure 6.9 Comparison of the process window prediction for SEBM-processed SS316L alloy by using (a) the standalone model and (b) TL model. The predicted process windows are circled in red.

6.4 Conclusions

To validate the generalization ability and efficiency of the ML method for process parameter optimization of a different material, only 24 sets of process parameter combinations were generated to fabricate SS316L samples using coarse powders. TL was implemented to use the trained weights from the Ti-6Al-4V baseline model as the initial training weights for SS316L model. As compared to the standalone model without TL, the TL (f=0) model shows significant improvements in the average performance and stability of the model's behavior for the prediction of relative density, top surface conditions and Vickers hardness. Vickers hardness was used as a simpler and cheaper alternative to evaluate the mechanical properties in lieu of UTS. The overlaid contour plot shows that the predicted optimal process window generally agrees with the one previously determined by DoE method. Besides, the data point located on the right half of the predicted process window has higher HV than the best value determined by DoE, which implies that an even better tensile property could be achieved. This work proves the good generalization ability of the proposed ML method. With the trained Ti-6Al-4V as the baseline models, TL enables the process optimization to be more streamlined for SS316L with an even smaller dataset, which is time- and cost-saving simultaneously.

Chapter 7 General Discussion

This chapter unites the various strands of knowledge created in the whole thesis. Firstly, the specific aims/objectives in each result chapter are revisited and evaluated. Secondly, the links across the chapters are discussed, especially on the comparison of DoE and ML methods. Finally, the contributions of this research in the global picture of metal AM are summarized in the context of both academic and industrial relevance. It should be noted that this chapter emphasizes the in-chapter and cross-chapter multi-level and evolving aims/objectives. The detailed technical discussions can be found in each previous result chapter.

7.1 In-chapter Discussion

7.1.1 Process Parameter Optimization for Stainless Steel 316L by Design of Experiments

As stated in section 2.4.1, the work in this chapter aims to upgrade SS316L alloy from class III material to class II material for SEBM via process parameter optimization. This aim has been achieved, as supported by the results that the SEBM-built samples could meet the proposed benchmark criteria associated with surface condition (flat), relative density (≥ 99%) and tensile properties (exceeding cast counterparts). Optimal process windows have been successfully discovered for fine and coarse powder samples, respectively.

The motivation of this work is to investigate whether the deeper energy penetration and elevated build temperature in SEBM processing could mitigate the weakness in interlayer bonding and anisotropy. The lack-of-fusion interlayer defects for both fine and coarse powder samples are not apparent, as evidenced by OM examination, and high tensile strength and elongation. The anisotropy in tensile properties also differs from those processed by SLM and DED, which are usually weaker when tested along the build direction. Specially, the fine powder samples exhibit better tensile properties parallel to build direction, while the coarse powder samples are nearly isotropic in mechanical response along different directions.

7.1.2 Process Parameter Study for Pre-mixed Ni-Ti Powders

The aim of this work is to optimize the process parameters of pre-mixed Ni-Ti powders so that they can enter the material list in Table 2.3. There are two motivations behind: as compared to pre-alloyed NiTi powders, the pre-mixed Ni-Ti powders are cheaper and more flexible in adjusting the Ni:Ti ratio, which drastically affects the phase transformation temperature; the vacuum environment and elevated build temperature during SEBM processing could minimize oxidation and promote microstructural homogeneity, thus improving the shape memory properties of NiTi parts. However, the stated aim has not been achieved. The powder bed was ignited during the mandatory sintering stage, due to the occurrence of self-sustaining high-temperature synthesis (SHS) as a result of the strong exothermic reaction between Ni and Ti elemental powders. It is recommended to use pre-alloyed NiTi powders for SEBM processing. Despite the lack of success, the mechanism investigated and the conclusions drawn are still valuable within the scope of materials development for SEBM.

7.1.3 Process Parameter Optimization and Process-Microstructure-Property Relationship Mapping for Ti-6Al-4VAlloy Using Machine Learning

As a commercialized material with the process parameters developed by Arcam, Ti-6Al-4V is already listed as the class I material according to Table 2.3. The main aim is to use Ti-6Al-4V as a proof of concept for the proposed ML methodology in process parameter study. The secondary aim is to use this material to build baseline models, so that the process development for new materials can be expedited in the long run.

The main aim has been achieved: the process maps are constructed by the ML method to predict the optimal process window for Ti-6Al-4V, where the samples fabricated within this window even exhibit ~ 5% higher UTS than those printed using the Arcam's default parameters; the complex yet unformulaic PMP relationships have been mapped with high accuracy by a ML-centered tetrahedral framework which incorporates top build surfaces. The trained baseline models are ready to be transferred to SS316L for faster and more precise process development, suggesting that the secondary aim is fulfilled.

This ML-centered tetrahedral framework is assessed as shown in Figure 7.1. The attempt to quantify PMP relationships is successful. This is substantiated by the establishment

of process-to-property (section 5.3.1), microstructure-to-property (section 5.3.2) and process-to-microstructure (section 5.3.3) linkages with high accuracy, which are of core interest in materials science. Considering surface as the fourth dimension of the traditional PMP relationships, the surface-to-property (section 5.3.2) and process-to-surface (section 5.3.3) linkages are built. The potential applications of surface will be elaborated in the next section. Nevertheless, the surface-to-microstructure linkage is still pending, which will be accomplished in the future using more advanced DL algorithms such as the image-to-image translation [217].

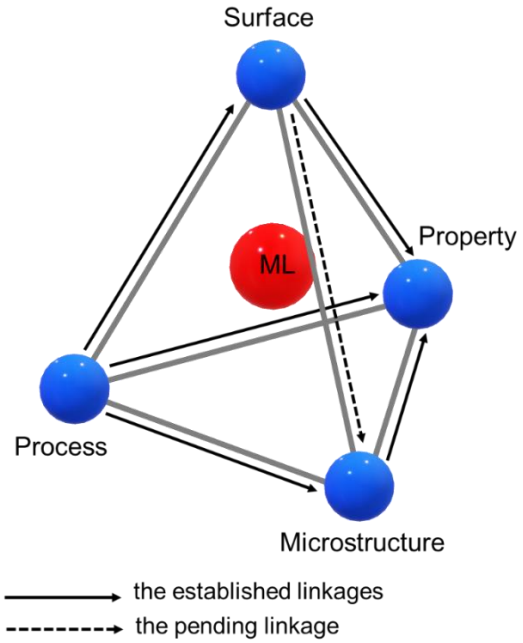

Figure 7.1 The assessment of the linkage established within the proposed ML-centered tetrahedral framework empowered by DL.

7.1.4 Process Parameter Optimization for Stainless Steel 316L Using Transfer Learning

The aim of this work is the same as Chapter 4 but was achieved from a different route, namely by ML methods. The knowledge acquired from the pre-trained Ti-6Al-4V baseline models can be transferred to SS316, enabling the discovery of its process window with an even smaller dataset. Besides, less experimentation is required for process development with TL. Therefore, the two concerns associated with the generalization ability and efficiency of the ML methodology have been well addressed.

7.2 Cross-chapter Discussion

The breakdown analysis of time and cost for the SEBM process development of SS316L using DoE and ML methods is shown in Table 7.1. The time calculated herein is still more conservative than the actual time taken. The material consumption includes the actual material required for fabricating the dense samples and the 5% material loss during powder recycling. Only the cost of the materials consumed (60 SGD/kg) is included. The actual total cost will multiply substantially if the cost of machine consumables/maintenance, utility, manpower, post-characterization and testing is factored in. The data show that ML could save the total development time by ~ 86% and material cost by ~ 90%. The results prove that ML can considerably accelerate the process development of SS316L for SEBM up to 5 times faster and 10 times cheaper than the conventional DoE method, provided that the baseline models (i.e. Ti-6Al-4V) are used.

Table 7.1 Time and cost breakdown analysis of process development for SS316L using DoE and ML methods. The savings are calculated for coarse powder samples only.

		DoE method		ML method	Saving (%)
		Fine powders	Coarse powders	Coarse powders	
No. of samples		32	42	24	43
No. of builds		7	6	1	83
Time consumption	Build time (hr)	103	125	10	92
	Pre/post processing, density/mechanical property evaluation time (hr)	153	138	27	80
	Total time (hr)	256	263	37	86
Materials consumption (kg)		32	31	3	90
Total material cost (SGD)		1920	1860	180	90

In addition to the significantly enhanced efficiency in process development, the ML method offers another four major advantages over DoE as demonstrated in Chapter 5. Firstly, it could map the full-scope PMP relationships over the entire SEBM parameter space, thus avoiding the local optima or incomplete process window; Secondly, it could process the raw surface/microstructure, extract the important features automatically and link them to property. This is challenging, if not impossible, for DoE to achieve, because the surface morphology and microstructure of SEBM-built samples are complex, and the resultant property does not solely depend on any single feature. Next, ML could generate plausible target surface/microstructure

images based on the input process parameters, which has not been reported by using the DoE method. Last but not least, the trained ML models for one material could be transferred to a different material with an even smaller dataset. As such, the costly experimentation does not have to start from scratch, which is unavoidable for DoE when the context changes.

The challenges elaborated in section 2.7.2 for ML in AM process development concerning the data size, interpretability and generalization ability have been addressed. Instead of collecting hundreds and thousands of data as commonly practiced for ML, the 56 data points are proven to be sufficient to achieve high accuracy in prediction (> 98% for UTS and > 99% for relative density) for SEBM-processed Ti-6Al-4V alloy. This implies that using a small dataset is feasible in AM, provided that the prediction error is within the tolerance range (e.g. 5% deviation for UTS is acceptable for Ti-6Al-4V). Despite the generally poor interpretability of other DL techniques, the abstract features contributing to UTS during CNN processing could be visualized by Grad-CAM. Finally, TL for SS316L can boost the generalization ability of the ML method, which could achieve an accuracy > 99.5% for relative density and > 97.5% for Vickers hardness prediction, with a ~ 57% smaller data size as compared to Ti-6Al-4V.

Overall, the objectives regarding using the DoE and ML methods for optimizing the SEBM process parameters and building the PMP relationships have been achieved, which were studied qualitatively for SS316L in Chapter 4 and quantitatively both for Ti-6Al-4V in Chapter 5 and SS316L in Chapter 6. With Chapter 4 serving as a benchmark, the ML method is proven to be more efficient in process development of SS316L for SEBM. Collectively, the works carried out in this thesis have fulfilled the purported aim: the process parameters have been optimized for SEBM-built Ti-6Al-4V and SS316L alloys with superior mechanical properties.

7.3 Overall Contributions to Metal Additive Manufacturing

The major contribution of this research is the optimization of SEBM process parameters for SS316L and Ti-6Al-4V alloys to fabricate parts with superior tensile properties, and the development of a novel ML method for fast and precise discovery of process window. The sub-contributions and their significances in both academic and industrial context are highlighted as follows.

7.3.1 Academia

- **Materials science:**
  SS316L has been upgraded to the class II material for SEBM, with significant improvements in tensile properties. Anisotropy in microstructure and tensile properties could be mitigated by using coarse powders. SEBM is found to be unsuitable for processing pre-mixed powder materials with strong exothermic reactions, including but not limited to NiTi.

- **ML method for process parameter optimization:**
  The developed ML method could identify the global optimal process window precisely for SEBM-processed materials with a small dataset. The Ti-6Al-4V part could be printed by SEBM with ~ 5% higher in UTS and ~ 87% faster in speed using the process parameters optimized by ML. This ML-assisted optimization method could be potentially applied to develop new materials for other metal AM processes such as laser-based PBF, DED and BJ.

- **ML-centered tetrahedral framework:**
  The proposed ML-centered tetrahedral framework could materialize high-fidelity mapping of the full-scope PMP correlations.

7.3.2 Industry

- **More variety of processable materials for SEBM:**
  The established ML-assisted optimization method could optimize the process parameters 5 times faster and 10 times cheaper than the classical statistic DoE method, which will considerably boost the development of new materials with properties similar to Ti-6Al-4V and SS316L for SEBM. Eventually, with the increase in the variety of class II and even class I materials, the progress for adopting SEBM as a preferred manufacturing technique in high value-added industries can be expedited. This work is also a part of the international efforts for materials qualification for metal AM as highlighted by Seifi et al. [82].

- **Non-destructive quality assessment:**

  The conceptually proven ML-centered tetrahedral framework could examine the relative density and mechanical property of the materials with the top fusion surfaces. This non-destructive and ultra-rapid technique empowered by DL algorithms could be used to perform quality assessment and quality control for SEBM-printed parts by simply inputting the fusion surface images. This all-in-one solution could be extended to other metal AM processings that carry top fusion surfaces.

Chapter 8 Conclusions and Future Work

In this chapter, the specific conclusions drawn from the detailed technical analysis of each result chapter are synthesized. The general conclusions standing in the global picture of AM in both academic and industrial context are presented. Finally, the limitations and recommended future work are discussed.

8.1 Main Findings

The study of process parameter optimization for different materials using SEBM in this thesis can be summarized as follows: firstly, the conventional DoE method was used to conduct process parameter study qualitatively for SS316L in Chapter 4 and for NiTi alloy in Appendix A; secondly, a novel ML method was developed in Chapter 5 for fast and precise process parameter optimization for Ti-6Al-4V and to quantify the PMP relationships; finally, TL was implemented in Chapter 6 to discover the optimal process window for SS316L with an even smaller dataset. Below are the main findings from these chapters:

- Using fine powders, the SEBM-built SS316L samples show typical <001> crystallographic texture with longitudinal microstructural heterogeneity. The samples exhibit strong anisotropy in tensile testing, e.g. higher strength and elongation along build direction than horizontal direction.
- Slow scanning (i.e. lower SF) should be avoided as it would induce precipitation of σ phase along the grain boundaries, which could lead to intergranular fracture and embrittlement of the material.
- Using coarse powders, a higher input energy was required to obtain fully dense SS316L samples which have near-equiaxed grains with obscure cellular dendrites, leading to isotropic tensile properties. The UTS and uniform strain are increased by 10.9% and 74.4% respectively, as compared to their fine powder counterparts.
- The powder size distribution can significantly affect the process window, crystallographic textures and tensile properties of SEBM-processed SS316L alloy.
- The mandatory preheating step makes SEBM unsuitable for processing Ni-Ti powder mixture, as it would cause the powder bed to be ignited and combusted via SHS, while a

lower preheating temperature would produce severely porous samples due to lack of fusion.

- A ML method was developed to predict the process window of Ti-6Al-4V with only 56 data points. The optimized process parameters could allow to fabricate samples with ~ 5% higher UTS and ~ 87% faster printing speed as compared to Arcam's default process parameters.
- CNN could map the surface and microstructure-to-property relationships with MAPE as low as 2.22% and 0.54% for UTS and relative density predictions, respectively. The CNN model was interpreted by the Grad-CAM to visualize the abstract surface features that contributed to high UTS.
- cGAN was utilized to predict top build surface, pore microstructure and SEM α/β dual-phase microstructure images from the two process parameters. The generated images were mapped over the entire parameter space, where the trends for the evolution of the image morphologies are consistent with the VAE latent space representation diagrams.
- The knowledge learned from the Ti-6Al-4V baseline models was cross-utilized on SS316L alloy with only 24 data points by TL with the weight initialization scheme. Vickers hardness was adopted as a cheaper alternative for UTS to predict the process window, which was shown to be well consistent with the previous optimal window determined by DoE method.

8.2 General Conclusions and Perspectives

In this work, SEBM process parameters were optimized for different materials via two dissimilar routes, where ML discovered the optimal process for SS316L 5 times faster and 10 times cheaper than the classical statistic DoE method. With the proposed ML-centered tetrahedral framework empowered by state-of-the-art DL algorithms, the relative density and mechanical properties could be predicted accurately and instantly, by simply inputting the surface image of the samples. It has demonstrated that the ML method could accelerate the materials development remarkably for those with properties similar to Ti-6Al-4V and SS316L, and perform non-destructive and instant quality assessment and control for SEBM-processed metallic materials that carry top fusion surfaces.

8.3 Limitations and Future Work

The limitations and recommended future work are discussed as follows:

- Tensile testing for SS316L samples in ML study:
  In the TL work, Vickers hardness was used as a more economical alternative to evaluate the tensile properties. It is recommended to fabricate a few tensile coupon samples in the ML-predicted process window for SS316L to verify whether the ductility is also comparable to the samples fabricated using the DoE-optimized process parameters, especially within the region where the samples exhibit higher HV. This will provide complementary information to the tensile properties, although ductility is not the focus of our current ML work.
- Process-microstructure mapping for SS316L samples:
  Only process-property mapping was conducted for SS316L samples using ML. It is recommended to map the process-microstructure relationships using cGAN. However, it is challenging to do so, because only 8 samples are near-fully dense, and TL is not possible as the microstructure of Ti-6Al-4V is drastically different from that of SS316 alloy. Hence, it is suggested to fabricate more samples under different process parameters generated by the random search method within the full-density zone predicted by ML. By doing so, the microstructure evolution with varying process parameters could be visualized. It is also possible to predict the columnar-to-equiaxed transition region if it exists.
- Surface-microstructure mapping for Ti-6Al-4V samples:
  The surface-to-microstructure mapping is still pending in this research, which is challenging to be achieved at the moment. However, more advanced GAN techniques such as image-to-image translation [217] can be explored in the future.
- Generalizability of the ML method across materials:
  Although the ML method is proven to be successful in this thesis, it is limited to pre-alloyed Ti-6Al-4V and SS316L. Other factors may need to be considered when processing materials with unique characteristics, such as pre-mixed Ni-Ti powders with strong exothermic reaction if the issue associated with pre-heating can be resolved. Hence, to further validate the performance and efficiency of the proposed ML method, it is suggested to extend it to other materials with distinctive physical, chemical and mechanical properties from these two alloys.

- Generalization ability of the ML method across SEBM machine systems and different PBF processes:

  The ML experimentation in this research was carried out with Arcam EBM A2XX machine. However, it is known that different SEBM systems may use different process parameter settings, even for the same material. This could be ascribed to the advancement of EBM Control algorithms and different hardware settings. Hence, the generalization ability of the ML results could be further verified across different SEBM systems. It is also recommended to test this method on other metal PBF process, such as SLM. Instead of using SF and FO, a more universal expression should be explored so that TL could also be leveraged across different metal AM processes. Moreover, the same method can be extended to include more than two process parameters.

- Inclusion of fracture critical properties:

  In this research, only the baseline mechanical properties, namely tensile properties and microhardness, were evaluated. The ML methods could be further extended to capture fracture critical properties such as fatigue and toughness. The optimized process window considering these two properties might differ from the results obtained for tension and hardness. Hence, the users need to determine which property is more critical for a specific application and subsequently refer to the corresponding process window. Considering the high cost and prolonged time to test the fatigue and toughness values, the data from literature can be incorporated to further reduce the number of samples that need to be tested, as for example performed by Zhang et al. [147].

Appendix A Process Parameter Study for Pre-mixed Ni-Ti Powders

This appendix elaborates the issue that occurred in SEBM processing of pre-mixed Ni-Ti powders, and a comprehensive investigation of the powder ignition mechanism is undertaken by comparing with SLM processing.

1. Introduction

To date, most of the published works from literature used pre-alloyed NiTi powders as ingredient materials. Nevertheless, in-situ alloying via AM from elemental powders is a promising cost-effective alternative which offers the flexibility to tailor the powder composition, thus controlling the material's properties or even creating novel alloys. This is particularly true for NiTi products, as their phase transformation temperature is highly sensitive to the alloy composition [218]. Extensive works have focused on in-situ elaborating high-quality NiTi parts using DED process [13, 99, 219-221]. Despite the advantages, the works on using PBF AM techniques to in-situ elaborate NiTi parts are very scarce. Thus far, only Zhang et al. has used SLM to in-situ synthesize solid NiTi samples [222]. On the other hand, no one has attempted to employ SEBM to produce NiTi alloys directly from elementally blended powders.

The vacuum environment in SEBM can prevent oxidation as titanium has high affinity to oxygen. Besides, the elevated build temperature can provide in-situ heat treatment, which has the potential to promote the microstructural homogeneity and improve the shape memory properties of the NiTi parts. Hence, it is of high interest to use SEBM to fabricate NiTi alloy.

In addition, the cost of pre-alloyed NiTi powder is much higher than pre-mixed Ni-Ti powder. The Ni:Ti ratio is also fixed in pre-alloyed powder, which makes it difficult to control the phase transformation temperature by adjusting the Ni:Ti ratio in powder feedstock. Due to the above two reasons, pre-mixed Ni-Ti powders were used to fabricate Ni-Ti alloy using SEBM.

One major challenge in preparation of Ni-Ti powder mixture is the long mixing time (~ 2 hrs) and the limited capacity (~ 0.5 L) of the mixing tumbler. It is not practical to use the original build envelope of the Arcam A2XX system to conduct the experiments. Therefore, an

adaptive build envelope design was used in EBM machine to minimize material consumption by reducing the build envelope.

2. Results

2.1 Preparation of Pre-mixed Ni-Ti powders

Figure A-1 shows the SEM images of the Ni and Ti powders after mixing in an argon gas-purged container for different time. Ti particles are bigger and darker in the images, while Ni particles are finer and brighter. Figure A-1 (a) and (b) depict that with short mixing time, the finer Ni powders were unable to uniformly disperse into the free space left by coarser Ti powder. Conversely, a prolonged mixing time triggered the powders to re-aggregate, as evidenced in Figure A-1 (d). Figure A-1 (c) shows that a 2-hr mixing time is sufficient to achieve a relatively high level of homogeneity, which is testified by EDS mapping in Figure 3.6 (b). The same mixing time also enabled the powders for SLM processing to attain good mixture homogeneity although Ti particles larger than 63 μm were sieved and discarded before mixing.

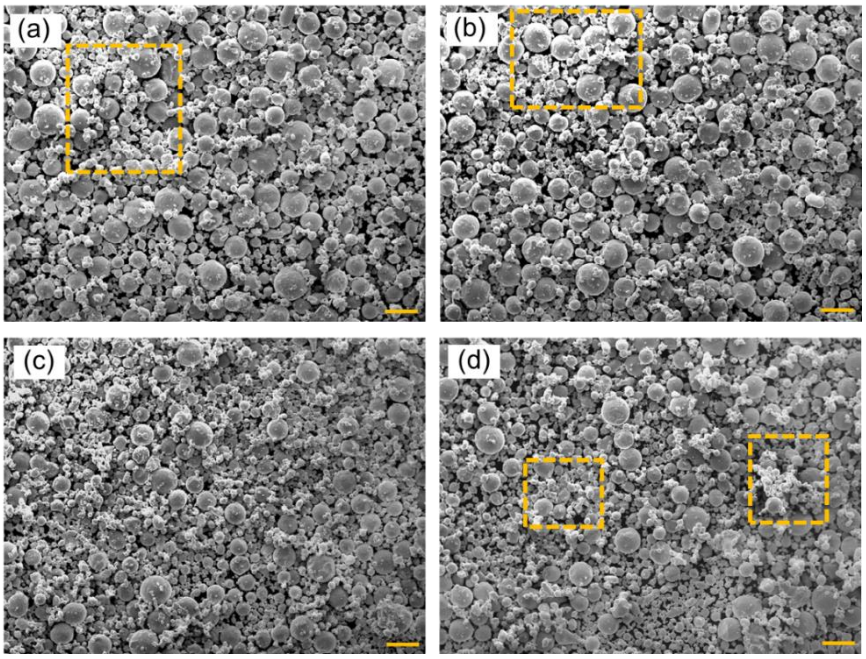

Figure A-1 SEM micrographs of Ni-Ti powder mixtures with a blending time of (a) 0.5 hr, (b) 1 hr, (c) 2 hrs, (d) 4 hrs. The larger and darker particles are Ti powders, while the smaller and brighter particles are Ni powders. The yellow dash bracket lines indicate powder agglomerations. All the scale bars are 100 μm.

2.2 Selective Electron Beam Melting of Ni-Ti Mixed Powders

Multiple builds were attempted to explore the processing window of SEBM to print NiTi using pre-mixed elemental powders. The temperature-time and pressure-time curves during printing are depicted in Figure A-2. The corresponding printing results are next to each graph. In build 1 (see Figure A-2 (a)), the target build temperature T was preset at 600 °C, followed by start-plate heating. At intermediate temperature, heat shield outgassing was activated to clean the start-plate and prevent the powder bed temperature from increasing too fast, as reflected by the plateau region of the temperature curve. Afterwards, when a new layer of powder mixture was coated over the hot start-plate, the powders were immediately ignited. The combustion instantly propagated through the entire Ni-Ti powder bed. The temperature drastically shot up to more than 1200 °C, which was beyond the measurement capability of the thermocouple attached to start-plate. This accident was accompanied by an exponential increase of chamber pressure. Subsequently, the temperature and pressure recovered to normal state when the combustion was completed.

In build 2 (see Figure A-2 (b)), the target temperature was reduced to 350 °C to circumvent powder bed ignition. Nevertheless, the low build temperature was unable to sufficiently sinter the loose Ni-Ti powder mixture after powder spreading. A multitude of severe sparking was triggered in the melting stage. The build temperature decreased continuously. Consequently, the samples fabricated were porous, accompanied by segregation of bright Ni melts and dark Ti melts. In addition, the un-melted particles are clearly visible.

In build 3 (see Figure A-2 (c)), the start-plate heating target temperature was increased to 450 °C to enhance sintering and minimize sparking. However, violent exothermic reaction between Ni and Ti powders occurred from time to time. The scorching molten metallic beads spattered around, which kindled other regions on the start-plate on a small scale. When this phenomenon was observed, manual-raking mode was applied to allow burning patches to naturally extinguish before depositing the next layer of powder. Disregard of our efforts, a large molten bead landed on the loose powder bed surrounding the start-plate, which eventually ignited the entire powder. The uncontrollable combustion caused the temperature and pressure to escalate rapidly.

In summary, the lack-of-fusion vs. powder-ignition dilemma makes this alloy challenging to produce out of pre-mixed Ni-Ti powder using SEBM technique.

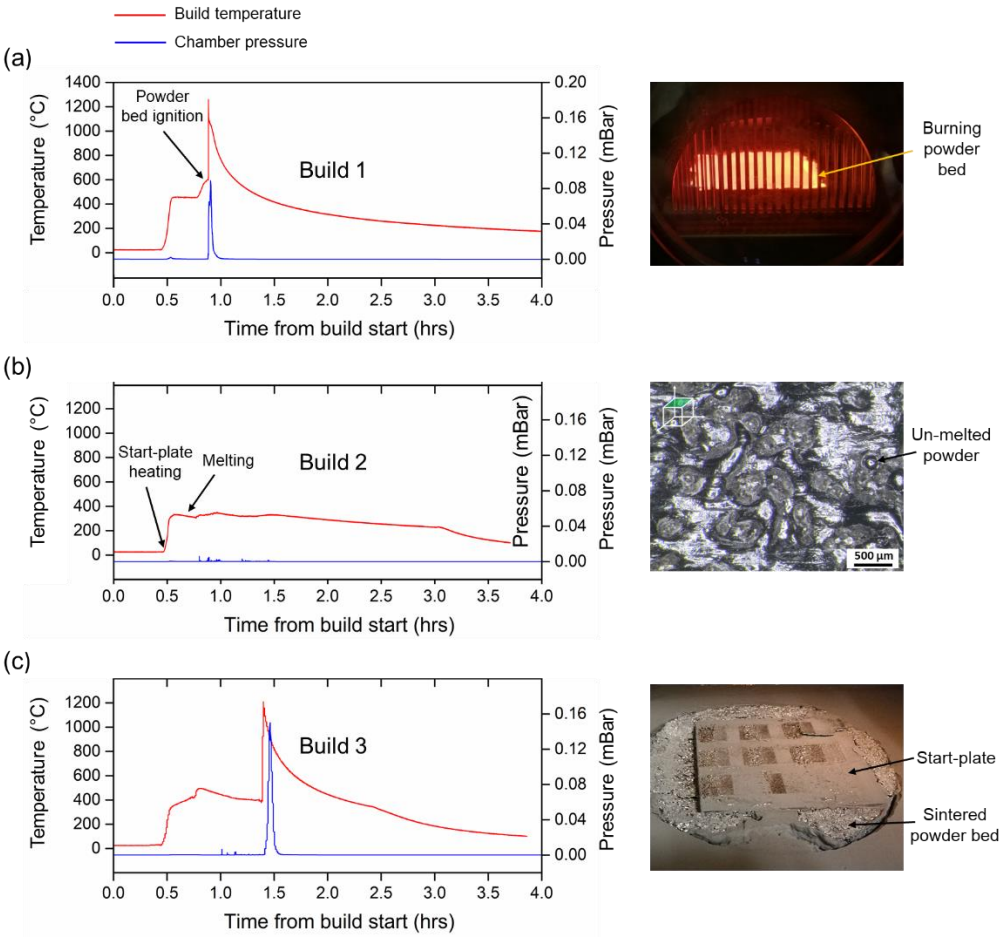

Figure A-2 Temperature-time and pressure-time curves for 3 different cases of NiTi sample fabrication by SEBM, with the corresponding images showing the printing results. (a) In build 1, the entire Ni-Ti mixture powder bed was ignited during the start-plate heating stage. This moment was captured through the observation window. (b) In build 2, a low energy input resulted in porous samples and serious elemental segregation. (c) In build 3, the hot molten metallic spattering ignited the entire powder bed during the melting stage. The picture next to it shows the entire powder bed was severely sintered and fused together with the start-plate after the accident.

2.3 Discussions

It is intriguing to understand why powder bed ignition would happen in SEBM but not in SLM processing, as Zhang et al. have used SLM to process pre-mixed Ni-Ti powders [222]. Referring to our previously published work [16], the same powders were also processed by SLM except that the elemental Ti powders were sieved to a size no bigger than 63 µm before mixing with Ni powder. In the abovementioned work, a preliminary study on process parameters was carried out with an energy density ranging from 30 to 150 J/mm^3 by varying the scanning speed. The SLM as-built NiTi samples were examined under OM to correlate the energy density to microstructure, as reflected in Figure A-3 (a), where sample 1 (energy

density = 40 J/mm^3), sample 2 (energy density = 80 J/mm^3) and sample 3 (energy density = 130 J/mm^3) are representatives of the printing results under different levels of energy density. At low energy density, a multitude of lack-of-fusion defects occurred. At intermediate energy input level, although NiTi alloys were better consolidated, the microstructure is inhomogeneous. The turbulence-like bright and dark shaded regions are nonuniformly blended. When further increasing the energy density, the micrograph became nearly monotone, but accompanied by many spherical pores resulted from the so-called keyhole effect [223].

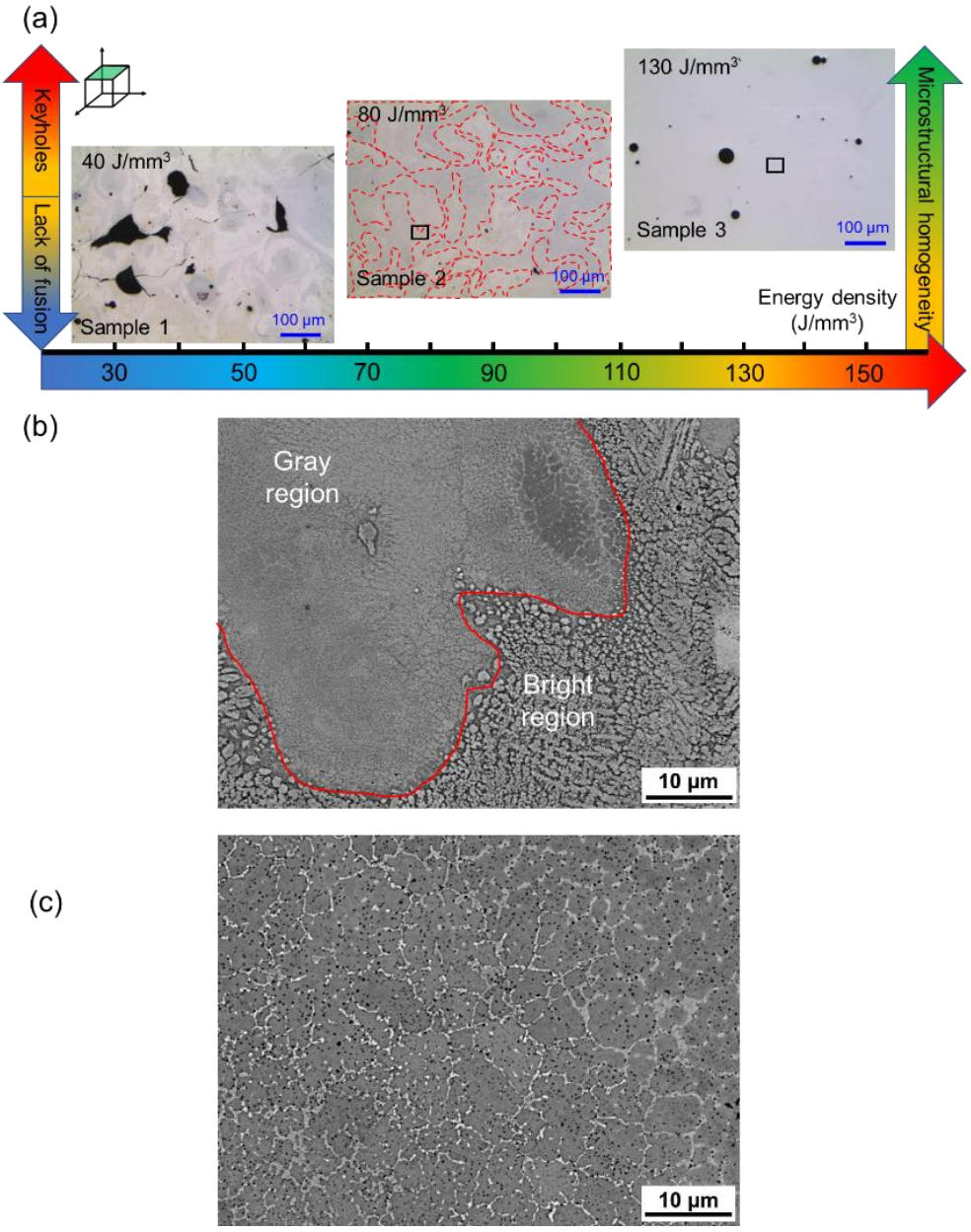

Figure A-3 (a) Influence of laser energy density on the microstructure of as-SLMed NiTi parts under OM. An increasing energy density eliminates lack-of-fusion defects and homogenizes the microstructure, but at the cost of introducing keyholes. (b) Top-view BSE image of the inset in sample 2 shows an inhomogeneous mixture of bright phase and gray phase, in contrast to a more homogeneous microstructure of sample 3 shown in (c). Cited from the work of Wang et al. [16].

At a higher magnification in BSE mode for sample 2, Figure A-3 (b) reveals that countless non-uniform bright island-like regions were formed. The bright shaded regions are dendritic in general. The EDS point detection on multiple sites shows that Ni:Ti ratio in bright shaded region is ~ 3:1, which is most likely to be the brittle Ni_3Ti phase. Nevertheless, the Ni:Ti ratio in gray region varies from site to site, indicating multiple Ni-rich intermetallic phases could have been formed. The overall Ni:Ti ratio by EDS mapping on multiple sites is ~ 1.9. In contrast, the microstructure of sample 3 is more homogeneous, as illustrated in Figure A-3 (c), where the overall Ni:Ti ratio is ~ 1.3.

Therefore, the exothermic reactions of NiTi pre-mixed powders have also induced instability in SLM processing, although powder bed ignition did not occur. It can be concluded that this pre-mixed powder material is also not suitable to be processed by SLM.

In SEBM process, the unexpected powder bed ignition can be analogized to a self-sustaining high-temperature synthesis (SHS) process [224, 225]. Due to the strong exothermic reaction between Ni and Ti, when the elemental powders are preheated by an external heat source above a certain temperature, the synthesis will be initiated and the self-propagating combustion waves can pass through the entire powder mixture, producing porous NiTi products [226]. Li et al. [227] have concluded that the combustion front is able to propagate when the preheating temperature is above 200 °C. However, melting of NiTi only occurs when preheated above 450 °C, which corresponds to a combustion temperature of ~ 1260 °C, close to the melting point of NiTi.

Based on the abovementioned mechanisms, in build 1, the start-plate temperature was above 450 °C before the powder deposition. When the first thin layer of powder was distributed over the hot start-plate, the reaction was triggered and the high-temperature combustion rapidly propagated. In build 2, the preheating temperature was only ~ 350°C when the powder was distributed. However, the powder bed melting could not happen below 450 °C, although solid-state reaction might have occurred at this temperature. The samples fabricated were porous due to insufficient powder bed sintering during preheating. In build 3, the start-plate temperature reached ~ 450 °C at the end of the start-plate heating stage. When the first layer of powder was coated, the exothermic reaction elevated the temperature to ~ 500 °C. To avoid repeating the scenario in build 1, the electron beam was switched off for a while in order to cool down start-plate and powder bed. The combustion was hence quenched when the heat loss was high and the heat source was cut off [227]. Nevertheless, the exothermic reaction was still ongoing.

Similar to the aforesaid SLM process, the exothermic reaction formed strong turbulence in melt pools, which produced irregular top surfaces. This inhibited the proper spreading of the next powder layer, which in turn aggravated the turbulence of melt pool. On the other hand, as the powder bed was still not well sintered, powder sparking was prominent. As a result, the powder bed was ignited by the high-temperature molten spattering.

Interestingly, powder bed ignition did not occur in SLM process, although both SEBM and SLM are powder bed metal AM process, where the same Ni-Ti powder feedstocks were used. This contrast can be ascribed to two reasons. Firstly, SLM did not require preheating, therefore the SHS process could not be initiated on the cold powder bed. Secondly, the thermal gradient of SLM process (~ 10^6 K/m) [45] is much higher than SEBM process (~ 10^5 K/m) process [228]. The melt pool quickly solidified before it could ignite powder bed. Moreover, the argon gas flow in the chamber could also dissipate heat by convection.

In summary, to avoid powder charging which produces porous samples, preheating is mandatory in SEBM process. However, preheating could in turn trigger SHS reaction for Ni-Ti powder feedstocks. This lack-of-fusion vs. powder-ignition dilemma in preheating stage hinders the adoption of SEBM to fabricate metallic components out of pre-mixed Ni-Ti powders.

2.4 Conclusions

Pre-mixed equimolar Ni-Ti powder feedstocks were used to fabricate NiTi samples via SEBM process. A homogeneous powder mixture could be achieved by blending at 30 rmp for 2 hrs using a tumbler mixer. Insufficient blending would cause powder agglomeration, whereas a prolonged blending would induce powder re-segregation. However, SEBM was unable to fabricate solid NiTi alloys from pre-mixed elemental powders. The mandatory preheating stage would trigger SHS, causing the entire powder bed to be combusted. On the contrary, reducing preheating temperature would produce porous samples. Hence, it is not recommended to use SEBM to process this material, due to the lack-of-fusion vs. powder ignition dilemma in preheating. Although powder ignition did not occur in SLM, it is hard to find a suitable process window. This is because a low energy density would produce porous parts with severe inhomogeneity in microstructure while an increasing energy density could better fuse the powder with improved microstructural homogeneity, but it may cause keyhole defects. This

was likely to be associated with the unstable melt pool solidification induced by an exothermic reaction of elemental Ni-Ti powders. Hence, it is not suitable to use PBF to process elemental Ni-Ti powders to fabricate quality NiTi parts. This conclusion can also be extended to other pre-mixed metal powder materials with strong exothermic reactions.

Nevertheless, it is still possible to engineer the phase transformation temperatures of PBF-processed NiTi alloy by varying the Ni:Ti ratio. This may be achieved by mixing the pre-alloyed NiTi powders with a controllable amount of either pure Ni or pure Ti powders, but not both. Theoretically, the addition of pure Ni or Ti powders can fine tune the ratio of the resultant NiTi alloy while exothermic reactions are minimized in the pre-alloyed NiTi powders. Future work needs to be done to validate the assumption.

Appendix B Details for Machine Learning Techniques

All the ML models were implemented with the open-source Python libraries including scikit-learn for traditional ML, pandas for data manipulation and analysis, and NumPy for scientific computation. Particularly, the DL models such as MLP, CNN and GAN were implemented using Keras with a TensorFlow backend.

The traditional ML models adopted include support vector machine (SVM), k-nearest neighbors (KNN) and decision trees (DT). The key hyperparameters for each technique were tuned and optimized separately by many rounds of trials, as listed in Table B-1.

Table B-1 Key hyperparameters used for each traditional ML method.

Models	Key hyperparameters
SVR	kernel=rbf, degree=3, gamma=scale, C=2, epsilon=0.01
KNN	n_neighbors = 3
DT	criterion=mse, splitter=best, max_depth=None

Multilayer Perceptron (MLP) Architecture

For regression tasks in this Ph.D. work, the MLP regressor network has 2 hidden layers, each having 100 neurons with a rectified linear unit (ReLU) activation. Linear activation function was used in the output layer. An adaptive stochastic gradient descent optimizer, namely Adam [229] with a learning rate of 1×10^{-3} and decay of $0.002 \times e^{-3}$ was employed to update the MLP weights amid backpropagation. Mean absolute percentage error (MAPE) was chosen as the loss function (Eq. B-1) as it performed best in the context compared to other loss functions. Y_i and $\widehat{Y}_i$ denote the true and predicted values for data point i, respectively. The models for Ti-6Al-4V was trained using 1000 epochs with a mini-batch size of 8, while the models for SS316L used a mini-batch size of 4 due to the smaller dataset. The train/test split ratio was 80/20, as a common practice in ML. All the above hyperparameters were optimized empirically by many rounds of trials. Batch size is an important hyperparameter. Using mini-batches achieves the best training stability and avoids high computational cost as well as local

minima. During the training, checkpoints were called to automatically save the model weights with the lowest validation loss.

$$MAPE = \frac{1}{n}\sum_{i=1}^{n} \left| \frac{Yi - \hat{Y}i}{Yi} \right| \quad \text{Eq. B-1}$$

For classification task, the MLP classifier network with 2 hidden layers, each having 16 and 12 neurons with a ReLU activation respectively, was constructed for classification task. Three neurons with a softmax function, which outputs the class with the highest probability, were used in the output layer for such 3-class classification problem. The discrete categorical data were converted into numerical form by one-hot encoding before feeding them to the ML algorithms, because high-dimensional sparse binary features in numerical form can yield better performance for class predictions [230]. Table B-2 demonstrates how the class labels for three representative data points are converted into a 3D vector. The Adam optimizer was used, and the categorical cross-entropy was adopted as the loss function. The same train/test split ratio, mini-batch size and number of epochs used in MLP regression task were adopted for training the MLP model for classification task.

Table B-2 One hot encoding to transform labels for top surface conditions from categorical form to numerical form.

Labels for top surface conditions	Categorical form	Numerical form [P, F, W]
Flat	F	[0, 1, 0]
Porous	P	[1, 0, 0]
Warping	W	[0, 0, 1]

Convolutional Neural Networks (CNN) Architecture

The CNN model owns 3 Conv blocks followed by 3 dense layers. Each Conv block consists of a 2D-convolutional layer, a BatchNormalization followed by a ReLU activation and a MaxPooling layer. The number of filters was set as 16, 32 and 64 for the 3 convolutional layers, respectively. The size of each filter was 3 × 3 followed by 'same padding'. The MaxPooling layers have a size of 2 × 2. The two fully connected layers have the nodes of 16 and 4. BatchNormalization and a dropout rate of 0.4 were applied only after the first dense layer. The output layer used the linear activation function for regression task. The full architecture of the CNN model is schematically illustrated in Figure 3.9. It should be noted that n × n × m represents the dimension of the input images, where n is the width and height of the

image (image size) and m is the number of channels. It should be noted that only 3D surface topography images use m=3, which has red-green-blue (RGB) channels. The other types of images use m=1 after they are converted to grayscale images. In the present study, the same CNN architecture was used for image-related regression tasks.

Multimodal Learning Architecture

In this work, MLP and CNN with the same architecture and hyperparameters as described in the previous sub-sections were concatenated for regression tasks, as shown in Figure 3.10. One dense layer with 4 neurons and ReLU activation was followed by one layer with one neuron and linear activation to output the predictions.

Variational Autoencoder (VAE) Architecture

The VAE consists of an encoder and a decoder (see Figure 3.11). A regressor model was also included to visualize the latent space of the process parameters. The inputs of the VAE model included images of 128 × 128 pixels and the two conditional parameters (i.e. SF and FO). The encoder model has 6 convolutional layers. The outputs of the encoder were connected to two dense layers for mean μ and standard deviation σ respectively, which were then passed to a sampling layer z with the dimension of 128. A regressor model with 4 dense layers (with neurons of 20, 20, 20 and 6 for each layer; linear activation for the output layer) was built to predict the two conditional parameters from the sampling layer z. The decoder model mirrored the structure of the encoder model with 6 deconvolutional layers. It was used to reconstruct the images from the sampling layer z. The Adadelta optimizer [231] was used to train the encoder, decoder and regressor model simultaneously. The loss for VAE model was the sum of the Kullback-Leibler divergence and the binary cross-entropy of the image reconstruction, while the loss for the regressor model was mean squared error. The train/test split ratio was 70/30. The combined model was trained for 100 epochs with a batch size of 64.

After training, the principal component analysis (PCA) [232] with a radial basis function kernel was employed to reduce the 128-dimensional latent space of the sampling layer z to 2, so that the latent space could be represented by a 2D graph. The images could be represented with the same technique, and their positions in the 2D graph corresponded to their respective process parameters. The images with similar features would cluster in the VAE

latent space. Therefore, the effects of the process parameters on the images could be easily visualized by using this tool.

Conditional Generative Adversarial Networks (cGAN) Architecture

The cGAN model consists of two modules (i.e. a generator and a discriminator) as shown in Figure 3.12. As compared to the basic GAN model, one extra input, namely conditional parameters, was employed for both generator and discriminator models. In our work, two inputs, including a 32-dimension latent space and 2 conditional parameters (i.e. SF and FO) were used for the generator model. More specifically, the 32-dimension latent space was followed by a dense layer with 32768 neurons and LeakyReLU activation function, so that it could be reshaped into a layer of 16×16 with 128 channels. Meanwhile, the 2 conditional parameters were followed by a dense layer and then reshaped into a 16×16 layer with 1 channel. The two 16×16 layers were concatenated to form a shape of 16×16×129. They were then upsampled 3 times by transpose convolutional layers with a stride size of 2 and 128 filters, followed by LeakyReLU functions. The final convolutional layer used hyperbolic tangent activation function and output the images with the shape of 128×128×1.

The conditional parameters adopted from the generator model, together with the generated images and real images, were fed into the discriminator model. Similarly, the two conditional parameters were followed by a dense layer with 16384 neurons and reshaped to a 128×128 layer with 1 channel. This layer was concatenated with the input images of shape 128×128×1 to form a layer of 128×128×2. They were downsampled 3 times by convolutional layers with stride size of 2 and 128 filters followed by LeakyReLU function. The last convolutional layer was activated by sigmoid function to discriminate the real images from generated images under the given conditional parameters. The discriminator was trained using Adam optimization function with the loss of binary cross-entropy. The learning rate was set as 0.0002 and the beta_1 was set at 0.5. The GAN model was trained for 320 epochs with a mini-batch size of 64.

Appendix C Full Dataset for Ti-6Al-4V Samples

Full dataset for Ti-6Al-4V showing 56 parametric combinations with their corresponding UTS, relative density, classes of top surface conditions and Vickers hardness.

Sample No.	SF	FO	UTS (MPa)	Elongation to fracture (%)	Relative density (%)	Top surface condition	HV
1	192	16.2	963	5.5	99.01	P	354.1
2	97	43.7	593.9	2.3	87.71	P	–
3	138	30.1	702.3	3.2	89.31	P	–
4	167	25.9	751.5	3.3	87.86	P	–
5	234	30.7	592.6	3.1	81.27	P	–
6	128	8.3	975.7	12.6	99.93	F	343.9
7	157	20.8	867.1	4.3	94.3	P	–
8	73	37.4	703.8	3.7	90.16	P	–
9	74	7.3	935.1	11.7	99.97	F	338.2
10	40	12.5	846.4	14.1	99.94	F	323.1
11	33	35.9	834	12.3	98.48	P	–
12	150	11.4	983.7	10.9	99.92	F	353.0
13	37	24.1	857.1	10.8	99.75	F	335.3
14	225	6.7	983.7	7.7	99.38	F	358.0
15	117	25	805.1	5.7	90.45	P	–
16	10	28.8	743.2	10.1	99.95	W	298.8
17	110	23	954	8.6	99.05	P	341.5
18	176	36	594.5	2.1	85.37	P	–
19	93	28.3	816.9	4.5	91.84	P	–
20	176	4.3	982.2	14.0	99.79	F	350.4
21	281	28.9	579.7	2.5	79.54	P	–
22	96	1.9	948.6	15.8	99.97	W	337.1
23	234	20.3	757.3	3.3	87.02	P	–
24	192	10.3	984.3	5.9	98.9	F	–
25	122	34.6	660.7	2.5	86.68	P	–
26	23	11.3	706.5	13.5	99.98	W	308.2
27	53	19.8	886.5	12.4	99.99	F	335.9
28	183	12.3	998.8	13.3	99.67	F	364.2
29	29	21.7	781.8	13.0	99.93	F	325.5
30	30	14.5	780.4	15.4	99.9	F	317.7
31	294	17.1	826.5	4.9	93.88	P	–
32	296	39.3	530.4	3.6	79.11	P	–
33	165	0.8	981.2	13.2	99.9	F	346.5
34	154	2.5	993.6	12.3	99.97	F	346.1
35	269	5.3	913.9	4.3	98.86	P	–
36	78	26.9	847.3	5.8	94.78	P	–
37	59	28.7	916.2	10.6	97.39	P	–

38	78	30.3	849.3	4.1	93.91	P	–
39	67	9.9	889.9	15.2	99.95	F	337.5
40	41	4.5	817	11.7	99.96	W	325.7
41	110	42.9	592	3.0	87.95	P	–
42	111	20.1	942.4	9.1	98.01	P	–
43	91	8	926.7	13.5	99.98	F	337.1
44	161	33.5	605.1	2.5	86.42	P	–
45	217	28.2	639.3	2.6	87.43	P	–
46	197	0.4	989.5	13.0	96.9	P	–
47	27	27.5	796.4	11.9	99.97	F	324.9
48	250	43	540.1	3.9	84.02	P	–
49	73	44.6	648.8	4.3	89.56	P	–
50	182	33.4	594.4	2.7	84.07	P	–
51	82	1.8	923.8	13.2	99.93	W	339.0
52	130	16.7	984	13.5	99.01	P	343.8
53	249	9.1	897.3	2.3	97.97	P	–
54	33	1.9	758.9	13.6	99.97	W	317.4
55	236	4.4	947.4	4.3	99.1	P	362.2
56	143	4.6	973.8	13.3	99.89	F	356.0
Arcam’s sample	98	3.0	951.7	13.9	99.87	F	342.0

Appendix D Surface and Microstructure Images of the Ti-6Al-4V Samples

Full dataset for 3D surface topography images of the 56 samples. The scale bar shown on the top left corner applies to all the images in this figure.

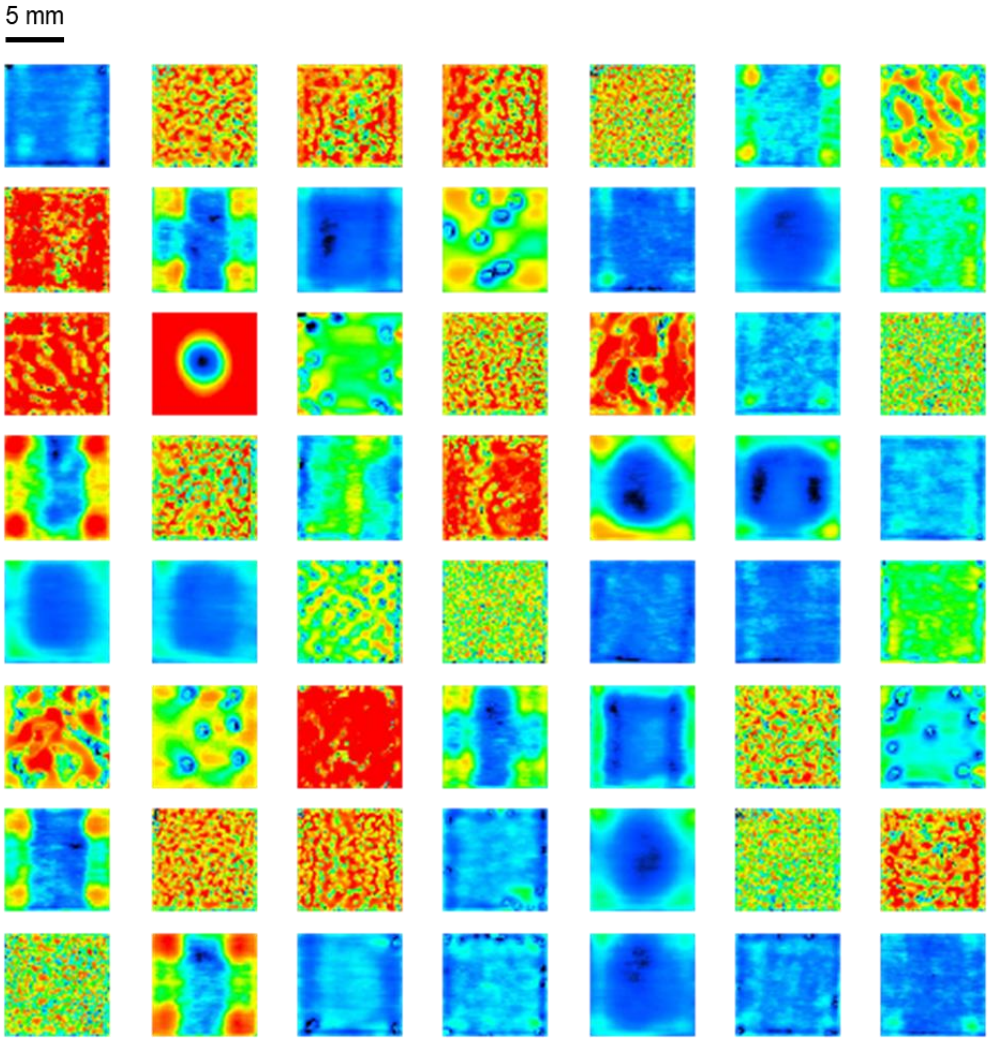

Full dataset for surface morphology images of the 56 samples. The scale bar shown on the top left corner applies to all the images in this figure.

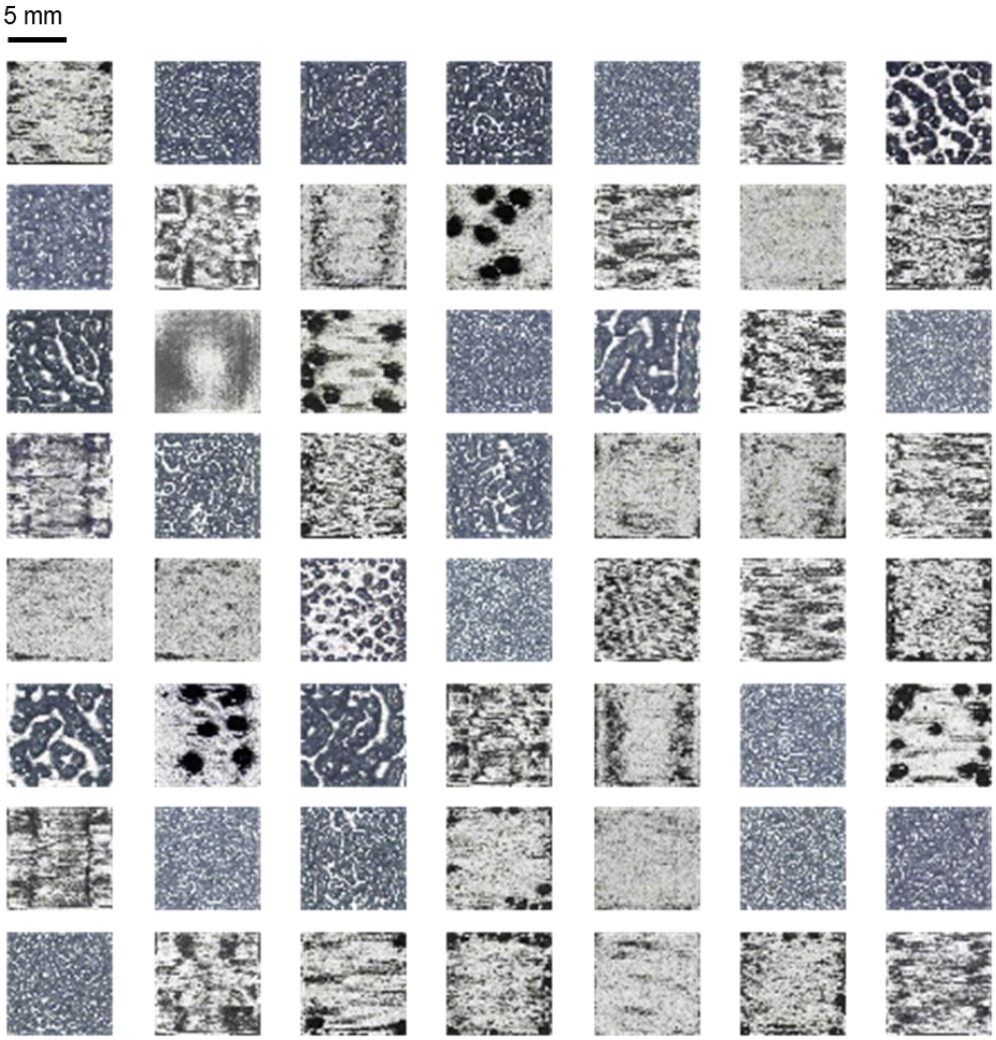

Full dataset for pore microstructure images of the 56 samples. The black background is used for ease of illustration. The scale bar shown on the top left corner applies to all the images in this figure.

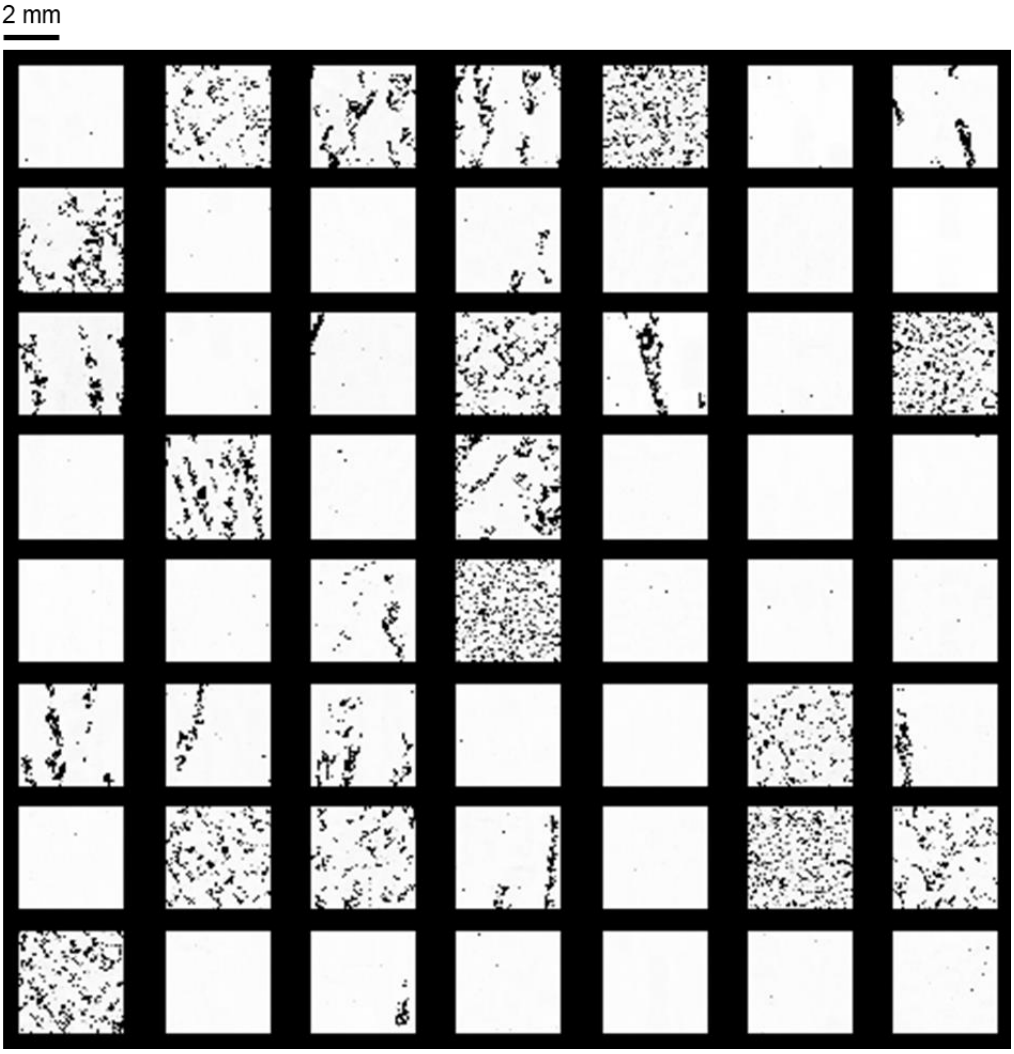

Representative image patches of SEM α/β dual-phase micrographs of the 24 samples including the sample printed using Arcam's default process parameters (enclosed by red box). The 300×300 pixels patches were randomly cropped from the original images of 1280×960 pixels for ease of illustration. The scale bar shown on the top left corner applies to all the images in this figure.

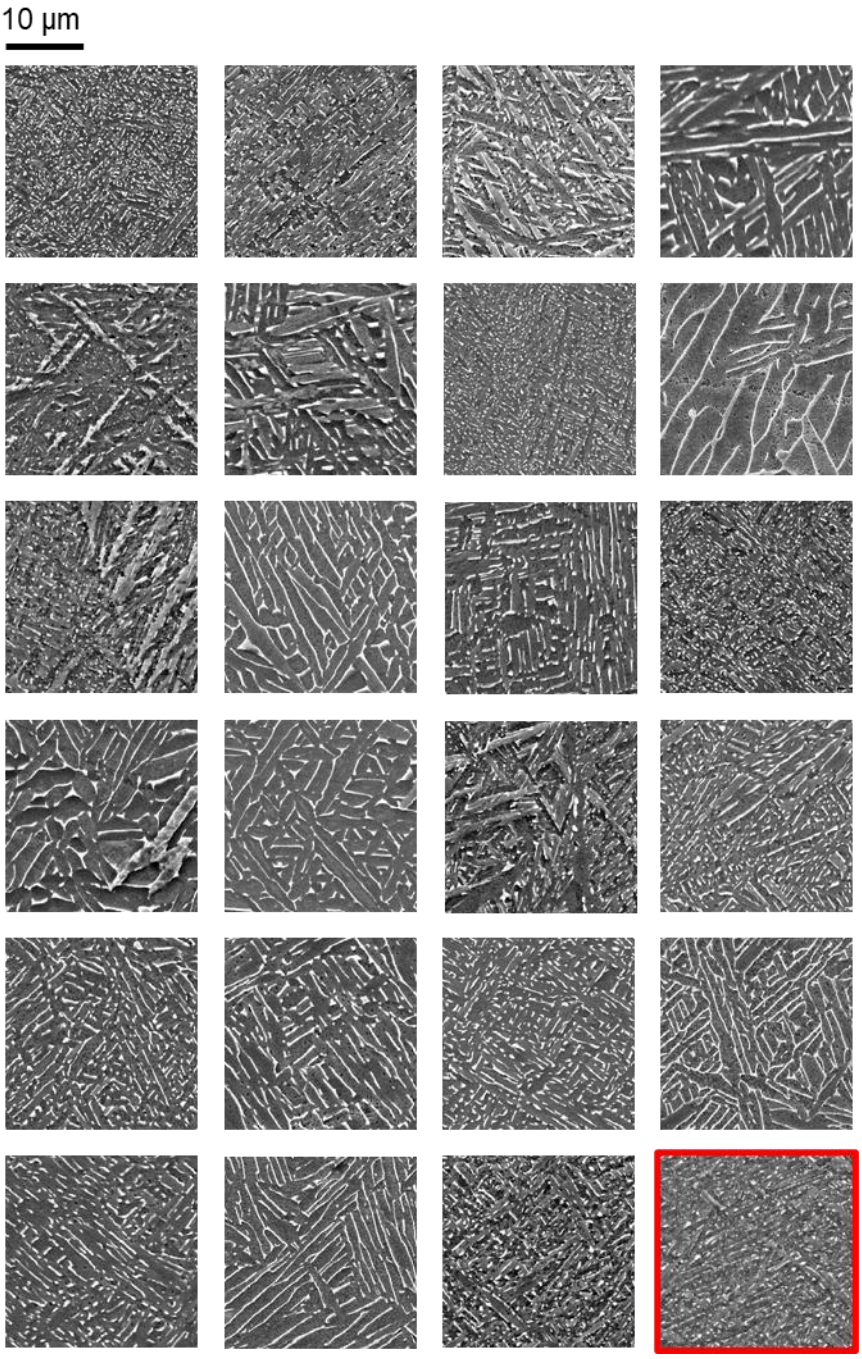

Appendix E Image Data Preparation for Ti-6Al-4V Samples

Referring to Appendix D, the top build surface images were processed to the size of 650 × 650 pixels with a resolution ~ 14 μm per pixel. The pore microstructure images were 750 × 750 pixels with a resolution of ~ 6 μm per pixel. 9 SEM α/β microstructure images were taken at random positions but away from the border regions, with a size of 1280 × 960 pixels and a resolution of ~ 0.1 μm per pixel.

For latent space representation using VAE and principal component analysis (PCA) for different types of images, a few rounds of trials were attempted in order to well cluster the images with similar morphologies and minimize the gaps among different clusters. By doing so, the latent space representation could be continuous in one big cluster instead of being scattered in a few island-shape clusters. Besides, the maximum information of the original images should be retained. To achieve the above two goals, 128 small patches of 250 × 250 pixels were randomly cropped from each surface morphology image, while 128 slightly larger patches of 375 × 375 pixels were randomly cropped from each pore microstructure image. This resulted in 7168 images in the dataset. The 3D surface topography images were not considered as the model has difficulty in clustering images with has red-green-blue (RGB) channels. The cropped images of surface morphology images were rescaled to 128 × 128 pixels to speed up the computation by VAE. 32 patches of 128 × 128 pixels were cropped from the SEM α/β microstructure images, resulting in a total of 6624 patches. It should be noted that for better clustering, the small patches cropped from pore microstructure images were rescaled to 64 × 64 pixels. In this case, the number of convolutional and deconvolutional layers were reduced from 6 to 5 in the corresponding VAE architecture, so that the input and output size could match 64 × 64 pixels.

To map the process-surface and microstructure relationships, cGAN model was firstly used to reconstruct the surface and pore microstructure images. 6 of the samples that served as test data were removed from the dataset. Hence, 50 samples were used as training data. For each surface morphology image, 128 patches with a size of 600 × 600 pixels were randomly extracted. This size is sufficient to represent the features of the surfaces. For pore microstructure images, 128 patches with a size of 650 × 650 pixels were randomly extracted. All the patches were rescaled into 128 × 128 pixels to speed up training. This resulted in a total of 6400 images for training data. To reconstruct SEM α/β microstructure images, the dataset has 23 samples. 3 of the samples served as test data and the remaining 20 samples were used

as training data. For each image, 64 patches with a size of 128 × 128 pixels were randomly extracted to represent the characteristics of the α/β microstructure, as it was assumed that the α/β microstructure features were distributed repeatedly over the images. This resulted in a total of 11520 image patches for training data.

Appendix F Full Dataset for SS316L Samples

Full dataset for SS316L showing 24 parametric combinations with their corresponding relative density, classes of top surface conditions and Vickers hardness.

Sample No.	SF	FO	Relative density (%)	Top surface condition	HV
1	84	42.0	92.21	P	–
2	208	30.3	86.77	P	–
3	97	27.9	94.59	P	–
4	47	44.7	96.25	P	–
5	168	10.3	94.43	P	–
6	158	40.8	86.09	P	–
7	240	3.3	91.81	P	–
8	28	12.5	99.97	W	151.94
9	152	14.9	96.91	P	–
10	116	31.2	95.15	P	–
11	100	4.4	99.32	W	168.84
12	167	36.9	86.46	P	–
13	237	35.6	85.95	P	–
14	92	18.6	99.26	F	168.66
15	49	34.2	95.76	P	–
16	132	8.6	99.22	F	171.6
17	16	18.1	99.96	W	145.3
18	109	43.0	93.92	P	–
19	39	6.8	99.90	W	158.14
20	71	22.8	99.85	F	160.82
21	53	9.2	99.91	W	161.86
22	250	15.6	92.54	P	–
23	183	22.3	91.00	P	–
24	210	19.7	94.56	P	–

References

[1] A. C. F. o. A. M. Technologies and A. C. F. o. A. M. T. S. F. o. Terminology, *Standard terminology for additive manufacturing technologies*. Astm International, 2012.

[2] W. E. Frazier, "Metal Additive Manufacturing: A Review," *Journal of Materials Engineering and Performance,* vol. 23, no. 6, pp. 1917-1928, 2014.

[3] BeAM. (29 Dec). *Magic 800*. Available: https://www.beam-machines.com/products/magic800

[4] X. P. T. Y. Kok, P. Wang, M.L.S. Nai, N.H. Loh, E. Liu, S.B. Tor, "Anisotropy and heterogeneity of microstructure and mechanical properties in metal additive manufacturing: a critical review. Under review," 2017.

[5] C. Körner, "Additive manufacturing of metallic components by selective electron beam melting—a review," *International Materials Reviews,* vol. 61, no. 5, pp. 361-377, 2016.

[6] C. Wang, X. Tan, E. Liu, and S. B. Tor, "Process parameter optimization and mechanical properties for additively manufactured stainless steel 316L parts by selective electron beam melting," *Materials & Design,* vol. 147, pp. 157-166, 2018.

[7] A. EBM. (04 Feb). *Manufacturing Unbound*. Available: http://www.arcam.com/wp-content/uploads/arcamebm-corp.pdf

[8] ARCAM. (19 May). *Arcam A1 The future in implant manufacturing*. Available: http://www.arcam.com/wp-content/uploads/Arcam-A1.pdf

[9] GE. (2018, 19 May). *The Blade Runners: This Factory Is 3D Printing Turbine Parts For The World's Largest Jet Engine*. Available: https://www.ge.com/reports/future-manufacturing-take-look-inside-factory-3d-printing-jet-engine-parts/

[10] G. Welsch, R. Boyer, and E. Collings, *Materials properties handbook: titanium alloys*. ASM international, 1993.

[11] M. Elahinia, N. S. Moghaddam, M. T. Andani, A. Amerinatanzi, B. A. Bimber, and R. F. Hamilton, "Fabrication of NiTi through additive manufacturing: A review," *Progress in Materials Science,* vol. 83, pp. 630-663, 2016.

[12] X. P. T. C. Wang, S.B. Tor, C.S. Lim, "Machine Learning in Additive Manufacturing: State-of-the-Art and Perspectives," *Additive Manufacturing* (Under review 2020).

[13] P. R. Halani and Y. C. Shin, "In situ synthesis and characterization of shape memory alloy nitinol by laser direct deposition," *Metallurgical and Materials Transactions A,* vol. 43, no. 2, pp. 650-657, 2012.

[14] T. Bormann, R. Schumacher, B. Müller, M. Mertmann, and M. de Wild, "Tailoring selective laser melting process parameters for NiTi implants," *Journal of Materials Engineering and Performance,* vol. 21, no. 12, pp. 2519-2524, 2012.

[15] A. Lores, N. Azurmendi, I. Agote, and E. Zuza, "A review on recent developments in binder jetting metal additive manufacturing: materials and process characteristics," *Powder Metallurgy,* vol. 62, no. 5, pp. 267-296, 2019.

[16] C. Wang *et al.*, "Additive manufacturing of NiTi shape memory alloys using pre-mixed powders," *Journal of Materials Processing Technology,* vol. 271, pp. 152-161, 2019.

[17] L. Löber, F. P. Schimansky, U. Kühn, F. Pyczak, and J. Eckert, "Selective laser melting of a beta-solidifying TNM-B1 titanium aluminide alloy," *Journal of Materials Processing Technology,* vol. 214, no. 9, pp. 1852-1860, 2014.

[18] M. Galati and L. Iuliano, "A literature review of powder-based electron beam melting focusing on numerical simulations," *Additive Manufacturing,* vol. 19, pp. 1-20, 2018.

[19] S. Solutions. (29 Dec). *SLM250HL*. Available: https://pdf.directindustry.com/pdf/slm-solutions/slm-250/114591-404513.html

[20] G. Additive. (29 Dec). *Arcam EBM A2X*. Available: https://www.ge.com/additive/sites/default/files/2020-01/EBM_A2X_DS_EN_US_1_v1.pdf

[21] ExOne. (02 Feb). *X125Pro*. Available: https://www.exone.com/en-US/3D-printing-systems/metal-3d-printers/X1-25Pro
[22] Additively. (28 Dec). *Electron Beam Melting (EBM)*. Available: https://www.additively.com/en/learn-about/electron-beam-melting
[23] A. Nouri and A. Sola, "Electron beam melting in biomedical manufacturing," in *Metallic Biomaterials Processing and Medical Device Manufacturing*: Elsevier, 2020, pp. 271-314.
[24] X. Gong, T. Anderson, and K. Chou, "Review on powder-based electron beam additive manufacturing technology," in *International Symposium on Flexible Automation*, 2012, vol. 45110, pp. 507-515: American Society of Mechanical Engineers.
[25] A. Y. Kumar, Y. Bai, A. Eklund, and C. B. Williams, "The effects of Hot Isostatic Pressing on parts fabricated by binder jetting additive manufacturing," *Additive Manufacturing,* vol. 24, pp. 115-124, 2018.
[26] S. Mirzababaei and S. Pasebani, "A review on binder jet additive manufacturing of 316L stainless steel," *Journal of Manufacturing and Materials Processing,* vol. 3, no. 3, p. 82, 2019.
[27] Y. Kok, X. Tan, S. B. Tor, and C. K. Chua, "Fabrication and microstructural characterisation of additive manufactured Ti-6Al-4V parts by electron beam melting: This paper reports that the microstructure and micro-hardness of an EMB part is thickness dependent," *Virtual and Physical Prototyping,* vol. 10, no. 1, pp. 13-21, 2015.
[28] P. Wang *et al.*, "Recent Progress of Additive Manufactured Ti-6Al-4V by Electron Beam Melting," in *27th Annual International Solid Freeform Fabrication Symposium—An Additive Manufacturing Conference, 2016*, 2016, pp. 691-704.
[29] T. R. Mahale, *Electron beam melting of advanced materials and structures*. North Carolina State University, 2009.
[30] Y. Zhong *et al.*, "Additive manufacturing of 316L stainless steel by electron beam melting for nuclear fusion applications," *Journal of nuclear materials,* vol. 486, pp. 234-245, 2017.
[31] B. Cheng, S. Price, J. Lydon, K. Cooper, and K. Chou, "On Process Temperature in Powder-Bed Electron Beam Additive Manufacturing: Model Development and Validation," *Journal of Manufacturing Science and Engineering,* vol. 136, no. 6, p. 061018, 2014.
[32] M. F. Zäh and S. Lutzmann, "Modelling and simulation of electron beam melting," *Production Engineering,* vol. 4, no. 1, pp. 15-23, 2010.
[33] U. Ackelid and M. Svensson, "Additive manufacturing of dense metal parts by electron beam melting," in *Proceedings of the Materials Science and Technology Conference, Pittsburgh, PA, USA*, 2009, vol. 2529.
[34] V. Cain, L. Thijs, J. Van Humbeeck, B. Van Hooreweder, and R. Knutsen, "Crack propagation and fracture toughness of Ti6Al4V alloy produced by selective laser melting," *Additive Manufacturing,* vol. 5, pp. 68-76, 2015.
[35] J. Yu, M. Rombouts, G. Maes, and F. Motmans, "Material properties of Ti6Al4 V parts produced by laser metal deposition," *Physics Procedia,* vol. 39, pp. 416-424, 2012.
[36] V. Juechter, T. Scharowsky, R. Singer, and C. Körner, "Processing window and evaporation phenomena for Ti–6Al–4V produced by selective electron beam melting," *Acta Materialia,* vol. 76, pp. 252-258, 2014.
[37] J. Schwerdtfeger and C. Körner, "Selective electron beam melting of Ti–48Al–2Nb–2Cr: Microstructure and aluminium loss," *Intermetallics,* vol. 49, pp. 29-35, 2014.
[38] I. M. Markl, "Additive manufacturing using selective electron beam melting," *Welding and Cutting,* vol. 16, no. 3, p. 177, 2017.
[39] Arcam. (2017, 18 Nov 2017). *EBM-Built Materials*. Available: http://www.arcam.com/technology/electron-beam-melting/materials/
[40] W. Sames, "Additive manufacturing of Inconel 718 using electron beam melting: Processing, post-processing, & Mechanical properties," 2015.
[41] S. S. Al-Bermani, "An investigation into microstructure and microstructural control of additive layer manufactured Ti-6Al-4V by electron beam melting," University of Sheffield, 2011.

[42] S. Tammas-Williams, H. Zhao, F. Léonard, F. Derguti, I. Todd, and P. Prangnell, "XCT analysis of the influence of melt strategies on defect population in Ti–6Al–4V components manufactured by Selective Electron Beam Melting," *Materials Characterization,* vol. 102, pp. 47-61, 2015.
[43] L.-E. Rännar, A. Koptyug, J. Olsén, K. Saeidi, and Z. Shen, "Hierarchical structures of stainless steel 316L manufactured by Electron Beam Melting," *Additive Manufacturing,* 2017.
[44] W. Ge, F. Lin, and C. Guo, "The effect of scan pattern on microstructure evolution and mechanical properties in electron beam melting Ti47Al2Cr2Nb," in *SFF symposium*, 2014, vol. 25, pp. 500-513.
[45] Z. Sun, X. Tan, S. B. Tor, and W. Y. Yeong, "Selective laser melting of stainless steel 316L with low porosity and high build rates," *Materials & Design,* vol. 104, pp. 197-204, 2016.
[46] J. Schwerdtfeger, R. F. Singer, and C. Körner, "In situ flaw detection by IR-imaging during electron beam melting," *Rapid Prototyping Journal,* vol. 18, no. 4, pp. 259-263, 2012.
[47] J. Schwerdtfeger, R. F. Singer, and C. Körner, "In situ flaw detection by IR‐imaging during electron beam melting," *Rapid Prototyping Journal,* 2012.
[48] J. Dawes, R. Bowerman, and R. Trepleton, "Introduction to the additive manufacturing powder metallurgy supply chain," *Johnson Matthey Technology Review,* vol. 59, no. 3, pp. 243-256, 2015.
[49] R. Li, Y. Shi, Z. Wang, L. Wang, J. Liu, and W. Jiang, "Densification behavior of gas and water atomized 316L stainless steel powder during selective laser melting," *Applied surface science,* vol. 256, no. 13, pp. 4350-4356, 2010.
[50] G. Chen, S. Zhao, P. Tan, J. Wang, C. Xiang, and H. Tang, "A comparative study of Ti-6Al-4V powders for additive manufacturing by gas atomization, plasma rotating electrode process and plasma atomization," *Powder technology,* vol. 333, pp. 38-46, 2018.
[51] A. Simchi, "The role of particle size on the laser sintering of iron powder," *Metallurgical and Materials Transactions B,* vol. 35, no. 5, pp. 937-948, 2004.
[52] H. Gu *et al.*, "Effects of powder variation on the microstructure and tensile strength of Ti6Al4V parts fabricated by selective laser melting," in *Proceedings of the 25th annual international solid freeform fabrication symposium, austin, tx, usa*, 2014, pp. 4-6.
[53] G. Additive. (28 JUN). *Arcam EBM*. Available: https://www.ge.com/additive/who-we-are/about-arcam
[54] QBEAM. (28 JUN). *QBEAM3D*. Available: http://www.qbeam-3d.com/default.asp
[55] S. METAL. (19 JUL 2020). *SAILONG METAL*. Available: http://www.slmetal.com/en/index.php?m=Product&a=index&id=30
[56] freemelt. (19 JUL 2020). *Freemelt ONE*. Available: https://freemelt.com/freemelt-one/
[57] Arcam. (17 Jan). *Ti6Al4V Titanium Alloy*. Available: https://pdf.directindustry.com/pdf/arcam/titanium-ti6al4v/19734-644503.html
[58] X. Tan *et al.*, "Graded microstructure and mechanical properties of additive manufactured Ti–6Al–4V via electron beam melting," *Acta Materialia,* vol. 97, pp. 1-16, 2015.
[59] S. M. Gaytan *et al.*, "Comparison of Microstructures and Mechanical Properties for Solid and Mesh Cobalt-Base Alloy Prototypes Fabricated by Electron Beam Melting," *Metallurgical and Materials Transactions A,* journal article vol. 41, no. 12, pp. 3216-3227, December 01 2010.
[60] M. Kirka, K. Unocic, N. Raghavan, F. Medina, R. Dehoff, and S. Babu, "Microstructure development in electron beam-melted Inconel 718 and associated tensile properties," *Jom,* vol. 68, no. 3, pp. 1012-1020, 2016.
[61] L. E. Murr *et al.*, "Microstructural architecture, microstructures, and mechanical properties for a nickel-base superalloy fabricated by electron beam melting," *Metallurgical and Materials Transactions A,* vol. 42, no. 11, pp. 3491-3508, 2011.
[62] Y. Lei *et al.*, "Process optimization and mechanical property investigation of non-weldable superalloy Alloy713ELC manufactured with selective electron beam melting," *Materials Science and Engineering: A,* p. 139485, 2020.

[63] M. Ramsperger, R. F. Singer, and C. Körner, "Microstructure of the nickel-base superalloy CMSX-4 fabricated by selective electron beam melting," *Metallurgical and Materials Transactions A,* vol. 47, no. 3, pp. 1469-1480, 2016.
[64] L. E. Murr *et al.*, "Microstructures of Rene 142 nickel-based superalloy fabricated by electron beam melting," *Acta Materialia,* vol. 61, no. 11, pp. 4289-4296, 2013/06/01/ 2013.
[65] L. E. Murr *et al.*, "Characterization of titanium aluminide alloy components fabricated by additive manufacturing using electron beam melting," *Acta Materialia,* vol. 58, no. 5, pp. 1887-1894, 2010/03/01/ 2010.
[66] D. Hu, X. Wu, and M. Loretto, "Advances in optimisation of mechanical properties in cast TiAl alloys," *Intermetallics,* vol. 13, no. 9, pp. 914-919, 2005.
[67] S. Biamino *et al.*, "Electron beam melting of Ti–48Al–2Cr–2Nb alloy: Microstructure and mechanical properties investigation," *Intermetallics,* vol. 19, no. 6, pp. 776-781, 2011/06/01/ 2011.
[68] H. Tang, G. Yang, W. Jia, W. He, S. Lu, and M. Qian, "Additive manufacturing of a high niobium-containing titanium aluminide alloy by selective electron beam melting," *Materials Science and Engineering: A,* vol. 636, pp. 103-107, 2015.
[69] K. Kuwabara, H. Shiratori, T. Fujieda, K. Yamanaka, Y. Koizumi, and A. Chiba, "Mechanical and corrosion properties of AlCoCrFeNi high-entropy alloy fabricated with selective electron beam melting," *Additive Manufacturing,* vol. 23, pp. 264-271, 2018.
[70] T. Fujieda *et al.*, "CoCrFeNiTi-based high-entropy alloy with superior tensile strength and corrosion resistance achieved by a combination of additive manufacturing using selective electron beam melting and solution treatment," *Materials Letters,* vol. 189, pp. 148-151, 2017.
[71] R. Gao, L. Zeng, H. Ding, T. Zhang, X. Wang, and Q. Fang, "Characterization of oxide dispersion strengthened ferritic steel fabricated by electron beam selective melting," *Materials & Design,* vol. 89, pp. 1171-1180, 2016.
[72] A. Jahn, A. Kovalev, A. Weiß, S. Wolf, L. Krüger, and P. R. Scheller, "Temperature Depending Influence of the Martensite Formation on the Mechanical Properties of High‐Alloyed Cr‐Mn‐Ni As‐Cast Steels," *steel research international,* vol. 82, no. 1, pp. 39-44, 2011.
[73] M. Droste, J. Günther, D. Kotzem, F. Walther, T. Niendorf, and H. Biermann, "Cyclic deformation behavior of a damage tolerant CrMnNi TRIP steel produced by electron beam melting," *International Journal of Fatigue,* vol. 114, pp. 262-271, 2018.
[74] C. A. Terrazas *et al.*, "Fabrication and characterization of high-purity niobium using electron beam melting additive manufacturing technology," *The International Journal of Advanced Manufacturing Technology,* vol. 84, no. 5-8, pp. 1115-1126, 2016.
[75] L. E. Murr *et al.*, "Microstructures and properties of solid and reticulated mesh components of pure iron fabricated by electron beam melting," *Journal of materials research and technology,* vol. 2, no. 4, pp. 376-385, 2013.
[76] H. Peng, C. Liu, H. Guo, Y. Yuan, S. Gong, and H. Xu, "Fabrication of WCp/NiBSi metal matrix composite by electron beam melting," *Materials Science and Engineering: A,* vol. 666, pp. 320-323, 2016.
[77] S. Momeni, R. Guschlbauer, F. Osmanlic, and C. Körner, "Selective electron beam melting of a copper-chrome powder mixture," *Materials Letters,* vol. 223, pp. 250-252, 2018.
[78] Q. Zhou *et al.*, "Selective electron beam melting of NiTi: Microstructure, phase transformation and mechanical properties," *Materials Science and Engineering: A,* vol. 744, pp. 290-298, 2019.
[79] B. E. Carroll, T. A. Palmer, and A. M. Beese, "Anisotropic tensile behavior of Ti–6Al–4V components fabricated with directed energy deposition additive manufacturing," *Acta Materialia,* vol. 87, pp. 309-320, 2015.
[80] D. Ding, Z. Pan, D. Cuiuri, and H. Li, "Wire-feed additive manufacturing of metal components: technologies, developments and future interests," *The International Journal of Advanced Manufacturing Technology,* vol. 81, no. 1, pp. 465-481, 2015.

[81] Y. Kok *et al.*, "Anisotropy and heterogeneity of microstructure and mechanical properties in metal additive manufacturing: A critical review," *Materials & Design,* vol. 139, no. Supplement C, pp. 565-586, 2018/02/05/ 2018.
[82] M. Seifi, A. Salem, J. Beuth, O. Harrysson, and J. J. Lewandowski, "Overview of materials qualification needs for metal additive manufacturing," *Jom,* vol. 68, no. 3, pp. 747-764, 2016.
[83] A. E. System. (29 April 2020). *Ti6Al4V ELI Titanium Alloy*. Available: http://www.arcam.com/wp-content/uploads/Arcam-Ti6Al4V-ELI-Titanium-Alloy.pdf
[84] B. Babu, "Physically based model for plasticity and creep of Ti-6Al-4V," Luleå tekniska universitet, 2008.
[85] X. Tan *et al.*, "Revealing martensitic transformation and α/β interface evolution in electron beam melting three-dimensional-printed Ti-6Al-4V," *Scientific reports,* vol. 6, p. 26039, 2016.
[86] W. Xu *et al.*, "Additive manufacturing of strong and ductile Ti–6Al–4V by selective laser melting via in situ martensite decomposition," *Acta Materialia,* vol. 85, pp. 74-84, 2015.
[87] A. W. Society. (1998). *Classification of Stainless Steel*. Available: https://app.aws.org/wj/1998/11/kotecki/
[88] P. Korinko and S. Malene, "Considerations for the weldability of types 304L and 316L stainless steel," *practical failure analysis,* vol. 1, no. 4, pp. 61-68, 2001.
[89] A. Saboori *et al.*, "An investigation on the effect of powder recycling on the microstructure and mechanical properties of AISI 316L produced by Directed Energy Deposition," *Materials Science and Engineering: A,* vol. 766, p. 138360, 2019.
[90] D. Kianersi, A. Mostafaei, and A. A. Amadeh, "Resistance spot welding joints of AISI 316L austenitic stainless steel sheets: Phase transformations, mechanical properties and microstructure characterizations," *Materials & Design,* vol. 61, pp. 251-263, 2014.
[91] B. Weiss and R. Stickler, "Phase instabilities during high temperature exposure of 316 austenitic stainless steel," *Metallurgical and Materials Transactions B,* vol. 3, no. 4, pp. 851-866, 1972.
[92] G. Miranda *et al.*, "Predictive models for physical and mechanical properties of 316L stainless steel produced by selective laser melting," *Materials Science and Engineering: A,* vol. 657, pp. 43-56, 2016.
[93] J. Cherry, H. Davies, S. Mehmood, N. Lavery, S. Brown, and J. Sienz, "Investigation into the effect of process parameters on microstructural and physical properties of 316L stainless steel parts by selective laser melting," *The International Journal of Advanced Manufacturing Technology,* vol. 76, no. 5-8, pp. 869-879, 2015.
[94] S. Tsopanos *et al.*, "The influence of processing parameters on the mechanical properties of selectively laser melted stainless steel microlattice structures," *Journal of Manufacturing Science and Engineering,* vol. 132, no. 4, p. 041011, 2010.
[95] Y. M. Wang *et al.*, "Additively manufactured hierarchical stainless steels with high strength and ductility," *Nature materials,* vol. 17, no. 1, pp. 63-71, 2018.
[96] Z. Sun, X. Tan, S. B. Tor, and C. K. Chua, "Simultaneously enhanced strength and ductility for 3D-printed stainless steel 316L by selective laser melting," *NPG Asia Materials,* vol. 10, no. 4, pp. 127-136, 2018.
[97] D. C. Lagoudas, *Shape memory alloys: modeling and engineering applications*. Springer Science & Business Media, 2008.
[98] C. M. Wayman and K. Ōtsuka, *Shape memory materials*. Cambridge University Press, 1998.
[99] R. F. Hamilton, T. A. Palmer, and B. A. Bimber, "Spatial characterization of the thermal-induced phase transformation throughout as-deposited additive manufactured NiTi bulk builds," *Scripta Materialia,* vol. 101, pp. 56-59, 2015/05/01/ 2015.
[100] H. Rojob, "Innovative near-surface mounted iron-based shape memory alloy for strengthening structures," University of Calgary, 2017.

[101] J. Khalil-Allafi, A. Dlouhy, and G. Eggeler, "Ni4Ti3-precipitation during aging of NiTi shape memory alloys and its influence on martensitic phase transformations," *Acta Materialia,* vol. 50, no. 17, pp. 4255-4274, 2002.
[102] M. N. Mokgalaka, S. L. Pityana, P. A. I. Popoola, and T. Mathebula, "NiTi intermetallic surface coatings by laser metal deposition for improving wear properties of Ti-6Al-4V substrates," *Advances in materials Science and engineering,* vol. 2014, 2014.
[103] G. Lütjering and J. C. Williams, "Titanium Based Intermetallics," in *Titanium*Berlin, Heidelberg: Springer Berlin Heidelberg, 2003, pp. 289-312.
[104] C. Velmurugan, V. Senthilkumar, S. Dinesh, and D. Arulkirubakaran, "Review on phase transformation behavior of NiTi shape memory alloys," *Materials Today: Proceedings,* vol. 5, no. 6, pp. 14597-14606, 2018.
[105] S. Li, H. Hassanin, M. M. Attallah, N. J. Adkins, and K. Essa, "The development of TiNi-based negative Poisson's ratio structure using selective laser melting," *Acta Materialia,* vol. 105, pp. 75-83, 2016.
[106] S. Saedi, A. S. Turabi, M. Taheri Andani, C. Haberland, H. Karaca, and M. Elahinia, "The influence of heat treatment on the thermomechanical response of Ni-rich NiTi alloys manufactured by selective laser melting," *Journal of Alloys and Compounds,* vol. 677, pp. 204-210, 2016/08/25/ 2016.
[107] M. H. Elahinia, *Shape memory alloy actuators: design, fabrication, and experimental evaluation*. John Wiley & Sons, 2016.
[108] B. V. Krishna, S. Bose, and A. Bandyopadhyay, "Laser Processing of Net-Shape NiTi Shape Memory Alloy," *Metallurgical and Materials Transactions A,* journal article vol. 38, no. 5, pp. 1096-1103, May 01 2007.
[109] J. J. Marattukalam, V. K. Balla, M. Das, S. Bontha, and S. K. Kalpathy, "Effect of heat treatment on microstructure, corrosion, and shape memory characteristics of laser deposited NiTi alloy," *Journal of Alloys and Compounds,* vol. 744, pp. 337-346, 2018.
[110] J. Ma *et al.*, "Spatial control of functional response in 4D-printed active metallic structures," *Scientific reports,* vol. 7, p. 46707, 2017.
[111] M. D. Hayat, G. Chen, N. Liu, S. Khan, H. P. Tang, and P. Cao, "Physical and Tensile Properties of NiTi Alloy by Selective Electron Beam Melting," in *Key Engineering Materials*, 2018, vol. 770, pp. 148-154: Trans Tech Publ.
[112] A. M. Aboutaleb, L. Bian, A. Elwany, N. Shamsaei, S. M. Thompson, and G. Tapia, "Accelerated process optimization for laser-based additive manufacturing by leveraging similar prior studies," *IISE Transactions,* vol. 49, no. 1, pp. 31-44, 2017.
[113] H. Ghasemi-Tabasi, J. Jhabvala, E. Boillat, T. Ivas, R. Drissi-Daoudi, and R. E. Logé, "An effective rule for translating optimal selective laser melting processing parameters from one material to another," *Additive Manufacturing,* vol. 36, p. 101496, 2020.
[114] P. Wang, W. J. Sin, M. L. S. Nai, and J. Wei, "Effects of processing parameters on surface roughness of additive manufactured Ti-6Al-4V via electron beam melting," *Materials,* vol. 10, no. 10, p. 1121, 2017.
[115] X. Ding *et al.*, "Microstructural control of alloy 718 fabricated by electron beam melting with expanded processing window by adaptive offset method," *Materials Science and Engineering: A,* vol. 764, p. 138058, 2019.
[116] C. Wang, X. Tan, S. B. Tor, and C. Lim, "Machine learning in additive manufacturing: State-of-the-art and perspectives," *Additive Manufacturing,* p. 101538, 2020.
[117] K. Aoyagi, H. Wang, H. Sudo, and A. Chiba, "Simple method to construct process maps for additive manufacturing using a support vector machine," *Additive Manufacturing,* vol. 27, pp. 353-362, 2019.
[118] W. Yan *et al.*, "Meso-scale modeling of multiple-layer fabrication process in selective electron beam melting: inter-layer/track voids formation," *Materials & Design,* vol. 141, pp. 210-219, 2018.

[119] B. Durakovic, "Design of experiments application, concepts, examples: State of the art," *Periodicals of Engineering and Natural Sciences,* vol. 5, no. 3, 2017.
[120] D. C. MONTGOMERY, "Design And Analysis of Experiments, Eight Ed., A John Wiley & Sons," ed: Inc, 2013.
[121] Y. L. Yap, C. Wang, S. L. Sing, V. Dikshit, W. Y. Yeong, and J. Wei, "Material jetting additive manufacturing: An experimental study using designed metrological benchmarks," *Precision engineering,* vol. 50, pp. 275-285, 2017.
[122] Y. W. Chen, H. V. Lee, and S. B. Abd Hamid, "A response surface methodology study: Effects of trivalent Cr3+ metal ion-catalyzed hydrolysis on nanocellulose crystallinity and yield," *BioResources,* vol. 11, no. 2, pp. 4645-4662, 2016.
[123] D. H. Abdeen and B. R. Palmer, "Effect of processing parameters of electron beam melting machine on properties of Ti-6Al-4V parts," *Rapid Prototyping Journal,* 2016.
[124] S. Franchitti *et al.*, "Investigation on Electron Beam Melting: Dimensional accuracy and process repeatability," *Vacuum,* vol. 157, pp. 340-348, 2018.
[125] A. Kirchner, B. Klöden, J. Luft, T. Weißgärber, and B. Kieback, "Process window for electron beam melting of Ti-6Al-4V," *Powder Metallurgy,* vol. 58, no. 4, pp. 246-249, 2015.
[126] S. L. Sing, W. Y. Yeong, F. E. Wiria, and B. Tay, "Characterization of titanium lattice structures fabricated by selective laser melting using an adapted compressive test method," *Experimental Mechanics,* vol. 56, no. 5, pp. 735-748, 2016.
[127] G. Casalino, S. Campanelli, N. Contuzzi, and A. Ludovico, "Experimental investigation and statistical optimisation of the selective laser melting process of a maraging steel," *Optics & Laser Technology,* vol. 65, pp. 151-158, 2015.
[128] N. Read, W. Wang, K. Essa, and M. M. Attallah, "Selective laser melting of AlSi10Mg alloy: Process optimisation and mechanical properties development," *Materials & Design (1980-2015),* vol. 65, pp. 417-424, 2015/01/01/ 2015.
[129] J. Mutua, S. Nakata, T. Onda, and Z.-C. Chen, "Optimization of selective laser melting parameters and influence of post heat treatment on microstructure and mechanical properties of maraging steel," *Materials & Design,* vol. 139, pp. 486-497, 2018.
[130] H. Gong *et al.*, "Melt pool characterization for selective laser melting of Ti-6Al-4V pre-alloyed powder," in *Solid freeform fabrication symposium*, 2014, pp. 256-267.
[131] N. A. Kistler, D. J. Corbin, A. R. Nassar, E. W. Reutzel, and A. M. Beese, "Effect of processing conditions on the microstructure, porosity, and mechanical properties of Ti-6Al-4V repair fabricated by directed energy deposition," *Journal of Materials Processing Technology,* vol. 264, pp. 172-181, 2019.
[132] B. Bax, R. Rajput, R. Kellet, and M. Reisacher, "Systematic evaluation of process parameter maps for laser cladding and directed energy deposition," *Additive Manufacturing,* vol. 21, pp. 487-494, 2018.
[133] H. Chen and Y. F. Zhao, "Process parameters optimization for improving surface quality and manufacturing accuracy of binder jetting additive manufacturing process," *Rapid Prototyping Journal,* 2016.
[134] E. G. Learned-Miller, "Introduction to supervised learning," *I: Department of Computer Science, University of Massachusetts,* 2014.
[135] W. Daelemans, V. Hoste, F. De Meulder, and B. Naudts, "Combined optimization of feature selection and algorithm parameters in machine learning of language," in *European Conference on Machine Learning*, 2003, pp. 84-95: Springer.
[136] S. K. Murthy, "Automatic construction of decision trees from data: A multi-disciplinary survey," *Data mining and knowledge discovery,* vol. 2, no. 4, pp. 345-389, 1998.
[137] M. Pal, "Random forest classifier for remote sensing classification," *International Journal of Remote Sensing,* vol. 26, no. 1, pp. 217-222, 2005.
[138] C.-F. Lin and S.-D. Wang, "Fuzzy support vector machines," *IEEE transactions on neural networks,* vol. 13, no. 2, pp. 464-471, 2002.

[139] C. K. Williams and C. E. Rasmussen, *Gaussian processes for machine learning* (no. 3). MIT press Cambridge, MA, 2006.
[140] M. W. Gardner and S. Dorling, "Artificial neural networks (the multilayer perceptron)—a review of applications in the atmospheric sciences," *Atmospheric environment,* vol. 32, no. 14-15, pp. 2627-2636, 1998.
[141] J.-S. Jang, "ANFIS: adaptive-network-based fuzzy inference system," *IEEE transactions on systems, man, and cybernetics,* vol. 23, no. 3, pp. 665-685, 1993.
[142] W. Zaremba, I. Sutskever, and O. Vinyals, "Recurrent neural network regularization," *arXiv preprint arXiv:1409.2329,* 2014.
[143] E. Olakanmi, R. Cochrane, and K. Dalgarno, "Densification mechanism and microstructural evolution in selective laser sintering of Al–12Si powders," *Journal of Materials Processing Technology,* vol. 211, no. 1, pp. 113-121, 2011.
[144] C. Wang *et al.*, "Additive manufacturing of NiTi shape memory alloys using pre-mixed powders," *Journal of Materials Processing Technology,* vol. 271, pp. 152-161, 2019.
[145] M. Mozaffar *et al.*, "Data-driven prediction of the high-dimensional thermal history in directed energy deposition processes via recurrent neural networks," *Manufacturing letters,* vol. 18, pp. 35-39, 2018.
[146] C. Tang, J. Tan, and C. Wong, "A numerical investigation on the physical mechanisms of single track defects in selective laser melting," *International Journal of Heat and Mass Transfer,* vol. 126, pp. 957-968, 2018.
[147] M. Zhang *et al.*, "High cycle fatigue life prediction of laser additive manufactured stainless steel: A machine learning approach," *International Journal of Fatigue,* p. 105194, 2019.
[148] A. Singh, D. Cooper, N. Blundell, G. Gibbons, and D. Pratihar, "Modelling of direct metal laser sintering of EOS DM20 bronze using neural networks and genetic algorithms," in *Proceedings of the 37th International MATADOR Conference*, 2012, p. 395: Springer Science & Business Media.
[149] G. Tapia, S. Khairallah, M. Matthews, W. E. King, and A. Elwany, "Gaussian process-based surrogate modeling framework for process planning in laser powder-bed fusion additive manufacturing of 316L stainless steel," *The International Journal of Advanced Manufacturing Technology,* vol. 94, no. 9-12, pp. 3591-3603, 2018.
[150] G. Tapia, A. Elwany, and H. Sang, "Prediction of porosity in metal-based additive manufacturing using spatial Gaussian process models," *Additive Manufacturing,* vol. 12, pp. 282-290, 2016.
[151] B. Kappes, S. Moorthy, D. Drake, H. Geerlings, and A. Stebner, "Machine learning to optimize additive manufacturing parameters for laser powder bed fusion of Inconel 718," in *Proceedings of the 9th International Symposium on Superalloy 718 & Derivatives: Energy, Aerospace, and Industrial Applications*, 2018, pp. 595-610: Springer.
[152] W. Zhang, A. Mehta, P. S. Desai, and C. Higgs, "Machine learning enabled powder spreading process map for metal additive manufacturing (AM)," in *Int. Solid Free Form Fabr. Symp. Austin, TX*, 2017, pp. 1235-1249.
[153] A. Douard, C. Grandvallet, F. Pourroy, and F. Vignat, "An Example of Machine Learning Applied in Additive Manufacturing," in *2018 IEEE International Conference on Industrial Engineering and Engineering Management (IEEM)*, 2018, pp. 1746-1750: IEEE.
[154] J. Xiong, G. Zhang, J. Hu, and L. Wu, "Bead geometry prediction for robotic GMAW-based rapid manufacturing through a neural network and a second-order regression analysis," *Journal of Intelligent Manufacturing,* vol. 25, no. 1, pp. 157-163, 2014.
[155] Y. Li, Y. Sun, Q. Han, G. Zhang, and I. Horváth, "Enhanced beads overlapping model for wire and arc additive manufacturing of multi-layer multi-bead metallic parts," *Journal of Materials Processing Technology,* vol. 252, pp. 838-848, 2018.
[156] F. Caiazzo and A. Caggiano, "Laser direct metal deposition of 2024 Al alloy: trace geometry prediction via machine learning," *Materials,* vol. 11, no. 3, p. 444, 2018.

[157] Z. Lu, D. Li, B. Lu, A. Zhang, G. Zhu, and G. Pi, "The prediction of the building precision in the Laser Engineered Net Shaping process using advanced networks," *Optics and Lasers in Engineering,* vol. 48, no. 5, pp. 519-525, 2010.
[158] J. J. Lewandowski and M. Seifi, "Metal additive manufacturing: a review of mechanical properties," *Annual review of materials research,* vol. 46, pp. 151-186, 2016.
[159] Keyence. (05 Mar). *3D Laser Scanning Microscope*. Available: https://engineering.unl.edu/downloads/files/UserManual-KeyenceVK-X200K.pdf
[160] M. Panalytical. (22 Dec). *Mastersizer 3000*. Available: https://www.malvernpanalytical.com/en/products/product-range/mastersizer-range/mastersizer-3000
[161] M. D. Abràmoff, P. J. Magalhães, and S. J. Ram, "Image processing with ImageJ," *Biophotonics international,* vol. 11, no. 7, pp. 36-42, 2004.
[162] R. J. Boik, "Testing additivity in two-way classifications with no replications: the locally best invariant test," *Journal of Applied Statistics,* vol. 20, no. 1, pp. 41-55, 1993.
[163] Y. Ma *et al.*, "EasySVM: A visual analysis approach for open-box support vector machines," *Computational Visual Media,* vol. 3, no. 2, pp. 161-175, 2017.
[164] P. Cunningham and S. J. Delany, "k-Nearest Neighbour Classifiers," *arXiv preprint arXiv:2004.04523,* 2020.
[165] Y. H. Cho, J. K. Kim, and S. H. Kim, "A personalized recommender system based on web usage mining and decision tree induction," *Expert systems with Applications,* vol. 23, no. 3, pp. 329-342, 2002.
[166] Y. LeCun, Y. Bengio, and G. Hinton, "Deep learning," *nature,* vol. 521, no. 7553, pp. 436-444, 2015.
[167] D. P. Kingma and M. Welling, "Auto-encoding variational bayes," *arXiv preprint arXiv:1312.6114,* 2013.
[168] M. Mirza and S. Osindero, "Conditional generative adversarial nets," *arXiv preprint arXiv:1411.1784,* 2014.
[169] S. J. Pan and Q. Yang, "A survey on transfer learning," *IEEE Transactions on knowledge and data engineering,* vol. 22, no. 10, pp. 1345-1359, 2009.
[170] R. Casati, J. Lemke, and M. Vedani, "Microstructure and fracture behavior of 316L austenitic stainless steel produced by selective laser melting," *Journal of Materials Science & Technology,* vol. 32, no. 8, pp. 738-744, 2016.
[171] A. Mertens, S. Reginster, Q. Contrepois, T. Dormal, O. Lemaire, and J. Lecomte-Beckers, "Microstructures and mechanical properties of stainless steel AISI 316L processed by selective laser melting," in *Mater. Sci. Forum*, 2014, vol. 783, no. 786, pp. 898-903.
[172] B. Zhang, L. Dembinski, and C. Coddet, "The study of the laser parameters and environment variables effect on mechanical properties of high compact parts elaborated by selective laser melting 316L powder," *Materials Science and Engineering: A,* vol. 584, pp. 21-31, 2013.
[173] W. E. Luecke and J. A. Slotwinski, "Mechanical properties of austenitic stainless steel made by additive manufacturing," *Journal of research of the National Institute of Standards and Technology,* vol. 119, p. 398, 2014.
[174] C. Song, Y. Yang, Y. Wang, D. Wang, and J. Yu, "Research on rapid manufacturing of CoCrMo alloy femoral component based on selective laser melting," *The International Journal of Advanced Manufacturing Technology,* vol. 75, no. 1-4, pp. 445-453, 2014.
[175] T. Vilaro, C. Colin, and J.-D. Bartout, "As-fabricated and heat-treated microstructures of the Ti-6Al-4V alloy processed by selective laser melting," *Metallurgical and Materials Transactions A,* vol. 42, no. 10, pp. 3190-3199, 2011.
[176] M. Simonelli, Y. Y. Tse, and C. Tuck, "Effect of the build orientation on the Mechanical Properties and Fracture Modes of SLM Ti–6Al–4V," *Materials Science and Engineering: A,* vol. 616, pp. 1-11, 2014.

[177] A. Mertens *et al.*, "Mechanical properties of alloy Ti–6Al–4V and of stainless steel 316L processed by selective laser melting: Influence of out-of-equilibrium microstructures," *Powder Metallurgy,* vol. 57, no. 3, pp. 184-189, 2014.

[178] Y. Zhong, L. Liu, S. Wikman, D. Cui, and Z. Shen, "Intragranular cellular segregation network structure strengthening 316L stainless steel prepared by selective laser melting," *Journal of Nuclear Materials,* vol. 470, pp. 170-178, 2016.

[179] D. Wang, C. Song, Y. Yang, and Y. Bai, "Investigation of crystal growth mechanism during selective laser melting and mechanical property characterization of 316L stainless steel parts," *Materials & Design,* vol. 100, pp. 291-299, 2016.

[180] S. Price, B. Cheng, J. Lydon, K. Cooper, and K. Chou, "On process temperature in powder-bed electron beam additive manufacturing: process parameter effects," *Journal of Manufacturing Science and Engineering,* vol. 136, no. 6, p. 061019, 2014.

[181] H. Gong, K. Rafi, N. Karthik, T. Starr, and B. Stucker, "Defect morphology in Ti–6Al–4V parts fabricated by selective laser melting and electron beam melting," in *24rd Annual International Solid Freeform Fabrication Symposium—An Additive Manufacturing Conference, Austin, TX, Aug*, 2013, pp. 12-14.

[182] A. Yadollahi, N. Shamsaei, S. M. Thompson, and D. W. Seely, "Effects of process time interval and heat treatment on the mechanical and microstructural properties of direct laser deposited 316L stainless steel," *Materials Science and Engineering: A,* vol. 644, pp. 171-183, 2015.

[183] N. Shamsaei, A. Yadollahi, L. Bian, and S. M. Thompson, "An overview of Direct Laser Deposition for additive manufacturing; Part II: Mechanical behavior, process parameter optimization and control," *Additive Manufacturing,* vol. 8, pp. 12-35, 2015.

[184] M. Montero Sistiaga, S. Nardone, C. Hautfenne, and J. Van Humbeeck, "Effect of heat treatment of 316L stainless steel produced by selective laser melting (SLM)," 2016.

[185] B. Zheng, Y. Zhou, J. Smugeresky, J. Schoenung, and E. Lavernia, "Thermal behavior and microstructure evolution during laser deposition with laser-engineered net shaping: part II. Experimental investigation and discussion," *Metallurgical and Materials Transactions A,* vol. 39, no. 9, pp. 2237-2245, 2008.

[186] B. Huang, X. Chen, S. Pang, and R. Hu, "A three-dimensional model of coupling dynamics of keyhole and weld pool during electron beam welding," *International Journal of Heat and Mass Transfer,* vol. 115, pp. 159-173, 2017.

[187] K. Zhang, J. Zou, T. Grosdidier, C. Dong, and D. Yang, "Improved pitting corrosion resistance of AISI 316L stainless steel treated by high current pulsed electron beam," *Surface and Coatings Technology,* vol. 201, no. 3-4, pp. 1393-1400, 2006.

[188] J. Olsén, Z. Shen, L. Liu, A. Koptyug, and L.-E. Rännar, "Micro- and macro-structural heterogeneities in 316L stainless steel prepared by electron-beam melting," *Materials Characterization,* vol. 141, pp. 1-7, 2018/07/01/ 2018.

[189] Y. Zhong *et al.*, "Additive manufacturing of ITER first wall panel parts by two approaches: Selective laser melting and electron beam melting," *Fusion Engineering and Design,* vol. 116, pp. 24-33, 2017/03/01/ 2017.

[190] M. Ziętala *et al.*, "The microstructure, mechanical properties and corrosion resistance of 316 L stainless steel fabricated using laser engineered net shaping," *Materials Science and Engineering: A,* vol. 677, pp. 1-10, 2016.

[191] K. Saeidi, X. Gao, Y. Zhong, and Z. J. Shen, "Hardened austenite steel with columnar sub-grain structure formed by laser melting," *Materials Science and Engineering: A,* vol. 625, pp. 221-229, 2015.

[192] O. Conejero, M. Palacios, and S. Rivera, "Premature corrosion failure of a 316L stainless steel plate due to the presence of sigma phase," *Engineering Failure Analysis,* vol. 16, no. 3, pp. 699-704, 2009.

[193] H. Sahlaoui and H. Sidhom, "Experimental investigation and analytical prediction of σ-phase precipitation in AISI 316L austenitic stainless steel," *Metallurgical and Materials Transactions A,* vol. 44, no. 7, pp. 3077-3083, 2013.
[194] Y. Kim *et al.*, "The effect of sigma phases formation depending on Cr/Ni equivalent ratio in AISI 316L weldments," *Materials & Design,* vol. 32, no. 1, pp. 330-336, 2011.
[195] P. Edwards, A. O'Conner, and M. Ramulu, "Electron beam additive manufacturing of titanium components: properties and performance," *Journal of Manufacturing Science and Engineering,* vol. 135, no. 6, p. 061016, 2013.
[196] C. Körner, H. Helmer, A. Bauereiß, and R. F. Singer, "Tailoring the grain structure of IN718 during selective electron beam melting," in *MATEC Web of Conferences*, 2014, vol. 14, p. 08001: EDP Sciences.
[197] X. Zhou *et al.*, "Textures formed in a CoCrMo alloy by selective laser melting," *Journal of Alloys and Compounds,* vol. 631, pp. 153-164, 2015.
[198] X. Lin, T. M. Yue, H. O. Yang, and W. D. Huang, "Laser rapid forming of SS316L/Rene88DT graded material," *Materials Science and Engineering: A,* vol. 391, no. 1, pp. 325-336, 2005/01/25/ 2005.
[199] Z. Yanushkevich, S. Dobatkin, A. Belyakov, and R. Kaibyshev, "Hall-Petch relationship for austenitic stainless steels processed by large strain warm rolling," *Acta Materialia,* vol. 136, pp. 39-48, 2017.
[200] Y. Kok *et al.*, "Anisotropy and heterogeneity of microstructure and mechanical properties in metal additive manufacturing: A critical review," *Materials & Design,* vol. 139, pp. 565-586, 2018.
[201] R. Kondo, S. Yamakawa, Y. Masuoka, S. Tajima, and R. Asahi, "Microstructure recognition using convolutional neural networks for prediction of ionic conductivity in ceramics," *Acta Materialia,* vol. 141, pp. 29-38, 2017.
[202] X. Li, Y. Zhang, H. Zhao, C. Burkhart, L. C. Brinson, and W. Chen, "A transfer learning approach for microstructure reconstruction and structure-property predictions," *Scientific reports,* vol. 8, 2018.
[203] Z.-L. Wang and Y. Adachi, "Property prediction and properties-to-microstructure inverse analysis of steels by a machine-learning approach," *Materials Science and Engineering: A,* vol. 744, pp. 661-670, 2019.
[204] P. C. Collins, S. Koduri, B. Welk, J. Tiley, and H. L. Fraser, "Neural networks relating alloy composition, microstructure, and tensile properties of α/β-processed TIMETAL 6-4," *Metallurgical and Materials Transactions A,* vol. 44, no. 3, pp. 1441-1453, 2013.
[205] J. Bergstra and Y. Bengio, "Random search for hyper-parameter optimization," *Journal of machine learning research,* vol. 13, no. Feb, pp. 281-305, 2012.
[206] D. Ramachandram and G. W. Taylor, "Deep multimodal learning: A survey on recent advances and trends," *IEEE Signal Processing Magazine,* vol. 34, no. 6, pp. 96-108, 2017.
[207] K. Simonyan, A. Vedaldi, and A. Zisserman, "Deep inside convolutional networks: Visualising image classification models and saliency maps," *arXiv preprint arXiv:1312.6034,* 2013.
[208] B. Zhou, A. Khosla, A. Lapedriza, A. Oliva, and A. Torralba, "Learning deep features for discriminative localization," in *Proceedings of the IEEE conference on computer vision and pattern recognition*, 2016, pp. 2921-2929.
[209] R. R. Selvaraju, M. Cogswell, A. Das, R. Vedantam, D. Parikh, and D. Batra, "Grad-cam: Visual explanations from deep networks via gradient-based localization," in *Proceedings of the IEEE international conference on computer vision*, 2017, pp. 618-626.
[210] W. Yan *et al.*, "Multi-physics modeling of single/multiple-track defect mechanisms in electron beam selective melting," *Acta Materialia,* vol. 134, pp. 324-333, 2017.
[211] L. Banko, Y. Lysogorskiy, D. Grochla, D. Naujoks, R. Drautz, and A. Ludwig, "Predicting structure zone diagrams for thin film synthesis by generative machine learning," *Communications Materials,* vol. 1, no. 1, pp. 1-10, 2020.

[212] U. Prisco, A. Astarita, A. El Hassanin, and S. Franchitti, "Influence of processing parameters on microstructure and roughness of electron beam melted Ti-6Al-4V titanium alloy," *Materials and Manufacturing Processes,* vol. 34, no. 15, pp. 1753-1760, 2019.
[213] H. Stein *et al.*, "A structure zone diagram obtained by simultaneous deposition on a novel step heater: A case study for Cu2O thin films," *physica status solidi (a),* vol. 212, no. 12, pp. 2798-2804, 2015.
[214] J. Brownlee, *Better Deep Learning: Train Faster, Reduce Overfitting, and Make Better Predictions*. Machine Learning Mastery, 2018.
[215] P. Zhang, S. Li, and Z. Zhang, "General relationship between strength and hardness," *Materials Science and Engineering: A,* vol. 529, pp. 62-73, 2011.
[216] D. Tabor, *The hardness of metals*. Oxford university press, 2000.
[217] J.-Y. Zhu, T. Park, P. Isola, and A. A. Efros, "Unpaired image-to-image translation using cycle-consistent adversarial networks," in *Proceedings of the IEEE international conference on computer vision*, 2017, pp. 2223-2232.
[218] J. Frenzel, E. P. George, A. Dlouhy, C. Somsen, M. F. X. Wagner, and G. Eggeler, "Influence of Ni on martensitic phase transformations in NiTi shape memory alloys," *Acta Materialia,* vol. 58, no. 9, pp. 3444-3458, 2010/05/01/ 2010.
[219] S. Shiva, I. Palani, S. Mishra, C. Paul, and L. Kukreja, "Investigations on the influence of composition in the development of Ni–Ti shape memory alloy using laser based additive manufacturing," *Optics & Laser Technology,* vol. 69, pp. 44-51, 2015.
[220] B. A. Bimber, R. F. Hamilton, J. Keist, and T. A. Palmer, "Anisotropic microstructure and superelasticity of additive manufactured NiTi alloy bulk builds using laser directed energy deposition," *Materials Science and Engineering: A,* vol. 674, pp. 125-134, 2016.
[221] P. R. Halani, I. Kaya, Y. C. Shin, and H. E. Karaca, "Phase transformation characteristics and mechanical characterization of nitinol synthesized by laser direct deposition," *Materials Science and Engineering: A,* vol. 559, pp. 836-843, 2013/01/01/ 2013.
[222] B. Zhang, J. Chen, and C. Coddet, "Microstructure and transformation behavior of in-situ shape memory alloys by selective laser melting Ti–Ni mixed powder," *Journal of Materials Science & Technology,* vol. 29, no. 9, pp. 863-867, 2013.
[223] H. Attar, M. Bönisch, M. Calin, L.-C. Zhang, S. Scudino, and J. Eckert, "Selective laser melting of in situ titanium–titanium boride composites: Processing, microstructure and mechanical properties," *Acta Materialia,* vol. 76, pp. 13-22, 2014/09/01/ 2014.
[224] S.-H. Lee, J.-H. Lee, Y.-H. Lee, D. H. Shin, and Y.-S. Kim, "Effect of heating rate on the combustion synthesis of intermetallics," *Materials Science and Engineering: A,* vol. 281, no. 1-2, pp. 275-285, 2000.
[225] N. Resnina, S. Belayev, and A. Voronkov, "Influence of chemical composition and pre-heating temperature on the structure and martensitic transformation in porous TiNi-based shape memory alloys, produced by self-propagating high-temperature synthesis," *Intermetallics,* vol. 32, pp. 81-89, 2013.
[226] H. Sina, S. Iyengar, and S. Melin, "Sintering and Reaction Behaviour in Ni-Ti Powder Mixtures," in *2012 International Conference on Powder Metallurgy & Particulate Materials*, 2012, vol. 5, pp. 05-57: Metal Powder Industries Federation, Princeton, New Jersey.
[227] B. Li, L. Rong, Y.-Y. Li, and V. Gjunter, "Synthesis of porous Ni–Ti shape-memory alloys by self-propagating high-temperature synthesis: reaction mechanism and anisotropy in pore structure," *Acta Materialia,* vol. 48, no. 15, pp. 3895-3904, 2000.
[228] J. Raplee *et al.*, "Thermographic microstructure monitoring in electron beam additive manufacturing," *Scientific reports,* vol. 7, p. 43554, 2017.
[229] D. P. Kingma and J. Ba, "Adam: A method for stochastic optimization," *arXiv preprint arXiv:1412.6980,* 2014.
[230] Y. Qu *et al.*, "Product-based neural networks for user response prediction," in *2016 IEEE 16th International Conference on Data Mining (ICDM)*, 2016, pp. 1149-1154: IEEE.

[231] M. D. Zeiler, "Adadelta: an adaptive learning rate method," *arXiv preprint arXiv:1212.5701,* 2012.
[232] M. Ringnér, "What is principal component analysis?," *Nature biotechnology,* vol. 26, no. 3, pp. 303-304, 2008.